Determination and first principles calculations, using the PAW/GIPAW method, of NMR parameters in inorganic fluorides

Mamata Biswal

l'université nantes angers le mans
PÔLE DE RECHERCHE ET D'ENSEIGNEMENT SUPÉRIEUR

Université du Maine
Le Mans - Laval

Thèse de Doctorat

Mamata BISWAL

Mémoire présenté en vue de l'obtention du
grade de Docteur de l'Université du Maine
sous le label de L'Université Nantes Angers Le Mans

École doctorale : *Matière, Molécules, Matériaux en Pays de la Loire (3MPL)*

Discipline : *Chimie des Matériaux*
Spécialité : *Chimie de l'Etat Solide*
Unité de recherche : *Institut des Molécules et des Matériaux du Mans (IMMM), UMR CNRS 6283*

Soutenue le *29 mai 2013*

Détermination et calcul premiers principes, par la méthode PAW/GIPAW, de paramètres RMN de fluorures inorganiques

JURY

Rapporteurs :	**Christian BONHOMME**, Professeur des universités, Université Pierre et Marie Curie
	Thibault CHARPENTIER, Ingénieur-Chercheur, HDR, CEA Saclay
Examinateur :	**Franck FAYON**, Chargé de recherche CNRS, Université d'Orléans
Invité :	**Jean-Yves BUZARÉ**, Professeur des universités, Université du Maine
Directeur de Thèse :	**Christophe LEGEIN**, Professeur des universités, Université du Maine
Co-directeur de Thèse :	**Florent BOUCHER**, Directeur de recherche CNRS, Université de Nantes
Co-encadrant de Thèse:	**Monique BODY,** Maître de Conférences, Université du Maine

Acknowledgements

This is a sincere attempt to express my gratitude to all the people who are involved in accomplishing this thesis.

The work presented in this thesis, a sincere attempt to discuss elaborately the results of the RMN3MPL project, was carried out under the supervision of Prof. Christophe Legein (thesis supervisor) and Dr. Monique Body (thesis co-advisor) from Institut des Molécules et des Matériaux du Mans (IMMM), CNRS UMR 6283, Université du Maine, and Dr. Florent Boucher (thesis associated supervisor) from Institut des Matériaux Jean Rouxel (IMN), Université de Nantes. It is my great privilege and I sincerely thank them for providing me the opportunity to work for this proposed thesis. I would like to thank them for their kind guidance, constant supports, encouragements and valuable advices throughout this research period.

I am also very grateful to Franck Fayon, chargé de recherché CNRS at Conditions Extrêmes et Matériaux: Haute Température et Irradiation (CEMHTI), UPR CNRS 3079, Orléans, for helping in carrying out the NMR experiments at high field and for his valuable suggestions and explanations in NMR. I wish to express my thankfulness to Aymeric Sadoc, who was a part of this RMN3MPL project during his two years postdoctoral research at Institut des Matériaux Jean Rouxel (IMN), Université de Nantes, for carrying out the computational work and for teaching me the GIPAW calculations.

I sincerely thank Prof. Christian Bonhomme from Laboratoire de Chimie de la Matière Condensée de Paris, UMR CNRS 7574, Collège de France, Université Pierre et Marie Curie, Paris, and Dr. Thibault Charpentier from CEA Saclay, DSM/IRAMIS/SIS2M, UMR CEA/CNRS 3299 for their interest in reviewing this manuscript. It is a great honor for me to have, Prof. Christian Bonhomme, Dr. Thibault Charpentier, Dr. Franck Fayon, and Prof. Jean-Yves Buzaré in the Jury committee.

I would like to thank Jean-Marc Grenèche, director of IMMM and Odile Bohnké and Philippe Lacorre, successive directors of the department of Oxydes et Fluorures (OF) and Florent Calvayrac, director of the department Physique de l'Etat Condensé (PEC) for allowing me to work freely in this institute.

It is my great pleasure to thank Gwenaël Corbel, chargé de recherche CNRS at IMMM for his help in VT X-ray diffraction study and structure refinement of $NaAsF_6$, and Pierrick Durand from X-ray diffraction facility of the Institute Jean Barriol of Université de Lorraine, for carrying out X-ray diffraction and DSC experiments of KPF_6.

I also thank Alain Demourgues, Directeur de Recherche and Etienne Durand, Ingénieur d'Etude, from ICMCB-Pessac for their help in the study of ScF_3 (fluorination experiments).

I wish to thank Dr. Xavier Rocquefelte from IMN for his valuable remarks and discussions on DFT calculations during our group meetings.

I would like to thank Prof. Jens Dittmer, Emeritus Professor Joël Emery and Prof. Alain Bulou from IMMM for their help and valuable suggestions in NMR and other studies.

It is my great pleasure to thank Cyrille Galven, assistant ingénieur, and Radouane Sellak, Ph. D. student, for their help in the DTA measurement, A.-M. Mercier, Jean-Yves Botquelen, Jean-Yves Guerlin, Tony Couapel and Francis Chavanon for the technical support and Brigitte Chevet and Jeannette Lemoine for their help in the administrative work. I am very grateful to all the staff from the departments OF and PEC for their kindness and availability. They have, directly or indirectly, contributed towards the completion of this thesis.

I would like to thank Région Pays de la Loire for the financial support of the RMN3MPL project. Financial support from the TGIR RMN THC FR3050 for conducting NMR experiments at high field is also gratefully acknowledged. The computational presented in this work have been carried out at the Centre Régional de Calcul Intensif des Pays de la Loire (CCIPL), financed by the French Research Ministry, the Région Pays de la Loire, and Nantes University. I am also thankful to CCIPL for CASTEP licenses financial support. I would also like to express my thankfulness to the organizing committee of 7^{th} alpine conference on solid state NMR for providing me a scholarship to attend the conference.

I am thankful to all my Ph.D. colleagues Shashi, Julien, Belto, Stephanie, Uday, Mounesh, Manjunath, Shahin, etc… for being with me in all the occasions and providing me the help whenever I needed and making my stay enjoyable in France.

Finally, my special thanks to my parents, sisters, brothers and near relatives for their never-ending support, unconditional love and care throughout my life. Lastly and most importantly, I wish to thank my dearest husband Susanta for his love, support and encouragement and for being with me whenever I needed. I also want to take this opportunity to thank you for bearing me, according to my mood swings and tantrums, during these three years for being apart from you.

Mamata Biswal

Summary

List of used abbreviations

- **1D:** one-Dimensional
- **2D:** two-Dimensional
- **AE:** All Electrons
- **APO:** Atomic Position Optimized/Optimization
- **ADP:** Anisotropic Displacement Parameters
- **APW:** Augmented Plane Wave
- **BABA:** BAck to Back
- **CPMAS:** Cross Polarization Magic Angle Spinning
- **CSA:** Chemical Shift Anisotropy
- **CW:** Continuous Wave
- **DOS:** Density Of States
- **DQ:** Double Quantum
- **DFT:** Density Functional Theory
- **DOS:** Density of States,
- **DSC:** Differential Scanning Calorimetry
- **DTA:** Differential Thermal Analysis
- **EFG:** Electric Field Gradient
- **ES:** Experimental Structure
- **FID:** Free Induction Decay
- **FO:** Full Optimized/Optimization
- **GGA:** Generalized Gradient Approximation
- **GIAO:** Gauge Invariant Atomic Orbitals
- **GIPAW:** Gauge Including Projector Augmented Wave
- **GTO:** Gaussian Type Orbital
- **HETCOR**: Heteronuclear Correlation
- **HT:** High Temperature
- **ICSD:** Inorganic Crystal Structure Database
- **IDP:** Isotropic Displacement Parameters
- **IGAIM:** Individual Gauge for Atoms In Molecules
- **IS:** Initial structure

- **LAB:** LABoratory frame
- **LAPW:** Linearized Augmented Plane Wave
- **LCAO:** Linear Combination of Atomic Orbitals
- **LT:** Low temperature
- **MAS:** Magic Angle Spinning
- **MTA:** Muffin-Tin Approximation
- **MTO:** Muffin-Tin Orbital
- **MQ-MAS**: Multiple Quantum Magic Angle Spinning
- **NCPP:** Norm Conserving PseudoPotentials
- **NMR:** Nuclear Magnetic Resonance
- **OTF_USPP:** On The Fly_UltraSoft PseudoPotential
- **PAS:** Principal Axis System
- **PAW:** Projector Augmented-wave
- **PBE:** Perdew, Burke and Ernzerhof exchange-correlation functional
- **PW:** Plane Wave
- **QI:** quadrupolar Interaction
- **RF:** Radio-Frequency
- **RT:** Room Temperature
- **SPINAL:** Small Phase INcremental ALternation
- **SPIP:** Sandwiched PI Pulse
- **SQ:** Single Quantum
- **STO:** Slater Type Orbital
- **T_1:** spin-lattice relaxation time (longitudinal)
- **T_2:** spin-spin relaxation time (transverse)
- **TPPM:** Two Pulse Phase-Modulated
- **USPP:** UltraSoft PseudoPotential
- **vdW:** van der Waals
- **VT:** Variable Temperature
- **XiX:** X inverse-X
- **XRPD:** X-ray Powder Diffraction

General introduction

Solid-state NMR is a powerful method for the structural characterization of solid materials (number and relative multiplicities of crystallographic sites, environment, through space and through bond connectivities,...).

The ^{19}F nucleus, a I = 1/2 spin, presents a high sensitivity, 100% natural abundance and large chemical shift dispersion. Thus, ^{19}F NMR provides valuable information on the local environment of fluorine atom. Since the installation of a solid-state NMR spectrometer in 1993 in Le Mans and owing to the longstanding collaboration with the "Oxydes et Fluorures" department, the development of ^{19}F NMR as a characterization tool of amorphous and crystalline, inorganic and hybrid fluorides has become a red thread in the "Caractérisation structurale et dynamique par RMN du solide et Modélisation" (CRM) team research. During the past two decades, this issue has beneficiated from major methodological and instrumental advances in solid state NMR technique as well as advances in calculations of NMR parameters as explained below.

Twenty years ago, the Magic Angle Spinning (MAS) technique was available up to 15 kHz, which allows averaging parts of the dipolar interaction and chemical shift anisotropy, both sources of NMR line broadening, and thus enhances spectral resolution. In numerous studies, the interpretation of ^{19}F MAS NMR spectra was commonly based on the intuitive assumption that similar structural environments lead to similar ^{19}F isotropic chemical shifts (δ_{iso}). By comparison with the ^{19}F δ_{iso} values measured for well-known crystalline binary fluorides, the ^{19}F resonances of crystalline or amorphous compounds can be assigned to different fluorine environments. In the case of sites with different multiplicities, the relative intensities of the corresponding resonances also provide additional constraints for the assignment.[1-12] Looking for a more reliable assignment method, a semi-empirical model is then developed by B. Bureau[13] during its Ph. D. thesis. In this model, the ^{19}F δ_{iso} is calculated from structural data and several phenomenological parameters.

Later on, advances in the MAS technique allow achieving higher spinning frequencies up to 35 kHz, leading to more efficient averaging of strong dipolar interactions and chemical shift anisotropy. With such line-narrowing efficiency, isotropic NMR lines are more resolved and the study of complex multisite fluorides becomes easier. ^{19}F NMR studies of barium and/or calcium and/or sodium fluoroaluminates were then undertaken. An assignment of the ^{19}F NMR lines to the F sites was attempted, using the semi-empirical model previously defined and we then realized that its phenomenological parameters may need to be refined, depending on the family of compounds.[14-17] This model was nonetheless helpful for the characterization of F environments in disordered oxyfluoride compounds.[18-20] Simultaneously, and to avoid the use of such phenomenological

parameters, *ab initio* calculations of shielding tensors were carried out, using the Gauge Including Atomic Orbital (GIAO) method in the Gaussian code.[21,22] This method is efficient on molecular systems but, in the case of crystalline compounds, they require non-trivial definitions of cluster to mimic the crystalline structure. Moreover, for these two approaches, uncertainties on calculation results were sometimes larger than the experimentally measured ^{19}F δ_{iso} difference between two distinct resonances, preventing an unambiguous assignment of the ^{19}F NMR resonances.

SATRAS[23,24] and MQ-MAS[25] sequences were applied on ^{23}Na and ^{27}Al nuclei, allowing precise determination of their quadrupolar parameters even in multisite compounds.[15,16,26-28] The Linearized Augmented Plane Wave (LAPW)[29] approach, using the periodic boundary conditions, implemented within the WIEN2k code[30] was used to predict Electric Field Gradient (EFG) tensors, and turns out to be really robust and accurate.[15,16,26,27,31] This method was then applied as a complementary tool to the solid state NMR and powder diffraction techniques for refinement or determination of the crystalline structures of β-Ba_3AlF_9,[27] β-$CaAlF_5$[15] and β-Pb_2ZnF_6.[32]

New developments in hardware and pulse sequence design occurred and correlation NMR sequences, which provide information about spatial proximities or through-bond connectivities, became feasible in solid-state. CP-MAS HETCOR,[33] *J*-HMQC[34,35] and DQ-SQ[36] have been used to probe heteronuclear ($^{19}F/^{27}Al$,[37] $^{19}F/^{207}Pb$[32,38]) and homonuclear ($^{19}F/^{19}F$) proximities[32,37-40] leading to partial or complete experimental assignments of F sites in several inorganic fluorides such as $Pb_5Ga_3F_{19}$, β-Pb_2ZnF_6, β-$BaAlF_5$, α-$CaAlF_5$, $Ba_3Al_2F_{12}$ and α-$LaZr_2F_{11}$. For β-$BaAlF_5$, α-$CaAlF_5$, $Ba_3Al_2F_{12}$ compounds,[37,39] these experimental assignments differ from those previously established with the semi-empirical model,[14] thus revealing the need for a more accurate method for calculation of ^{19}F δ_{iso} values. The great potential in combining powder diffraction, multidimensional and multinuclear NMR to determine structures of crystalline compounds, and *ab initio* calculations to refine the atomic positions was illustrated on $Pb_5Ga_3F_{19}$[38] and β-Pb_2ZnF_6.[32] Moreover, the multiple-quantum filtered *J*-resolved experiment[41] has been proposed to accurately measure heteronuclear ^{19}F-^{207}Pb ^1J-coupling constants, even though these couplings are not visible on high speed ^{19}F 1D MAS spectra.

Ulltrafast MAS (up to 70 kHz) and ultrahigh field (up to 23.3 T) are now available allowing another substantial improvement of the resolution of ^{19}F 1D and 2D NMR spectra and were applied on β-$BaAlF_5$, α-$CaAlF_5$[15] and $Ba_3Al_2F_{12}$,[38,39] β-ZrF_4 and CeF_4[17], α- and β-$NaCaAlF_6$[16] and α-$LaZr_2F_{11}$.[40]

In 2001, the pioneering work of Pickard and Mauri gives rise to a major breakthrough in calculations of NMR parameters of crystalline systems using periodic boundary conditions, leading to the GIPAW[42,43] approach. Implemented in the CASTEP[44] code, it allows the calculation of shielding

and EFG tensors (PAW[45,46] approach) and has widespread applications.[47,48] More recently, Joyce *et al.*[49] has extended the GIPAW approach for the calculation of *J*-coupling tensors.

The calculation of NMR parameters (shielding, EFG and *J*-coupling tensors) from first-principles may significantly enhance the utility of NMR. To test the accuracy and robustness of this PAW/GIPAW approach, we then plan to apply, on inorganic fluoride materials, high resolution solid state NMR methods for accurate determination of NMR parameters and experimental assignments when possible, and to compare them with the corresponding calculated parameters and assignments. This project, named RMN3MPL (Résonance Magnétique Nucléaire Multidimensionnelle et Modélisation des Matériaux en Pays de la Loire), was selected and has received financial support from the Région des Pays de la Loire. The first GIPAW calculations on inorganic fluorides have been published[50] between the submission of the project and its beginning. It involves the Institut des Molécules et des Matériaux du Mans (IMMM, UMR CNRS 6283), the Institut des Matériaux Jean Rouxel (IMN, UMR CNRS 6502) of Nantes and the Conditions Extrêmes et Matériaux: Haute Température et Irradiation (CEMHTI, UPR CNRS 3079) of Orléans. This project was divided into two parts. A part was carried out by A. Sadoc (post doctoral position at IMN between 09/2009 and 08/2011) and was devoted to DFT calculations (application and development of GIPAW method), from crystallographic data, of NMR parameters (chemical shifts, quadrupolar parameters and *J*-couplings). This thesis work includes high resolution solid state NMR for precise measurement of NMR parameters, determination of correlation between the various nuclei of the material and assignment of NMR resonances to the crystallographic sites, calculations of EFG using WIEN2k and also calculations applying the PAW/GIPAW method after a training undertaken by A. Sadoc.

The overview of the thesis is as follows.

The **first chapter** of the thesis deals with the basic principles of NMR spectroscopy, the different solid state NMR interactions and the experimental techniques used to study the inorganic fluorides. The general ideas behind the PAW/GIPAW method and its applications are also discussed in this chapter.

The **second chapter** focuses on establishing a correlation between experimental ^{19}F δ_{iso} and calculated ^{19}F isotropic shieldings (σ_{iso}) in binary fluorides with obvious assignment of the ^{19}F NMR lines to the fluorine crystallographic sites, in order to predict the ^{19}F δ_{iso} values with reliable accuracy. We have also determined and calculated the quadrupolar parameters for these binary fluorides which were unknown or not determined/calculated accurately. This chapter is made up of

two papers corresponding to the sections 2.2, on alkali, alkaline earth and rare earth fluorides[51] and 2.3, on column 13 metal fluorides.[52] A third section deals with columns 11, 12 and 14 metal fluorides. Calculations presented in sections 2.2 and 2.3 were achieved by A. Sadoc.

The **third chapter** is devoted to the study of binary fluorides with several fluorine crystallographic sites with one main objective: the assignment of their ^{19}F NMR lines to their crystallographic sites. The studied binary fluorides are column 5 fluorides (TaF_5 and NbF_5, section 3.2)[53] and MF_4 compounds (M = Zr, Hf (column 4), Ce and Th, section 3.3) with narrower chemical shift ranges, on which correlation experiments, based on through space ^{19}F-^{19}F dipolar coupling interaction, have been achieved.

The **fourth chapter** is devoted to the study of ternary fluorides exhibiting large ^{19}F-X ^{1}J-coupling resolved on 1D MAS NMR spectra and phase transitions at temperatures close to room temperature. The structural analysis of $NaAsF_6$ has been carried out by VT X-ray powder diffraction, multinuclear solid state NMR and DFT calculations (section 4.2 made up of one paper).[54] The ongoing study of KPF_6 is included in this chapter (section 4.3).

References

(1) J. M. Miller, *Prog. Nucl. Magn. Reson. Spectrosc.* **1996**, *28*, 255–281.

(2) B. Bureau, G. Silly, J.-Y. Buzaré, J. Emery, C. Legein, C. Jacoboni, *J. Phys.: Condens. Matter* **1997**, *9*, 6719–6736.

(3) L. S. Du, F. Wang, C. P. Grey, *J. Solid State Chem.* **1998**, *140*, 285–294.

(4) B. Bureau, G. Silly, J.-Y. Buzaré, C. Jacoboni, *J. Non-Cryst. Solids* **1999**, *258*, 110–118.

(5) J. F. Stebbins, Q. Zeng, *J. Non-Cryst. Solids* **2000**, *262*, 1–5.

(6) Q. Zeng, J. F. Stebbins, *Am. Mineral.* **2000**, *85*, 863–867.

(7) J. C. C. Chan, H. Eckert, *J. Non-Cryst. Solids* **2001**, *284*, 16–21.

(8) R. E. Youngman, M. J. Dejneka, *J. Am. Ceram. Soc.* **2002**, *85*, 1077–1082.

(9) T. J. Kiczenski, J. F. Stebbins, *J. Non-Cryst. Solids* **2002**, *306*,160–168.

(10) S. Chaudhuri, F. Wang, C. P. Grey, *J. Am. Chem. Soc.* **2002**, *124*, 11746–11757.

(11) T. J. Kiczenski, L.-S. Du, J. F. Stebbins, *J. Non-Cryst. Solids* **2004**, *337*, 142–149.

(12) R. E. Youngman, S. Sen, *Solid State Nucl. Magn. Reson.* **2005**, *27*, 77–89.

(13) B. Bureau, G. Silly, J.-Y. Buzaré, J. Emery, *J. Chem. Phys.* **1999**, *249*, 89-104.

(14) M. Body, G. Silly, C. Legein, J.-Y. Buzaré, *Inorg. Chem.* **2004**, *43*, 2474–2485.

(15) M. Body, G. Silly, C. Legein, J.-Y. Buzaré, F. Calvayrac, P. Blaha, *J. Solid State Chem.* **2005**, *178*, 3655–3661.

(16) C. Martineau, M. Body, C. Legein, G. Silly, J.-Y. Buzaré, F. Fayon, *Inorg. Chem.* **2006**, *45*, 10215–10223.

(17) C. Legein, F. Fayon, C. Martineau, M. Body, J.-Y. Buzaré, D. Massiot, E. Durand, A. Tressaud, A. Demourgues, O. Péron, B. Boulard, *Inorg. Chem.* **2006**, *45*, 10636–10641.

(18) F. Le Berre, M.-P. Crosnier-Lopez, C. Galven, J.-L. Fourquet, C. Legein, M. Body, J.-Y. Buzaré, *Dalton Trans.* **2007**, 2457–2466.

(19) L. Sronek, J. Lhoste, M. Gaudon, C. Legein, J.-Y. Buzaré, M. Body, G. Crinière, A. Tressaud, S. Pechev, A. Demourgues, *J. Phys. Chem. C* **2008**, *112,* 860–866.

(20) C. Galven, C. Legein, M. Body, J.-L. Fourquet, J.-Y. Buzaré, F. Le Berre, M.-P. Crosnier-Lopez, *Eur. J. Inorg. Chem.* **2010**, 5272–5283.

(21) G. Silly, M. Body, J.-Y. Buzaré, C. Legein, B. Bureau, *C. R.Chimie* **2004**, *7*, 403–416.

(22) M. Body, G. Silly, C. Legein, J.-Y. Buzaré, *J. Phys. Chem. B* **2005**, *109,* 10270–10278.

(23) J. Skibsted, N. C. Nielsen, H. J. Bildsoe, H. J. Jakobsen, *J. Magn. Reson.* **1991**, *95*, 88–117.

(24) C. Jäger in B. Blümich (Eds.), Solid State NMR II, Springer-Verlag, Berlin, **1994**, p. 133.

(25) L. Frydman, J. S. Harwood, *J. Am. Chem. Soc.* **1995**, *117*, 5367–5368.

(26) G. Silly, C. Legein, J.Y. Buzaré, F. Calvayrac, *Solid State Nucl. Magn. Reson.* **2004**, *25*, 241–251.

(27) M. Body, G. Silly, C. Legein, J.-Y. Buzaré, F. Calvayrac, P. Blaha, *Chem. Phys. Lett.* **2006**, *424*, 321–326.

(28) M. Body, C. Legein, J.-Y. Buzaré, G. Silly, *Eur. J. Inorg. Chem.* **2007**, 1980–1988.

(29) P. Blaha, K. Schwarz, P. Herzig, *Phys. Rev. Lett.* **1985**, *54*, 1192–1195.

(30) P. Blaha, K. Schwarz, G. K. H. Madsen, D. Kvasnicka, J. Luitz, WIEN2k, An Augmented Plane Wave + Local Orbitals Program for Calculating Crystal Properties, 2001.

(31) M. Body, C. Legein, J.-Y. Buzaré, G. Silly, P. Blaha, C. Martineau, F. Calvayrac, *J. Phys. Chem. A* **2007**, *111,* 11873–11884

(32) C. Martineau, F. Fayon, C. Legein, J.-Y. Buzaré, M. Body, D. Massiot, F. Goutenoire, *Dalton Trans.* **2008**, 6150–6158.

(33) P. Caravatti, L. Braunschweiler, R. R. Ernst, *Chem. Phys. Lett.* **1983**, *100*, 305–310.

(34) A. Lesage, D. Sakellariou, S. Steuernagel, L. Emsley, *J. Am. Chem. Soc.* **1998**, *120*, 13194–13201.

(35) D. Massiot, F. Fayon, B. Alonso, J. Trébosc, J. P. Amoureux, *J. Magn. Reson.* **2003**, *164*, 160–164.

(36) H. Geen, J. J. Titman, J. Gottwald, H. W. Spiess, *Chem. Phys. Lett.* **1994**, *227*, 79–86.

(37) C. Martineau, C. Legein, J.-Y. Buzaré, F. Fayon, *Phys. Chem. Chem. Phys.* **2009**, *11*, 950–957.

(38) C. Martineau, F. Fayon, C. Legein, J.-Y. Buzaré, F. Goutenoire, E. Suard, *Inorg. Chem.* **2008**, *47*, 10895–10905.

(39) Q. Wang, B. Hu, F. Fayon, Julien Trébosc, C. Legein, O. Lafon, F. Deng, J.-P. Amoureux, *Phys. Chem. Chem. Phys.* **2009**, *11*, 10391–10395.

(40) C. Martineau, C. Legein, M. Body, O. Péron, B. Boulard, F. Fayon, *J. Solid State Chem.* **2013**, *199*, 326–333.

(41) C. Martineau, F. Fayon, C. Legein, J.-Y. Buzaré, G. Silly, D. Massiot, *Chem. Commun.* **2007**, 2720–2722.

(42) C. J. Pickard, F. Mauri, *Phys. Rev. B* **2001**, *63*, 245101.

(43) J. R. Yates, C. J. Pickard, F. Mauri, *Phys. Rev. B* **2007**, *76*, 024401.

(44) S. J. Clark, M. D. Segall, C. J. Pickard, P. J. Hasnip, M. J. Probert, K. Refson, M. C. Payne, *Z. Kristallogr.* **2005**, *220*, 567−570.

(45) H. M. Petrilli, P. E. Blöchl, P. Blaha, K. Schwarz, *Phys. Rev. B* **1998**, *57*, 14690–14697.

(46) M. Profeta, F. Mauri, C. J. Pickard, *J. Am. Chem. Soc.* **2003**, *125*, 541–548.

(47) T. Charpentier, *Solid State Nucl. Magn. Reson.* **2011**, *40*, 1–20.

(48) C. Bonhomme, C. Gervais, F. Babonneau, C. Coelho, F. Pourpoint, T. Azaïs, S. E. Ashbrook, J. M. Griffin, J. R. Yates, F. Mauri, C. J. Pickard, *Chem. Rev.* **2012**, *112*, 5733−5779.

(49) S. A. Joyce, J. R. Yates, C. J. Pickard, F. Mauri, *J. Chem. Phys.* **2007**, *127*, 204107.

(50) A. Zheng, S.-B. Liu, F. Deng, *J. Phys. Chem. C* **2009**, *113*, 15018–15023.

(51) A. Sadoc, M. Body, C. Legein, M. Biswal, F. Fayon, X. Rocquefelte, F. Boucher, *Phys. Chem. Chem. Phys.* **2011***, 13,* 18539-18550.

(52) A. Sadoc, M. Biswal, M. Body, C. Legein, F. Boucher, D. Massiot, F. Fayon, submitted to *Solid State Nucl. Magn. Reson.*, September 11th 2013.

(53) M. Biswal, M. Body, C. Legein, A. Sadoc, F. Boucher, *J. Solid State Chem.* **2013**, *207*, 208-217.

(54) M. Biswal, M. Body, C. Legein, G. Corbel, A. Sadoc, F. Boucher, *J. Phys. Chem. C* **2012**, *116*, 11682-11693.

Chapter 1: Solid state nuclear magnetic resonance and first-principles calculation

1.1 Introduction

This chapter describes the general principles of Nuclear Magnetic Resonance (NMR) spectroscopy in the first section. In the second section, the different interactions that are of importance in the solid-state are described and the corresponding Hamiltonians are given. In section 3, the experimental techniques, such as magic-angle spinning (MAS) NMR, decoupling, Hahn echo, double quantum-single quantum (DQ-SQ) correlation experiment, and which are used in this manuscript are presented. In section 4, the main ideas underlying the linearized augmented plane wave (LAPW) and projector augmented wave/gauge including projector augmented wave (PAW/GIPAW) approaches within the density functional theory (DFT) are discussed. Conventions used for the tensor parameters are summarized at the end of this section.

1.2 Basic of NMR spectroscopy

NMR involves detailed manipulations of nuclear spins. In order to understand NMR spectroscopy, it is necessary to understand how nuclei, which have a nuclear spin angular momentum *I* and a magnetic moment μ, behave in a static magnetic field B_0. The different steps, (1- behaviour of the nuclear spin system when placed in an external magnetic field, 2- irradiation of the sample through the application of a radio frequency (*rf*) pulse, and 3- detection of magnetization accompanying its return to the initial state when the *rf* pulse is removed) involved to obtain an NMR signal are also explained below. This section also includes the basic idea behind a two dimensional experiment.

1.2.1 Nuclear spin and angular momentum

An object has an angular momentum when it rotates about an axis. Spin, which is an intrinsic property of elementary particles, is a form of angular momentum. The overall nuclear spin results from a combination of all spin angular momentum contributions from its nucleons. It is quantized and the total spin quantum number can be any integer or half-integer. The magnitude *P* of total angular momentum of a nucleus having a spin is given by:

$$P = \hbar\sqrt{I(I+1)}$$

where *I* is the nuclear spin quantum number and $\hbar = \frac{h}{2\pi}$ (*h* is Planck's constant).

The z component of the spin angular momentum is $P_z = m\hbar$, where *m* is the magnetic or directional quantum number with values $m = I, I-1, \ldots, -I$ which gives a total of $(2I+1)$ possible

values. In the absence of external field, each of these $(2I + 1)$ states has the same energy: they are degenerate.

1.2.2 Nucleus in a static magnetic field

If a nucleus with spin angular momentum *I* is placed in a static strong magnetic field B_0, then the magnetic moment μ and the spin angular momentum are proportional to each other according to $\mu = \gamma I$ where γ is the magnetogyric ratio of the studied nucleus. Similar to the z component of spin angular momentum, the z component of nuclear magnetic moment is given by $\mu_z = \gamma m\hbar$.

Placed in an external magnetic field B_0, the magnetic moment of the spin precesses around the field. The frequency of the precession, ω_0, also known as the Larmor frequency, is expressed as $\omega_0 = -\gamma B_0$. The application of this magnetic field breaks the degeneracy as the $(2I + 1)$ states have now slightly different energy levels $E = -\gamma m\hbar B_0$. This splitting is called the Zeeman effect.

Some properties of nuclei studied by NMR in this manuscript are listed in Table 1.

Table 1. Nuclear spin *I*, magnetogyric ratio γ (10^7 rad T^{-1} s^{-1}), natural abundance (%), quadrupolar moment Q[1] (mbarn) and Larmor frequency at 7 T (MHz) for spin $I = \frac{1}{2}$ and quadrupolar $\left(I > \frac{1}{2}\right)$ nuclei studied in the manuscript.

Nucleus	*I*	γ	Natural abundance	Q	Larmor frequency
^{19}F	1/2	25.18	100	/	282.40
^{23}Na	3/2	7.08	100	104	79.39
^{25}Mg	5/2	-1.64	10	199.4	18.36
^{75}As	3/2	4.60	100	314	51.39
^{71}Ga	3/2	8.18	39.9	107	91.53
^{115}In	9/2	5.90	95.7	770	65.73
^{207}Pb	1/2	5.58	22.6	/	68.76

1.2.3 Observation of NMR signal: a single pulse experiment

In the absence of an external magnetic field, the directions of the spin angular momentum vectors, also called the spin polarization axes,[2] are uniformly distributed, pointing in all possible directions in space. The total nuclear magnetic moment, *M*, obtained by summation of the individual contributions of the sample, is nearly equal to zero. When an external magnetic field B_0 is applied, all the nuclear spins in the sample precess around the direction of the applied field. However, due to the thermal motion of the atomic environment, the spin polarization axes vary

slightly, thus breaking their initial isotropic distribution and a macroscopic nuclear magnetic moment *M* appears along the direction of B_0, which is called the longitudinal magnetization. The build-up of this longitudinal magnetization is characterized by a relaxation time T_1 also called spin-lattice relaxation time.

Since detection along the direction of the external field (by convention, the *z*-axis) is not feasible, therefore what is usually measured by NMR is the magnetization perpendicular to the field. This is made possible by rotating the longitudinal magnetization with the help of an *rf* pulse of appropriate frequency and duration. The resulting net magnetic moment, now perpendicular to B_0 , is called transverse magnetization. When the *rf* pulse is switched off, the transverse magnetization starts to precess in the *xy* plane. In order to detect this precession, a wire coil is placed near the sample, with its axis aligned in the *xy* plane. The transverse magnetization precession induces an oscillating current in the coil, called Free Induction Decay (FID), which is recorded as a function of time. The decay of the transverse magnetization is due to two phenomena: the return of *M* along the z-axis, characterized by T_1, and the loss of coherence between the nuclear spins, characterized by a relaxation time T_2 called spin-spin relaxation time.

1.2.4 Two-dimensional experiments

The basic difference between the 2D and 1D NMR experiments is that in 1D experiment the signal is recorded as a function of a single time variable, whereas in 2D experiment it is recorded as a function of two time variables, t_1 and t_2. In general, these 2D experiments involve four steps, *i.e.* preparation, evolution, mixing and detection (Fig. 1). The preparation period involves the generation of magnetization through the application of a single or a series of *rf* pulses. This magnetization then evolves during t_1, which corresponds to the evolution period. Then one or more pulses are applied during the mixing period, to obtain a transverse magnetization. The last step involves the detection of the signal during the t_2 time. These four periods form a 2D pulse sequence.

The pulse sequence is repeated many times, and the duration of the evolution period, t_1 is stepwise incremented. For each value of t_1, a separate FID is recorded as a function of t_2. Thereby a range of FIDs is collected, forming a data set that is a function of the two time variables, t_1 and t_2. A double Fourier Transformation then converts the time signals to the corresponding frequency domains, F1 and F2. Finally, the 2D spectrum obtained is characterized by a contour plot with frequency axes labeled F1 and F2.

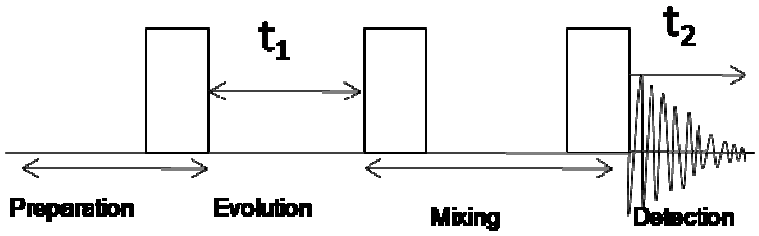

Fig. 1. A general representation of the pulse sequence of a 2D experiment.

1.3 Interactions in solids

In order to deal with NMR in the solid state, it is necessary to consider the important interactions that a nuclear spin experiences in a solid. A typical nuclear spin Hamiltonian may be represented as:

$$\widehat{H} = \widehat{H}_z + \widehat{H}_{rf} + \widehat{H}_{CS} + \widehat{H}_{DD} + \widehat{H}_Q + \widehat{H}_J,$$

and the terms are explained as follows:

- $\widehat{H}_Z$, the Zeeman Hamiltonian that describes the interaction of the nuclear spins with the external magnetic field, B_0;
- $\widehat{H}_{rf}$, the *rf* Hamiltonian that describes the interaction of the nuclear spins with the external time dependent field, $\mathrm{B}_1(t)$;
- $\widehat{H}_{CS}$, the chemical shift Hamiltonian that describes the indirect magnetic interaction of the external magnetic field and nuclear spins through the involvement of the electrons;
- $\widehat{H}_{DD}$, the dipole-dipole coupling Hamiltonian that describes the through-space spin-spin interaction;
- $\widehat{H}_Q$, the quadrupolar coupling Hamiltonian that describes interaction of nuclei having $I > \frac{1}{2}$ with the surrounding electric field gradient;
- $\widehat{H}_J$, the scalar coupling Hamiltonian that describes the spin-spin interaction that is mediated by the bonding electrons.

The first two terms, $\widehat{H}_Z$ and $\widehat{H}_{rf}$ are called “external” interactions as the B_0 and $B_1(t)$ fields are generated externally whereas the remaining terms are considered as “internal” interactions. Here we will give a brief discussion about the important internal interactions experienced by a solid.

1.3.1. Chemical shift and chemical shift anisotropy

In a sample, nuclei of atoms are surrounded by electrons. When an external magnetic field B_0 is applied, a local field is generated, due to the interaction between B_0 and the electrons surrounding a nucleus, which shields this nucleus from B_0. The effective magnetic field B_{eff} experienced by the nucleus is defined as

$$B_{eff} = B_0\,(1-\sigma),$$

with σ the shielding tensor. Differences in shieldings arise, due to the differences in the electronic environments.

The shielding tensor σ is a second-rank tensor, which is described by a diagonal matrix when expressed in its principal axis system (PAS):

$$\sigma = \begin{pmatrix} \sigma_{xx} & 0 & 0 \\ 0 & \sigma_{yy} & 0 \\ 0 & 0 & \sigma_{zz} \end{pmatrix},$$

with $|\sigma_{zz}-\sigma_{iso}| \geq |\sigma_{xx}-\sigma_{iso}| \geq |\sigma_{yy}-\sigma_{iso}|$.

The isotropic shielding, σ_{iso}, is defined as the average of the diagonal elements of the shielding tensor: $\sigma_{iso} = \frac{1}{3}(\sigma_{xx}+\sigma_{yy}+\sigma_{zz})$. Similarly the anisotropic part of the shielding and the asymmetry parameter are defined as:

$$\sigma_{csa} = (\sigma_{zz}-\sigma_{iso}) \text{ and } \eta_{csa} = \frac{(\sigma_{yy}-\sigma_{xx})}{\sigma_{iso}}.$$

The Hamiltonian representing the shielding is given by $\hat{H}_{CS} = \gamma\, h\, \hat{I}_z.\sigma_{zz}^{lab}.B_0$, where σ_{zz}^{lab} is the z-component of the shielding tensor in the laboratory (LAB) frame and is obtained by performing the appropriate set of rotations from the PAS to the LAB frame and this tensor element is given by,

$$\sigma_{zz}^{LAB} = \sigma_{iso} + \frac{\sigma_{csa}}{2}\left[(3\cos^2\theta - 1) + \eta_{csa}(sin^2\theta\cos 2\phi)\right],$$

with θ and ϕ the polar angles.

In NMR experiments, the frequency of lines is measured relative to a reference and it is called chemical shift with respect to that reference. So, the shielding and chemical shift, expressed in ppm, are related by,

$$\delta_{sample} = \frac{\sigma_{ref}-\sigma_{sample}}{1-\sigma_{ref}} \times 10^6 \approx (\sigma_{ref}-\sigma_{sample}) \times 10^6\,.$$

Therefore, the isotropic chemical shift is defined as $\delta_{iso} = \frac{1}{3}(\delta_{xx}+\delta_{yy}+\delta_{zz})$, with the following convention of the principal components: $|\delta_{zz}-\delta_{iso}| \geq |\delta_{xx}-\delta_{iso}| \geq |\delta_{yy}-\delta_{iso}|$. As for the

shielding tensor, an anisotropic parameter δ_{csa}, and an asymmetry parameter η_{csa} are given by the following equations:

$$\delta_{csa} = (\delta_{zz} - \delta_{iso}) \text{ and } \eta_{csa} = \frac{(\delta_{yy} - \delta_{xx})}{\delta_{iso}}.$$

The chemical shift interaction is sensitive to the electronic environment of nuclei and can provide valuable structural information, especially on the coordination number and nature of the first neighbors.

1.3.2 Dipolar interaction

The dipolar interaction results from the interaction of one nuclear spin with a magnetic field generated by another nuclear spin, and vice versa. This is a direct through space interaction which is dependent upon the γ of each nucleus and the inverse cube of the internuclear distance between the two spins. The heteronuclear dipolar coupling arises from an interaction between the nuclear magnetic moments of two different nuclear spins, *I* and *S*, and its secular part is given by,[3]

$$\hat{H}_{DD}^{hetero} = -d(3cos^2\theta - 1)\hat{I}_z\hat{S}_z$$

where $d = \left(\frac{\mu_0}{4\pi}\right)\frac{\gamma_I\gamma_S}{r_{IS}^3}\hbar$ and is called the dipolar coupling constant, r_{IS} is the internuclear distance, μ_0 is the permeability of free space, γ_I and γ_S are the magnetogyric ratios of the *I* and *S* nuclei, respectively, and $\hat{I}_z$ and $\hat{S}_z$ are the z-components of $\hat{I}$ and $\hat{S}$, respectively. The θ angle describes the orientation of the internuclear vector with respect to the orientation of B_0.

A similar kind of coupling also exists between like spins called homonuclear dipolar coupling and the secular part for homonuclear dipolar coupling is given by,[3]

$$\hat{H}_{DD}^{homo} = -d' \frac{(3\cos^2\theta - 1)}{2}\left(3\hat{I}_z\hat{S}_z - \hat{I}\cdot\hat{S}\right)$$

with $d' = \left(\frac{\mu_0}{4\pi}\right)\frac{\gamma_I^2}{r_{12}^3}\hbar$, the dipolar coupling constant and $\hat{I}\cdot\hat{S} = \hat{I}_x\hat{S}_x + \hat{I}_y\hat{S}_y + \hat{I}_z\hat{S}_z$.

Strong homo and hetero nuclear dipolar couplings give rise to large line broadening and this will lead to low resolution of the NMR spectrum. These interactions are usually strong and common in the case of abundant nuclei with large magnetogyric ratio, such as ^{1}H or ^{19}F. However, two possible ways are available to reduce or remove this dipolar interaction, one is to take advantage of the widely used MAS technique and the other is decoupling. Both the techniques are discussed in the next section.

1.3.3 Quadrupolar interaction

Quadrupolar nuclei ($I > \frac{1}{2}$) possess a nuclear quadrupole moment *Q* due to the non-spherical symmetry of the nuclear charge distribution. The interaction between *Q* and the electric field gradient (EFG) due to the non-cubic local symmetry is called quadrupolar interaction (QI). The EFG, defined as the second derivative of the electrostatic potential, is a second-rank tensor. In principal axis system, it is described by the following matrix:

$$V = \begin{pmatrix} V_{XX} & 0 & 0 \\ 0 & V_{YY} & 0 \\ 0 & 0 & V_{ZZ} \end{pmatrix} \text{ with the convention } |V_{ZZ}| \geq |V_{YY}| \geq |V_{XX}|.$$

As the tensor is traceless, only two of its three components need to be determined. In general, the largest component V_{ZZ} and the asymmetry parameter η_Q are used to characterize the QI. η_Q is defined by the following equation:

$$\eta_Q = \frac{V_{XX} - V_{YY}}{V_{ZZ}} \text{ with } 1 \geq \eta_Q \geq 0.$$

Two parameters are defined to characterize the magnitude of QI, the quadrupolar coupling constant, $C_Q = \frac{eV_{zz}Q}{h}$ and the quadrupolar frequency, $\nu_Q = \frac{3C_Q}{2I\,(2I-1)} = \frac{3eV_{zz}Q}{2I(2I-1)h}$, with *e* the electron charge, *h* the Planck's constant, *Q* the quadrupolar moment and *I* the nuclear spin of the nucleus.

The total Hamiltonian for a quadrupolar nucleus can be expressed as the sum of the Hamiltonians for the Zeeman and quadrupolar interactions (without taking into consideration the interactions from dipolar coupling and chemical shielding anisotropy), $\widehat{H} = \widehat{H}_z + \widehat{H}_Q$.

When the quadrupolar interaction is much smaller than the Zeeman interaction, then to a first order approximation, the frequency of the transition $m \leftrightarrow m-1$ is given by:

$$\nu^{(1)}_{m\leftrightarrow m-1} = \nu_0 - \frac{1}{4}\nu_Q(2m-1) \times [3cos^2\theta - 1 + \eta\, sin^2\theta\, cos2\phi],$$

where θ and ϕ are the polar angles describing the orientation of the tensor PAS in the LAB frame. The central transition remains unaffected by the first order quadrupolar interaction.

For quadrupolar nuclei having larger value of quadrupolar interaction, the first order approximation is no more sufficient to describe the spectrum and approximation to the second order has to be considered. In such cases, the frequency of the transition $\frac{1}{2} \leftrightarrow -\frac{1}{2}$ is now given by:[4]

$$\nu^{(2)}_{\frac{1}{2}\leftrightarrow -\frac{1}{2}} = -\frac{1}{6\nu_0}\nu_Q^2\left[I(I+1) - \frac{3}{4}\right][A(\eta,\phi)cos^4\beta + B(\eta,\phi)cos^2\beta + C(\eta,\phi)],$$

where $A(\eta,\phi) = \frac{-27}{8} + \frac{9}{4}\,\eta\, cos2\phi - \frac{3}{8}\eta^2 cos^2 2\phi$, $B(\eta,\phi) = -\frac{30}{8} - \frac{\eta^2}{2} - 2\eta\cos 2\phi + \frac{3}{4}\eta^2 cos^2 2\phi$, and $C(\eta,\phi) = -\frac{3}{8} + \frac{\eta^2}{3} - \frac{\eta}{4}\cos 2\phi - \frac{3}{8}\eta^2 cos^2 2\phi$.

The second order quadrupolar interaction affects all the transitions, although it is dominant for the central transition and causes a shift of the central resonance. The effects of first and second order quadrupolar interactions on the energy levels are shown for a spin 3/2 nucleus in Fig. 2.

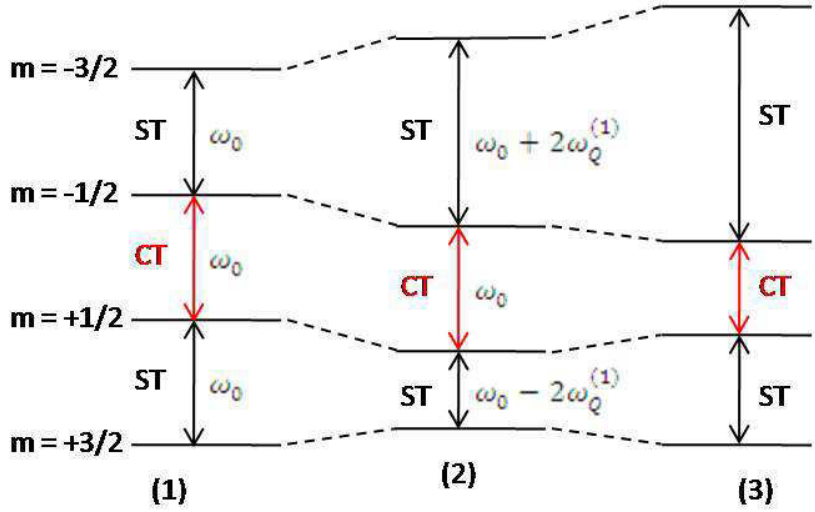

Fig. 2: Schematic energy level diagram for spin I = 3/2 nucleus showing the effect of the (1) Zeeman, (2) first order and (3) second order quadrupolar interactions on the energy levels. The central transition is unaffected by the first order quadrupolar interaction, while all transitions are affected by the second order quadrupolar interaction

1.3.4 *J*-coupling

The scalar coupling or *J*-coupling is considered as a through bond interaction, arising from the interaction of nuclear spins through the chemical bonds. However, hydrogen-bond-mediated *J*-couplings[5,6] and a "through space" ^{19}F-^{19}F *J*-coupling[7] have been observed. *J*-coupling results in splitting of the NMR resonances. The *J*-coupling is rarely observed on solid-state NMR spectra as it is very small in comparison to the other solid-state NMR interactions, *i.e.* dipolar coupling and quadrupolar interactions. However, it gives important structural information about interatomic connectivities. As the chemical bonds are the basis of the *J*-coupling interaction, therefore it is mainly observed in compounds having covalent bonds. The spin Hamiltonian for the *J*-coupling interaction between spins I_j and I_k is written as

$$\hat{H}_{jk}^{J} = 2\pi \hat{I}_j . J_{jk} . \hat{I}_k$$

where J_{jk} is the *J*-coupling tensor. In general this tensor contains isotropic and anisotropic components. The isotropic *J*-coupling is defined as $J_{jk}^{iso} = \frac{1}{3}\left(J_{xx}^{jk} + J_{yy}^{jk} + J_{zz}^{jk}\right)$.

The value of the *J*-coupling depends mainly on the number and nature of bonds between the coupled nuclei, the magnetogyric ratios γ and the extent of overlapping of atomic orbitals. Compounds containing heavy atoms give rise to larger *J*-coupling values as the orbitals of these atoms present larger spatial expansion. *J*-coupling values between ^{19}F and various nuclei are reported in the introduction of the chapter 4.

1.3.4.1 J-coupling multiplet pattern between spin ½ nuclei

The number of peaks observed and their intensity ratios in the *J*-coupling splitting pattern of the NMR spectra follow a binomial distribution. The number of peaks in a multiplet, N_p, can be calculated using the rule $N_p = 2nI + 1$, with n the number of equivalent neighboring nuclei and *I* the spin of the coupled nucleus.

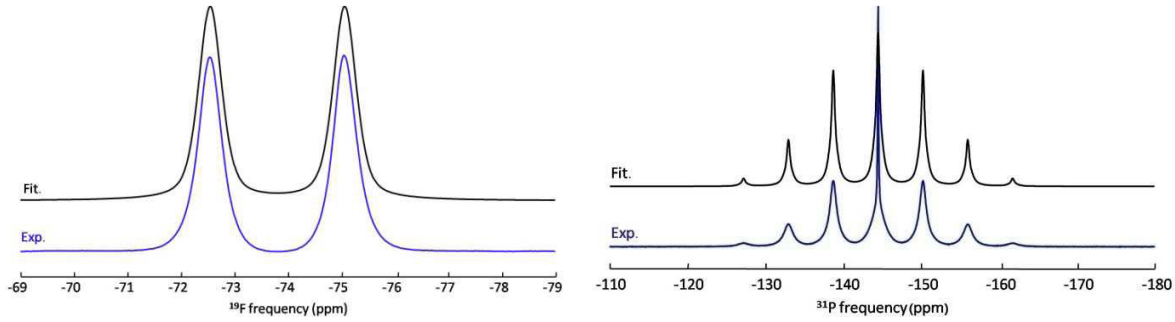

Fig. 3. Experimental (Exp.) and fitted (Fit.) ^{19}F (left) and ^{31}P (right) NMR spectra of KPF_6, recorded at 332 K (sample temperature) and at a spinning frequency of 30 kHz.

The structure of the room temperature phase of KPF_6 presents one F site, one P site and one Li site, and is built-up from isolated PF_6 octahedra.[8] The F atoms are then connected to one P atom, whereas each P atom is coordinated to six F atoms. According to the formula $N_p = 2nI + 1$, the ^{19}F and ^{31}P isotropic lines, shown in fig. 3, are split into a doublet and a septet, respectively. The ^{31}P-^{19}F ^{1}J-coupling values issued from the reconstruction of both the spectra (710 Hz and 700 Hz for the ^{19}F and ^{31}P spectrum reconstructions, respectively) are in agreement with previously determined values of 743 (±12) Hz[9] and 747 Hz[10] for this phase.

A second case of *J*-coupling between two spin ½ nuclei, ^{19}F and ^{207}Pb, is discussed in chapter 2 (see 2.4). The ^{19}F nucleus is 100% abundant but ^{207}Pb, the only lead isotope having non-zero nuclear

spin, has a natural abundance of 22.6 %. Therefore, for a F atom coordinated to x Pb atoms, several F(^{207}Pb)$_n$(Pb)$_{x-n}$ magnetically inequivalent environments are possible (where Pb represents lead nuclei with nuclear spin I = 0, n is the number of ^{207}Pb isotopes and x the total number of lead atoms coordinated to a F one). Each of the magnetically inequivalent environments gives rise to a multiplet whose relative intensity is proportional to its probability of occurrence. The probabilities can be calculated using the following formula:

$P = (1 - A)^{x-n}.(A)^n.C_x^n$,[11] with $C_x^n = \frac{x!}{n!(x-n)!}$ with A the natural abundance of ^{207}Pb.

Therefore the final multiplet observed on NMR spectra is the sum of all the possible multiplets. The details about the *J*-coupling values and intensities of the multiplets for α-PbF_2 are given in the second chapter (2.4.1).

1.3.4.2 J-coupling multiplet pattern between spin ½ and quadrupolar nuclei

When *J*-coupling occurs between a spin ½ nucleus and a quadrupolar one, isotropic lines will be also split into multiplets. On the NMR spectra of the spin ½ nucleus, each isotropic line will show a multiplet of $N_p = 2nS + 1$ lines with S the spin of the quadrupolar nucleus. For $n = 1$, all peaks have the same intensity. The structure of α-$NaAsF_6$ presents one F site, one As site and one Na site, and is built-up from isolated AsF_6 octahedra.[12] Thereby, the ^{19}F NMR spectrum of α-$NaAsF_6$, shown in fig. 4 (left), exhibits four lines of equal intensity, *i.e.* a 1:1:1:1 quartet, arising from the *J*-coupling between ^{19}F and ^{75}As (I = 3/2) (see the section 2 of chapter 4 for more detail).

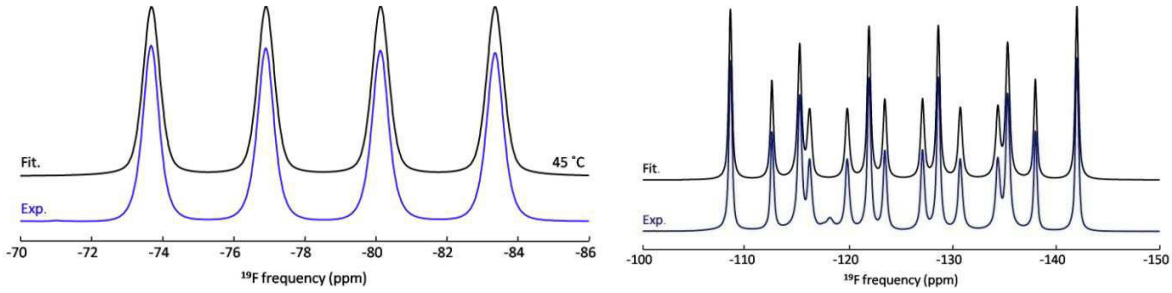

Fig. 4. Experimental (Exp.) and fitted (Fit.) ^{19}F MAS Hahn echo spectra of α-$NaAsF_6$ (left) at spinning frequency of 25 kHz and of β-$KSbF_6$ phase (right) at spinning frequency of 30 kHz.

The NMR spectra of the spin ½ nucleus become more complicated when the quadrupolar nucleus presents several magnetically active isotopes. Then, for each isotope, a $(2nS + 1)$-line multiplet will occur, with a relative intensity proportional to the natural abundance of the isotope. This case is illustrated on the ^{19}F NMR spectrum of the room temperature phase of $KSbF_6$, shown in fig. 4 (right). β-$KSbF_6$ structure presents three F sites, and each F atom is connected to only one Sb

atom, so $n = 1$.[13] The quadrupolar nucleus Sb has two magnetically active isotopes, ^{121}Sb (I = 5/2, γ= 6.4435 x 10^7 rad.T^{-1}.s^{-1}) and ^{123}Sb (I = 7/2, γ= 3.4892 x 10^7 rad.T^{-1}.s^{-1}) with natural abundances equal to 57.2 and 42.8 %, respectively. On the ^{19}F NMR spectrum, we can observe one 8-lines and one 6-lines mutiplets, due to ^{121}Sb-^{19}F and ^{123}Sb-^{19}F J-couplings respectively. The reconstruction parameters are gathered in table 2. The experimental relative intensities (58.9 and 41.1 %) of the two multiplets are in good agreement with the natural abundances of the two isotopes (57.2 and 42.8 %). Moreover, the ratio $\frac{^{121}\text{Sb}-^{19}\text{F}\ J-\text{coupling}}{^{123}\text{Sb}-^{19}\text{F}\ J-\text{coupling}}$ agrees well with the $\frac{^{121}\text{Sb}\ \gamma}{^{123}\text{Sb}\ \gamma}$ ratio (calculated equal to 1.835 and 1.847, respectively). The ^{121}Sb-^{19}F and ^{123}Sb-^{19}F J-coupling values are also in fine agreement with the values previously determined: ^{19}F-^{123}Sb =1018 (± 10) Hz[9] and ^{19}F-^{121}Sb = 1914 (± 20) Hz and 1820 (± 20) Hz.[9,14]

Table 2. ^{19}F δ_{iso} (ppm), multiplet, ^{121,123}Sb-^{19}F ^1J-coupling (Hz) and relative intensities (%) used for reconstruction of β-$KSbF_6$ NMR spectrum.

δ_{iso}	multiplet	^1J-coupling	Relative intensity
-125.3	6-lines	1890	58.9
-125.3	8-lines	1030	41.1

The J-coupling pattern may also be affected by a strong residual dipolar coupling between spin ½ and quadrupolar nuclei. This arises when the second order quadrupolar effect is transferred to spin ½ nuclei through dipolar coupling and results in a complex J-coupling pattern with asymmetric multiplets, uneven spacing between the peaks and missing peaks in the splitting pattern. The effect of residual dipolar coupling on the NMR spectra of spin ½ nuclei can be taken into account by utilizing the first order perturbation theory when $C_Q/(4S(2S-1)) \ll \nu_{0S}$, with S and ν_{0S} the spin and Larmor frequency of the quadrupolar nucleus, respectively. The combined effects of J-coupling and residual dipolar coupling lead to a shift in the resonance frequencies of the peaks of the multiplet given by,[15]

$$\Delta\nu_m = -m_s J_{iso} + \frac{S(S+1)-3m_s^2}{S(2S-1)}\Delta \text{ with } \Delta = \left(\frac{3D'C_Q}{20\nu_{0S}}\right)[(3cos^2\beta^D - 1) + \eta\, sin^2\beta^D cos2\alpha^D]$$

where $\Delta\nu_m$ is the difference between the resonance frequency of a peak in the spin ½ multiplet and the isotropic frequency, Δ is the residual dipolar shift, D' is the effective dipolar coupling constant which depends on the dipolar coupling constant and the J-coupling anisotropy, *i.e.* $D' = D - \frac{\Delta J}{3}$. It is assumed that the J-tensor is axially symmetric and it unique axis is directed along the bond vector. α^D and β^D are the polar and azimuthal angles which describe the orientation of the dipolar vector with respect to the EFG tensor.

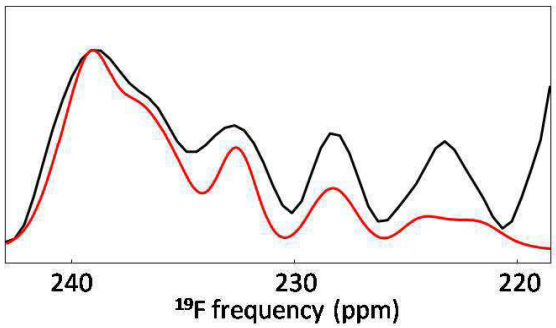

Fig. 5. Experimental (black) and simulated (red) ^{19}F MAS NMR spectrum for F1 site of NbF_5 at a spinning frequency of 32 kHz.

A ^{19}F-^{93}Nb *J*-coupling splitting pattern affected by residual dipolar coupling is clearly visible on the ^{19}F NMR spectrum shown in Fig. 5 (see also 3.2). The F1 site of NbF_5 is bonded to one neighbouring niobium atom[16] and since ^{93}Nb is a spin 9/2 nucleus, ten peaks of same intensities and evenly spaced should be observed on the corresponding ^{19}F NMR spectrum. However due to the residual dipolar coupling, a distorted multiplet is obtained. The parameters used for the simulation are ^{19}F-^{93}Nb *J* = 350 Hz, D' = 4300 Hz, C_Q = 115 MHz, η_Q = 0.2 and $\beta^D = 15°$. A more detailed discussion is given in the chapter 4 (see 4.2).

Up to this point, we have considered only how the spin ½ NMR spectra were affected by the *J*-coupling interaction. The NMR spectra of quadrupolar nuclei also present alteration of their shape, due to the *J*-coupling interaction. All transitions are affected, and each presents a splitting pattern. The number of lines in the *J*-coupling multiplets is given by $N_p = 2nI + 1$, with n the number of equivalent neighboring nuclei and *I* the spin of the coupled nucleus, whereas their intensity ratios follow a binomial distribution.

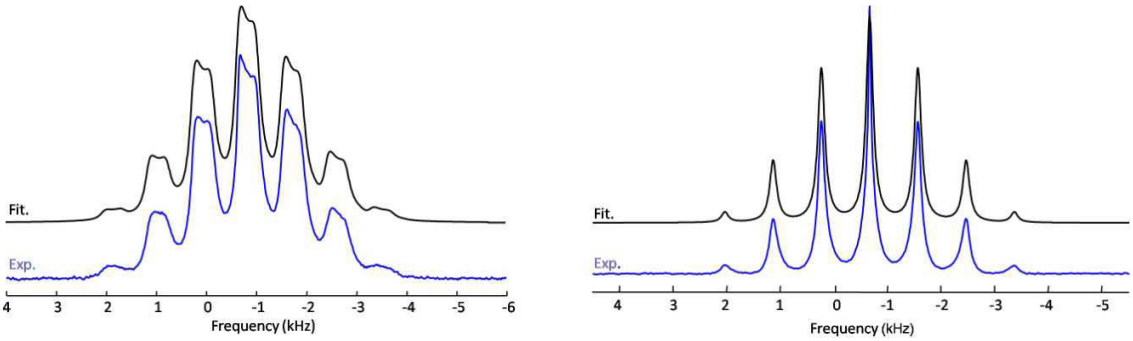

Fig. 6. Experimental (Exp.) and fitted (Fit.) ^{75}As MAS Hahn echo NMR spectra of α-$NaAsF_6$ (left) at 35 °C and a spinning frequency of 20 kHz and of β-$NaAsF_6$ (right) at 70 °C and a spinning frequency of 25 kHz.

Fig. 6 gathers two ^{75}As NMR spectra, affected by *J*-coupling, *i.e.* both exhibiting a septet characteristic of one ^{75}As atom bound to six equivalent fluorine atoms. For the α-$NaAsF_6$ phase, the central transition, presented fig.6 (left), is split in seven lines which are all affected by the quadrupolar second order broadening. On the opposite, in the β-$NaAsF_6$ phase, the ^{75}As nucleus is in

a cubic symmetry site, and thus experiences no quadrupolar interaction. In such a case, the ^{75}As NMR spectrum shape (fig. 6, right) is similar to a spin ½ NMR one (Fig. 3, right).

1.4 Basic Experimental Techniques

This section provides details of the experimental techniques used to record high-resolution solid-state NMR spectra of the various nuclei of the studied inorganic fluorides.

1.4.1 Magic Angle Spinning

MAS[17] is one of the routinely used techniques in the solid state NMR communities as this technique dramatically increases the resolution of the NMR resonances for solids by partially averaging the effect of anisotropic interactions mainly shielding anisotropy, dipolar coupling and quadrupolar interactions. This averaging takes place as these interactions contain the angular factor $(3cos^2\theta - 1)$, where θ is the angle between the principal z-axis of the corresponding interaction tensor and the applied magnetic field (Fig. 7). When the sample spins about an axis making an angle α with B_0, averaging of the orientation dependent interactions occurs and it is expressed by the equation,

$$\langle 3cos^2\theta - 1\rangle = \frac{1}{2}(3cos^2\alpha - 1)(3cos^2\beta - 1)$$

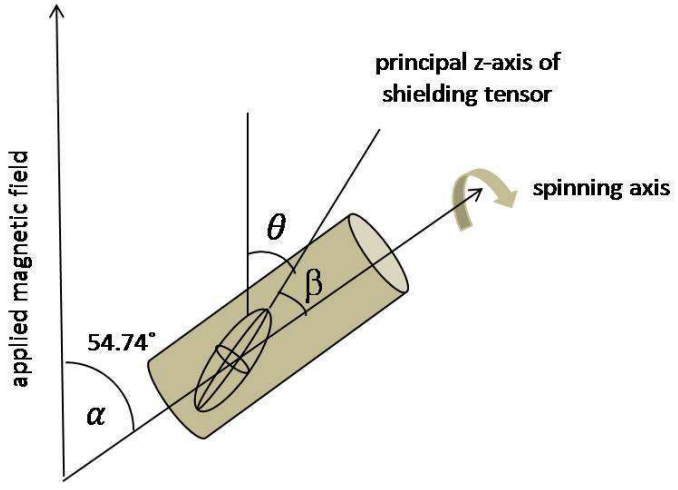

Fig. 7. Rotor spinning about an axis at an angle α with respect to the applied field. The chemical shielding tensor in the form of an ellipsoid and its principal z-axis are shown.

where β is the angle between the principal z-axis of the corresponding interaction tensor and the axis of rotation. When α = 54.74˚, then $(3cos^2\alpha - 1) = 0$ and consequently the average, $\langle 3cos^2\theta - 1\rangle$, is also equal to zero.

The rate of MAS must be greater than or equal to the magnitude of the anisotropic interaction to

average it to zero, otherwise, a manifold of spinning sidebands, separated by the spinning frequency (ν_R), appears on the spectrum (Fig. 8). The isotropic peak which is not always the most intense one remains at the same frequency if the sample temperature is constant.

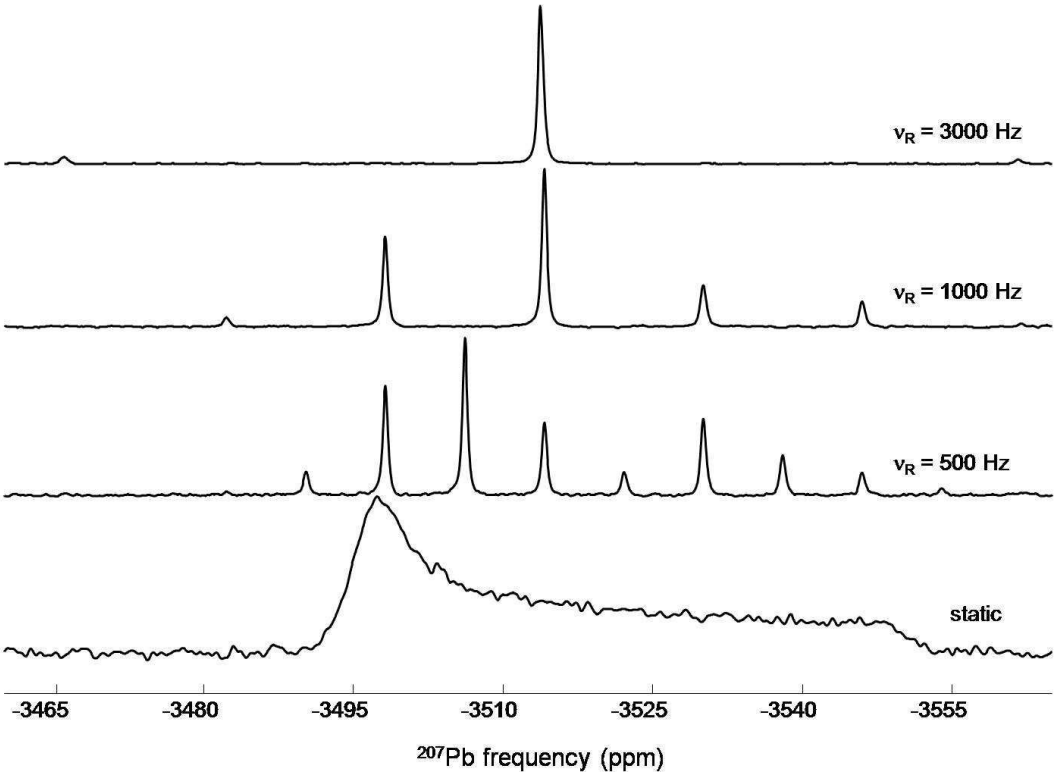

Fig. 8. ^{207}Pb static and MAS NMR spectra of $Pb(NO3)_2$.

1.4.2 Determination of quadrupolar parameters from MAS NMR spectrum of quadrupolar nuclei

As already discussed, the quadrupolar interaction is described by two parameters, the quadrupolar coupling constant, C_Q, and the asymmetry parameter, η_Q. Usually, what we determine from the simulation of the experimental NMR spectrum of quadrupolar nuclei are the quadrupolar frequency ν_Q and the asymmetry parameter η_Q. The width of the spectrum of quadrupolar nuclei having quadrupolar interaction is related to ν_Q, whereas the line shape is related to η_Q.

In principle, MAS is capable of eliminating the first order quadrupolar interaction for quadrupolar nuclei. However the broadening due to the first order quadrupolar interaction is often very large in comparison to the possible spinning frequency. Therefore, the satellite transitions appear as an envelope of spinning sidebands separated by the spinning frequency. For low QI, the central transition, which is not affected by the first order quadrupolar interaction, may appear as a

shapeless line. On the other hand, in most cases, the magnitude of QI is very large, so the effects of second order have to be considered in addition to the effects of first order. The second order QI affects both the central and satellite transitions. MAS is not able to completely average out the second-order quadrupolar broadening as the second order quadrupolar interaction has a more complex angular dependence.

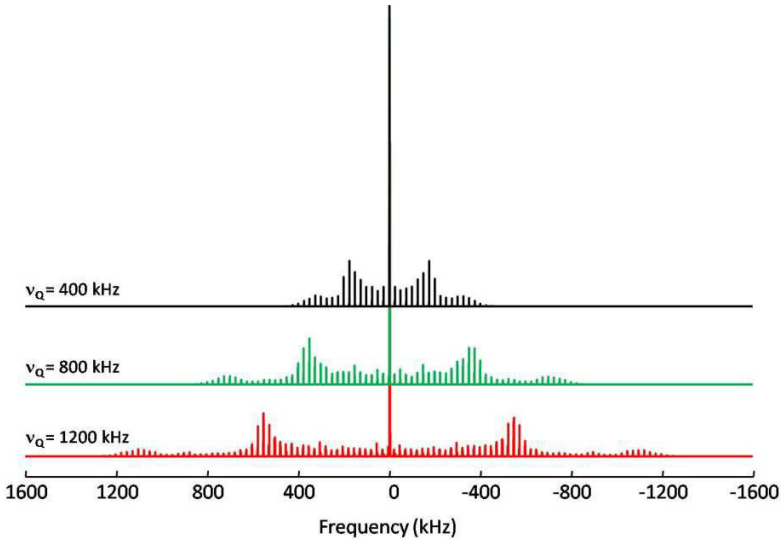

Fig. 9. Evolution of ^{23}Na (I = 3/2) MAS NMR spectra simulated with different values of ν_Q, η_Q = 0, spinning frequency of 25 kHz and line width of 100 Hz.

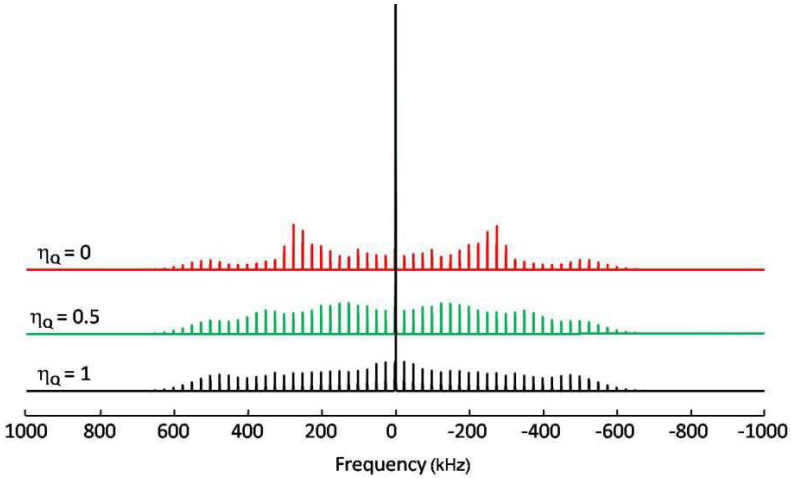

Fig. 10. Evolution of ^{23}Na (I = 3/2) MAS NMR spectra simulated with different values of η_Q and ν_Q = 600 kHz, spinning frequency of 25 kHz and line width of 100 Hz.

In Fig. 9 and 10 are presented the evolutions of the shape of the spinning side band envelope for different values of C_Q and η_Q for ^{23}Na simulated spectra. For nuclei experiencing large QI, the

distribution of satellite transitions under MAS may lead to spinning sidebands of very weak intensity, as shown in fig. 9. However, in such cases the quadrupolar interactions can be determined from the simulation of the central transition. Fig. 11 shows the evolution of the central transition MAS NMR spectrum of a spin 3/2 nucleus with different values of η_Q.

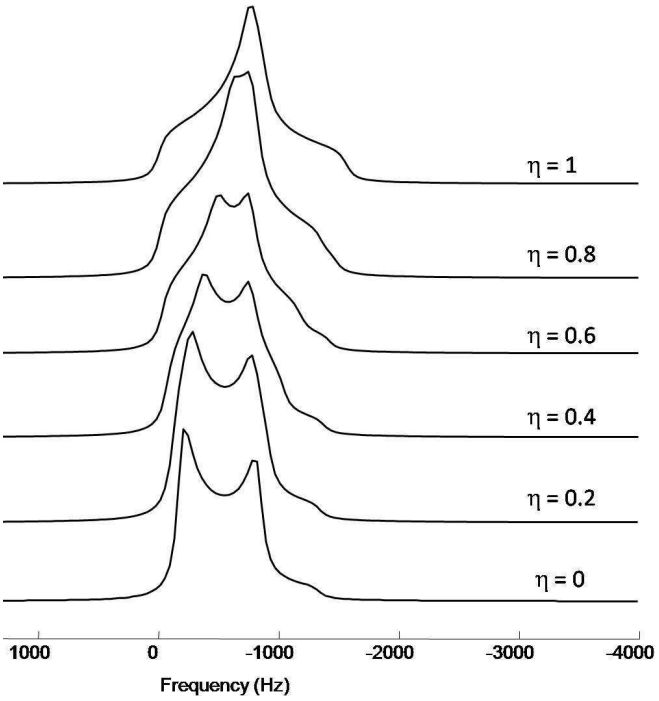

Fig. 11. Evolution of ^{23}Na central transition NMR spectra simulated with ν_Q = 700 kHz, and different values of η_Q, spinning frequency of 20 kHz and line width of 100 Hz.

When the quadrupolar frequencies are low, the central transition is often shapeless and the quadrupolar parameters can be determined from the line shape analysis, observed under MAS, of the satellite transitions (Fig. 9 and 10). This has been explained in detail by various authors.[18-20] The main requirements for these kind of experiments are to have stable spinning frequency and perfect magic angle setting. These experiments are performed by applying non-selective pulse of short time duration for irradiating all the satellite transitions. When all crystallites of the powder sample behave in the same way, we are in the linear regime and the condition is

$\left(I + \frac{1}{2}\right) \nu \, t_p \leq \frac{1}{12}$, where t_p is the pulse length.

1.4.3 Hahn echo

When the FID decays rapidly with respect to the dead time of the spectrometer, Fourier Transformation leads to signal intensities which are strongly reduced and distorted baseline. This technical problem can be minimized in the NMR experiments based on Hahn echo pulse sequence $\left(90^{\circ}_{\mathrm{X}} - \tau - 180^{\circ}_{\mathrm{Y}} - \tau - \mathrm{FID}\right)$ presented Fig. 12, where τ is the echo-delay time. During Hahn echo sequence, the spin system is treated with an initial pulse and, after a delay, is subjected to another pulse (or pulse sequence) which causes the dephasing spin system to rephase (the refocusing pulse).[21] In order to see the full Hahn echo FIDs, the data collection can be started immediately after 180˚ pulses.

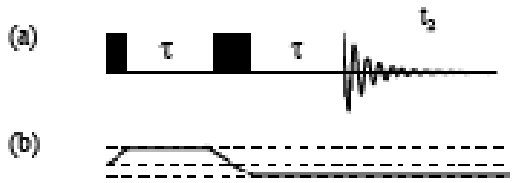

Fig. 12. Hahn echo pulse sequence and the coherence pathways.

The Hahn echo sequence has been used to record all the ^{19}F NMR spectra presented in the manuscript to avoid artifacts and distortion introduced during the first few microseconds of spectrometer dead time at the beginning of the FID. In order to perform Hahn echo experiments on spinning samples, echo delays should be synchronized with the rotor periods.

1.4.4 Heteronuclear decoupling

Higher spectral resolution means that a larger number of resonances will be resolved and thus leads to higher sensitivity. Among other techniques, heteronuclear decoupling is widely used in solid state NMR to achieve high resolution. High-power continuous wave (CW) decoupling is the simplest method and mostly used. As discussed by Melinda Duer,[3] if high power decoupling is used under magic angle spinning, some factors need to be considered, *i.e.* decoupling amplitude and MAS frequency. If the decoupling amplitude and MAS frequency are similar, the two processes interfere. There should be no problem for moderate spinning frequencies (5-20 kHz) and high decoupling amplitudes (> 60 kHz). However a low power decoupling can be more efficient when the spinning frequency is very high. Several other techniques can be used for efficient heteronuclear decoupling, such as the two pulse phase modulation (TPPM)[22], small phase incremental alternation (SPINAL),[23] X inverse-X (XiX)[24] sequences.

Fig. 13 shows the effect of the ^{207}Pb decoupling on the ^{19}F NMR spectra of α-PbF_2. Without ^{207}Pb decoupling, the ^{19}F isotropic resonances are split into multiplets due to the ^{19}F-^{207}Pb *J*-coupling.

From the reconstruction of the ^{19}F NMR spectrum recorded with ^{207}Pb decoupling, we are able to determine precisely the δ_{iso} values and the number of fluorine sites.

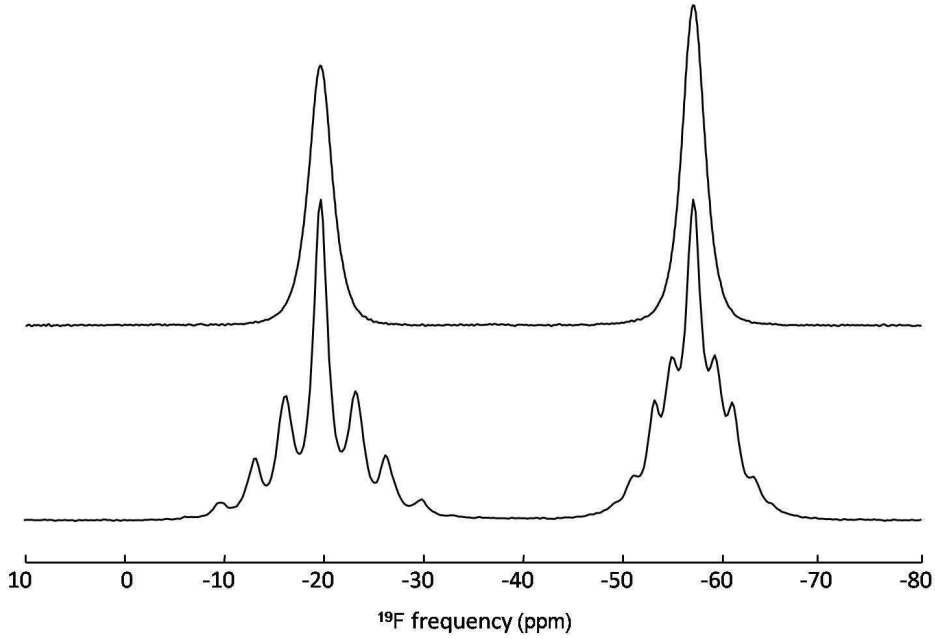

Fig. 13. ^{19}F MAS NMR spectra of α-PbF_2 recorded with (ν_R = 25kHz - top) and without ^{207}Pb decoupling (ν_R = 30kHz - bottom) at a magnetic field of 7.0 T.

1.4.5. 2D DQ-SQ correlation experiments

The basic theme of DQ-SQ correlation experiment involves first the excitation of DQ coherence, which subsequently evolves during an incremented period t_1. The DQ coherence is then converted into observable SQ coherence, which is detected in the acquisition period, t_2. These experiments are used to correlate homonuclear spin ½ nuclei which are coupled through dipolar interaction.

The investigation of dipolar coupling can provide information about spatial connectivity and local geometry since it depends on the inverse cube of the inter-nuclear distance. However in solid-state MAS NMR experiments, the orientation dependent dipolar interactions are averaged out under fast MAS. Therefore to obtain structural information from MAS experiments, it is necessary to reintroduce the dipolar coupling through recoupling experiments. The homonuclear recoupling sequences that have been used so far are the CN_n^ν and RN_n^ν[25,26] symmetry based schemes and the BAck to BAck (BABA)[27] sequences. For slow spinning speeds ($\nu_R \leq$ 15-20 kHz) Post-C7,[28] $C9_1^4$,[29] and $R14_2^6$,[30] sequences can be used as they require the *rf* pulse field strength to be proportional to spinning frequency. The BABA sequence is one of the most popular techniques for DQ homonuclear

dipolar recoupling under fast MAS but is not robust to CSA and to large chemical shift differences. In the case of ^{19}F, such recoupling technique is challenging since ^{19}F NMR spectra exhibits large dispersion of δ_{iso} and large CSA values. An alternative sequence is the sandwiched pi pulse (SPIP)[31] sequence (Fig. 14). It is based on the super-cycled version of the symmetry-based $R2_2^1$ pulse sequence. It is compatible to fast MAS and shows higher robustness to offset and CSA than BABA. Recently the efficiency of SPIP DQ recoupling sequence has been evaluated for high resolution DQ-SQ NMR and used to probe ^{19}F-^{19}F proximities in powdered fluoroaluminates.[32]

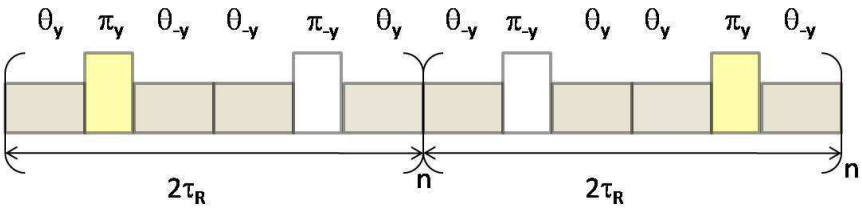

Fig. 14. SPIP pulse sequence for DQ↔SQ excitation or reconversion. The SPIP sequence shown here consists of n-blocks of $2\tau_R$ each belonging to $R2_2^1$ symmetry followed by n-blocks of $2\tau_R$ each belonging to $R2_2^{-1}$ symmetry.

1.4.6 Fit of the NMR spectra

All the NMR spectra presented in this manuscript are fitted using Dmfit software[33] except the ^{19}F NMR spectrum of NbF_5 recorded without ^{93}Nb decoupling which is fitted with Wsolids,[34] allowing to determine independently the direct dipole-dipole coupling constant and the quadrupolar coupling constant.

The 2D one pulse (TOP) procedure[35] has been applied to the ^{115}In MAS spectrum of InF_3 (see 2.3). It allows the reconstruction of the 2D TOP spectrum separating the different spinning sidebands by order and then the reconstruction of the sum spectrum corresponding to an ‘‘ideal infinite spinning rate’’ spectrum which can be modeled using the Dmfit program.[33]

1.5 First principle calculation of NMR parameters

The efficiency of the combined application of solid-state NMR and quantum mechanical calculations for structural characterization is well-known. To complement the experimental work presented in this thesis, first-principles calculations of NMR parameters (shielding and EFG) have been carried out. Two codes, based on Density Functional Theory (DFT), were used that both take into account the periodicity of the crystalline structure through the implementation of periodic boundary conditions. The shielding tensors were calculated using the Gauge Including Projector Augmented Wave (GIPAW)[36,37] approach implemented in the NMR-CASTEP code.[38,39] Recently the two well-documented reviews by Charpentier[40] and Bonhomme et al.[41] demonstrated the extended applications of the calculation of NMR parameters using this GIPAW method. In comparison to the calculation of shielding, calculation of the EFG is rather simple as it depends on the ground state properties *i.e.* ground state charge density and wave function. The EFG tensors were obtained either with the PAW method[42] from NMR-CASTEP or the Linearized Augmented Plane Wave (LAPW)[43,44] approach employed in the WIEN2k code.[45] The ideas to describe the LAPW, PAW and GIPAW methods lie within the density functional theory.

1.5.1 Basics of Density fuctional theory

According to quantum mechanics the energy and the behavior of a collection of electrons and nuclei can be predicted by solving the Schrödinger equation for the system:

$$\hat{H}\psi = E\psi$$

where $\hat{H}$ is the Hamiltonian operator for a molecular system consisting of M nuclei and N electrons in the absence of magnetic or electric fields. $\hat{H}$ is a differential operator representing the total energy:

$$\hat{H} = -\frac{1}{2}\sum_{i=1}^{N}\nabla_i^2 - \frac{1}{2}\sum_{A=1}^{M}\frac{1}{\mathrm{M_A}}\nabla_A^2 - \sum_{i=1}^{N}\sum_{A=1}^{M}\frac{Z_A}{r_{iA}} - \sum_{i=1}^{N}\sum_{j>1}^{N}\frac{1}{r_{ij}} + \sum_{A=1}^{M}\sum_{B>A}^{M}\frac{Z_A Z_B}{R_{AB}}$$

Here, *A* and *B* run over the M nuclei while *i* and *j* denote the N electrons in the system. The first two terms describe the kinetic energy of the electrons and nuclei. The other three terms represent the attractive electrostatic interaction between the nuclei and the electrons and repulsive potential due to the electron-electron and nucleus-nucleus interactions.

The first approximation used to simplify the above complicated equation is that the mass of the nuclei is much greater than the mass of the electrons and it is known as Born-Oppenheimer

approximation. However even this approximation does not allow to solve the Schrödinger equation, as the difficulty lies in the many-body nature of the interacting electrons. The Kohn-Sham formulation of density functional theory takes into consideration this difficulty.

1.5.2 DFT and Kohn-Sham equations

In DFT the central quantity is not the wave function but the electronic charge density ρ(r). In Kohn–Sham formulation, ρ(r) is treated as the fundamental variable and the many-body equation is transferred to a set of *N* equations involving single-particle wave functions.[46]

Within the Kohn-Sham formalism, a set of non-interacting one-electron orbitals $\psi_i(r)$ are defined allowing the computation of $\rho(r)$ as,

$$\rho(r) = \sum_{i}^{occ} |\psi_i(r)|^2$$

where the summation occurs over the occupied orbitals.

These orbitals are obtained from solving the Schrödinger-like Kohn-Sham equations,

$$\left\{-\frac{1}{2}\nabla^2 + V_{eff}(r)\right\}\psi(r) = \varepsilon\Psi(r)$$

with $V_{eff}(r) = V_H[\rho(r)] + V_{ext}(r) + V_{xc}[\rho(r)]$. $V_H[\rho(r)]$ is the Hartree potential (electron–electron repulsion), $V_{ext}(r)$ is the external potential (electron–nuclei interactions) and $V_{xc}[\rho(r)]$ is the so-called exchange-correlation (XC) potential.

The quantum mechanics focuses on the exchange-correlation potential as it is the only unknown term in the Kohn-Sham approach. Therefore one has to go for approximations, which is often a challenging task. For many properties, the use of generalized gradient approximations (GGA) provides good results. Although several GGAs have been proposed, the one defined by Perdew, Burke, and Ernzerhof (PBE)[47] has been used for many solid-state NMR calculations.

1.5.3 Solving the DFT equation, Basis sets and wave functions

Nowadays several codes are available that can solve the DFT equation but they differ in the basis sets. The different basis sets used are linear combination of atomic orbitals (LCAO), Gaussian or Slater type orbitals (GTOs, STOs), plane wave (PW) basis sets with or without augmentations, muffin tin orbitals (MTOs). The wave functions, which represent the basis sets, can be nodeless pseudo-wave functions or all-electron wave functions.

1.5.3.1 The full-potential linearized augmented plane wave (LAPW) method

One of the most accurate methods for solving the Kohn–Sham equations is the full-potential linearized augmented plane wave (FP-LAPW) method implemented in the WIEN2k code. The LAPW method is a procedure for solving the Kohn-Sham equations for the ground state density, total energy, and (Kohn-Sham) eigenvalues of a many-electron system by introducing a finite basis set. The LAPW method is fundamentally a modification of the original augmented plane wave method (APW).[42]

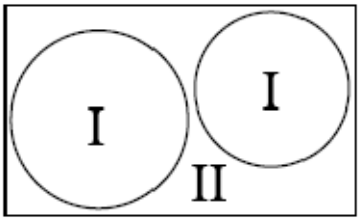

Fig. 15. Partitioning of the unit cell into atomic spheres (I) and an interstitial region (II).

In the LAPW method, the unit cell is partitioned into two different types of regions. One consists of non-overlapping atomic spheres centered on atoms (I), and the other one which consists of the remaining part is called interstitial region (II) (Fig. 15). In order to construct the basis functions the muffin tin approximation (MTA) is used and therefore in region (I) atomic-like functions are used to describe the rapid changes of the wave function whereas plane waves are used in the remaining interstitial region.

Inside the atomic sphere of radius *R*, the wave functions are linear combinations of spherical harmonics and are given by:

$$\emptyset_{K_n} = \sum_{lm}\left[A_{lm,k_n} u_l(r, E_l) + B_{lm,k_n} u_l'(r, E_l)\right] Y_{lm} ,$$

where $u_l(r, E_l)$ is the regular solution of the radial Schrödinger equation for energy E_l and $u_l'(r, E_l)$ is the energy derivative of u_l at the same energy E_l. A linear combination of these two functions constitutes the linearization of the radial function. The two coefficients A_{lm} and B_{lm} are functions of K_n and can be chosen such as this basis function matches (in value and slope) with the plane wave in the corresponding interstitial region. The u_l and u_l' are obtained by the integration of the radial Schrödinger equation on a radial mesh inside the sphere.

Inside the interstitial region a plane wave expansion is used as a basis,

$$\emptyset_{K_n} = \frac{1}{\sqrt{\omega}} e^{ik_n.r}$$

where $k_n = k + K_n$; K_n are the reciprocal lattice vectors and k belongs to the first Brillouin zone.

In a similar way the potential and charge density are expanded by linear combinations of spherical harmonics inside each atomic sphere and as a Fourier series in the interstitial region:

$$V(r) = \begin{cases} \sum_{LM} V_{LM}(r) Y_{LM}(r) & \text{inside sphere} \\ \sum_{K} V_k \, e^{ik.r} & \text{outside sphere.} \end{cases}$$

1.5.3.2. Gauge Including Projector Augmented Wave (GIPAW) method

The *ab-initio* methods available for the calculation of shielding using Gaussian program[48] suit best to systems containing isolated molecules or small cluster models. The method developed by Mauri, Pfrommer and Louie (MPL)[49] for the first time allows the calculation of shielding using periodic boundary conditions in the plane wave pseudopotential formalism. This method allows performing calculations on truly infinite systems and is considered as the first step towards the development of GIPAW[36,37] method introduced by Mauri and Pickard in 2001.[36] It is an extension of PAW method and allows the calculation of all-electron response to a uniform magnetic field and also fulfills the gauge invariance requirement by introducing a large number of projectors.

The GIPAW method, implemented in the PARATEC code,[50] allowed performing calculation using only the norm-conserving pseudopotentials. In the NMR-CASTEP code, the efficiency of GIPAW method has been improved by introducing both the norm-conserving pseudopotential[51] and the ultra-soft pseudopotential (USPP) developed by Vanderbilt.[52] This pseudopotential approach based on the frozen core approximation assumes that the core electrons do not take part in chemical bonding. Therefore their contribution to the magnetic shielding is independent of the chemical environment and can be obtained from a simple calculation on a free atom. Thus the GIPAW method, which uses pseudopotentials and plane wave basis sets and performs calculations on infinite periodic systems, is considered as an effective method for modeling of NMR parameters in solids. For all shielding calculations presented in the manuscript, the core-valence interactions were described by USPP.

There are latest developments in the GIPAW related to the calculation of the *J*-coupling tensor. However they are not yet available to the common-users. Few studies have been reported in the context of calculation of *J*-coupling for light elements.[7,53-58]

1.5.4 Optimization of structures

The dilemma in optimization, *i.e.* if optimization is required or not and if required whether to relax either only atomic positions (atomic position optimization – APO) or both atomic positions and unit cell parameters (full optimization – FO), remains from the beginning of *ab initio* calculations. The NMR parameters, especially the asymmetry ones, are very sensitive to the slight structural

modifications. In some cases a structure optimization (APO or FO) leads to a better agreement between the experimental and calculated NMR results. However to allow relaxation of some or all of the atomic positions or to perform full optimization prior to NMR parameters calculations depends entirely on the system. Clearly, if the error limits on experimental structures are large, then the relaxation can be justified. Still, calculations are carried out at zero K, and in some cases calculations with experimental structure may lead to better agreement with NMR data (normally obtained at 300 K).

We have performed the NMR parameter calculations using several structural data sets such as the structures issued from experimental data (experimental structure – ES), from PBE[47]-DFT APO and FO. Nevertheless, it is well known that the GGA approximation with the PBE functional often overestimates interatomic bond lengths and consequently cell parameters and unit-cell volumes.[12,59-72] In such cases, and to take into account this overestimation, the optimized lattice parameters are rescaled to the experimental volume but keeping atomic positions unchanged, leading to another structural data set (FO rescaled structure).

1.5.5. Conventions used for calculations of NMR parameters

The output of the first-principles calculation, absolute shielding tensor, $\overline{\sigma}$, is defined as the ratio between a uniform external magnetic field, B_0, and the induced magnetic field, $B_{ind}(r)$.

$$B_{ind}(r) = -\bar{\sigma}(r)\, B_0.$$

The shielding tensor is described by three parameters, the isotropic shielding (σ_{iso}), the shielding anisotropy (σ_{csa}) and the asymmetry parameter (η_{csa}) defined respectively as $\sigma_{iso}(ppm) = \frac{1}{3}\left(\sigma_{xx} + \sigma_{yy} + \sigma_{zz}\right)$, $\sigma_{csa}(ppm) = \sigma_{zz} - \sigma_{iso}$ and $\eta_{csa} = (\sigma_{yy} - \sigma_{xx})/\sigma_{csa}$, with the principal components defined in the sequence $|\sigma_{zz} - \sigma_{iso}| \geq |\sigma_{xx} - \sigma_{iso}| \geq |\sigma_{yy} - \sigma_{iso}|$. Additionally, in NMR-CASTEP code, the shielding anisotropy σ_{aniso} is defined as $\sigma_{aniso} = \sigma_{zz} - \frac{\sigma_{xx}+\sigma_{yy}}{2} = \frac{3}{2}\sigma_{csa}$.

The chemical shift tensor is also described by three parameters, the isotropic chemical shift (δ_{iso}), the chemical shift anisotropy (δ_{csa}) and the asymmetry parameter (η_{csa}), determined experimentally, and defined as $\delta_{iso}(ppm) = \frac{1}{3}(\delta_{xx} + \delta_{yy} + \delta_{zz})$, $\delta_{csa}(ppm) = \delta_{zz} - \delta_{iso}$, $\eta_{csa} = (\delta_{yy} - \delta_{xx})/\delta_{csa}$, with the principal components defined in the sequence $|\delta_{zz} - \delta_{iso}| \geq |\delta_{xx} - \delta_{iso}| \geq |\delta_{yy} - \delta_{iso}|$.

For nucleus having spin greater than ½, *i.e.* quadrupolar nuclei, the quadrupolar frequency ν_Q, the quadrupolar coupling constant C_Q and the asymmetry parameter η_Q are related to the electric field gradient tensor components through the following equations: $\nu_Q = 3\,C_Q/[2I(I-1)]$ with $C_Q = eQV_{zz}/h$, and $\eta_Q = (V_{xx} - V_{yy})/V_{zz}$. The V_{ii} are the eigenvalues of the EFG tensor with the convention $|V_{zz}| \geq |V_{yy}| \geq |V_{xx}|$, *e* is the electronic charge, *I* the nuclear spin quantum number and *h* is Planck's constant.

My thesis work is mainly focused on the ^{19}F shielding calculation of inorganic fluorides. To predict ^{19}F δ_{iso} values, the calculated ^{19}F σ_{iso} values have to be converted into the isotropic chemical shift scale. Theoretically, $\delta_{iso} \approx \sigma_{ref} - \sigma_{iso}$. Calculated ^{19}F σ_{iso} values can be converted into ''calculated'' ^{19}F δ_{iso} values once σ_{ref} has been determined. Calculated ^{19}F σ_{iso} values can also be converted into ''calculated'' ^{19}F δ_{iso} values using the experimental absolute scale for fluorine. However to avoid these referencing problems and possible errors coming from the determination of the ^{19}F σ_{ref} value, ''calculated'' ^{19}F δ_{iso} values can also be deduced (i) from the linear regression between calculated ^{19}F σ_{iso} values and experimental ^{19}F δ_{iso} values (which means that an assignment was already done) for the compounds under study or (ii) from a linear regression previously established on numerous compounds and this last approach seems to become the standard practice.

Shielding calculations are carried out with the NMR-CASTEP code whereas EFG tensors are calculated with both the WIEN2k and NMR-CASTEP codes.

1.6 References

(1) P. Pyykkö, *Mol. Phys.* **2008**, *106*, 1965–1974.
(2) M. H. Levitt, *Spin Dynamics, Basics of Nuclear Magnetic Resonance*, Wiley, Chichester, **2001**.
(3) M. J. Duer, *Introduction to Solid-State NMR Spectroscopy*, Blackwell, Oxford, **2004**.
(4) K. J. D. Mackenzie, M.E. Smith, *Multinuclear solid-state NMR of Inorganic Materials*, Elsevier, Oxford, **2002**.
(5) S. P. Brown, M. Perez-Torralba, D. Sanz, R. M. Claramunt, L. Emsley, *Chem. Commun.* **2002**, 1852–1853.
(6) T. N. Pham, J. M. Griffin, S. Masiero, S. Lena, G. Gottarelli, P. Hodgkinson, C. Filip, S. P. *Phys. Chem. Chem. Phys.* **2007**, *9*, 3416–3423.
(7) J. M. Griffin, J. R. Yates, A. J. Berry, S. Wimperis, S. E. Ashbrook, *J. Am. Chem. Soc.* **2010**, *132*, 15651–15660.
(8) K. Kitashita, R. Hagiwara, Y. Ito, O. Tamada, *J. Fluorine Chem.* **2000**, *101*, 173−179.
(9) E. R. Andrew, M. Firth, A. Jasinski, P. J. Randall, *Phys. Lett.* **1970**, *31*, 446−447.
(10) R. Challoner, T. Schaller, A. Sebald, *J. Magn. Reson. A* **1993**, *101*, 106−108.
(11) C. Martineau, Thèse de l'université du Maine, **2008**.
(12) M. Biswal, M. Body, C. Legein, G. Corbel, A. Sadoc, F. Boucher, *J. Phys. Chem. C* **2012**, *116*, 11682−11693.
(13) G. J. Kruger, C. W. F. T. Pistorius, A. M. Heyns, *Acta Cryst. B* **1976**, *32*, 2916−2948.
(14) E. R. Andrew, L. F. Farnell, T. D. Gledhill, *Phys. Rev. Lett.* **1967**, *19*, 6−7.
(15) R. K. Harris, A. C. Oliviery, *Prog. Nucl. Magn. Reson. Spectrosc.* **1992**, *24*, 435–456.
(16) A. J. Edwards, *J. Chem. Soc. A* **1964**, 3714−3718.
(17) I. J. Lowe, *Phys. Rev. Lett***. 1959**, *2*, 285−287.
(18) A. Samoson, *Chem. Phys. Lett.* **1985**, *119*, 29−32.
(19) C. Jaeger, in: B. Blumich, R. Kosfeld (Eds.) NMR Basic Principles and Progress, Springer Verlag, Berlin, **1994**, *31*, 135.
(20) M. E. Smith, E. R. H. Van Eck, *Prog. Nucl. Magn. Reson. Spectrosc.* **1999**, *34*, 159–201.
(21) E. L. Hahn, *Phys. Rev.* **1950**, *80*, 580−594.
(22) A. E. Bennett, C. M. Rienstra, M. Auger, K. V. Lakshmi, R. G. Griffin, *J. Chem. Phys.* **1995**, *103*, 6951−6958.
(23) B. M. Fung, A. K. Khitrin, K. Ermolaev, *J. Magn. Reson.* **2000**, *142*, 97–101.
(24) A. Detken, E. H. Hardy, M. Ernst, B. H. Meier, *Chem. Phys. Lett.* **2002**, *356*, 298–304.
(25) A. Brinkman, M. H. Levitt, *J. Chem. Phys.* **2001**, *115*, 357–384.
(26) M. H. Levitt, *Encyclopedia of Nuclear Magnetic Resonance,* Wiley *2002*, 165–196.
(27) M. Feike, D.E. Demco, R.Graf, J. Gottwald, S. Hafner, H.W. Spiess, *J. Magn. Reson. Series*. *A* **1996**, *122*, 214–221.
(28) M. Hohwy, H. J. Jakobsen, M. Edén, M. H. Levitt, N. C. Nielsen, *J. Chem. Phys.* **1998**, *108*, 2686–2694.
(29) P. K. Madhu, E. Vinogradov, S. Vega, *Chem. Phys. Lett.* **2004**, *394*, 423–428.
(30) M. Carravetta, M. Edén, A. Brinkmann, X. Zhao, M. H. Levitt, *Chem. Phys. Lett*. **2000**, *321*, 205–215.
(31) B. Hu, Q. Wang, O. Lafon, J. Trébosc, F. Deng, J.-P. Amoureux, *J. Magn. Reson.* **2009**, *198*, 41–48.
(32) Q. Wang, B. Hu, O. Lafon, J. Trébosc, F. Deng, J.-P. Amoureux, *Phys. Chem. Chem. Phys.* **2009**, *11*, 10391−10395.

(33) D. Massiot, F. Fayon, M. Capron, I. King, S. Le Calvé, B. Alonso, J.-O. Durand, B. Bujoli, Z. Gan, G. Hoatson, *Magn. Reson. Chem.* **2002**, *40*, 70−76.
(34) K. Eichele, WSolids1, Version 1.20.17; Universität Tübingen, **2012**.
(35) D. Massiot, J. Hiet, N. Pellerin, F. Fayon, M. Deschamps, S. Steuernagel, P. J. Grandinetti, *J. Magn. Reson.* **2006**, *181*, 310–315
(36) C. J. Pickard, F. Mauri, *Phys. Rev. B* **2001**, *63*, 245101.
(37) J. R. Yates, C. J. Pickard, F. Mauri, *Phys. Rev. B* **2007**, *76*, 024401.
(38) M. D. Segall, P. L. D. Lindan, M. J. Probert, C. J. Pickard, P. J. Hasnip, S. J. Clark, M. C. Payne, *J. Phys.: Condens. Matter* **2002**, *14*, 2717–2744.
(39) S. J. Clark, M. D. Segall, C. J. Pickard, P. J. Hasnip, M. J. Probert, K. Refson, M. C. Payne, *Z. Kristallogr.* **2005**, *220*, 567–570.
(40) T. Charpentier, *Solid state Nucl. Magn. Reson.* **2011**, *40*, 1–20.
(41) C. Bonhomme, C. Gervais, F. Babonneau, C. Coelho, F. Pourpoint, T. Azaïs, S. E. Ashbrook, J. M. Griffin, J. R. Yates, F. Mauri, C. J. Pickard, *Chem. Rev.* **2012**, *112*, 5733−5779.
(42) P. E. Blöchl, *Phys. Rev. B*, **1994**, *50*, 17953–17979.
(43) O. K. Anderson, *Phys. Rev. B* **1975**, *12*, 3060−3083.
(44) D. D. Koelling and G. O. Arbman, *J. Phys. F: Met. Phys.* **1975**, *5*, 2041–2054.
(45) P. Blaha, K. Schwarz, G. K. H. Madsen, D. Kvasnicka and J. Luitz, WIEN2k, An Augmented Plane Wave + Local Orbitals Program for Calculating Crystal Properties **2001**.
(46) W. Kohn, L. J. Sham, *Phys. Rev.* **1965***, 140*, A1133–A1138.
(47) J. P. Perdew, K. Burke, M. Ernzerhof, *Phys. Rev. Lett.* **1996**, *77*, 3865−3868.
(48) M. J. Frisch, G. W. Trucks, H. B. Schlegel, G. E. Scuseria, M. A. Robb, J. R. Cheeseman, V. G. Zakrzewski, J. A. Jr. Montgomery, R. E. Stratmann, J. C. Burant, S. Dapprich, J. M. Millam, A. D. Daniels, K. N. Kudin, M. C. Strain, O. Farkas, J. Tomasi, V. Barone, M. Cossi, R.Cammi, B. Mennucci, C. Pomelli, C. Adamo, S. Clifford, J. Ochterski, G. A. Petersson, P. Y. Ayala, Q. Cui, K. Morokuma, D. K. Malick, A. D. Rabuck, K. Raghavachari, J. B. Foresman, J. Cioslowski, J. V. Ortiz, A. G. Baboul, B. B. Stefanov, G. Liu, A. Liashenko, P. Piskorz, I. Komaromi, R. Gomperts, R. L. Martin, D. J. Fox, T. Keith, M. A. Al-Laham, C. Y. Peng, A. Nanayakkara, M. Challacombe, P. M. W.Gill, B. Johnson, W. Chen, M. W. Wong, J. L. Andres, C. Gonzalez, M. Head-Gordon, E. S. Replogle, J. A. Pople, Gaussian 98, Revision A.9; Gaussian, Inc.: Pittsburgh, PA, **1998**.
(49) F. Mauri, B. G. Pfrommer, S. G. Louie, *Phys. Rev. Lett.* **1996**, *77*, 5300−5303.
(50) B. Pfrommer, D. Raczkowski, A. Canning, S. G. Louie, PARATEC, Lawrence Berkeley National Laboratory, www.nersc.gov/projects/paratec.
(51) D. R. Hamann, M. Schlüter, C. Chiang, *Phys. Rev. Lett.* **1979**, *43*, 1494−1497.
(52) D. Vanderbilt, *Phys. Rev. B* **1990**, *41*, 7892−7895.
(53) S. A. Joyce, J. R. Yates, C. J. Pickard, F. Mauri, *J. Chem. Phys.* **2007**, *127*, 204107, 1−9.
(54) S. A. Joyce, J. R. Yates, C. J. Pickard, S. P. Brown, *J. Am. Chem. Soc.* **2008**, *130*, 12663−12670.
(55) I. Hung, A.-C. Uldry, J. Becker-Baldus, A. L. Webber, A. Wong, M. E. Smith, J. R. Yates, C. J. Pickard, R. Dupree, S. P. Brown, *J. Am. Chem. Soc.* **2009**, *131*, 1820–1834.
(56) J. R. Yates, *Magn. Reson. Chem*. **2010**, *48*, S23–S31
(57) C. Bonhomme, C. Gervais, C. Coelho, F. Pourpoint, T. Azaïs, L. Bonhomme-Coury, F. Mauri, *Magn. Reson. Chem.* **2010**, *48*, S86–S102.
(58) N. S. Barrow, J. R. Yates, S. A. Feller, D. Holland, S. E. Ashbrook, P. Hodgkinson, S. P. Brown, *Phys. Chem. Chem. Phys.* **2011**, *13*, 5778.
(59) D. R. Hamann, *Phys. Rev. Lett.* **1996**, *76*, 660−663.
(60) T. Demuth, Y. Jeanvoine, J. Hafner, J. G. Ángyán, *J. Phys.: Condens. Matter* **1999**, *11*, 3833–3874.

(61) M. Profeta, M. Benoit, F. Mauri, C. J. Pickard, *J. Am. Chem. Soc.* **2004**, *126*, 12628–12635.
(62) T. Charpentier, S. Ispas, M. Profeta, F. Mauri, C. J. Pickard, *J. Phys. Chem. B* **2004**, *108*, 4147–4161.
(63) J. Du, L. R. Corrales, *J. Phys. Chem. B* **2006**, *110*, 22346–22352.
(64) S. E. Ashbrook, M. Cutajar, C. J. Pickard, R. I. Walton, S. Wimperis, *Phys. Chem. Chem. Phys.* **2008**, *10*, 5754–5764.
(65) F. Vasconcelos, S. Cristol, J.-F. Paul, G. Tricot, J.-P. Amoureux, L. Montagne, F. Mauri, L. Delevoye, *Inorg. Chem.* **2008**, *47*, 7327–7337.
(66) T. Charpentier, P. Kroll, F. Mauri, *J. Phys. Chem. C* **2009**, *113*, 7917–7929.
(67) J. Cuny, E. Furet, R. Gautier, L. Le Pollès, C. J. Pickard, J.-B. d'Espinose de Lacaillerie, *Chem. Phys. Chem.* **2009**, *10*, 3320–3329.
(68) D. H. Brouwer, I. L. Moudrakovski, R. J. Darton, R. E. Morris, *Magn. Reson. Chem.* **2010**, *48*, S113–S121.
(69) S. Ispas, T. Charpentier, F. Mauri, D. R. Neuville, *Solid State Sci.* **2010**, *12*, 183–192.
(70) A. Soleilhavoup, J.-M. Delaye, F. Angeli, D. Caurant, T. Charpentier, *Magn. Reson. Chem.* **2010**, *48*, S159–S170.
(71) L. A. Truflandier, F. Boucher, C. Payen, R. Hajjar, Y. Millot, C. Bonhomme, N. Steunou, *J. Am. Chem. Soc.* **2010**, *132*, 4653–4668.
(72) F. Vasconcelos, S. Cristol, J.-F. Paul, L. Montagne, F. Mauri, L. Delevoye, *Magn. Reson. Chem.* **2010**, *48*, S142–S150.

Chapter 2: Binary fluorides with obvious assignment of the ^{19}F NMR lines to the fluorine crystallographic sites: looking for a correlation between ^{19}F isotropic chemical shielding and shift.

2.1 Introduction

A correlation between the measured isotropic chemical shift δ_{iso} and the calculated isotropic chemical shielding σ_{iso} is required for δ_{iso} prediction. However two different correlations with significantly different slopes have been reported in the two first studies on this issue.[1,2] We then decided to reconsider the definition of a calibration curve for inorganic fluorides. The studied compounds are binary fluorides: alkali, alkaline earth and rare earth (column 3) fluorides in the section 2.2, column 13 metal fluorides in the section 2.3 and columns 11, 12 and 14 metal fluorides in the section 2.4.

Additionally, ^{25}Mg, ^{139}La, ^{27}Al, ^{71}Ga, ^{115}In and ^{67}Zn quadrupolar parameters are determined and/or their electric field gradients (EFG) are calculated in MgF_2, LaF_3, α-, β- and η-AlF_3, GaF_3, InF_3 and ZnF_2. Indeed, due to the high sensitivity of these parameters to variations of the atomic positions around the studied nucleus, EFG calculations could represent a valuable tool to ascertain the precision of the experimental and geometry optimized structures.

2.2 Alkali, alkaline earth and rare earth fluorides

PCCP

Dynamic Article Links

Cite this: *Phys. Chem. Chem. Phys.*, 2011, **13**, 18539–18550

www.rsc.org/pccp

PAPER

NMR parameters in alkali, alkaline earth and rare earth fluorides from first principle calculations†

Aymeric Sadoc,*[a] Monique Body,[b] Christophe Legein,[c] Mamata Biswal,[c] Franck Fayon,[d] Xavier Rocquefelte[a] and Florent Boucher[a]

Received 20th April 2011, Accepted 20th July 2011
DOI: 10.1039/c1cp21253b

^{19}F isotropic chemical shifts for alkali, alkaline earth and rare earth of column 3 basic fluorides are measured and the corresponding isotropic chemical shieldings are calculated using the GIPAW method. When using the PBE exchange–correlation functional for the treatment of the cationic localized empty orbitals of Ca^{2+}, Sc^{3+} (3d) and La^{3+} (4f), a correction is needed to accurately calculate ^{19}F chemical shieldings. We show that the correlation between experimental isotropic chemical shifts and calculated isotropic chemical shieldings established for the studied compounds allows us to predict ^{19}F NMR spectra of crystalline compounds with a relatively good accuracy. In addition, we experimentally determine the quadrupolar parameters of ^{25}Mg in MgF_2 and calculate the electric field gradients of ^{25}Mg in MgF_2 and ^{139}La in LaF_3 using both PAW and LAPW methods. The orientation of the EFG components in the crystallographic frame, provided by DFT calculations, is analysed in terms of electron densities. It is shown that consideration of the quadrupolar charge deformation is essential for the analysis of slightly distorted environments or highly irregular polyhedra.

Introduction

During the last decade, the characterisation of the fluorine environment in rigid solids by nuclear magnetic resonance (NMR) spectroscopy has become easier with the increase in routinely available magic angle spinning (MAS) frequency which allows an efficient averaging of the chemical shift anisotropy and dipolar interactions. As the ^{19}F ($I = 1/2$) isotropic chemical shift (δ_{iso}) is very sensitive to the environment of the fluorine atom, MAS NMR is a powerful structural tool for studying complex fluoride crystalline materials having multiple crystallographic sites. In numerous studies, the interpretation of ^{19}F MAS NMR spectra is commonly based on the intuitive assumption that similar structural environments lead to similar ^{19}F δ_{iso}.[1–8] By comparison with the ^{19}F δ_{iso} values measured for well-known binary fluorides, the ^{19}F resonances of a crystalline compound can be assigned to different fluorine environments. In the case of fluorine sites with different multiplicities, the relative intensities of the corresponding resonances also provide additional constraints for the assignment. Nonetheless, complete unambiguous assignment of complex ^{19}F solid-state MAS NMR spectra often remains challenging. In such cases, two-dimensional (2D) NMR correlation experiments, which provide information about inter-atomic connectivities, can be used for line assignment purposes. In inorganic crystalline fluorides, various 2D heteronuclear correlation MAS experiments (CP-MAS HETCOR,[9] TEDOR-MQMAS,[10] CP 3QMAS[11] and J-HMQC[12,13]) have been applied to several spin pairs (^{19}F/^{27}Al,[14–17] ^{19}F/^{23}Na,[16,18–20] ^{19}F/^{31}P[14,21] and ^{19}F/^{207}Pb[22–24]) to probe heteronuclear spatial proximities. In oxyfluoride[25,26] and in fluoride materials,[17,23,24,27] the fluorine–fluorine proximities or through bond connectivities evidenced through 2D ^{19}F double-quantum single-quantum[28] (DQ-SQ)

[a] *Institut des Matériaux Jean Rouxel (IMN), Université de Nantes, CNRS, 2 rue de la Houssinière, BP 32229, 44322 Nantes Cedex 3, France. E-mail: Aymeric.Sadoc@cnrs-imn.fr; Fax: + 33 2 40 37 39 95; Tel: + 33 2 40 37 64 11*
[b] *Laboratoire de Physique de l'Etat Condensé, CNRS UMR 6087, Institut de Recherche en Ingénierie Moléculaire et Matériaux Fonctionnels (CNRS FR 2575) Université du Maine, Avenue Olivier Messiaen, 72085 Le Mans Cedex 9, France*
[c] *Laboratoire des Oxydes et Fluorures, CNRS UMR 6010, Institut de Recherche en Ingénierie Moléculaire et Matériaux Fonctionnels (CNRS FR 2575) Université du Maine, Avenue Olivier Messiaen, 72085 Le Mans Cedex 9, France*
[d] *Conditions Extrêmes et Matériaux: Haute Température et Irradiation, CNRS UPR 3079, 1D Avenue de la Recherche Scientifique, 45071 Orléans Cedex 2, France and Université d'Orléans, Faculté des Sciences, Avenue du Parc Floral, 45067 Orléans Cedex 2, France*

† Electronic supplementary information (ESI) available: Experimental ^{19}F MAS NMR spectra of alkali fluorides, alkaline earth fluorides, YF_3 and LaF_3. Solid state NMR and XRPD study of ScF_3. Practical details to generate the pseudopotentials. Atomic coordinates of IS and APO structures of MgF_2, YF_3 and LaF_3. Mg–F bond lengths and F–Mg–F bond angles determined from the IS and APO structures of MgF_2. Y–F bond lengths determined from the IS and APO structures of YF_3. La–F bond lengths determined from the IS and APO structures of LaF_3. Experimental ^{19}F δ_{iso} and calculated ^{19}F σ_{iso} values presented in Fig. 5. Eigenvectors of the calculated EFG tensors of ^{25}Mg in MgF_2 and of ^{139}La in LaF_3. See DOI: 10.1039/c1cp21253b

MAS correlation experiments were also used to assign the ^{19}F resonances. However, in the case of distinct fluorine sites having the same connectivity scheme and relatively similar inter-atomic distances, these 2D correlation NMR methods do not allow a straightforward assignment of the corresponding resonances.[17,29]

An alternative approach is to correlate experimental ^{19}F δ_{iso} values to the ones calculated from structural data. A semi-empirical model[30–35] can be used for this purpose but this requires the refinement of phenomenological parameters which are usually valid for a specific family of compounds. First-principles molecular calculations are very efficient on molecular systems but, in the case of crystalline compounds, these methods critically require the non trivial definition of cluster size to mimic the crystalline structure.[25,36–45] Moreover, for these two approaches, uncertainties on calculation results are sometimes larger than the experimentally measured ^{19}F δ_{iso} difference between two distinct resonances, preventing an unambiguous assignment of the ^{19}F NMR resonances.

The more elegant approach for crystalline systems consists in using the periodic boundary conditions. Two different methods can be used for this purpose, the GIPAW (Gauge Including Projector Augmented Wave) method introduced by Pickard *et al.*[46–48] that enables the calculation of the chemical shielding tensor (σ) and indirect spin–spin (J) coupling constant[26,49–53] and the recently implemented "converse approach"[54] that was demonstrated to be a very efficient alternative for the chemical shielding tensor calculations.[55] Two groups have recently published GIPAW calculations on fluorides. From ^{19}F isotropic chemical shielding (σ_{iso}) calculations for numerous compounds including alkali and alkaline earth basic fluorides, Zheng *et al.*[56] proposed a calibration curve between calculated and experimental ^{19}F δ_{iso} values. Griffin *et al.*[26] have also calculated ^{19}F σ_{iso} values for several fluorides including some alkali and alkaline earth fluorides and a rare earth fluoride, LaF_3. However, using the same exchange–correlation functional, a significantly different calibration curve was obtained. The origin of this difference is discussed later on and arises mostly from the consideration of LaF_3 in the correlation reported by Griffin *et al.*[26] One can also notice in the paper of Zheng *et al.*[56] some significant differences between experimental and calculated δ_{iso} values, especially for CaF_2 (30 ppm).[56]

To further investigate these problems we decided to reconsider this crucial step for providing predictive results allowing the assignment of ^{19}F NMR resonances, *i.e.* the definition of a calibration curve for inorganic fluorides. We have thus calculated the ^{19}F σ_{iso} for alkali, alkaline earth and rare earth (column 3) basic fluorides using the CASTEP code.[57] To obtain reliable experimental data and avoid any reference problem (see below for more details), the experimental ^{19}F δ_{iso} values for all the compounds under investigation have been measured again using the same reference sample ($CFCl_3$). In a first step, the fluorine pseudopotential used for the calculation of ^{19}F σ_{iso} has been validated. As it is classically done,[55,58,59] a molecular benchmark was used for comparing our GIPAW results to all-electrons (AE) calculations. In a second step, the correlation between the calculated ^{19}F σ_{iso} values for twelve binary crystalline compounds and experimental ^{19}F δ_{iso} values is investigated. A critical problem that was already observed for Ca in oxides[60] is evidenced in fluorides: The PBE-DFT (Perdew, Burke and Ernzerhof-Density Functional Theory) method[61] is deficient in describing 3d and 4f localized empty orbitals when considering NMR shielding calculations. To circumvent this problem the Ca, Sc, and La pseudopotentials have been adapted using the methodology described in ref. 60 and a reference calibration curve is proposed. We then show that the correlation established for the studied compounds fits nicely with the calculations on other inorganic fluorides reported in ref. 26 and 56.

For two of the twelve studied compounds (MgF_2 and LaF_3), the quadrupolar nuclei occupying the cationic site (*i.e.* ^{25}Mg, $I = 5/2$ and ^{139}La, $I = 7/2$) are affected by the quadrupolar interaction since the corresponding site symmetries lead to a non-zero Electric Field Gradient (EFG). We have measured the ^{25}Mg NMR parameters in MgF_2 which were unknown despite two recent ^{25}Mg NMR studies of numerous compounds[62,63] and the recently determined ^{139}La NMR parameters in LaF_3[64,65] are also reported. The EFG tensors of ^{25}Mg in MgF_2 and ^{139}La in LaF_3 calculated from the AE method and projector augmented-wave (PAW) approach[66,67] using the WIEN2K[68,69] and CASTEP codes,[57] respectively, are compared to these experimental values. Finally, the orientation of the EFG tensor components in terms of site distortion and deformation of the electronic density around the cationic positions is discussed.

Experimental and computational details

Solid state NMR

Experimental conditions used to record ^{19}F solid-state MAS NMR spectra are given as ESI.† The ^{25}Mg MAS (7 kHz) NMR spectra of MgF_2 were recorded at two magnetic fields of 17.6 and 9.4 T using Avance 750 and 400 Bruker spectrometers operating at Larmor frequencies of 45.92 and 24.49 MHz, respectively. A Hahn echo pulse sequence with a 5.0 μs 90° pulse (nutation frequency of 50 kHz) was employed. The inter-pulse delays were synchronized with the rotor period and ^{19}F continuous wave decoupling was applied during signal acquisition. The recycle delays were set to 5 s and 1.5 s at 17.6 and 9.4 T, respectively. The ^{25}Mg chemical shift was referenced relative to an aqueous 1 M solution of $MgCl_2$. All the NMR spectra were reconstructed using the DMFit software.[70]

Computational methods

The GIPAW method implemented in the CASTEP code is an efficient and accurate method for determining NMR shielding tensor in periodic systems. By combining a plane-wave basis set and Ultrasoft Pseudopotential (USPP) a quite large number of atoms can be considered using periodic boundary conditions. However, the pseudopotential construction (mainly the GIPAW projectors definition) should be realized with care in order to avoid unphysical behaviour that could lead to misleading conclusions.

To test the validity of the GIPAW USPP used to calculate ^{19}F σ_{iso}, a molecular benchmark of eight experimentally well characterized simple molecules is used (see Table 1). They were chosen because they span a large range of ^{19}F σ_{iso} values (about 750 ppm). Two sets of calculations are performed using the PBE functional, the first one using AE basis sets as implemented in the Gaussian03 code[71] and the second one using USPP and the GIPAW method as implemented in the CASTEP 5.0 package.

Table 1 Molecules used for pseudopotential tests. Geometries are obtained from PBE geometry optimization. Local point groups, space groups, bond lengths and angles are reported. The space group is used for calculation with the periodic code

Molecule	Local point group	Space group	Distances/Å		Angles/°	
CH_3F	C_s	P_{31m}	C–F = 1.403	C–H = 1.099	F–C–H = 108.7	
HF	$C_{\infty v}$	P_{4mm}	H–F = 0.940			
C_6F_6	D_{2h}	$P_{6/mmm}$	C–F = 1.343	C–C = 1.395	C–C–C = 120.0	F–C–C = 120.0
CH_2F_2	C_{2v}	P_{mm2}	C–F = 1.376	C–H = 1.100	H–C–H = 113.9	F–C–F = 108.5
CF_4	T_d	P_{-4m3}	C–F = 1.342		F–C–F = 109.5	
$CFCl_3$	C_s	P_{31m}	C–F = 1.363	C–Cl = 1.769	Cl–C–Cl = 110.6	Cl–C–F = 108.3
NF_3	C_{3v}	P_{31m}	N–F = 1.409		F–N–F = 101.7	
F_2	$D_{\infty h}$	$P_{4/mmm}$	F–F = 1.418			

For the AE calculations, the well known GIAO (gauge invariant atomic orbitals)[72,73] and IGAIM (individual gauges for atoms in molecules)[74,75] methods are used. AE calculations are performed using four different types of basis sets from Dunning's hierarchy[76] with increasing accuracy, namely aug-cc-pCVDZ, aug-cc-pCVTZ, aug-cc-pCVQZ and aug-pCV5Z taken from the ESML basis set exchange library.[77] The USPP are generated using the on the fly generator (OTF_USPP) included in CASTEP and the following parameters for the fluorine atoms: (i) $r_{loc} = r_{nloc} = 1.4$ a.u., (ii) $r_{aug} = 1.0$ a.u. and (ii) $q_c = 7.5$ a.u.$^{1/2}$. Two ultrasoft projectors were used for the 2s and 2p nonlocal components. An energy cut-off of 700 eV is used for the plane wave basis set expansion. Prior to ^{19}F chemical shielding calculations, symmetry-constrained molecular geometry optimizations are performed using the PBE[61] functional (Table 1). The molecular state is simulated in CASTEP using a box large enough (1000 Å^3) to avoid interactions between molecular images.

For the calculation of ^{19}F σ_{iso} on crystalline systems (CASTEP code) twelve binary compounds are considered. Two structural data sets are used, the experimental structures reported in the literature (named IS in the following for initial structures) and the structures obtained after PBE-DFT atomic position optimization (APO structures) when allowed by symmetry, which is only the case for MgF_2,[78] YF_3[79] and LaF_3.[80] Effectively, the alkali fluorides (LiF,[81] NaF,[82] KF,[83] RbF[84] and CsF[85]) adopt the NaCl structure type, three of the four studied alkaline earth basic fluorides (CaF_2,[86] SrF_2[87] and BaF_2[88]) adopt the fluorite structure type and ScF_3 adopts a ReO_3 type structure.[89,90] For these nine compounds, the atomic coordinates are therefore constrained by the local symmetry. To obtain converged ^{19}F σ_{iso} values, a plane wave basis set energy cut-off of 700 eV is necessary and a Monkhorst–Pack grid density approximately equal to 0.04 Å^{-1} (corresponding to a k-point mesh of $8 \times 8 \times 8$ for all structures except for YF_3 ($4 \times 4 \times 6$) and LaF_3 ($4 \times 4 \times 4$)) is enough. For the electronic loops, the PBE functional[61] is used for the exchange–correlation kernel. Total energies are converged up to changes smaller than 2×10^{-5} eV. APO are obtained by minimizing the residual forces on the atom up to $|F|_{max}$ below 20 meV Å^{-1}, keeping symmetry constraints and fixing the cell parameters to the experimentally determined values.

As previously proposed by Profeta *et al.*[60] for the Ca^{2+} ion ($3d^0$), the local potentials of Sc^{3+} ($3d^0$) and La^{3+} ($4f^0$) USPP are also artificially shifted higher in energy compared to the default definition proposed by the Materials Studio package (practical details are given as ESI†). This overcomes the deficiency of the PBE functional which generates too much covalent interaction between those empty states and the anionic p states. To show the limit of the PBE-DFT functional to describe these cations, calculations of the density of states (DOS) using hybrid PBE0 functional[91] are also performed for CaF_2. Norm-conserving pseudopotentials (NCPP) with a higher energy cut-off value (1088 eV) have to be used, USPP being not yet supported with hybrid functional.

EFG are calculated for ^{25}Mg in MgF_2 and ^{139}La in LaF_3 using the PAW[66] method implemented in CASTEP and the linearized augmented plane wave (LAPW)[69] method implemented in the WIEN2K package. The same PBE functional is used to compare calculated values of the EFG. The atomic sphere radii (R_{MT}) were set to 1.85 a.u. for Mg and F in MgF_2 and to 2.41 and 2.13 a.u. for La and F, respectively, in LaF_3. Core states are 1s for Mg and F and from 1s to 4d for the La. The plane wave cut-off is defined by $R_{MT}K_{MAX} = 8$. We use the same Monkhorst–Pack scheme as for CASTEP ($8 \times 8 \times 8$ for MgF_2 and $4 \times 4 \times 4$ for LaF_3). Both sets of structures are used, the IS reported in the literature and the APO structures obtained using the CASTEP package.

Conventions

In this study, the calculated σ_{iso} value is defined as:

$$\sigma_{iso} = (\sigma_{xx} + \sigma_{yy} + \sigma_{zz})/3,$$

σ_{ii} being the principal components of the shielding tensor defined in the sequence $|\sigma_{zz} - \sigma_{iso}| \geq |\sigma_{xx} - \sigma_{iso}| \geq |\sigma_{yy} - \sigma_{iso}|$.

The isotropic chemical shift is defined as:

$$\delta_{iso} = -[\sigma_{iso} - \sigma_{ref}]$$

The quadrupolar coupling constant (C_Q) and the asymmetry parameter (η_Q) are defined as:

$$C_Q = (eQV_{zz})/h,$$

$$\eta_Q = (V_{xx} - V_{yy})/V_{zz}$$

V_{ii} being the principal components of the EFG tensor defined in the sequence $|V_{zz}| \geq |V_{yy}| \geq |V_{xx}|$.

The quadrupolar moments (Q) of ^{25}Mg and ^{139}La are taken from ref. 92.

Results and discussion

NMR shielding calculation on molecular systems: USPP validation

To validate the fluorine USPP used for the ^{19}F σ_{iso} GIPAW calculations, the GIPAW results are faced to AE calculations

for a molecular benchmark. To ensure the computation accuracy of AE methods, we first compare the ^{19}F σ_{iso} calculated with GIAO and IGAIM methods and then ^{19}F σ_{iso} GIAO calculation results are compared to the values issued from the GIPAW method (Table 2). In this work we avoid direct comparison with experimental δ_{iso} values which has been already extensively discussed by Harding *et al.*[93] For molecular systems more sophisticated methods are required. This is out of the scope of the present work.

The molecules used in our benchmark allow us to validate our USPP on a large range of NMR shielding from a highly shielded ^{19}F atom (highly ionic C–F interaction on the CH_3F molecule) to a much unshielded ^{19}F atom (covalent F–F interaction on the F_2 molecule). Between both GIAO and IGAIM AE methods, we notice a convergence of the ^{19}F σ_{iso} values when increasing the accuracy of the basis sets from double zeta (aug-cc-pCVDZ) to quintuple zeta (aug-cc-pCV5Z), the differences between the two methods becoming negligible for the very large aug-cc-pCV5Z basis set. This ensures the validity of these AE references to test the fluorine USPP.

As reported by Ceresoli *et al.*,[55] the largest differences (from 10 to 15 ppm) between the AE methods and the USPP GIPAW calculations are observed for molecules having a highly negative ^{19}F σ_{iso} value. The weak shielding due to the covalent N–F or F–F interactions results in the contraction of the core orbitals. In this case, the number of Gaussian functions needed to correctly describe the atomic behaviour is a crucial parameter.[93] This can be clearly seen in the evolution of the ^{19}F σ_{iso} values which still decrease by about 3.5 ppm for F_2 but only 0.2 ppm for CH_3F when increasing the basis set from quadruple zeta (aug-cc-pCVQZ) to quintuple zeta (aug-cc-pCV5Z). This would suggest that the calculated σ_{iso} value is not yet completely converged with respect to the basis set size for the F_2 molecule. Such negative values for the shielding being not observed for crystalline systems, one can consider that the description of the core by GIPAW USPP is as good as the description by a very large AE basis set. Probably GIPAW USPP calculations could be improved for much unshielded fluorine atoms by allowing core states relaxation (for the OTF_USPP generator) during the self consistent electronic procedure but this was beyond the scope of the present study.

Fig. 1 shows the correlation between the σ_{iso} values obtained with the all-electron GIAO method and the GIPAW method using the USPP of the Material Studio package. The remarkable agreement proves the correctness of the USPP fluorine atoms for calculating ^{19}F σ_{iso} when using the PBE functional. They will be used in the following for crystalline systems.

Table 2 ^{19}F σ_{iso} values (ppm) using different AE basis sets, with increasing accuracy, within the GIAO and IGAIM (in italic) methods. The last column reports the results obtained using USPP within the GIPAW method

	All-electron				Pseudopotential
Molecule	aug-cc-pCVDZ	aug-cc-pCVTZ	aug-cc-pCVQZ	aug-cc-pCV5Z	USPP
CH_3F	453.2	452.6	452.1	451.9	452.1
	446.0	*452.0*	*452.0*	*451.9*	
HF	405.2	401.2	400.5	400.1	398.8
	401.6	*401.3*	*400.5*	*400.1*	
C_6F_6	322.5	319.8	317.5	316.9	310.6
	320.0	*319.0*	*317.6*	*316.8*	
CH_2F_2	310.7	304.4	302.4	301.6	298.7
	304.2	*303.8*	*302.3*	*301.6*	
CF_4	225.0	216.8	213.9	212.6	207.0
	221.1	*216.5*	*213.9*	*212.6*	
$CFCl_3$	138.2	125.8	121.9	120.3	113.2
	128.2	*125.0*	*121.9*	*120.3*	
NF_3	−36.7	−50.1	−56.2	−58.8	−73.5
	−40.4	*−50.3*	*−56.2*	*−58.7*	
F_2	−257.1	−273.2	−282.5	−286.2	−296.3
	−258.3	*−273.6*	*−282.8*	*−286.3*	

NMR shielding calculations on crystalline systems

To perform a reliable comparison between experimental and DFT-GIPAW calculated ^{19}F isotropic chemical shifts for alkali, alkaline earth and rare earth of column 3 basic fluorides, the consideration of accurate experimental values referenced relative to the same standard is a crucial point. Unfortunately, there are some discrepancies between the ^{19}F δ_{iso} values previously reported for these compounds.[1,4–6,30,64,94–103] In addition, these values are referenced relative to different fluorine standards ($CFCl_3$, C_6F_6) and thus need to be expressed with respect to $CFCl_3$, the primary fluorine standard. Such a conversion procedure was used in previous works[26,56] (some experimental values seem erroneously converted in the paper of Zheng *et al.*[56]). In order to obtain reliable data for comparison with calculations, we have therefore measured again the ^{19}F δ_{iso} values for these fluorides with respect to $CFCl_3$ (measured ^{19}F δ_{iso} are given in Table 3 and the corresponding experimental ^{19}F NMR spectra are presented as ESI†). For the compounds involving a single fluorine crystallographic site, ^{19}F MAS NMR spectra were recorded at 7.0 T with the MAS spinning frequency ranging from 15 to 30 kHz. For compounds containing several distinct F sites (YF_3 and LaF_3), a higher magnetic

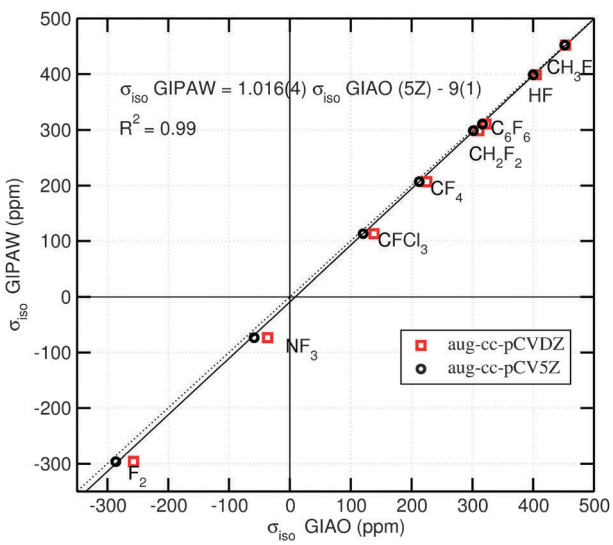

Fig. 1 Calculated ^{19}F σ_{iso} values using the USPP GIPAW method *versus* AE aug-cc-pCVDZ and aug-cc-pCV5Z basis sets with the GIAO method, using the PBE functional and the same molecular geometries (see Table 1 for details). The solid line represents the calculated linear regression corresponding to the equation reported on the graph for the aug-cc-pCV5Z basis set. The dotted line represents the ideal expected correlation σ_{iso} GIPAW = σ_{iso} GIAO.

Table 3 Experimental ^{19}F δ_{iso} values, ^{19}F σ_{iso} values calculated using USPP within the GIPAW method for IS and APO structures, and calculated δ_{iso} values deduced from the linear regression obtained for YF_3, alkali and alkaline earth compounds without CaF_2 ($\delta_{iso}/CFCl_3 = -0.80(3)\ \sigma_{iso} + 89(9)$)

	σ_{iso} calc/ppm		δ_{iso} calc/ppm		
Compounds	IS	APO	IS	APO	δ_{iso} exp/ppm
LiF	369.3	—	−206	—	−204.3(3)
NaF	395.8	—	−228	—	−224.2(2)
KF	268.1	—	−125	—	−133.3(2)
RbF	221.3	—	−88	—	−90.9(2)
CsF	136.3	—	−20	—	−11.2(2)
MgF_2	362.7	362.7	−201	−201	−197.3(4)
CaF_2	220.0	—	−87	—	−108.0(2)
	246.2[a]	—	−108[a]	—	
SrF_2	215.3	—	−83	—	−87.5(2)
BaF_2	151.9	—	−33	—	−14.3(2)
ScF_3	97.2	—	11	—	−36(1)
	156.0[b]	—	−36[b]	—	
YF_3 (F1)	180.1	181.3	−55	−56	−68.1(2)
YF_3 (F2)	170.8	170.0	−48	−47	−56.9(2)
LaF_3 (F1)	93.7	91.8	14	15	−23.6(2)
	133.6[c]	132.1[c]	−18[c]	−17[c]	
LaF_3 (F2)	39.1	38.7	58	58	25.3(2)
	82.6[c]	82.3[c]	23[c]	23[c]	
LaF_3 (F3)	47.2	52.5	51	47	16.9(2)
	89.3[c]	94.2[c]	18[c]	14[c]	

[a] A shift of 1.81 eV was applied on the 3d orbitals. [b] A shift of 1.96 eV was applied on the 3d orbitals. [c] A shift of 4.55 eV was applied on the 4f orbitals.

field of 17.6 T and fast MAS spinning frequency (up to 65 kHz) were employed to obtain very high resolution ^{19}F MAS NMR spectra. The assignments of the NMR lines are unambiguous for the twelve studied compounds since they have only one fluorine site[78,81–90] or several fluorine sites with different multiplicities (2 for YF_3[79] and 3 for LaF_3[80]). Some difficulties were encountered with the determination of the ^{19}F δ_{iso} value of ScF_3 due to local disorder related to its negative thermal expansion.[104] Experimental results on this compound are discussed in the ESI.†

A second point that must be considered with attention is the conversion of calculated ^{19}F σ_{iso} values into ^{19}F δ_{iso} values. In the work of Zheng *et al.*,[56] the calculated ^{19}F σ_{iso} values were converted into ^{19}F δ_{iso} values with respect to C_6F_6 from the calculated σ_{iso} value of the C_6F_6 reference molecule, as previously done by Yates *et al.*[105] Then, the experimentally measured ^{19}F δ_{iso} value of C_6F_6 relative to $CFCl_3$ is used to deduce "calculated" ^{19}F δ_{iso} values relative to $CFCl_3$. Unfortunately, the experimental ^{19}F δ_{iso} value of C_6F_6 used in ref. 56 and 105 are different and one can find in the literature several different ^{19}F δ_{iso} values for C_6F_6 (relative to $CFCl_3$). Another approach would be to transform experimental δ_{iso} values into experimental σ_{iso} values using the established experimental absolute scale for fluorine ($\sigma(^{19}F$ neat liq. $CFCl_3$, spherical, 300 K) = 188.7 ppm).[106,107] To avoid these referencing problems and possible errors coming from the calculation of the ^{19}F σ_{iso} value of the isolated molecule chosen as reference, we have directly deduced the "calculated" ^{19}F δ_{iso} values from the linear regression between calculated ^{19}F σ_{iso} values and experimental ^{19}F δ_{iso} values referenced to $CFCl_3$.[58,59]

The ^{19}F DFT-GIPAW σ_{iso} values for alkali, alkaline earth and rare earth of column 3 basic fluorides calculated using the USPP and computational parameters presented in previous section and the corresponding measured ^{19}F δ_{iso} are given in Table 3.

The linear correlation between experimental δ_{iso} and calculated σ_{iso}, from APO structures (see ESI†) when allowed by symmetry, is shown Fig. 2. Except for the F3 site in LaF_3, the σ_{iso} values calculated from IS and APO structures are very similar. This is in agreement with slight optimization effects on F–Mg, F–Y or F–La distances (see ESI†) and tends to show that these three structures were precisely determined. The slope of the linear regression (−0.70) is far below the theoretically expected value of minus one. However, same kind of deviations have been noted previously for other halogens (Cl, Br and I)[108–111] and other nuclei such as ^{29}Si,[112,113] ^{31}P,[114,115] ^{43}Ca,[116] or ^{93}Nb[117] and therefore does not seem to be a specific problem associated with fluorine NMR parameters. Similar trends were also reported by Zheng *et al.*[56] and by Griffin *et al.*,[26] with slopes equal to −0.86 and −0.68, respectively. This deviation from the theoretically expected slope of minus one already reported for PBE-DFT calculations implies establishing an empirical calibration curve to predict calculated isotropic chemical shift values. Another striking point is that the slope obtained here, which is relatively close to that obtained by Griffin *et al.*,[26] differs significantly from the slope reported by Zheng *et al.*[56] This difference arises mainly from the consideration of the calculated σ_{iso} values for LaF_3, ScF_3 and CaF_2, two of these compounds containing cations (Ca^{2+} and La^{3+}) already known to be inaccurately described with PBE-DFT.[60,118] In the work of Griffin *et al.*, two of these three compounds (CaF_2 and LaF_3) were considered while only CaF_2 was studied by Zheng *et al.* leading to a larger absolute slope.

The deficiency of PBE-DFT in calculating the NMR shielding of anions neighboured by Ca^{2+} cations has already been reported by Profeta *et al.*[60] They have shown that the PBE

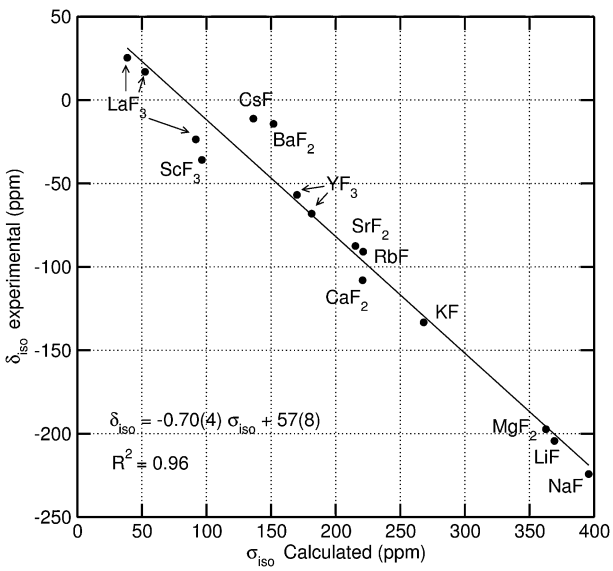

Fig. 2 Calculated ^{19}F σ_{iso} values using the PBE functional for APO structures when allowed by symmetry *versus* experimentally measured ^{19}F δ_{iso} values. The solid line represents the calculated linear regression.

functional leads to an inaccurate calculation of ^{17}O σ_{iso} in CaO due to an overestimation of the Ca–O bond covalence. More precisely, too much interaction is found by PBE between the Ca(3d) and O(2p) states. To overcome this PBE-DFT deficiency, the energy level of the 3d Ca orbitals was shifted to higher energy without changing the position of the s and p states in the Ca pseudopotential.[60] This method has been afterwards successfully applied on ^{43}Ca NMR parameters calculations.[119,120] Following these works, we have applied an empirical shift on the Ca(3d) orbitals for building the Ca USPP. To determine the optimal 3d-shift a reference correlation between δ_{iso} and σ_{iso} is needed and we have thus established a new correlation presented in Fig. 3 by discarding CaF_2, ScF_3 and LaF_3.

It leads to:

$$\delta_{iso}/CFCl_3 = -0.80(3)\ \sigma_{iso} + 89(9) \qquad (1)$$

From this new linear regression (eqn (1)), the ideal ^{19}F σ_{iso} value for the fluorine in CaF_2 can be established (Fig. 3(a)) and further used to adjust the 3d-shift for the Ca(3d) orbitals. An optimal shift of 1.81 eV is obtained (see Fig. 3(b)). This value is significantly smaller than for CaO (3.2 eV).[60] This difference can be explained as (i) we used USPP whereas Profeta *et al.* used NCPP[60] and (ii) the degrees of covalency of the Ca–O and Ca–F bonds are different. To ascertain this empirical procedure, the density of states (DOS) obtained using the PBE functional for the two different definitions of the Ca USPP is compared with the DOS obtained using the hybrid functional PBE0, which is expected to give a better description of the covalency in the system (Fig. 4).

The effect of the shift applied on the 3d orbitals is clearly observed in the conduction band: the energy of the band having mostly a Ca(3d) character is increased and becomes closer to the one obtained using the hybrid functional. The band gap stays unchanged (mainly imposed by the position of Ca(4s) states in the conduction band) and is calculated to 6.3 eV using the PBE functional. As expected, the use of the hybrid functional gives a higher band gap value (8.4 eV) which is closer to the experimental one (11.8 eV).[121]

Since the calculated ^{19}F σ_{iso} of ScF_3 also deviates significantly from the linear regression established for YF_3, alkali and alkaline earth compounds excluding CaF_2 (as evidenced from Fig. 3(a)) and because the DOS calculation (not shown) shows that the bottom of the conduction band has a strong 3d character, it appears that a similar correction is also needed to properly describe the 3d orbitals of the Sc atom when using PBE functional. As done for Ca, we thus adjusted the corresponding 3d-shift for the Sc USPP such that the calculated ^{19}F σ_{iso} corresponds to the value determined from the experimental δ_{iso} using eqn (1). Fig. 3(c) shows that the effect of the applied 3d-shift on the calculated σ_{iso} value is more pronounced for ScF_3 than for CaF_2. It should be noticed that the values of the 3d-shift required for the Sc^{3+} ion in ScF_3 (1.96 eV) and for the Ca^{2+} ion in CaF_2 (1.81 eV) are very close. This observation gives some confidence about the relevance of this empirical procedure to overcome the deficiency of the PBE functional in describing cations with localized 3d empty states.

It is also known that standard GGA/DFT is not well suitable to elements with localized 4f empty states. For example, a recent theoretical investigation has shown that it is necessary to add an on-site Hubbard correction (U_{eff} = 10.3 eV) on the 4f(La) orbitals to properly describe their localizations and then their energy positions, allowing the XPS/BIS and reflectance experimental spectra of LaF_3 to be properly simulated.[118] In our case, the very large deviation observed for LaF_3 (Fig. 3(a)) shows that the La^{3+} ion ($4f^0$) has a similar symptomatic behaviour as Ca^{2+} and Sc^{3+} ions. Therefore, we have applied the Profeta *et al.*[60] procedure to shift 4f orbitals. LaF_3 having three fluorine sites, the 4f-shift was determined by simultaneously minimizing for the three sites the differences between the experimental ^{19}F δ_{iso} and the δ_{iso} values deduced from the calculated ^{19}F σ_{iso} using eqn (1). The optimum value obtained following this protocol (4.55 eV, Fig. 3(d)), is much higher than the one determined for the 3d orbitals of Ca^{2+} and Sc^{3+}.

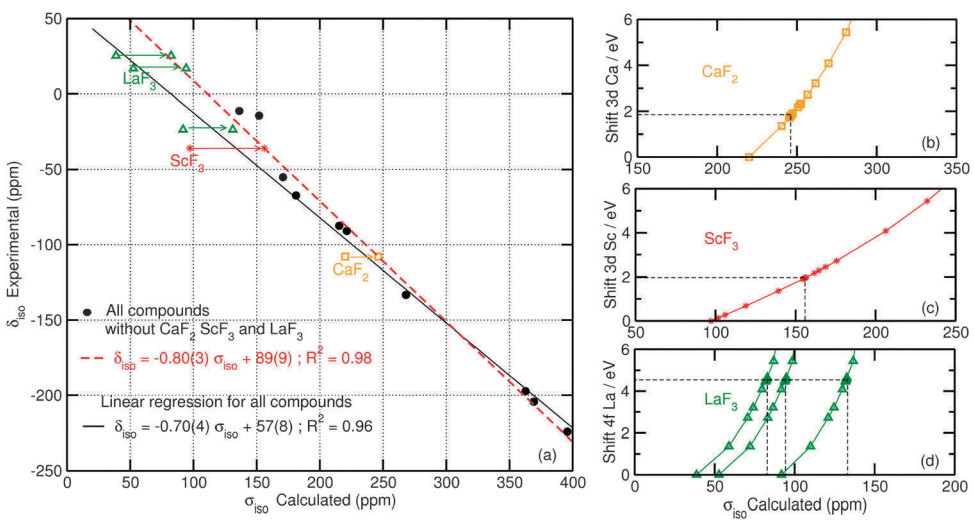

Fig. 3 (a) Experimental ^{19}F δ_{iso} (/$CFCl_3$) values *versus* calculated σ_{iso} values. The solid line represents the linear regression when considering all compounds and the dashed line represents the linear regression when considering YF_3 and alkali and alkaline earth compounds without CaF_2. The arrows represent the change in σ_{iso} when applying a shift on the 3d orbitals of Ca and Sc and on the 4f orbitals of La. The panels on the right side report the σ_{iso} evolution with the applied shifts on the 3d orbitals of Ca (b) and Sc (c) and on the 4f orbitals of La (d).

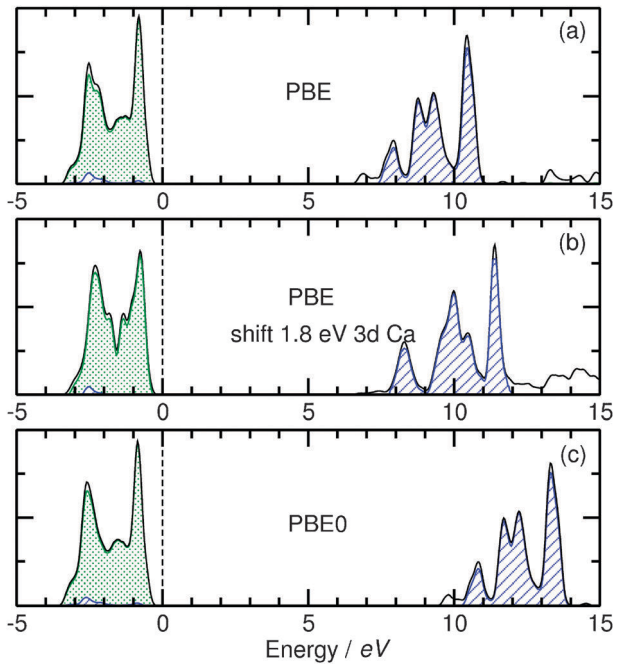

Fig. 4 The DOS for CaF_2 using (a) the PBE functional, (b) the PBE functional with a 3d-shift of 1.81 eV for Ca and (c) the PBE0 hybrid functional. The hatched area represents the partial density of states projected on the 3d orbitals of the Ca element and the dashed area the partial density of states projected on the 2p orbitals of the F element. The experimental band gap is 11.8 eV.[121]

The validity of eqn (1), used to determine the 3d- and 4d-shifts required to calculate the ^{19}F σ_{iso} of compounds for which the lowest energy states of the conduction bands have strong 3d or 4d characters (*i.e.* CaF_2, ScF_3 and LaF_3), is illustrated in Fig. 5. In this plot, we have reported the ^{19}F δ_{iso} values previously measured for several other inorganic fluorides together with the corresponding ^{19}F σ_{iso} values calculated by Zheng *et al.*[56] and by Griffin *et al.*[26] using the PBE-DFT GIPAW method with the same fluorine USPP (see ESI†). Great care was taken to consider only compounds for which ^{19}F δ_{iso} values were determined from high-resolution spectra (*i.e.* recorded at relatively high magnetic fields using a MAS spinning frequency larger than 10 kHz) and for which an unambiguous assignment of the resonances is provided. These compounds include ZnF_2,[30] CdF_2,[30] α-PbF_2 (2 distinct F sites),[122] HgF_2,[102] α-AlF_3,[123] GaF_3,[30] InF_3,[30] $BaLiF_3$,[30] $Na_5Al_3F_{14}$[20] (3 distinct F sites), β-$BaAlF_5$[17] (10 distinct F sites) and $Ba_3Al_2F_{12}$[17,29] (8 distinct F sites). It should be mentioned that the GIPAW calculations of the ^{19}F isotropic shielding by Griffin *et al.*[26] and Zheng *et al.*[56] were carried out using slightly different computation parameters than those used in this work. Griffin *et al.*[26] used a cut-off energy of 680 eV and a k-spacing of 0.04 $Å^{-1}$, and a full geometry optimization (variation of both the lattice parameters and internal atomic coordinates) was performed prior to the σ_{iso} calculations. Zheng *et al.*[56] employed much smaller cut-off energies of 300 eV for the optimizations of atomic positions and 550 eV for the GIPAW calculations, which does not allow obtaining fully converged ^{19}F σ_{iso} values (see Experimental section). Taking these aspects into account, it is clearly observed in Fig. 5

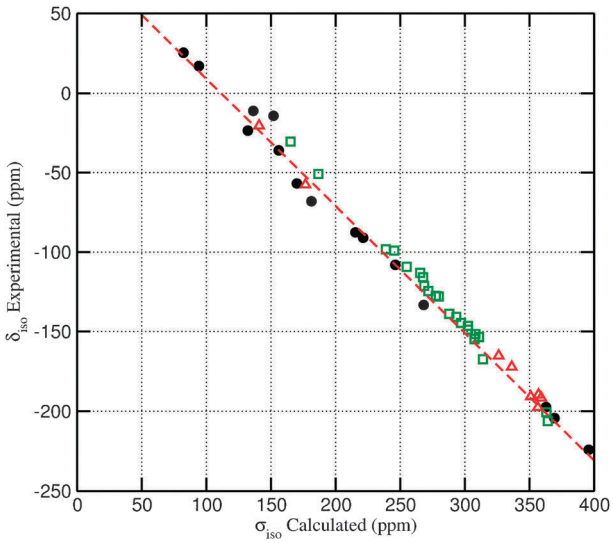

Fig. 5 Calculated ^{19}F σ_{iso} values using the PBE functional *versus* experimentally measured ^{19}F δ_{iso} values. The circles represent the values reported in Table 3. The triangles represent the values calculated by Griffin *et al.*[26] for CdF_2, HgF_2, α-PbF_2, α-AlF_3 and $Na_5Al_3F_{14}$. The squares represent the values calculated by Zheng *et al.*[56] for ZnF_2, GaF_3, InF_3, $BaLiF_3$, β-$BaAlF_5$ and $Ba_3Al_2F_{12}$. The values presented in this figure are reported as ESI.† The dashed line corresponds to eqn (1) ($\delta_{iso}/CFCl_3 = -0.80(3)\ \sigma_{iso} + 89(9)$).

that eqn (1) ($\delta_{iso}/CFCl_3 = -0.80(3)\ \sigma_{iso} + 89(9)$) fits perfectly with these results obtained for other inorganic fluorides, the linear regression obtained considering these 11 compounds in addition to the 12 studied fluorides being $\delta_{iso}/CFCl_3 = -0.79(1)\ \sigma_{iso} + 90(3)$.

By applying eqn (1) to the calculated ^{19}F σ_{iso} values plotted in Fig. 5 (except those of CaF_2, ScF_3 and LaF_3 for which this equation was used to adjust the 3d-and 4f-shifts), a RMS deviation between experimental and "calculated" ^{19}F δ_{iso} of 7 ppm is obtained. This indicates that this equation can be used to predict the ^{19}F NMR spectra of crystalline compounds from the PBE-DFT GIPAW calculation with a quite good accuracy. More importantly, it should be pointed out that for all of the compounds having multiple fluorine crystallographic sites (2 sites in YF_3, 3 sites in LaF_3, 2 sites in α-PbF_2, 10 sites in β-$BaAlF_5$ and 8 sites in $Ba_3Al_2F_{12}$), the relative positions of the calculated σ_{iso} values (and the corresponding "calculated" δ_{iso} values) are similar to the relative positions of the experimental δ_{iso} values, showing that such calculations allow an unambiguous assignment of ^{19}F resonances for compounds having several fluorine sites with the same multiplicity.

Electric field gradient calculations

In the second part of this work, we compare the calculated EFG tensor to the one experimentally determined using solid-state NMR. According to the symmetry of the cationic sites in the studied compounds, the EFG tensors of the quadrupolar nuclei occupying cationic sites are expected to be different from zero only for ^{25}Mg in MgF_2 and ^{139}La in LaF_3. The quadrupolar parameters C_Q and η_Q are directly related to the principal components of the EFG tensor which originates from the deformation of the electronic density around the nucleus.

Consequently, C_Q and η_Q parameters are very sensitive to the site symmetry and/or site distortion and provide additional structural information. The quadrupolar parameters for ^{25}Mg in MgF_2 which adopts the rutile structure type ($P4_2/mnm$ space group),[78] are measured for the first time. These parameters and those of ^{139}La in LaF_3 determined by Ooms *et al.*[65] and Lo *et al.*[64] are gathered in Table 4. The EFG tensor components calculated with both CASTEP and WIEN2K codes for the IS and APO structures of MgF_2 and LaF_3 are also reported in Table 4, together with the quadrupolar parameters of ^{139}La in LaF_3 previously calculated by Ooms *et al.*[65] using LAPW method.[69]

As shown in Fig. 6, the ^{25}Mg MAS NMR spectra of MgF_2 recorded at two different magnetic fields (9.4 and 17.6 T) exhibit typical second order quadrupolar broadened line shapes. Good fits of the two ^{25}Mg experimental spectra can be obtained taking into account only the second order quadrupolar interaction indicating that the effect of the ^{25}Mg chemical shift anisotropy can be neglected even at 17.6 T. The ^{25}Mg isotropic chemical shift determined from the fits of experimental spectra is -4 ± 1 ppm. The calculated δ_{iso} deduced from the isotropic shielding σ_{iso} calculated with CASTEP (564.6 ppm) using the equations reported by Pallister *et al.*[63] ($\delta_{iso} = -0.933\ \sigma_{iso} + 528.04$) and Cahill *et al.*[62] ($\delta_{iso} = -1.049\ \sigma_{iso} + 565.23$) are respectively equal to 1.4 and -0.6 ppm which are both in fine agreement with the experimental value.

As reported in Table 4, there are slight discrepancies between the measured V_{ii} values and those calculated for the experimental structure of MgF_2 using the PAW USPP (CASTEP) or LAPW AE (WIEN2K) methods, the calculated V_{zz} and $|V_{xx}|$ principal components of the EFG tensor being underestimated. As previously done for the ^{19}F chemical shielding, the principal components of the EFG tensors were also calculated for the APO structure. The PBE-DFT optimisation of the fluorine atomic position leads to slight modifications of the MgF_6 octahedron: the mean Mg–F distance remains the same (1.982 Å) but the radial distortion increases and the angular distortion decreases (see ESI†). For the APO structure, a better agreement between experimental and calculated V_{zz} values is obtained. Nevertheless, the V_{xx} and V_{yy} components calculated with the PAW USPP method are respectively larger and smaller than the experimental values leading to a discrepancy between the calculated and experimental asymmetry parameters (η_Q). In contrast, the V_{ii} values (and thus C_Q and η_Q parameters) calculated using the LAPW AE method are in very good agreement with the experimental ones.

Table 4 Experimental V_{ii}, C_Q and η_Q, calculated V_{ii}, C_Q and η_Q using CASTEP and WIEN2K for initial and APO structures. Since only the absolute value of C_Q can be determined from NMR experiments on powdered samples, the sign of the experimental C_Q is set to the sign of the calculated C_Q. The quadrupolar moment Q values are equal to 0.1994×10^{-28} m^2 and 0.2000×10^{-28} m^2 for ^{25}Mg and ^{139}La, respectively[a]

		V_{zz}/ 10^{21} V m^{-2}	V_{yy}/ 10^{21} V m^{-2}	V_{xx}/ 10^{21} V m^{-2}	C_Q/MHz	η_Q
MgF_2						
Exp		0.728(6)	−0.480(8)	−0.248(8)	3.51(3)	0.32(2)
IS	CASTEP	0.631	−0.434	−0.196	3.04	0.38
	WIEN2K	0.637	−0.498	−0.139	3.06	0.56
APO	CASTEP	0.655	−0.364	−0.291	3.16	0.11
	WIEN2K	0.658	−0.431	−0.228	3.17	0.31
LaF_3						
Exp		−3.29(1)	2.99(8)	0.30(8)	−15.90(5)[b]	0.82(5)[b]
		−3.309	2.994	0.314	−16.0[c]	0.81[c]
IS	WIEN2K	−3.311	2.831	0.480	−16.01[b]	0.71[b]
IS	CASTEP	−3.147	2.755	0.393	−15.22	0.75
	WIEN2K	−3.307	2.963	0.344	−15.99	0.79
APO	CASTEP	−3.722	3.432	0.290	−18.00	0.84
	WIEN2K	−3.947	3.678	0.269	−19.09	0.86

[a] From ref. 92. [b] From ref. 65. [c] From ref. 64.

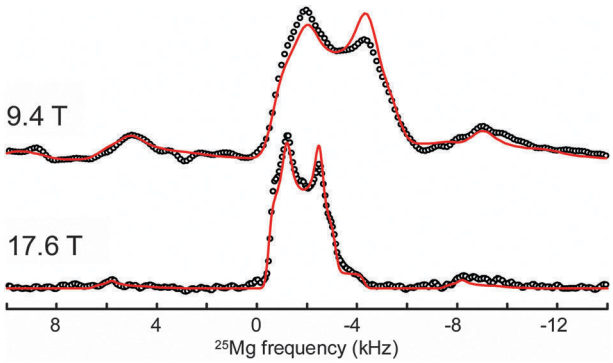

Fig. 6 Experimental (dots) ^{25}Mg MAS (7 kHz) Hahn echo NMR spectra of MgF_2 recorded at 9.4 (top) and 17.6 T (bottom) and their best fits (lines).

As shown in Fig. 7(a) which depicts the orientation of the ^{25}Mg EFG tensor (see ESI† for details), the V_{ii} components are along the intersections of the three mirror planes of the Mg site (mmm symmetry) and, for the Mg atom located at (0,0,0), V_{zz} and V_{xx} lie in the (a,b) plane while V_{yy} is along the c crystallographic axis. In the MgF_2 structure, the MgF_6 octahedron is characterized by low radial and high angular distortions (see ESI†). In such a situation, the largest component of the EFG tensor (V_{zz}) is not expected to be oriented along M–F bonds.[124] Indeed, V_{zz} and V_{yy} are both oriented between two Mg–F bonds in the plane presenting the angular distortion while V_{xx} is oriented along the shortest Mg–F bond perpendicular to this plane. It should also be noted that the sign of the calculated V_{ii} components is in agreement with the angular distortion analysis model proposed by Body *et al.*,[124] *i.e.* a positive/above 90° (negative/below 90°) angular distortion leads to a charge depletion (concentration) in the V_{ii} direction and then to a positive (negative) V_{ii} value (Table 4). More detailed information about the origin of the EFG at the nucleus is traditionally obtained from the charge density distribution visualized on electron density difference $\Delta\rho$ maps.[124–126] $\Delta\rho$ represents the difference between the crystalline electron density and the superposition of electron densities from the neutral atoms. The $\Delta\rho$ maps for the plane containing the V_{xx} component and four fluorine atoms with Mg–F distances of 1.975 (x2) and 1.986 Å (x2) and for the plane containing V_{zz} and V_{yy} are shown in Fig. 7(c) and (d), respectively. The V_{xx} component being rather small, the corresponding charge deformation is not easily evidenced. On the other hand, in the V_{zz}/V_{yy} plane (Fig. 7(d)), the expected depletion of charge in the V_{zz} direction (*i.e.* between the two Mg–F bonds which form an angle equal to 98.8°) relative to the V_{yy} direction (*i.e.* between the two Mg–F bonds which form an angle equal to 81.2°) is clearly observed. Isolines on the $\Delta\rho$ map close to the nucleus are effectively slightly compressed (elongated) along the V_{zz} (V_{yy})

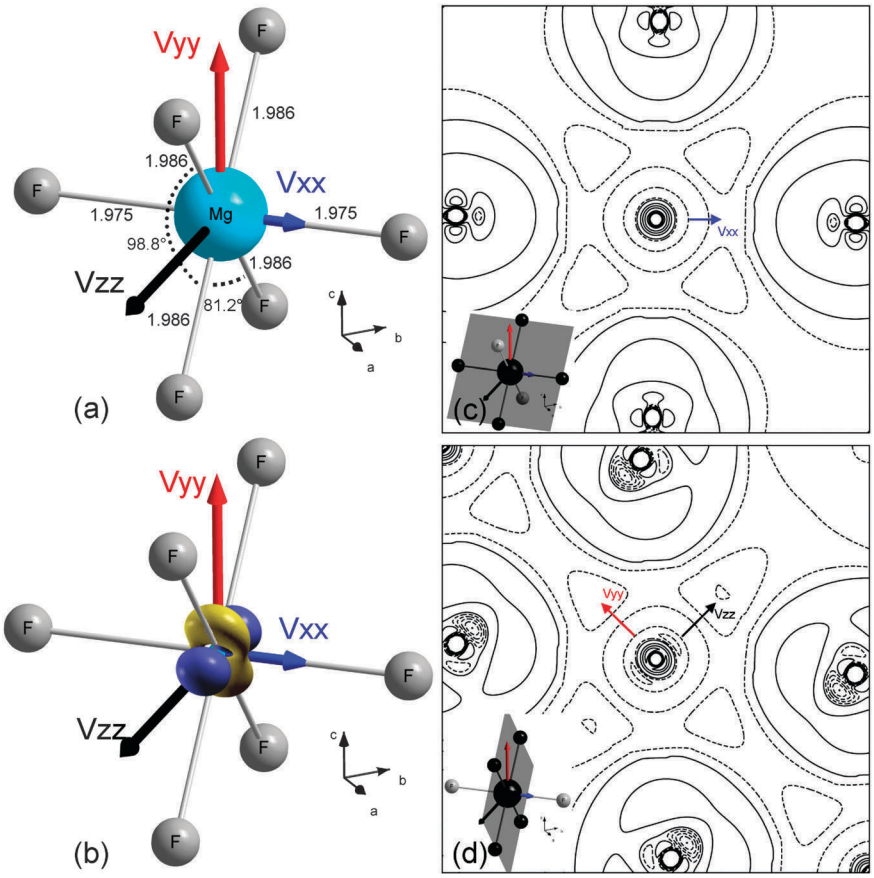

Fig. 7 (a) The orientation of the ^{25}Mg EFG tensor components, calculated with WIEN2K on the APO structure, represented on the MgF_6 octahedron. Mg–F bond lengths (Å) and F–Mg–F bond angles (°) are indicated. The norms of the eigenvectors are proportional to the eigenvalues of the EFG tensor components (see Table 4). (b) The isosurface of the quadrupolar charge deformation considering only the $|L| = 2$ terms inside the Mg sphere. A light colour is used for positive values and a dark colour for negative values. For graphical convenience the volume has been increased by more than an order of magnitude. (c) A $\Delta\rho$ map in the plane containing the V_{xx} component and four Mg–F bonds. (d) A $\Delta\rho$ map in the plane containing the V_{zz} and V_{yy} components. On these maps, solid and dashed lines represent respectively positive (from 0.002 to 0.065 e/a.u.^{3} with a step of 0.016 e/a.u.^{3}) and negative (from −0.002 to −0.040 e/a.u.^{3} with a step of 0.004 e/a.u.^{3}) values of the electronic density.

direction due to this depletion (increase) of the electronic density. As mentioned above, the $\Delta\rho$ maps are not well suitable to establish a relationship between the EFG and the electronic density asphericity near the nucleus when the distortion is small. Another approach proposed by Schwarz *et al.*[127] consists in calculating the difference with respect to the ionic spherical density. However, this approach requires the construction of isolated ions (F^-, Mg^{2+}) which is not always straightforward. For simplicity we only consider the non-spherical contribution of the electronic density inside the Mg sphere (Fig. 7(b)). One can observe that V_{zz}, which is positive, is oriented along the negative part of this non spherical density. We also note that the asymmetry of the positive part of the density which is less important along the V_{xx} direction than along the V_{yy} direction is in agreement with the lower absolute value of V_{xx} compared to V_{yy}.

The trigonal structure of LaF_3 (*P*-3*c*1 space group) contains a single La crystallographic site (6f Wyckoff position).[80] The La coordination polyhedron is made of 9 fluorine atoms with La–F distances ranging from 2.417 to 2.636 Å and 2 additional fluorine atoms at a longer La–F distance of ∼3 Å (see Fig. 8 and ESI†). The La site has a twofold symmetry axis which lies along the La–F3 bond, parallel to the crystallographic *a*-axis. As already reported,[65] the ^{139}La quadrupolar parameters calculated for the experimental structure using the PAW USPP or LAPW AE methods are very close to the measured C_Q and η_Q values and the best agreement is obtained for the LAPW AE method (see Table 4). In contrast, some discrepancies between the V_{ii} values calculated for the APO structure and the experimental ones are observed, the two computation methods leading to a notably overestimated V_{zz} and V_{yy} components. These overestimations of the values calculated after the geometry optimization step remain difficult to explain since the variation of the La environment, which is difficult to analyze for this coordination polyhedron, is small considering the La–F distances (see ESI†). It should be pointed out that the initial structure of LaF_3 was determined with a very high accuracy (neutron diffraction on single crystal)[80] and, in such a case, the weak variation of the structural parameters induced by the PBE-DFT geometry optimization leads to less accurate calculated EFG values.

As shown in Fig. 8(a), V_{yy} is oriented along the twofold symmetry axis (*i.e.* lies along the La–F3 bond). The complexity of the La environment prevents predicting the relative orientation of the ^{139}La EFG tensor components from simple

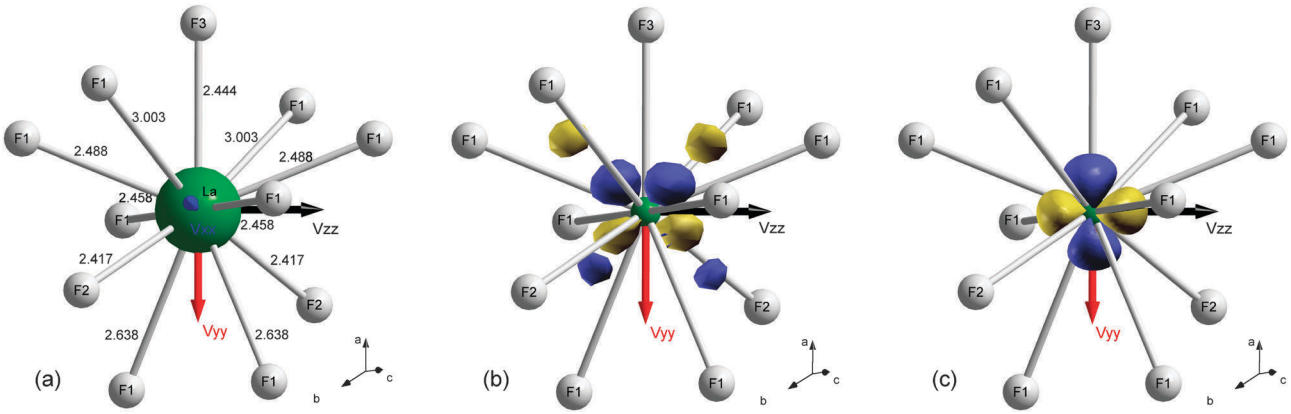

Fig. 8 The orientation of the ^{139}La EFG tensor components, calculated with WIEN2K on the initial structure, represented on the LaF_{11} polyhedron. The lengths of the vectors are proportional to the eigenvalues of the EFG tensor. (a) The bond lengths/Å are reported and the V_{xx} component is multiplied by ten for graphical visualization (see Table 4). Representations of the electronic densities inside the La sphere: (b) reports the contributions to the density when the spherical terms have been removed and (c) reports the contributions to the density when only the $|L| = 2$ terms are considered. A light colour is used for positive values and a dark colour for negative values. For graphical convenience the volume has been increased by more than an order of magnitude.

coordination polyhedron geometry considerations,[124] and to go further in the analysis, electronic density differences were calculated. In a first step, the spherical part of the charge density is removed keeping all non-spherical terms in the LM expansion (Fig. 8(b)). However, this does not allow finding a correlation between the electronic density and the orientation of the EFG eigenvalues. In a second step, only the $|L| = 2$ terms of the LM expansion are considered (Fig. 8(c)) and a good correlation between the electronic density deformation and the orientation of the EFG eigenvectors is then found. A depletion of charge is observed along the twofold axis in agreement with the positive value of V_{yy}. Along this direction, the number of neighbouring fluorine atoms is rather small with longer La–F bonds (La–F1 bond lengths equal to 2.638 Å and 3.003 Å). In contrast, an accumulation of charge is observed along the V_{zz} direction, in agreement with the negative value of V_{zz}. Along this direction, the number of neighbouring fluorine atoms is larger with shorter La–F bonds (La–F1 bond lengths equal to 2.458 and 2.488 Å and La–F2 bond lengths equal to 2.417 Å) leading to stronger La–F interactions. Finally, it should be noted that the depletion of charge in the V_{yy} direction and the accumulation of charge in the V_{zz} direction have similar amplitudes in agreement with similar absolute values of these eigenvalues (η_Q value close to 1) and accordingly, only a tiny deformation of the electronic density is observed along the direction of V_{xx} (Fig. 8(c)).

Conclusion

We have investigated the relationship between experimental ^{19}F δ_{iso} and calculated ^{19}F σ_{iso} values from first-principles calculations using the GIPAW method and the PBE functional, for alkali, alkaline earth and rare earth of column 3 fluorides. On this basis, we show that the PBE functional is unable to reproduce the measured ^{19}F δ_{iso} value in CaF_2 as it overestimates the Ca–F covalence but this deficiency is corrected by applying a shift on the 3d orbitals. We also evidence that the same type of correction is required in the case of ScF_3 and LaF_3 for which the bottom of the conduction band has a strong 3d and 4f character, respectively, and we have determined the shifts of the 3d(Sc) orbitals and 4d(La) orbitals needed to accurately calculate the ^{19}F shielding tensors of these compounds using the PBE functional. Taking into account this deficiency of the PBE functional, we propose a correlation between the calculated ^{19}F σ_{iso} values and the experimental ^{19}F δ_{iso} values that allows the prediction of ^{19}F NMR spectra with a relatively good accuracy. Nevertheless, our results highlight the need of to compute the NMR shielding using improved exchange–correlation functionals such as hybrid functionals. In this context, the converse approach recently developed by Thonhauser *et al.*[54] seems to be a promising solution. In this work, we also determined and calculated the quadrupolar parameters of ^{25}Mg in MgF_2 and, from the analysis of charge distribution through electron density maps, it is shown that the orientation of the EFG components of ^{25}Mg reflects the angular distortion of the MgF_6 octahedron. Finally, we have shown that the electronic density deformation determined by considering only the $|L| = 2$ terms of the LM expansion gives a reliable picture of the EFG tensors of ^{25}Mg in MgF_2 and ^{139}La in LaF_3.

Acknowledgements

The authors thank the Région Pays de la Loire for the financial support of the RMN3MPL project, especially M. Biswal (doctoral grant) and A. Sadoc (post-doctoral fellowship). Financial support from the TGIR RMN THC FR3050 is also gratefully acknowledged. The computational presented in this work have been carried out at the Centre Régional de Calcul Intensif des Pays de la Loire (CCIPL), financed by the French Research Ministry, the Région Pays de la Loire, and Nantes University. We thank CCIPL for CASTEP licenses financial support.

We also thank Cyrille Galven (Laboratoire des Oxydes et Fluorures), Alain Demourgues and Etienne Durand (ICMCB-Pessac) for their help in the study of ScF_3 (XRPD and fluorination experiments).

Notes and references

1 J. M. Miller, *Prog. Nucl. Magn. Reson. Spectrosc.*, 1996, **28**, 255–281.
2 B. Bureau, G. Silly, J.-Y. Buzaré, J. Emery, C. Legein and C. Jacoboni, *J. Phys.: Condens. Matter*, 1997, **9**, 6719–6736.
3 L. S. Du, F. Wang and C. P. Grey, *J. Solid State Chem.*, 1998, **140**, 285–294.
4 J. F. Stebbins and Q. Zeng, *J. Non-Cryst. Solids*, 2000, **262**, 1–5.
5 Q. Zeng and J. F. Stebbins, *Am. Mineral.*, 2000, **85**, 863–867.
6 T. J. Kiczenski and J. F. Stebbins, *J. Non-Cryst. Solids*, 2002, **306**, 160–168.
7 S. Chaudhuri, F. Wang and C. P. Grey, *J. Am. Chem. Soc.*, 2002, **124**, 11746–11757.
8 R. E. Youngman and S. Sen, *Solid State Nucl. Magn. Reson.*, 2005, **27**, 77–89.
9 P. Caravatti, L. Braunschweiler and R. R. Ernst, *Chem. Phys. Lett.*, 1983, **100**, 305–310.
10 J. P. Amoureux, J. Trebosc and G. Tricot, *Magn. Reson. Chem.*, 2007, **45**, S187–S191.
11 M. Pruski, D. P. Lang, C. Fernandez and J. P. Amoureux, *Solid State Nucl. Magn. Reson.*, 1997, **7**, 327–331.
12 A. Lesage, D. Sakellariou, S. Steuernagel and L. Emsley, *J. Am. Chem. Soc.*, 1998, **120**, 13194–13201.
13 D. Massiot, F. Fayon, B. Alonso, J. Trebosc and J. Amoureux, *J. Magn. Reson.*, 2003, **164**, 160–164.
14 F. Taulelle, M. Pruski, J. P. Amoureux, D. Lang, A. Bailly, C. Huguenard, M. Haouas, C. Gerardin, T. Loiseau and G. Férey, *J. Am. Chem. Soc.*, 1999, **121**, 12148–12153.
15 M. Fechtelkord, H. Behrens, F. Holtz, J. L. Bretherton, C. A. Fyfe, L. A. Groat and M. Raudsepp, *Am. Mineral.*, 2003, **88**, 1046–1054.
16 J. Dutour, N. Guillou, C. Huguenard, F. Taulelle, C. Mellot-Draznieks and G. Férey, *Solid State Sci.*, 2004, **6**, 1059–1067.
17 C. Martineau, C. Legein, J.-Y. Buzaré and F. Fayon, *Phys. Chem. Chem. Phys.*, 2009, **11**, 950–957.
18 K. H. Lim and C. P. Grey, *Chem. Phys. Lett.*, 1999, **312**, 45–56.
19 K. H. Lim and C. P. Grey, *J. Chem. Phys.*, 2000, **112**, 7490–7504.
20 L. S. Du, A. Samoson, T. Tuherm and C. P. Grey, *Chem. Mater.*, 2000, **12**, 3611–3616.
21 F. Taulelle, *Solid State Sci.*, 2001, **3**, 795–800.
22 C. Martineau, F. Fayon, C. Legein, J.-Y. Buzaré, G. Silly and D. Massiot, *Chem. Commun.*, 2007, 2720–2722.
23 C. Martineau, F. Fayon, C. Legein, J.-Y. Buzaré, F. Goutenoire and E. Suard, *Inorg. Chem.*, 2008, **47**, 10895–10905.
24 C. Martineau, F. Fayon, C. Legein, J.-Y. Buzaré, M. Body, D. Massiot and F. Goutenoire, *Dalton Trans.*, 2008, 6150–6158.
25 T. M. Alam, J. S. Clawson, F. Bonhomme, S. G. Thoma, M. A. Rodriguez, S. Zheng and J. Autschbach, *Chem. Mater.*, 2008, **20**, 2205–2217.
26 J. M. Griffin, J. R. Yates, A. J. Berry, S. Wimperis and S. E. Ashbrook, *J. Am. Chem. Soc.*, 2010, **132**, 15651–15660.
27 C. D. Martin, S. Chaudhuri, C. P. Grey and J. B. Parise, *Am. Mineral.*, 2005, **90**, 1522–1533.
28 H. Geen, J. J. Titman, J. Gottwald and H. W. Spiess, *Chem. Phys. Lett.*, 1994, **227**, 79–86.
29 Q. Wang, B. Hu, F. Fayon, J. Trebosc, C. Legein, O. Lafon, F. Deng and J.-P. Amoureux, *Phys. Chem. Chem. Phys.*, 2009, **11**, 10391–10395.
30 B. Bureau, G. Silly, J.-Y. Buzaré and J. Emery, *Chem. Phys.*, 1999, **249**, 89–104.
31 M. Body, G. Silly, C. Legein and J.-Y. Buzaré, *Inorg. Chem.*, 2004, **43**, 2474–2485.
32 C. Martineau, M. Body, C. Legein, G. Silly, J.-Y. Buzaré and F. Fayon, *Inorg. Chem.*, 2006, **45**, 10215–10223.
33 C. Legein, F. Fayon, C. Martineau, M. Body, J.-Y. Buzaré, D. Massiot, E. Durand, A. Tressaud, A. Demourgues, O. Péron and B. Boulard, *Inorg. Chem.*, 2006, **45**, 10636–10641.
34 F. Le Berre, M.-P. Crosnier-Lopez, C. Galven, J.-L. Fourquet, C. Legein, M. Body and J.-Y. Buzaré, *Dalton Trans.*, 2007, 2457–2466.
35 L. Sronek, J. Lhoste, M. Gaudon, C. Legein, J.-Y. Buzaré, M. Body, G. Crinière, A. Tressaud, S. Pechev and A. Demourgues, *J. Phys. Chem. C*, 2008, **112**, 860–866.
36 M. Mortimer, E. A. Moore and N. F. Peirson, *J. Chem. Soc., Faraday Trans.*, 1996, **92**, 1117–1120.
37 S. H. Cai, Z. Chen, X. Xu and H. L. Wan, *Chem. Phys. Lett.*, 1999, **302**, 73–76.
38 S. H. Cai, Z. Chen, Z. W. Chen and H. L. Wan, *Chem. Phys. Lett.*, 2002, **362**, 13–18.
39 S. H. Cai, Z. Chen and H. L. Wan, *J. Phys. Chem. A*, 2002, **106**, 1060–1066.
40 Y. Liu and H. Nekvasil, *Am. Mineral.*, 2002, **87**, 339–346.
41 S. H. Cai, X. Y. Yu, Z. Chen and H. L. Wan, *Magn. Reson. Chem.*, 2003, **41**, 902–907.
42 Y. Liu and J. Tossell, *J. Phys. Chem. B*, 2003, **107**, 11280–11289.
43 G. Silly, M. Body, J.-Y. Buzaré, C. Legein and B. Bureau, *C. R. Chim.*, 2004, **7**, 403–416.
44 M. Body, G. Silly, C. Legein and J.-Y. Buzaré, *J. Phys. Chem. B*, 2005, **109**, 10270–10278.
45 M. Gerken, P. Hazendonk, A. Iuga, J. Nieboer, M. Tramsek, E. Goreshnik, B. Zemva, S. Zheng and J. Autschbach, *Inorg. Chem.*, 2007, **46**, 6069–6077.
46 C. J. Pickard and F. Mauri, *Phys. Rev. B: Condens. Matter*, 2001, **63**, 245101.
47 J. R. Yates, C. J. Pickard and F. Mauri, *Phys. Rev. B: Condens. Matter Mater. Phys.*, 2007, **76**, 024401.
48 J. R. Yates and C. J. Pickard, *Computations of Magnetic Resonance Parameters for Crystalline Systems: Principles*, John Wiley: Chichester, UK, 2008.
49 S. A. Joyce, J. R. Yates, C. J. Pickard and F. Mauri, *J. Chem. Phys.*, 2007, **127**, 204107.
50 S. A. Joyce, J. R. Yates, C. J. Pickard and S. P. Brown, *J. Am. Chem. Soc.*, 2008, **130**, 12663–12670.
51 I. Hung, A.-C. Uldry, J. Becker-Baldus, A. L. Webber, A. Wong, M. E. Smith, S. A. Joyce, J. R. Yates, C. J. Pickard, R. Dupree and S. P. Brown, *J. Am. Chem. Soc.*, 2009, **131**, 1820–1834.
52 J. R. Yates, *Magn. Reson. Chem.*, 2010, **48**, S23–S31.
53 C. Bonhomme, C. Gervais, C. Coelho, F. Pourpoint, T. Azaïs, L. Bonhomme Coury, F. Babonneau, G. Jacob, M. Ferrari, D. Canet, J. R. Yates, C. J. Pickard, S. A. Joyce, F. Mauri and D. Massiot, *Magn. Reson. Chem.*, 2010, **48**, S86–S102.
54 T. Thonhauser, D. Ceresoli, A. A. Mostofi, N. Marzari, R. Resta and D. Vanderbilt, *J. Chem. Phys.*, 2009, **131**, 101101.
55 D. Ceresoli, N. Marzari, M. G. Lopez and T. Thonhauser, *Phys. Rev. B: Condens. Matter Mater. Phys.*, 2010, **81**, 184424.
56 A. Zheng, S.-B. Liu and F. Deng, *J. Phys. Chem. C*, 2009, **113**, 15018–15023.
57 S. J. Clark, M. D. Segall, C. J. Pickard, P. J. Hasnip, M. J. Probert, K. Refson and M. C. Payne, *Z. Kristallogr.*, 2005, **220**, 567–570.
58 L. Truflandier, M. Paris and F. Boucher, *Phys. Rev. B: Condens. Matter Mater. Phys.*, 2007, **76**, 035102.
59 L. Truflandier, M. Paris, C. Payen and F. Boucher, *J. Phys. Chem. B*, 2006, **110**, 21403–21407.
60 M. Profeta, M. Benoit, F. Mauri and C. J. Pickard, *J. Am. Chem. Soc.*, 2004, **126**, 12628–12635.
61 J. P. Perdew, K. Burke and M. Ernzerhof, *Phys. Rev. Lett.*, 1996, **77**, 3865–3868.
62 L. S. Cahill, J. V. Hanna, A. Wong, J. C. C. Freitas, J. R. Yates, R. K. Harris and M. E. Smith, *Chem.–Eur. J.*, 2009, **15**, 9785–9798.
63 P. J. Pallister, I. L. Moudrakovski and J. A. Ripmeester, *Phys. Chem. Chem. Phys.*, 2009, **11**, 11487–11500.
64 A. Y. H. Lo, V. Sudarsan, S. Sivakumar, F. van Veggel and R. W. Schurko, *J. Am. Chem. Soc.*, 2007, **129**, 4687–4700.
65 K. J. Ooms, K. W. Feindel, M. J. Willans, R. E. Wasylishen, J. V. Hanna, K. J. Pike and M. E. Smith, *Solid State Nucl. Magn. Reson.*, 2005, **28**, 125–134.
66 H. M. Petrilli, P. E. Blöchl, P. Blaha and K. Schwarz, *Phys. Rev. B: Condens. Matter*, 1998, **57**, 14690–14697.
67 P. E. Blöchl, *Phys. Rev. B: Condens. Matter*, 1994, **50**, 17953–17979.
68 P. Blaha, K. Schwarz, G. K. H. Madsen, D. Kvasnicka and J. Luitz, *WIEN2k, An Augmented Plane WaVe + Local Orbitals Program for Calculating Crystal Properties*, 2001.
69 P. Blaha, K. Schwarz and P. Herzig, *Phys. Rev. Lett.*, 1985, **54**, 1192–1195.
70 D. Massiot, F. Fayon, M. Capron, I. King, S. Le Calve, B. Alonso, J. O. Durand, B. Bujoli, Z. H. Gan and G. Hoatson, *Magn. Reson. Chem.*, 2002, **40**, 70–76.
71 *Gaussian 03*, ed. M. J. Frisch, G. W. Trucks, H. B. Schlegel, G. E. Scuseria, M. A. Rob, J. R. Cheeseman, J. A. M. Jr.,

T. Vreven, K. N. Kudin, J. C. Burant, J. M. Millam, S. S. Iyengar, J. Tomasi, V. Barone, B. Mennucci, M. Cossi, G. Scalmani, N. Rega, G. A. Petersson, H. Nakatsuji, M. Hada, M. Ehara, K. Toyota, R. Fukuda, J. Hasegawa, M. Ishida, T. Nakajima, Y. Honda, O. Kitao, H. Nakai, M. Klene, X. Li, J. E. Knox, H. P. Hratchian, J. B. Cross, V. Bakken, C. Adamo, J. Jaramillo, R. Gomperts, R. E. Stratmann, O. Yazyev, A. J. Austin, R. Cammi, C. Pomelli, J. W. Ochterski, P. Y. Ayala, K. Morokuma, G. A. Voth, P. Salvador, J. J. Dannenberg, V. G. Zakrzewski, S. Dapprich, A. D. Daniels, M. C. Strain, O. Farkas, D. K. Malick, A. D. Rabuck, K. Raghavachari, J. B. Foresman, J. V. Ortiz, Q. Cui, A. G. Baboul, S. Clifford, J. Cioslowski, B. B. Stefanov, G. Liu, A. Liashenko, P. Piskorz, I. Komaromi, R. L. Martin, D. J. Fox, T. Keith, M. A. Al-Laham, C. Y. Peng, A. Nanayakkara, M. Challacombe, P. M. W. Gill, B. Johnson, W. Chen, M. W. Wong, C. Gonzalez and J. A. Pople, Gaussain, Inc., Wallingford, CT, 2003.
72 R. Ditchfield, *J. Chem. Phys*., 1972, **56**, 5688–5691.
73 K. Wolinski, J. F. Hinton and P. Pulay, *J. Am. Chem. Soc*., 1990, **112**, 8251–8260.
74 T. A. Keith and R. F. W. Bader, *Chem. Phys. Lett*., 1992, **194**, 1–8.
75 T. A. Keith and R. F. W. Bader, *Chem. Phys. Lett*., 1993, **210**, 223–231.
76 T. H. Dunning, *J. Chem. Phys*., 1989, **90**, 1007–1023.
77 K. L. Schuchardt, B. T. Didier, T. Elsethagen, L. Sun, V. Gurumoorthi, J. Chase, J. Li and T. L. Windus, *J. Chem. Inf. Model*., 2007, **47**, 1045–1052.
78 W. H. Baur and A. A. Khan, *Acta Crystallogr*., 1971, **B 27**, 2133–2139.
79 A. K. Cheetham and N. Norman, *Acta Chem. Scand., Ser. A*, 1974, **28**, 55–60.
80 A. Zalkin and D. H. Templeton, *Acta Crystallogr., Sect. B: Struct. Sci*., 1985, **41**, 91–93.
81 J. Thewlis, *Acta Crystallogr*., 1955, **8**, 36–38.
82 V. T. Deshpande, *Acta Crystallogr*., 1961, **14**, 794.
83 G. Finch and S. Fordham, *Proc. Phys. Soc*., 1936, **48**, 85–94.
84 V. M. Goldschmidt, *Naturwissenschaften*, 1926, **14**, 477–485.
85 E. Posnjak and R. W. G. Wyckoff, *J. Wash. Acad. Sci*., 1922, **12**, 248.
86 B. T. M. Willis, *Acta Crystallogr*., 1965, **112**, 8251–8260.
87 J. B. Forsyth, C. C. Wilson and T. M. Sabine, *Acta Crystallogr., Sect. A: Found. Crystallogr*., 1989, **45**, 244–247.
88 A. S. Radtke and G. E. Brown, *Am. Mineral*., 1974, **59**, 885–888.
89 K. H. Jack, *Acta Crystallogr*., 1957, **10**, 780.
90 P. P. Fedorov, G. A. Lovetskaya and B. P. Sobolev, *Russ. J. Inorg. Chem*., 1995, **40**, 1504–1505.
91 C. Adamo and V. Barone, *J. Chem. Phys*., 1999, **110**, 6158.
92 P. Pyykkö, *Mol. Phys*., 2008, **106**, 1965–1974.
93 M. E. Harding, M. Lenhart, A. A. Auer and J. Gauss, *J. Chem. Phys*., 2008, **128**, 244111.
94 C. Bessada, A. L. Rollet, A. Rakhmatullin, L. Nuta, P. Florian and D. Massiot, *C. R. Chim*., 2006, **9**, 374–380.
95 A. L. Rollet, C. Bessada, A. Rakhmatoulline, Y. Auger, P. Melin, M. Gailhanou and D. Thiaudiere, *C. R. Chim*., 2004, **7**, 1135–1140.
96 T. Schaller, D. B. Dingwell, H. Keppler, W. Knoller, L. Merwin and A. Sebald, *Geochim. Cosmochim. Acta*, 1992, **56**, 701–707.
97 J. H. Clark, E. M. Goodman, D. K. Smith, S. J. Brown and J. M. Miller, *J. Chem. Soc., Chem. Commun*., 1986, 657–658.
98 R. K. Harris and P. Jackson, *Chem. Rev*., 1991, **91**, 1427–1440.
99 H. A. Prescott, Z. J. Li, E. Kemnitz, J. Deutsch and H. Lieske, *J. Mater. Chem*., 2005, **15**, 4616–4628.
100 S. Wuttke, G. Scholz, S. Ruediger and E. Kemnitz, *J. Mater. Chem*., 2007, **17**, 4980–4988.
101 C. W. Ponader, R. E. Youngman and C. M. Smith, *J. Am. Ceram. Soc*., 2005, **88**, 2447–2450.
102 A. T. Kreinbrink, C. D. Sazavsky, J. W. Pyrz, D. G. A. Nelson and R. S. Honkonen, *J. Magn. Reson*., 1990, **88**, 267–276.
103 C. Bessada, A. Rakhmatullin, A.-L. Rollet and D. Zanghi, *J. Nucl. Mater*., 2007, **360**, 43–48.
104 B. K. Greve, K. L. Martin, P. L. Lee, P. J. Chupas, K. W. Chapman and A. P. Wilkinson, *J. Am. Chem. Soc*., 2010, **132**, 15496–15498.
105 J. R. Yates, S. E. Dobbins, C. J. Pickard, F. Mauri, P. Y. Ghi and R. K. Harris, *Phys. Chem. Chem. Phys*., 2005, **7**, 1402–1407.
106 D. K. Hindermann and C. D. Cornwell, *J. Chem. Phys*., 1968, **48**, 4148–4154.
107 C. J. Jameson, A. K. Jameson and J. Honarbakhsh, *J. Chem. Phys*., 1984, **81**, 5266–5267.
108 D. L. Bryce and E. B. Bultz, *Chem.–Eur. J*., 2007, **13**, 4786–4796.
109 R. P. Chapman and D. L. Bryce, *Phys. Chem. Chem. Phys*., 2009, **11**, 6987–6998.
110 C. M. Widdifield and D. L. Bryce, *J. Phys. Chem. A*, 2010, **114**, 2102–2116.
111 C. M. Widdifield and D. L. Bryce, *J. Phys. Chem. A*, 2010, **114**, 10810–10823.
112 M. Profeta, F. Mauri and C. J. Pickard, *J. Am. Chem. Soc*., 2003, **125**, 541–548.
113 C. Gervais, M. Profeta, F. Babonneau, C. J. Pickard and F. Mauri, *J. Phys. Chem. B*, 2004, **108**, 13249–13253.
114 S. Cadars, A. Lesage, C. J. Pickard, P. Sautet and L. Emsley, *J. Phys. Chem. A*, 2009, **113**, 902–911.
115 F. Pourpoint, A. Kolassiba, C. Gervais, T. Azais, L. Bonhomme-Coury, C. Bonhomme and F. Mauri, *Chem. Mater*., 2007, **19**, 6367–6369.
116 D. L. Bryce, E. B. Bultz and D. Aebi, *J. Am. Chem. Soc*., 2008, **130**, 9282–9292.
117 J. V. Hanna, K. J. Pike, T. Charpentier, T. F. Kemp, M. E. Smith, B. E. G. Lucier, R. W. Schurko and L. S. Cahill, *Chem.–Eur. J*., 2010, **16**, 3222–3239.
118 F. El Haber, X. Rocquefelte, C. Andraud, B. Amrani, S. Jobic, O. Chauvet and G. Froyer, *J. Opt. Soc. Am. B*., submitted.
119 M. Benoit, M. Profeta, F. Mauri, C. J. Pickard and M. E. Tuckerman, *J. Phys. Chem. B*, 2005, **109**, 6052–6060.
120 C. Gervais, D. Laurencin, A. Wong, F. Pourpoint, J. Labram, B. Woodward, A. P. Howes, K. J. Pike, R. Dupree, F. Mauri, C. Bonhomme and M. E. Smith, *Chem. Phys. Lett*., 2008, **464**, 42–48.
121 T. Tsujibayashi, K. Toyoda, S. Sakuragi, M. Kamada and M. Itoh, *Appl. Phys. Lett*., 2002, **80**, 2883–2885.
122 F. Wang and C. P. Grey, *J. Am. Chem. Soc*., 1998, **120**, 970–980.
123 P. J. Chupas, M. F. Ciraolo, J. C. Hanson and C. P. Grey, *J. Am. Chem. Soc*., 2001, **123**, 1694–1701.
124 M. Body, C. Legein, J.-Y. Buzaré, G. Silly, P. Blaha, C. Martineau and F. Calvayrac, *J. Phys. Chem. A*, 2007, **111**, 11873–11884.
125 M. Iglesias, K. Schwarz, P. Blaha and D. Baldomir, *Phys. Chem. Miner*., 2001, **28**, 67–75.
126 M. R. Hansen, G. K. H. Madsen, H. J. Jakobsen and J. Skibsted, *J. Phys. Chem. A*, 2005, **109**, 1989–1997.
127 K. Schwarz, C. Ambrosch-Draxl and P. Blaha, *Phys. Rev. B: Condens. Matter*, 1990, **42**, 2051–2061.

Electronic Supplementary Material (ESI) for Physical Chemistry Chemical Physics

NMR parameters in alkali, alkaline earth and rare earth fluorides from first principle calculations

Aymeric Sadoc, Monique Body, Christophe Legein, Mamata Biswal, Franck Fayon, Xavier Rocquefelte and Florent Boucher

Electronic Supplementary Information
Table of content

Experimental conditions used for ^{19}F solid state NMR spectroscopy

The ^{19}F solid-state MAS NMR experiments were conducted on Avance 300 (magnetic field of 7.0 T) and Avance 750 (magnetic field of 17.6 T) Bruker spectrometers operating at Larmor frequencies of 282.2 and 705.85 MHz, respectively, using 2.5 mm and 1.3 mm CPMAS probehead. All spectra were acquired using a Hahn echo sequence with an inter-pulse delay equal to one rotor period, except CaF_2 and LaF_3 for which a single pulse sequence was used. The recycle delays were set to 10 s for LiF, NaF, KF, RbF, CsF, MgF_2, CaF_2, SrF_2, BaF_2 and ScF_3 and 30 s for YF_3 and LaF_3. ^{19}F nutation frequencies ranging between 93 (2.5 mm prohead) and 195 kHz (1.3 mm probehead) were used. The ^{19}F chemical shifts were referenced to $CFCl_3$ at 0 ppm.

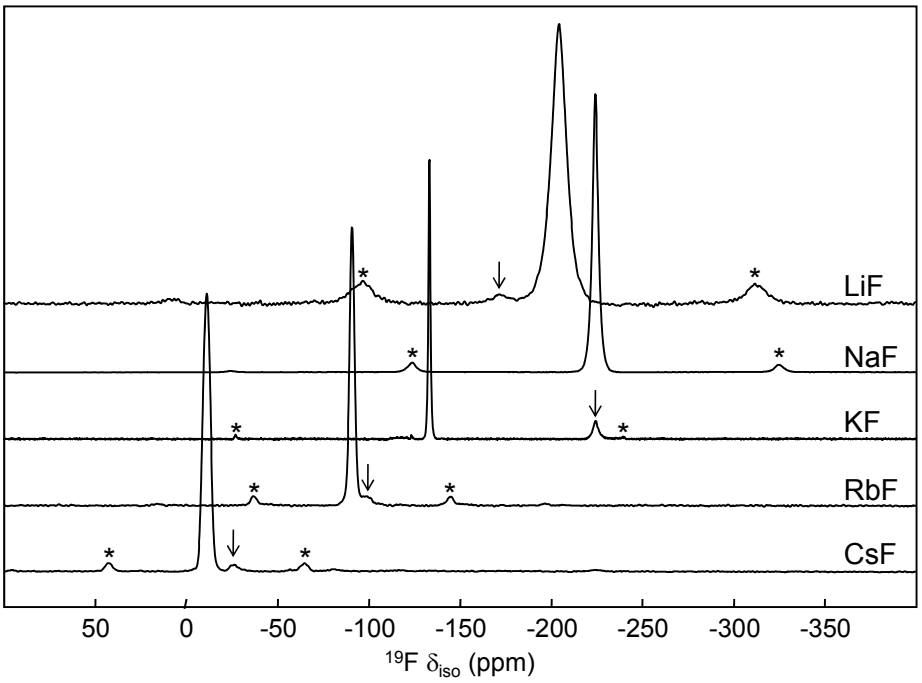

Figure S1. ^{19}F MAS NMR spectra of alkaline fluorides obtained at a magnetic field of 7.0 T using spinning frequencies of 30 kHz for LiF, 25 kHz for NaF and KF and 15 kHz for RbF and CsF. The arrows on the NMR spectra of LiF, RbF and CsF indicate unidentified impurities. The arrow on the spectrum of KF indicates an impurity identified as NaF. The asterisks indicate spinning sidebands.

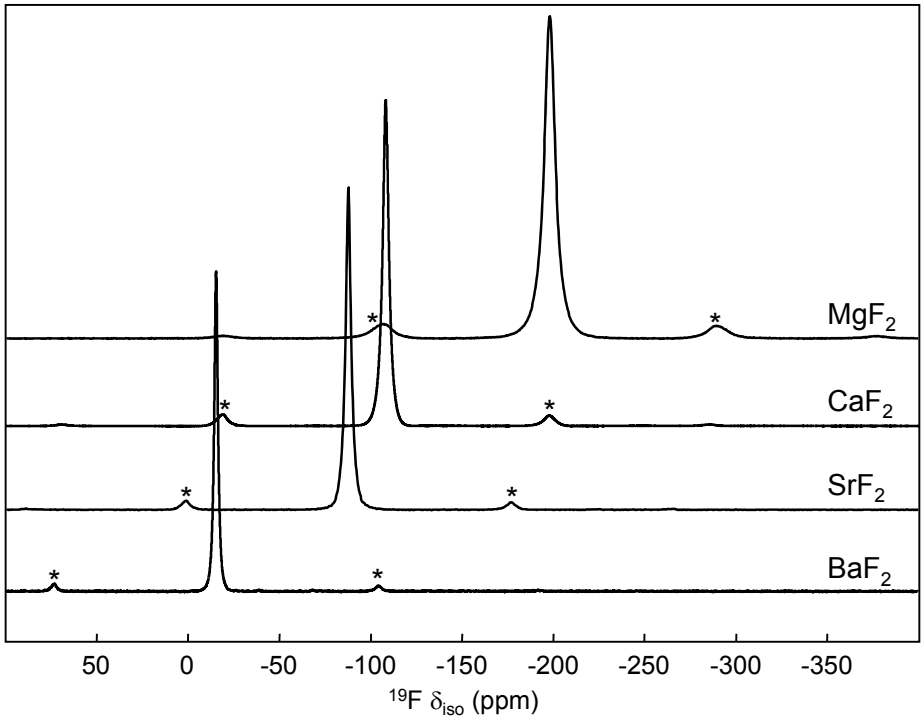

Figure S2. ^{19}F MAS NMR spectra of alkaline earth fluorides obtained at a magnetic field of 7.0 T using spinning frequencies of 25 kHz. The asterisks indicate spinning sidebands.

Solid state NMR and PXRD study of ScF_3

ScF_3 was recently studied by both ^{19}F and ^{45}Sc solid-state MAS NMR but the reported results[1] appear to us somewhat surprising and the results obtained in our study were also not straightforward to interpret.

Firstly, two different crystalline structures are reported for ScF_3 at ambient temperature and pressure: a cubic one[2,3] (ReO_3 type, space group: Pm-3m) and a rhombohedral one[4-6] (distorted ReO_3 type, space group: R32). Lo *et al.* report that their ScF_3 sample adopts a rhombohedral structure. However the small 2θ range of their powder X-ray diffraction (PXRD) pattern[1] does not allow confirming this assumption since both cubic and rhombohedral structures give very similar patterns, except for large 2θ values. The PXRD patterns recorded for our sample (Aldrich, 99.99%, lot number 04937HE) on the 2θ ranges 20-125°, 117.7-119.3°, 139.5-142.5° and 146.1-149.5° are shown in Figure 3. These diagrams do not evidence any rhombohedral splitting (Table 1) indicating that ScF_3 adopts a cubic structure at ambient temperature and pressure, in agreement with a recent study of the pronounced negative thermal expansion (NTE) of ScF_3.[7]

Both cubic and rhombohedral structures of ScF_3 contain a single Sc site and a single F site in the unit cell. Nevertheless, we were not able to reconstruct the ^{19}F MAS NMR spectrum with a single resonance (Figure 2). A satisfying reconstruction is obtained with three lines having close δ_{iso} values but significantly different chemical shift anisotropies (Table 2). Lo *et al.* report a δ_{iso} value equal to -35.9 ppm,[1] in good agreement with previously reported results,[8] and a CSA equal to ca. 305 ppm. This large value is in agreement with the observed intense spinning sidebands (the ^{19}F reconstructed spectrum is not presented).

Moreover, Lo *et al.*[1] estimated the ^{45}Sc quadrupolar coupling constant to 1.3(2) MHz and they claimed that "this small value is consistent with the high spherical symmetry around ^{45}Sc" whereas, as outlined by themselves, this nucleus has a moderately sized quadrupole moment ($Q = -0.22 \times 10^{-28}$ m^2).[9] We have also recorded a ^{45}Sc NMR spectrum of ScF_3 (Figure 3). Assuming a cubic structure, in which the Sc atom occupy the site with m-3m symmetry (1a Whyckoff position), a quadrupolar coupling constant equal to zero is expected. As Lo *et al.*[1], we observe a spinning sideband manifold, indicating quadrupolar frequency different from zero, and the shape of this spinning sideband manifolds likely

indicates some disorder in the structure. This spectrum is consequently difficult to reconstruct with a single set of parameters and the quadrupolar frequency can only be roughly estimated to 20 kHz (C_Q=280 kHz). Whereas the determined ^{45}Sc δ_{iso} value (-51.8 ppm) is very similar to the one determined by Lo et al. (-52 ppm), our quadrupolar coupling constant is significantly lower indicating less distorted Sc^{3+} sites.

At first glance, these results which can only be explained by the presence of some structural disorder in ScF_3 seem puzzling. Nevertheless, disorder was previously mentioned in ScF_3 to explain its marked NTE.[7] The assumed mechanism, *i. e.* rocking motion of essentially rigid ScF_6^{3-} octahedra, is supported by the large transverse component of the anisotropic displacement parameters (ADPs) for the fluoride anions.[7] ADPs may represent either atomic motion or static displacive disorder and static disorder was also invoked since it has been suggested for AlF_3 above its rhomboedral-to-cubic phase transition (the Al-F-Al links are locally bent in the cubic phase).[10,11] Both dynamic (depending on the motion frequency) and static disorders explain the non-zero quadrupolar frequency of ^{45}Sc (Figure 3) and the several lines used for the reconstruction of the ^{19}F NMR spectrum (Figure 2 and Table 2).

Local structural disorder in ScF_3 could also arise from incomplete fluorination leading to $ScF_{3-2x}O_x\square_x$ compounds and/or from occurrence of hydroxyl groups substituting fluoride ions into the network. Both these assumptions can be ruled out since the fluorinations of our sample, using either HF or F_2 at 600°C, do not lead to any changes on the NMR spectra.

Since several lines are used for the reconstruction of the ^{19}F NMR spectrum, ^{19}F δ_{iso} value for ScF_3 can only be roughly determined and the uncertainty is higher than for the others studied compounds. We choose the chemical shift value at the peak maximum, *i. e.* -36 ppm.

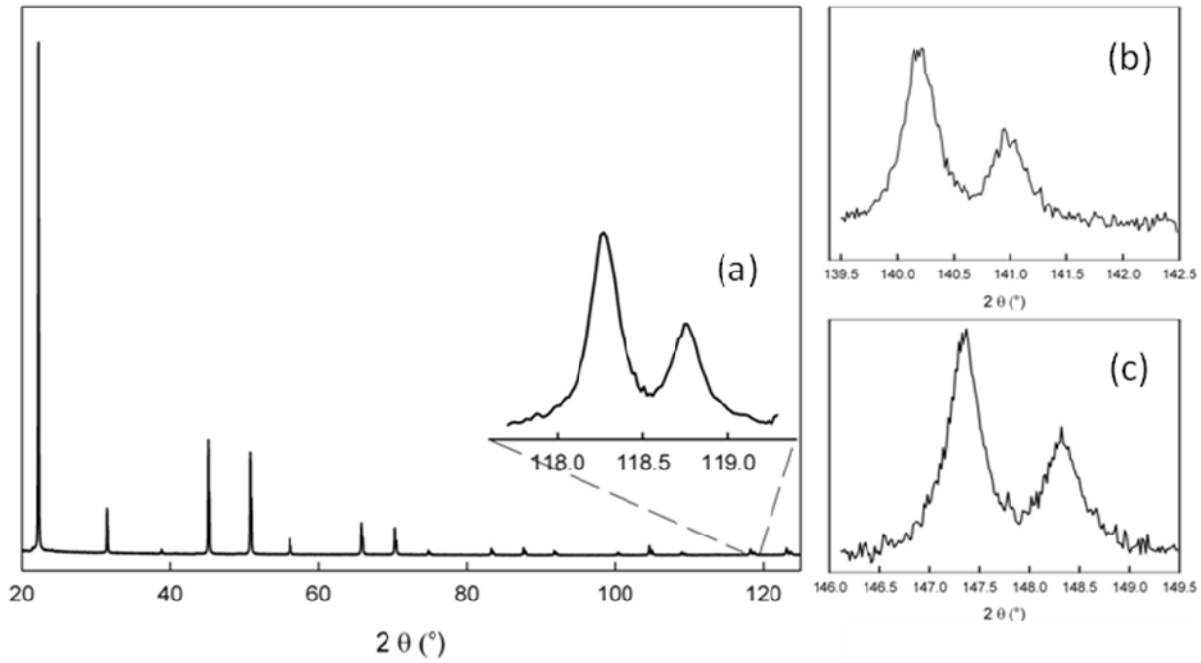

Figure S3. X-ray powder diffraction diagrams of ScF_3. In (a), (b) and (c) are shown the (4,2,0), (4,2,2) and (4,3,3) reflections, respectively. These diagrams were recorded under air, at room temperature with a PANalytical X'pert PRO diffractometer equipped with a X'Celerator detector using monochromated CuKα radiation (λ = 1.54056 Å). Measurements were done with an interpolated step of 0.017°, in the 2θ ranges 20-125°, (a) 117.7-119.3°, (b) 139.5-142.5° and (c) 146.1-149.5°, and total collecting times of 2 h 06 min, (a) 24 min, (b) 12 min and (c) 35 min.

Table S1. (h,k,l) reflections and corresponding 2θ values (°) of ScF_3 assuming Pm-3m[3] (ICSD[12] file number 36011) and R32[6] (ICSD[12] file number 77071) space groups (λ = 1.54056 Å).

Pm-3m				**R32**			
h	k	l	2θ	h	k	l	2θ
0	2	4	118.373	0	2	4	117.725
				-2	0	4	118.070
2	2	4	140.376	2	2	4	139.010
				-2	2	4	139.711
				-2	-2	4	139.948
0	3	4	147.565	0	3	4	146.189
0	0	5	147.565	0	0	5	146.602
				-3	0	4	147.019

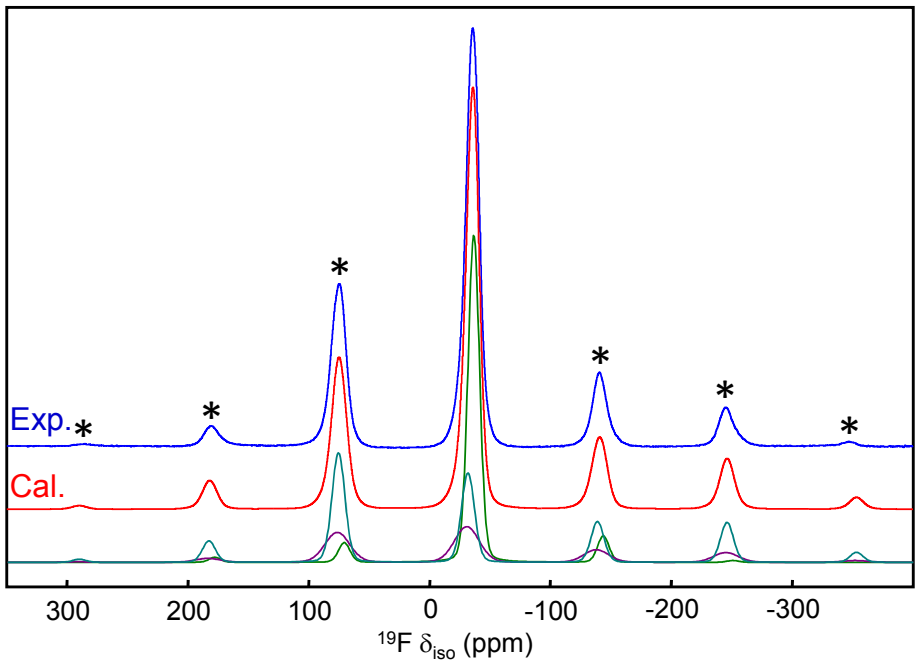

Figure S4. Experimental (exp.) and reconstructed (cal.) ^{19}F MAS NMR spectra of ScF_3 obtained at a magnetic field of 7.0 T using a spinning frequency of 30 kHz. The three individual contributions to the reconstructed spectrum are shown below. The asterisks indicate spinning sidebands.

Table S2. ^{19}F isotropic chemical shifts (δ_{iso}, ppm), chemical shift anisotropies (δ_{aniso}, ppm), asymmetry parameters (η), line widths and relative intensities (%) determined from the reconstruction of the ^{19}F NMR spectrum of ScF_3.

Line	δ_{iso} (±0.5)	δ_{aniso} (±10)	η (±0.05)	Width (±0.5)	Intensity (±0.5)
1	-36.5	107	0	11.2	40.7
2	-31.7	-279	0	12.7	38.0
3	-30.8	-322	0.2	24.1	21.3

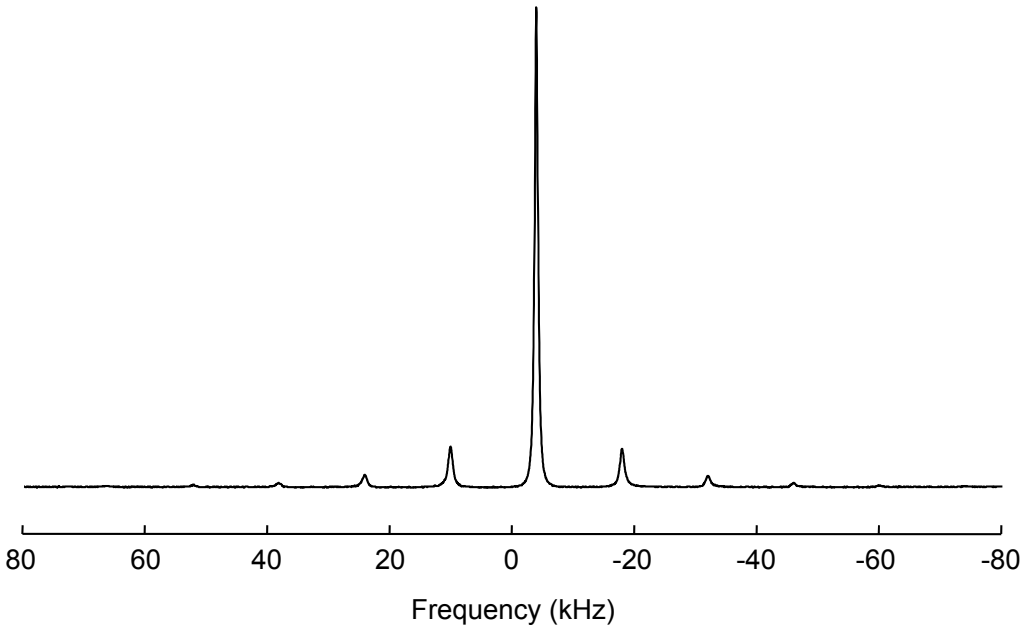

Figure S5. Experimental ^{45}Sc SATRAS (SAtellite TRAnsition Spectroscopy[13,14]) MAS NMR spectrum of ScF_3 recorded on a Bruker Avance 300 (7.0 T) spectrometer operating at a Larmor frequency of 72.906 MHz using a 2.5 mm probehead. The spinning frequency was 14 kHz. The quantitative excitation of all transitions[15] was ensured by using a short pulse duration (1 μs) with low-radio-frequency (RF) field strength (70 kHz). The recycle delay was set to 5 s. The ^{45}Sc chemical shift was referenced to a 1 M $Sc(NO_3)_3$ aqueous solution.

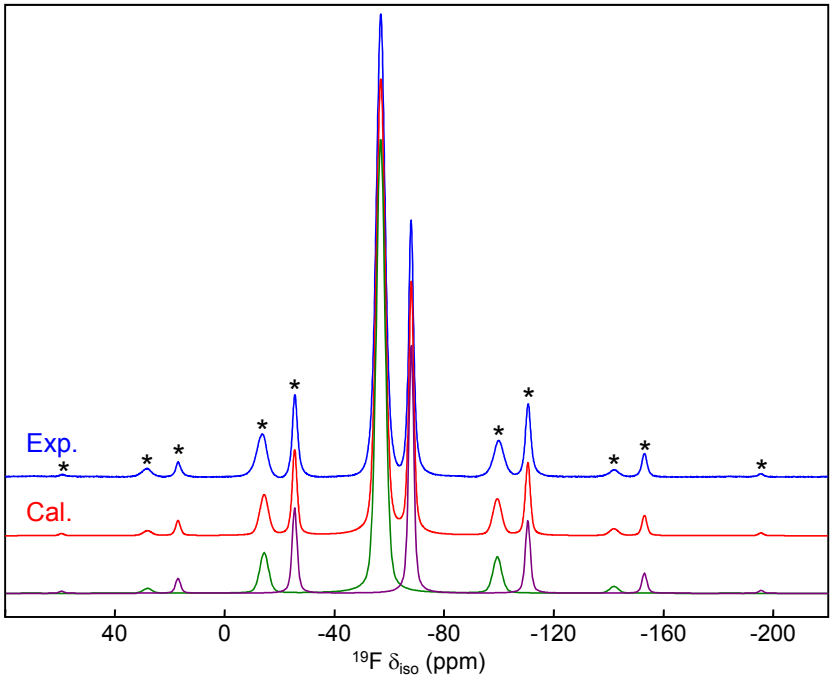

Figure S6. ^{19}F experimental (exp.) and reconstructed (cal.) ^{19}F MAS NMR spectra of YF_3 recorded at a magnetic field of 17.6 T using a spinning frequency of 30 kHz. The two individual contributions to the reconstructed spectrum are shown below. The asterisks indicate spinning sidebands.

Table S3. ^{19}F isotropic chemical shifts (δ_{iso}, ppm), chemical shift anisotropies (δ_{aniso}, ppm), asymmetry parameters (η), line widths (ppm), relative intensities (%) determined from the reconstruction of the ^{19}F NMR spectrum of YF_3 and line assignment.

Line	δ_{iso} (±0.2)	δ_{aniso} (±5)	η (±0.05)	Width (±0.1)	Intensity (±0.5)	Assignment
1	-56.9	-42.5	0.75	3.8	66.4	F2
2	-68.1	-76.5	0.80	2.1	33.6	F1

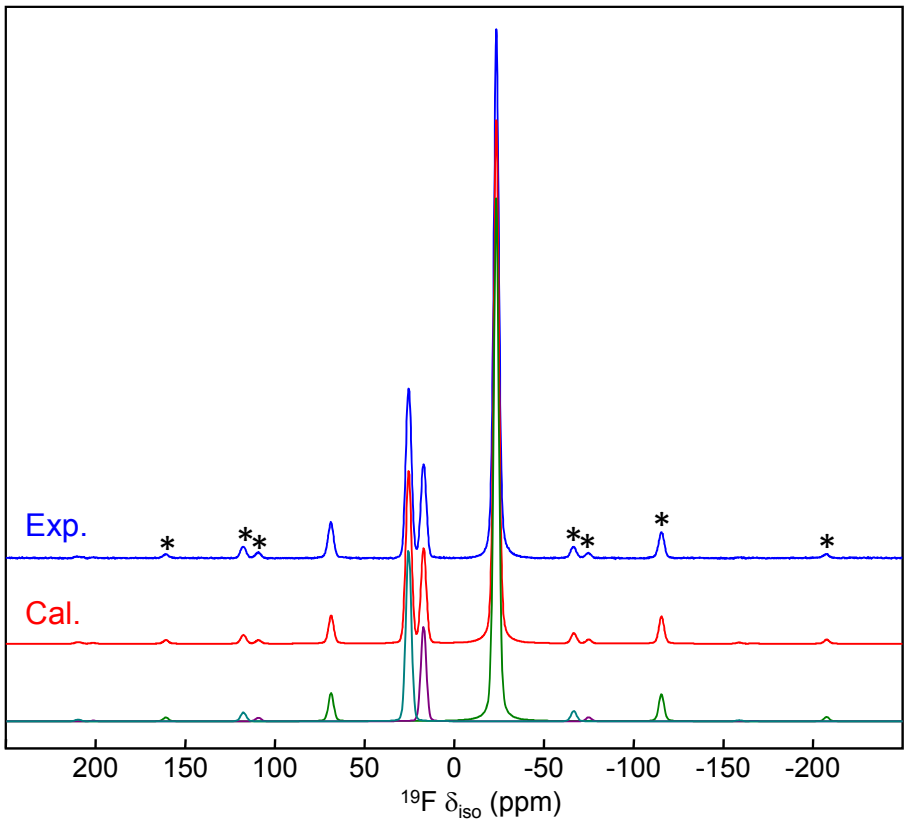

Figure S7. ^{19}F experimental (exp.) and reconstructed (cal.) MAS NMR spectra of LaF_3 recorded at a magnetic field of 17.6 T using a spinning frequency of 65 kHz. The three individual contributions to the reconstructed spectra are shown below. The asterisks indicate spinning sidebands.

Table S4. ^{19}F isotropic chemical shifts (δ_{iso}, ppm), chemical shift anisotropies (δ_{aniso}, ppm), asymmetry parameters (η), line widths (ppm), relative intensities (%) determined from the reconstruction of the ^{19}F NMR spectrum of LaF_3 and line assignment.

Line	δ_{iso} (±0.2)	δ_{aniso} (±5)	η (±0.05)	Width (±0.1)	Intensity (±0.5)	Assignment
1	-23.6	-71	0.9	3.3	66.7	F1
2	16.9	66	0.55	3.5	11.3	F3
3	25.3	78	0.55	3.6	22.0	F2

Table S5. Parameters used to generate the OTF USPP pseudopotentials. Details on the string can be found on the Castep website (http://www.castep.org/) in the documentation section.

Atom	**OTF USPP string**
F	2|1.4|16.537|18.375|20.212|20UU:21UU(qc=7.5)[]
Li	1|1.2|11|13.2|15|10U:20UU(qc=5.5)[]
Na	2|1.3|1.3|1.0|16|19|21|20UU:30UU:21U(qc=7)[]
K	2|1.8|1.8|1.6|11|14.7|16.7|30U:40UU:31UU(qc=5.5)[]
Rb	2|2.5|2.5|2.1|5.5|6.6|8.1|40U:50U+0U+0.125:41UU(qc=3.5)[]
Cs	2|2.7|2.7|1.6|4.4|5.9|7.4|50U:60U+0U+0.125:51UU(qc=3.5)[]
Mg	2|1.6|2|1.4|6|7|8|30NH:21U:31UU:32LGG(qc=4.5)[]
Ca	3|1.6|2|1.4|7.5|9.2|10.3|30U=-1.72:40U=-0.14: 31U=-1.03U=+0.25:32U=+0U=+1[]
Ca **shift 1.81 eV**	3|1.6|2|1.4|7.5|9.2|10.3|30U=-1.72:40U=-0.14: 31U=-1.03U=+0.25:32U=+0@+0.0665U=+1@+0.0665[]
Sr	3|2|2|1.2|7.4|9.2|11|40U:50U:41UU:42UU[]
Ba	2|3|2.9|2.2|6.4|8.1|9|50U:60UU:51U2.5U2.5(qc=3.5)[]
Sc	3|1.8|1.8|1.6|9.6|10.8|11.7|30U=-2.01:40U=-0.16: 31U=-1.235U=+0.25:32U=-0.125U=+0.25[]
Sc **shift 1.96 eV**	3|1.8|1.8|1.6|9.6|10.8|11.7|30U=-2.01:40U=-0.16: 31U=-1.235U=+0.25: 32U=-0.125@0.0720U=+0.25@0.0720[]
La	2|2|2|1.4|8|12|13|50N:60NH:51UU:52LGG: 43U1.6+0U1.6+0.1{5d0.9,4f0.1}(qc=6)[]
La **shift 4.55 eV**	2|2|2|1.4|8|12|13|50N:60NH:51UU:52LGG: 43U1.6+0@0.1672U1.6+0.1@0.1672{5d0.9,4f0.1}(qc=6)[]
Y	3|2|2|2|8.5|10|11.1|40U:50U:41UU:42UU[]

Table S6. Fractional atomic coordinates from the initial (IS)[16] and and PBE-DFT geometry-optimized (APO) structures for MgF_2.

Atom	Site		*x*	*y*	*z*
Mg	2a		0	0	0
F	4f	*IS*	*0.3028*	*0.3028*	*0*
		APO	0.3022	0.3022	0

Table S7. Mg-F bond lengths and F-Mg-F bond angles deduced from the initial[16] (IS) and PBE-DFT geometry-optimized (APO) structures for MgF_2.

Bond lengths/Å		Bond angles/°	
IS	APO	IS	APO
1.979	1.975	81.04	81.22
1.984	1.986	98.96	98.78

Table S8. Eigenvectors of the calculated ^{25}Mg EFG tensor, after optimization, expressed in Cartesian coordinates for MgF_2 at the (0,0,0) position. The definition of the Cartesian axis with respect to the lattice parameters is given below.

Axis	V_{xx}	V_{yy}	V_{zz}
i	0.7071	0	-0.7071
j	0.7071	0	0.7071
k	0	1	0

With $\begin{pmatrix} a \\ b \\ c \end{pmatrix} = \begin{pmatrix} 4.6213 & 0.0000 & 0.0000 \\ 0.0000 & 4.6213 & 0.0000 \\ 0.0000 & 0.0000 & 3.0159 \end{pmatrix} \times \begin{pmatrix} i \\ j \\ k \end{pmatrix}$

and $a = b = 4.6213$ Å, $c = 3.0159$ Å ; $\alpha = \beta = \gamma = 90°$

Table S9. Fractional atomic coordinates from the initial (IS)[17] and PBE-DFT geometry-optimized (APO) structures for YF_3.

Atom	Site		*x*	*y*	*z*
Y	4c	*IS*	*0.3673*	*1/4*	*0.0591*
		APO	0.3687	1/4	0.0604
F1	4c	*IS*	*0.5227*	*1/4*	*0.5910*
		APO	0.5231	1/4	0.5906
F2	8d	*IS*	*0.1652*	*0.0643*	*0.3755*
		APO	0.1655	0.0629	0.3775

Table S10. Y-F bond lengths deduced from the initial[17] (IS) and PBE-DFT geometry-optimized (APO) structures for YF_3.

Bond lengths/Å	IS	APO
Y-F1	2.282	2.285
	2.287	2.294
	2.538	2.528
Y-F2	2.281 (x2)	2.291 (x2)
	2.299 (x2)	2.296 (x2)
	2.310 (x2)	2.299 (x2)

Table S11. Fractional atomic coordinates from the initial (IS)[18] and PBE-DFT geometry-optimized (APO) structures for LaF_3.

Atom	Site		x	y	z
La	6f	*IS*	*0.6598*	*0*	*1/4*
		APO	0.6578	0	1/4
F1	12g	*IS*	*0.3659*	*0.0536*	*0.0813*
		APO	0.3688	0.0584	0.0805
F2	4d	*IS*	*1/3*	*2/3*	*0.1830*
		APO	1/3	2/3	0.1825
F3	2a		0	0	1/4

Table S12. La-F bond lengths deduced from the initial[18] (IS) and PBE-DFT geometry-optimized (APO) structures for LaF_3.

Bond lengths/Å	IS	APO
La-F1	2.458 (x2)	2.457 (x2)
	2.489 (x2)	2.477 (x2)
	2.638 (x2)	2.629 (x2)
	3.003 (x2)	3.038 (x2)
La-F2	2.417 (x2)	2.415 (x2)
La-F3	2.444	2.458

Table S13. Eigenvectors of the calculated ^{139}La EFG tensor in LaF_3 for IS, expressed in a Cartesian coordinate system (*i, j, k*) and along the crystallographic axis (*a, b, c*) for the La position at (0.6578, 0, 1/4). The definition of the Cartesian axis with respect to the lattice parameters is given below.

Axis	V_{xx}	V_{yy}	V_{zz}
i	0.2880	-0.8660	-0.4087
j	0.4989	0.5	-0.7079
k	0.8174	0	0.5761
a	0.0466	-0.1391	-0.0654
b	0.0933	0.0000	-0.1308
c	0.1106	0.0000	0.0789

With $\begin{pmatrix} a \\ b \\ c \end{pmatrix} = \begin{pmatrix} 6.2224 & -3.5925 & 0 \\ 0 & 7.1850 & 0 \\ 0 & 0 & 7.3510 \end{pmatrix} \times \begin{pmatrix} i \\ j \\ k \end{pmatrix}$

and $a = b = 7.1850$ Å, $c = 7.3510$ Å ; $\alpha = \beta = 90°$, $\gamma = 120°$

Table S14. Experimental ^{19}F isotropic chemical shifts relative to $CFCl_3$ and calculated ^{19}F isotropic shieldings for the eleven compounds additionally considered in Figure 5. The "calculated" ^{19}F isotropic chemical shifts according to $\delta_{iso}/CFCl_3 = -0.80(3)\ \sigma_{iso} + 89(9)$ are also reported.

Compounds	Site	$\sigma_{iso}^{calc.}$ (ppm)	$\delta_{iso}^{calc.}$ (ppm)	$\delta_{iso}^{exp.}$ (ppm)
CdF_2	F1	350.9[a]	-192	-190.7[c]
HgF_2	F1	356.4[a]	-196	-197.6[d]
α-PbF_2	F1	140.8[a]	-24	-20.5[e]
	F2	176.6[a]	-52	-57.7[e]
α-AlF_3	F1	336.2[a]	-180	-172.0[f]
$Na_5Al_3F_{14}$	F1	358.9[a]	-198	-191.4[g]
	F2	326.1[a]	-172	-165.0[g]
	F3	356.9[a]	-197	-189.5[g]
ZnF_2	F1	363.0[b]	-201	-200.7[c]
GaF_3	F1	314.0[b]	-162	-167.2[c]
InF_3	F1	364.1[b]	-202	-206.2[c]
$BaLiF_3$	F1	238.8[b]	-102	-98.2[c]
β-$BaAlF_5$	F1	307.4[b]	-157	-154.6[h]
	F2	287.9[b]	-141	-138.9[h]
	F3	268.5[b]	-126	-121.3[h]
	F4	254.9[b]	-115	-109.2[h]
	F5	302.4[b]	-153	-148.8[h]
	F6	277.5[b]	-133	-127.5[h]
	F7	293.3[b]	-146	-140.8[h]
	F8	245.4[b]	-107	-99.0[h]
	F9	271.7[b]	-128	-124.5[h]
	F10	297.0[b]	-149	-144.6[h]
$Ba_3Al_2F_{12}$	F1	310.9[b]	-160	-153.3[h]
	F2	308.2[b]	-158	-151.6[h]
	F3	165.1[b]	-43	-30.5[h]
	F4	186.6[b]	-60	-50.8[h]
	F5	267.6[b]	-125	-115.7[h]
	F6	265.4[b]	-123	-113.0[h]
	F7	279.8[b]	-135	-127.9[h]
	F8	302.3[b]	-153	-146.4[h]

[a] Calculated values from reference [19].
[b] Calculated values from reference [20].
[c] Experimental values from reference [21].
[d] Experimental values from reference [22].
[e] Experimental values from reference [23].
[f] Experimental values from reference [24].
[g] Experimental values from reference [25].
[h] Experimental values from reference [26].

References

[1] A. Y. H. Lo, V. Sudarsan, S. Sivakumar, F. van Veggel, R. W. Schurko, *J. Am. Chem. Soc.* 2007, **129**, 4687.
[2] K. H. Jack, *Acta Cryst.* 1957, **10**, 780.
[3] P. P. Fedorov, V. Trncova, G. I. Kocherba, B. P. Sobolev, *Kristallografiya* 1995, **40**, 716 ; *Crystallogr. Rep.* 1995, **40**, 663.
[4] W. Nowacki, *Z. Kristallogr. Kristallgeom. Kristallphys. Kristallchem.* 1939, **101**, 273.
[5] E. G. Ippolitov, A. G. Maklachkov, *Inorg. Mater. (Engl. Transl.)* 1970, **6**, 1251.
[6] R. Loesch, C. Hebecker, Z. Z. Ranft, *Anorg. Allg. Chem.* 1982, **491**, 199.
[7] B. K. Greve, K. L. Martin, P. L. Lee, P. J. Chupas, K. W. Chapman, A. P. Wilkinson, *J. Am. Chem. Soc.* 2010, **132**, 15496.
[8] L. M. Avkhutskii, Y. V. Gagarinskii, S. A. Polishchuk, S. P. Gabuda, *Spectrosc. Lett.* 1969, **2**, 75.
[9] P. Pyykko, *Mol. Phys.* 2001, **99**, 1617.
[10] S. Chaudhuri, P. J. Chupas, M. Wilson, P. Madden, C. P. Grey, *J. Phys. Chem. B* 2004, **108**, 3437.
[11] P. J. Chupas, S. Chaudhuri, J. C. Hanson, X. Qiu, P. L. Lee, S. D. Shastri, S. J. L. Billinge, C. P. Grey, *J. Am. Chem. Soc.* 2004, **126**, 4756.
[12] Inorganic Crystal Structure Database (ICSD), version 1.7.1, 2010.
[13] J. Skibsted, N. C. Nielsen, H. Bildsoe, H. J. Jakobsen, *J. Magn. Reson.*, 1991, **95**, 88.
[14] B. B. C. Jäger, in *Solid State NMR II*, (Ed.: B. Blümich), Springer-Verlag: Berlin, 1994, 163.
[15] A. Samoson, E. Lippmaa, *Phys. Rev. B*, 1983, **28**, 6567.
[16] W. H. Baur, A. A. Khan, *Acta Crystallogr.* 1971, **B27**, 2133.
[17] A. K. Cheetham, N. Norman, *Acta Chem. Scand. Ser. A* 1974, **28**, 55.
[18] A. Zalkin, D. H. Templeton, *Acta Crystallogr.* 1985, **B41**, 91.
[19] J. M. Griffin, J. R. Yates, A. J. Berry, S. Wimperis, S. E. Ashbrook, *J. Am. Chem. Soc.* 2010, **132**, 15651.
[20] A. Zheng, S.-B. Liu, and F. Deng, *J. Phys. Chem. C* 2009, **113**, 15018.
[21] B. Bureau, G. Silly, J.-Y. Buzaré, J. Emery, *Chem. Phys*. 1999, **249**, 89.
[22] A. T. Kreinbrink, C. D. Sazavsky, J. W. Pyrz, D. G. A. Nelson, S. R. Honkonen, *J. Magn. Reson.* 1990, **88**, 267.
[23] F. Wang, C. P. Grey, *J. Am. Chem. Soc.* 1998, **120**, 970.
[24] P. J. Chupas, M. F. Ciraolo, J. C. Hanson, C. P. Grey, *J. Am. Chem. Soc.* 2001, **123**, 1694.
[25] L.-S. Du, A. Samoson, T. Tuherm, C. P. Grey, *Chem. Mater.* 2000, **12**, 3611.
[26] C. Martineau, C. Legein, J.-Y. Buzaré, F. Fayon, *Phys. Chem. Chem. Phys.* 2009, **11**, 950.

2.3 Column 13 metal fluorides

NMR parameters in column 13 metal fluoride compounds (AlF_3, GaF_3, InF_3 and TlF) from first principle calculations

Aymeric Sadoc[a], Mamata Biswal[b], Monique Body[b], Christophe Legein[b,*], Florent Boucher[b], Dominique Massiot[c] , Franck Fayon[c]

[a] Institut des Matériaux Jean Rouxel (IMN), Université de Nantes, CNRS, 2 rue de la Houssinière, BP 32229, 44322 Nantes Cedex 3, France.

[b] LUNAM Université, Université du Maine, CNRS UMR 6283, Institut des Molécules et des Matériaux du Mans, Avenue Olivier Messiaen, 72085 Le Mans Cedex 9, France.

[c] Conditions Extrêmes et Matériaux: Haute Température et Irradiation, CNRS UPR 3079, 1D Avenue de la Recherche Scientifique, 45071 Orléans Cedex 2, France and Université d'Orléans, Faculté des Sciences, Avenue du Parc Floral, 45067 Orléans Cedex 2, France.

* Corresponding author. E-mail address: christophe.legein@univ-lemans.fr. Tel: + 33 2 43 83 33 49

Abstract

The relationship between the experimental ^{19}F isotropic chemical shift and the ^{19}F isotropic shielding calculated using the gauge including projector augmented-wave (GIPAW) method with PBE functional is investigated in the case of GaF_3, InF_3, TlF and several AlF_3 polymorphs. It is shown that the linear correlation between experimental and DFT-PBE calculated values previously established on alkali, alkaline earth and rare earth of column 3 basic fluorides (A. Sadoc et al., Phys. Chem. Chem. Phys. 13 (2011) 18539-18550) remains valid in the case of column 13 metal fluorides, indicating that it allow predicting ^{19}F solid state NMR spectra of a broad range of crystalline fluorides with a relatively good accuracy. For the isostructural α-AlF_3, GaF_3 and InF_3 phases, PBE-DFT geometry optimization leads to noticeably overbended M-F-M bond angles and underestimated ^{27}Al, ^{71}Ga and ^{115}In calculated quadrupolar coupling constants. For the studied compounds, whose structures are built of corner shared MF_6 octahedra, it is shown that the electric field gradient (EFG) tensor at the cationic sites is not related to distortions of the octahedral units, in contrast to what previously observed for isolated AlF_6 octahedra in fluoroaluminates.

Keywords

First principle calculations, solid state NMR, crystalline fluorides

1. Introduction

The GIPAW [1,2] (gauge including projector-augmented wave) method, which is based on the plane-wave pseudopotential formalism of the density functional theory (DFT), has been shown to allow efficient computation of the NMR shielding in a variety of compounds [3,4]. However, when using the Perdew-Burke-Ernzerhof (PBE) functional [5] in the generalized gradient approximation (GGA), the slope of the correlation between the GIPAW calculated isotropic shielding (σ_{iso}) values and measured isotropic chemical shifts (δ_{iso}) generally deviates from the expected ideal value of -1.0 [4,6], in relation with the well-known band-gap problem [6]. In such a case, the definition of a calibration curve between calculated σ_{iso} and experimental δ_{iso} values is required to provide predictive results allowing the assignment of the NMR resonances from GIPAW computations. In the case of ^{19}F, the relationship between calculated and experimental values has been previously considered and it was shown that a scaling factor on the GIPAW calculated values is required to reproduce experimental trends [7,8]. However, significantly different scaling factors were reported in these works [7,8]. Recently, we have shown that this discrepancy is related to an incorrect description of the cationic localized empty orbitals of Ca^{2+}, Sc^{3+} (3d) and La^{3+} (4f) when using the PBE exchange–correlation functional and that a correction (*i. e.* a shift in energy) of the local potential of the corresponding ultra-soft pseudopotential (USPP) is required for these elements to accurately calculate the ^{19}F shielding [9]. On this basis, we have established a linear regression between experimental ^{19}F δ_{iso} values and calculated ^{19}F σ_{iso} values ($\delta_{iso}/CFCl_3$ = - 0.80(3) σ_{iso} + 89(9)) in the case of alkali, alkaline earth and rare earth of column 3 basic fluorides [9]. In this work, the validity of this relationship is investigated in the case of column 13 metal fluoride compounds (AlF_3, GaF_3, InF_3 and TlF). For these compounds, ^{19}F δ_{iso} values have already been reported in the literature [10-17]. For GaF_3 [16], InF_3 [16] and TlF [17], these values were referenced using the secondary fluorine standard, C_6F_6, and thus need to be expressed with respect to $CFCl_3$, the primary fluorine standard. Such conversion procedure used in previous works can lead to discrepancies because several different ^{19}F δ_{iso} values for C_6F_6 are given in the literature. In this work, the ^{19}F δ_{iso} of GaF_3, InF_3 and the low- and high-temperature phases of TlF were thus accurately measured relative to $CFCl_3$ and compared to GIPAW calculations. GIPAW computations of the ^{19}F shielding tensors were also performed for the α-, β- and η-AlF_3 phases for whose suitable experimental data are available [10,12,14,15]. The experimental data obtained by König *et al.* [15] for κ- and θ-AlF_3 samples exhibiting some local disorder were not considered here because, in such a case, the computation of NMR parameters would require establishing more complex structural models taking into account this local disorder. In the studied compounds, except for TlF ($^{203,205}Tl$, nuclear spin I = 1/2) the cationic sites are occupied by quadrupolar nuclei (*i.e.* ^{27}Al, I = 5/2; $^{69,71}Ga$, I = 3/2; $^{113,115}In$, I = 9/2) which are affected by the quadrupolar interaction since the corresponding site symmetries lead to a non-zero electric field gradient (EFG). The quadrupolar parameters of these cations were thus calculated using the PAW method [18,19] and compared to

experimental data from the literature for α-, β- and η-AlF_3 [12,15,20] and to the values measured in this study for GaF_3 and InF_3.

2. Experimental

2.1. Samples

The α-AlF_3 and GaF_3 samples were purchased from Cerac Inc. (lot numbers X20991 and X20393-1, respectively). The InF_3 and TlF samples were purchased from Astron (lot number 121077) and Alfa Aesar (lot number K06T017), respectively. The purity of these samples was checked by X-Ray Powder Diffraction.

2.2. Solid State NMR

^{19}F solid-state Magic Angle Spinning (MAS) NMR experiments were performed on an Avance 300 Bruker spectrometer operating at 7.0 T (^{19}F Larmor frequency of 282.2 MHz), using a 2.5 mm CP-MAS probehead. The room temperature ^{19}F MAS spectra of AlF_3, GaF_3 and InF_3 were recorded at a spinning frequency of 30 kHz using a Hahn echo sequence with an inter-pulse delay equal to one rotor period. The 90° pulse lengths varied between 1.75 μs and 2 μs and the recycle delays were set to 10 sec for AlF_3 and GaF_3 and to 5 sec for InF_3. The VT ^{19}F MAS spectra of TlF were acquired at spinning frequency of 25 kHz using a 90° pulse length of 2 μs and a recycle delay of 10 sec. The sample temperature was measured using the ^{207}Pb δ_{iso} of $Pb(NO_3)_2$ as an internal NMR thermometer [21,22]. The estimated temperature gradient was about 10°C. Additional room-temperature ^{19}F MAS NMR spectra of TlF with spinning frequencies varying from 25 to 60 kHz were recorded at a higher magnetic field of 20 T using an Avance 850 Bruker spectrometer (^{19}F Larmor frequency of 800.1 MHz) and a 1.3 mm triple resonance MAS probehead. The pulse duration was 0.5 μs corresponding to a flip angle of π/8 and the recycle delay was set to 10 sec.

The ^{71}Ga NMR experiments were also carried out on an Avance 300 Bruker spectrometer operating at 7.0 T (Larmor frequency of 91.53 MHz) using a 2.5 mm probehead. The ^{71}Ga MAS spectrum of GaF_3 was acquired at a spinning frequency of 25 kHz with a pulse duration of 1 μs, corresponding to a π/14 flip angle, and the recycle delay was set to 2 sec.

The ^{115}In solid-state MAS NMR experiments were conducted on a Avance 750 Bruker spectrometer operating at 17.6 T (^{115}In Larmor frequency of 164.35 MHz) using a 2.5 mm CPMAS probehead. ^{115}In MAS NMR spectra were recorded at spinning frequencies of 33 and 35 kHz using a short pulse duration of 0.25 μs corresponding to a π/16 flip angle. The recycle delay was set to 1 s.

^{19}F, ^{71}Ga and ^{115}In spectra are referenced to $CFCl_3$, 1 M $Ga(NO_3)_3$ aqueous solution and 0.1 M $In(NO_3)_3$ aqueous solution, respectively. All solid-state NMR spectra were fitted by using the DMFit software [23].

2.3. Computational methods

Two structural data sets were used for the GIPAW [1,2] calculations performed with the NMR-CASTEP [24] code: the experimental structures (named IS in the following for initial structures) and the structures obtained after PBE-DFT atomic position optimization (APO structures).

To obtain converged ^{19}F σ_{iso} values, a plane wave basis set energy cut-off of 700 eV was necessary and a Monkhorst-Pack grid density in the range 0.03 $Å^{-1}$ - 0.04 $Å^{-1}$ (corresponding to a *k*-point mesh of 8 × 8 × 8 for α-AlF_3 and InF_3, 9 × 9 × 9 and 8 × 8 × 8 for GaF_3, 5 × 3 × 5 for β-AlF_3, 6 × 6 × 6 for η-AlF_3 and 7 × 7 × 4 and 4 × 5 × 5 for TlF-I and II, respectively) was enough. For the electronic loops, the PBE functional [5] was used for the exchange-correlation kernel. Atomic positions were optimized by minimizing the residual forces on all atoms below 10 meV.$Å^{-1}$ using the Broyden–Fletcher–Goldfarb–Shanno (BFGS) method [25], keeping symmetry constraints and fixing the cell parameters to the experimentally determined values.

The computations of the EFG tensors were performed for the same structural data sets using the PAW method [18,19] implemented in the NMR-CASTEP code [24]. The orientation of the EFG tensor eigenvectors in the crystal frame are given as supplementary data.

2.4. Conventions

In this study, the calculated σ_{iso} value is defined as $\sigma_{iso} = (\sigma_{xx} + \sigma_{yy} + \sigma_{zz})/3$, σ_{ii} being the principal components of the shielding tensor defined in the sequence $|\sigma_{zz} - \sigma_{iso}| \geq |\sigma_{xx} - \sigma_{iso}| \geq |\sigma_{yy} - \sigma_{iso}|$. The isotropic chemical shift is defined as $\delta_{iso} \approx -[\sigma_{iso} - \sigma_{ref}]$.

The quadrupolar frequency (ν_Q), the quadrupolar coupling constant (C_Q) and the asymmetry parameter (η_Q) are defined as $\nu_Q = 3C_Q/[2I(2I-1)]$, $C_Q = eQV_{zz} / h$ and $\eta_Q = (V_{xx} - V_{yy}) / V_{zz}$, V_{ii} being the principal components of the EFG tensor defined in the sequence $|V_{zz}| \geq |V_{yy}| \geq |V_{xx}|$, *e* being the electronic charge, *I* the nuclear spin quantum number and *h* being Planck's constant.

The quadrupolar moments (*Q*) of ^{27}Al (146.6 mb), ^{71}Ga (107 mb), ^{113}In (759 mb) and ^{115}In (770 mb) are taken from ref. [26].

3. Results and discussion

3.1. Solid-state NMR study

The α-AlF_3 thermodynamically stable perovskite-like phase adopts a rhombohedral [27] structure (VF_3 structure type, Fig. 1) containing only one F and one Al sites. All other AlF_3 phases are metastables and transform directly and irreversibly into α-AlF_3 at various temperatures around 450-650°C [15,28]. The structure of the catalytically active [29-31] β-AlF_3 phase is closely related to the hexagonal tungsten bronze structure (HTB, Fig. 1) and contains four inequivalent F sites and two Al sites [32]. The η-phase adopts a cubic pyrochlore structure (Fig. 1) with a single F site and a single Al site. [28]. For α-AlF_3, the measured ^{19}F δ_{iso} (Fig. S1 in supplementary data) reported in Table 1 is in

very good agreement with earlier works [12,15]. The ^{19}F δ_{iso} values previously determined for the β-AlF_3 [10] and θ-AlF_3 [15] phases are also given in Table 1. The ^{27}Al quadrupolar coupling parameters [12,15,20] of these three polymorphs are reported in Table 2. It should be noted that, for β-AlF_3, the resonances corresponding to the four distinct F sites and to the two Al distinct sites of the structure were not resolved in ^{19}F and ^{27}Al MAS NMR spectra, respectively, and only single average ^{19}F and ^{27}Al δ_{iso} values and ^{27}Al quadrupolar parameters were reported [12].

GaF_3 is isostructural with α-AlF_3 [33,34]. Its structure, which is made of corner-sharing GaF_6 octahedra, contains a single fluorine site and a single cationic site. In agreement with structural data, the ^{19}F MAS NMR spectrum of GaF_3 exhibits a single resonance with a ^{19}F δ_{iso} of -171.3 ppm (Fig. S1 in supplementary data). As well, the ^{71}Ga MAS NMR spectrum, which shows a single narrow line associated the <1/2, -1/2> central transition (CT) and a spinning sideband manifold corresponding to the <±1/2, ±3/2> satellite transitions (ST) is consistent with the presence of a single Ga site in the structure (Fig. 2). The ^{71}Ga δ_{iso} (-94.7 ppm) and quadrupolar coupling parameters (Table 2) have been determined from the simulation of the whole experimental spectrum (CT and ST spinning sideband manifold spanning over ~ 1 MHz, Fig. 2). The C_Q value is in good agreement with the slightly different previously reported values [35,36]. The measured asymmetry parameter (η_Q = 0) is in agreement with the $\bar{3}$ symmetry of the Ga site.

InF_3 is also isostructural with α-AlF_3 [37]. Accordingly, the ^{19}F MAS NMR spectrum of InF_3 exhibits a single resonance located at δ_{iso} = -209.3 ppm (Fig. S1 in supplementary data). The two Indium isotopes, ^{115}In and ^{113}In, both have a 9/2 nuclear spin and exhibit similar Larmor frequencies (165.2 and 164.8 MHz at 17.6 T) and large nuclear quadrupole moments (770 and 759 mb, respectively [26]). However, the natural abundance of ^{115}In (95.7%) is much larger than that of ^{113}In (4.3%), and consequently, ^{115}In has a much higher sensitivity. The ^{115}In MAS NMR spectrum of InF_3 is shown in Fig. 3. In agreement with the structural data, this spectrum is characteristic of a single In site. It shows an intense peak corresponding to the CT and extended spinning sideband manifolds associated to the different ST. The CT peak and the (±1/2-±3/2) and (±5/2-±7/2) ST sidebands exhibit characteristic second-order quadupolar broadened lineshapes. The sidebands associated to the (±3/2-±5/2) ST transitions, which are much less affected by second-order quadrupolar effects, show nearly Gaussian lineshapes while the (±7/2-±9/2) ST sidebands, which are much more strongly broadened, are not observed. The ^{115}In δ_{iso} (-214 ppm) and quadrupolar coupling parameters (Table 2) were obtained from the simulations of the whole experimental MAS spectrum. The measured asymmetry parameter (η_Q = 0) is in agreement with the $\bar{3}$ symmetry of the In site. It should be noted that the resonance associated to the ^{113}In CT transition also appears in the ST spinning sideband manifold of the ^{115}In spectrum at about -2370 ppm (Fig. 3c). A quadrupolar coupling constant C_Q = 20.45 MHz is determined for ^{113}In, in good agreement with the value expected from the ratio between the ^{113}In and ^{115}In nuclear quadrupolar moments.

TlF exhibits an orthorhombic structure (TlF-II) at room temperature and adopts a tetragonal structure (TlF-I) above 82°C [38]. The structures of these two phases, both containing a single fluorine site and a single thallium site, can be derived from an idealized rocksalt-type arrangement with extensive distortions of the anion sublattice due to the presence of the $6s^2$ lone pair of the Tl^+ cations. In both phases, the F^- and Tl^+ ions are surrounded by only five nearest neighbours (Tl^+ and F^-, respectively) forming square pyramids (Fig. 4) [38]. The ^{19}F MAS NMR spectra of the TlF-II and TlF-I phases, recorded in-situ at 53 and 100°C, are shown in Fig. 5. The ^{19}F δ_{iso} measured for the low- and high-temperature phases are -19.5 and -16.7 ppm, respectively (Table 1). It should be noted that, in both spectra, the line width of the ^{19}F resonance is unusually large. Experiments performed at a higher magnetic field of 20 T show that the line broadening in Hertz of the ^{19}F resonance in TlF-II increases only very slightly (3.9 kHz at 7 T and 4.3 kHz at 20 T) with the magnetic field (corresponding to a narrowing in ppm). In addition, the linewidth was found constant when increasing the spinning frequency from 25 up to 60 kHz. These findings indicate that the line broadening is not related to a distribution of the ^{19}F isotropic chemical shift nor dipolar coupling but originates from isotropic $^1J(^{203,205}Tl\text{-}^{19}F)$ couplings. Indeed, the two Tl isotopes are well known to give rise to large *J*-coupling constants [39] due to their large gyromagnetic ratios ($\gamma_{^{203}Tl}$=15.54 10^7 rad.s^{-1}.T^{-1}, $\gamma_{^{205}Tl}$=15.69 10^7 rad.s^{-1}.T^{-1} [40] and the large atomic number of Tl.

3.2. Computation of the NMR parameters

For the studied column-13 metal fluorides, the ^{19}F shielding tensors and the quadrupolar parameters of the nucleus ($I > 1/2$) occupying the cationic site of the structure have been computed using the GIPAW [1,2] and PAW [18,19] methods, respectively.

3.2.1. PBE-DFT geometry optimization

Since the agreement between experimental and calculated NMR parameters is generally improved after a DFT optimization of the structure geometry [3,4] computations were performed for both the experimental structures (IS) and the structures resulting from PBE-DFT atomic position optimization (APO). The ^{19}F DFT-GIPAW σ_{iso} values and ^{27}Al, ^{71}Ga, ^{115}In quadrupolar parameters calculated for the IS and APO structures of α-AlF_3, β-AlF_3, η-AlF_3, GaF_3, InF_3, TlF-II and TlF-I are given in Tables 1 and 2. For all compounds, the atomic positions of the IS and APO structures are given as supplementary data. In the case of η-AlF_3, the fluorine atomic coordinate (x, 1/8, 1/8) of the IS structure is not reported and was then deduced from the reported Al-F bond length and F-Al-F and Al-F-Al bond angles [28]. In the case of the α-, β- and η-AlF_3, GaF_3 and InF_3 structures made of MF_6 octahedra (M = Al, Ga, In), the DFT-PBE geometry optimization leads to an increase of the M-F bond lengths (see supplementary data). These increases, which remain very weak for the AlF_3 phases, are more significant for GaF_3 and InF_3 (from 1.892 Å to 1.913 Å or from 1.885 Å to 1.914 Å in GaF_3, and from 2.054 Å to 2.096 Å in InF_3). This trend could be expected since the PBE functional is well-

known to overestimate interatomic bond lengths [19,41,42]. For the TlF-I and TlF-II structures build of TlF_5 square pyramids, the geometry optimization step results in an increase of the shortest F-Tl bond lengths and a decrease of the longest F-Tl bond lengths leading to less distorted coordination polyhedra.

While the PBE-DFT geometry optimization leads only to moderate decreases of the calculated ^{19}F σ_{iso} values (Table 1, from 0.5 to 17 ppm, depending on the increase of the M-F bond lengths) for the studied compounds, it results in significant changes of the calculated quadrupolar coupling parameters highlighting the strong sensitivity of the EFG tensor to small changes in the cationic local environment (Table 2). For the β- and η-AlF_3 phases, an improved agreement between experimental and calculated ^{27}Al quadrupolar parameters is observed for the APO structures. A different trend is observed for the α-AlF_3, GaF_3 and InF_3 phases and, in contrast, the quadrupolar coupling constants of ^{27}Al, ^{71}Ga and ^{115}In calculated for the APO structures are significantly underestimated relative to the experimental values (Table 2). It has been already observed and discussed for α-AlF_3 [43]. It should be noted that these three isostructural compounds undergo a first order phase transition from a rhombohedral structure ($R\bar{3}c$) to a cubic structure (ReO_3 type, $Pm\bar{3}m$) at 448 °C, 807 °C and 373 °C, respectively [44]. The low-temperature rhombohedral structures of these compounds consist in zigzag chains of MF_6 octahedra with M-F-M bond angles of 157.1° in α-AlF_3 [27], 144.9° [33] or 146.8° [34] in GaF_3 and 146.8° in InF_3 [37] (see supplementary data), while the high temperature structures are made of linear chains with M-F-M bond angles equal to 180°. In these isostructural compounds, the M-F-M bond angles are known to vary significantly with the temperature and to increase continuously upon heating [12] up to 180° in the high-temperature cubic structures [44]. Due to these strong variations of the M-F-M bond angle as a function of the temperature, the APO structure which corresponds to the lowest energy structure at 0 K is expected to exhibit overbended M-F-M bond angle. It should be pointed out that the M-F-M angle overbending (M-F-M angle of 154.9° in α-AlF_3, 141.2° or 141.6° in GaF_3 and 139.8° in InF_3) is also amplified by the overestimation of the F-M distances with the PBE functional. Therefore, for these three compounds only the NMR parameters computed from the IS structures are considered in the following.

3.2.2. Calculated ^{19}F shielding

As discussed above, the calculated ^{19}F σ_{iso} values retained are those obtained from APO structures for β-AlF_3, η-AlF_3, TlF-II and TlF-I and from IS structures for α-AlF_3, GaF_3 and InF_3. One can notice the very similar (differences smaller than one tenth of ppm) calculated σ_{iso} values for the four fluorine sites of β-AlF_3 in good agreement with the observation of a single ^{19}F resonance in MAS spectra [12]. The "calculated" ^{19}F δ_{iso} values for all compounds were deduced from calculated σ_{iso} values by using the linear correlation previously established for alkali, alkaline earth and rare earth fluorides ($\delta_{iso}/CFCl_3 = -0.80\ \sigma_{iso} + 89$) [9], and successfully applied to $RbLaF_4$ [45], $NaAsF_6$ [46], and α-$LaZr_2F_{11}$ [47]. Overall, the agreement between the experimental and these ''calculated'' ^{19}F δ_{iso}

values is good with a RMS deviation of 7 ppm, suggesting that this relationship is also valid in the case of column-13 metal fluorides. This is also clearly illustrated in Fig. 6 which shows the correlation between calculated ^{19}F σ_{iso} and experimental ^{19}F δ_{iso} values for the compounds under study and for alkali, alkaline earth and rare earth fluorides [9]. Indeed, both the slope and intercept of the linear regression, calculated considering all these values ($\delta_{iso}/CFCl_3$ = - 0.795(15) σ_{iso} + 89(4)) are very similar to those previously reported [9]. It should also be noted that very similar slopes of -0.83 (between "calculated" and experimental δ_{iso}) and -0.78 have also been obtained for $Ba_5Al_3F_{19}$ [48] and TaF_5 [49], respectively. These findings therefore clearly confirm that the previously proposed relationship [9] could allow predicting ^{19}F NMR spectra for a broad range of crystalline metal fluorides compounds with a relatively good accuracy. For completeness, it should be noted that Pedone *et al.* [50] obtain a slope of -0.963 on five compounds among which three contain Ca^{2+}, by applying a larger shift of the local potential of the USPP of Ca^{2+} and that a slope close to -1 has been obtained for NbF_5 [49].

3.2.3. Calculated quadrupolar parameters and orientation of the electric field gradients

As mentioned above, a nice agreement between experimental quadrupolar parameters and PAW [18,19] calculated values for the IS structures of α-AlF_3 and InF_3 is observed (Table 2), showing the accuracy of these crystalline structures. For GaF_3, β-AlF_3 and η-AlF_3, more pronounced differences between experimental and calculated quadrupolar parameters are found. For GaF_3, the best agreement is obtained for the IS structure reported by Roos *et al.* [34], while, for β-AlF_3 and η-AlF_3, the bets agreements are obtained after DFT-PBE geometry optimization which leads to slight variations of the bond lengths and bond angles (Table 2 and supplementary data). It should be noted that, for β-AlF_3, the calculated ^{27}Al quadrupolar parameters (and isotropic shieldings) of the two distinct Al sites of the structure are very similar, making difficult to resolve the two corresponding ^{27}Al resonances in experimental MAS spectra, as reported by Chupas *et al* . [12].

Since the nuclear spin interaction must conform to crystal symmetry [51] the ^{27}Al, ^{71}Ga and ^{115}In site symmetry ($\bar{3}$) in the isostructural α-AlF_3 GaF_3 and InF_3 phases imposes the V_{zz} direction to be along the three-fold axis (parallel to the c-axis of the hexagonal cells) orthogonal to opposite faces (Fig. 7 and supplementary data) and the EFG tensor to be axially symmetric ($V_{xx} = V_{yy}$, *i.e.* $\eta_Q = 0$). In the same way, the ^{27}Al site symmetry in η-AlF_3 ($\bar{3}m$) enforces the V_{zz} direction of the axially symmetric EFG tensor to be along the three-fold axis ([111] direction of the cubic cell). In the case of the Al1 site of β-AlF_3 ($2/m$ site symmetry), V_{zz} is perpendicular to $\vec{a}$ and bisects adjacent Al1-F2 bonds (Fig. 7) while V_{yy}, which is parallel to $\vec{a}$ and to the twofold axis, bisects adjacent Al1-F2 bonds. For the Al2 site ($\bar{1}$ site symmetry), V_{zz} bisects adjacent F1-Al2 and F2-Al2 bonds.

In several cases, correlations between the quadrupolar coupling constants (and thus the V_{zz} value of the EFG tensor) and structural parameters describing the distortion [52,53] of the coordination

polyhedron have been proposed [54]. For α-AlF_3, GaF_3, InF_3 and η-AlF_3, the M-F distances of the octahedron are the same ($\bar{3}$ or $\bar{3}m$ site symmetry) and there is no radial distortion of the coordination polyhedron. In such a case, the quadrupolar coupling constant cannot be related to the quadratic elongation [52] or longitudinal strain [53] parameters. Indeed, for fluoroaluminate compounds in which the AlF_6 octahedra exhibit any or either small (that is the case of β-AlF_3) radial distortions, it was previously shown [43] that (i) the magnitude of V_{zz} is small, (ii) the principal axis of the EFG tensor are not aligned along the Al-F bonds and (iii) the V_{ii} values are correlated with the angular distortion parameters defined as $\alpha = 1/6 \sum_{i=1}^{6} \alpha_i - 90°$ and $\beta = 1/2 \sum_{i=1}^{2} \beta_i - 90°$, where α_i (°) are the six angles between two adjacent Al–F bonds involving fluorine atoms belonging to octahedron faces orthogonal to the V_{ii} direction and β_i (°) are the two angles between two adjacent Al-F bonds bisected by V_{ii}. Accordingly, a negative (positive) angular distortion is expected to correspond to a charge concentration (depletion) in the V_{ii} direction and then to a negative (positive) V_{ii} value [43]. It should be noted that these correlations between α and β angular distortion parameters and V_{ii} values were observed for fluoroaluminates containing only isolated AlF_6 octahedra (non-bridging fluorine atoms). For the five compounds considered here, the MF_6^{3-} octahedra are connected via corner-shared fluorine atoms and, in such a case, the comparison between angular distortion and quadrupolar coupling parameters calculated before and after DFT-PBE geometry optimization clearly indicates that these trends are no longer valid (see Fig. 7 and supplementary data). In the case of α-AlF_3 and η-AlF_3 for example, the value of the parameter α is larger for the APO structure than for the IS structure while the magnitude of the calculated V_{zz} value is smaller for the APO structure than for the IS structure. As well, for the IS structures of α-AlF_3 and GaF_3 and the APO structure of η-AlF_3 (where α is related to V_{zz}, see Fig. 7 and supplementary data) a positive V_{zz} value is expected according to the value of α ($\alpha > 0$) while the calculated V_{zz} value is negative. The very small value of the angular distortion ($\alpha =$ 0.02° for IS) was then wrongly invoked to explain the discrepancy observed for α-AlF_3 [43]. These observations indicate that, in the studied compounds, the quadrupolar coupling parameters are not driven by the angular distortions of the MF_6 octahedra and the EFG principal values seem more likely sensitive to the M-F-M bond angles. A similar trend has recently been observed for α-$NaAsF_6$, where the EFG at the ^{23}Na nucleus is not quantitatively sensitive to the angular distortion (F-Na-F angle) but sensitive to the Na-F-As angle, *i.e.*, to the orientation of the AsF_6 octahedra [46].

4. Conclusions

The relationship between the experimental ^{19}F δ_{iso} and the ^{19}F σ_{iso} calculated using the GIPAW method with PBE functional has been investigated in the case of GaF_3, InF_3 TlF_3 and several AlF_3 polymorphs. For this purpose, the ^{19}F δ_{iso} of α-AlF_3, GaF_3, InF_3 and of the low and high temperature phases of TlF have been accurately measured. We have shown that the linear correlation between

experimental ^{19}F δ_{iso} and DFT-PBE calculated σ_{iso} previously established on alkali, alkaline earth and rare earth of column 3 basic fluorides remains valid is the case of column 13 metal fluorides, indicating that it allow predicting ^{19}F NMR spectra of a broad range of crystalline fluorides with a relatively good accuracy. It was also observed that, for the isostructural α-AlF_3, GaF_3 and InF_3 phases, PBE-DFT atomic position optimization leads to noticeably overbended M-F-M bond angles and that the ^{27}Al, ^{71}Ga and ^{115}In quadrupolar coupling constants calculated using the PAW method for these optimized structures are significantly underestimated relative of experimental values. In these fluorides which contain corner shared MF_6 octahedra, the EFG tensor at the cationic sites is not related to distortions of the octahedral units and the correlation between angular distortions and V_{ii} values, previously established for fluoroaluminates containing isolated AlF_6 octahedra with any or either small radial distortions, is not observed. In contrast, the EFG tensors seem more likely sensitive to M-F-M bond angles, as recently observed for the EFG at the ^{23}Na nucleus in α-$NaAsF_6$.

Acknowledgments

The authors thank the Région Pays de la Loire for the financial support of the RMN3MPL project, especially M. Biswal (doctoral grant) and A. Sadoc (post-doctoral fellowship). Financial support from the TGIR RMN THC FR3050 is also gratefully acknowledged. The computational presented in this work have been carried out at the Centre Régional de Calcul Intensif des Pays de la Loire (CCIPL), financed by the French Research Ministry, the Région Pays de la Loire, and Nantes University. The authors thank CCIPL for NMR-CASTEP licenses financial support. We also thank Cyrille Galven (Institut des Molécules et Matériaux du Mans) for his help for DTA measurements.

Appendix A. Supporting information

Supplementary data associated with this article can be found in the online version at http://dx.doi.org/

^{19}F MAS NMR spectra of α-AlF_3, GaF_3 and InF_3, initial and PBE-DFT geometry-optimized fractional atomic coordinates and corresponding atomic displacements for α-, β-, η-AlF_3, GaF_3, InF_3, TlF-II and TlF-I, M-F bond lengths, F-M-F and M-F-M bond angles from structure refinement and PBE-DFT geometry-optimization, eigenvectors of the calculated EFG tensors expressed in the crystallographic axis, calculated EFG tensor and angular distortions from IS and APO structures.

References

[1] C. J. Pickard, F. Mauri, Phys. Rev. B 63 (2001) 245101.

[2] J. R. Yates, C. J. Pickard, F. Mauri, Phys. Rev. B 76 (2007) 024401.

[3] T. Charpentier, Solid State Nucl. Magn. Reson. 40 (2011) 1−20.

[4] C. Bonhomme, C. Gervais, F. Babonneau, C. Coelho, F. Pourpoint, T. Azais, S. E. Ashbrook, J. M. Griffin, J. R. Yates, F. Mauri, C. J. Pickard, Chem. Rev. 112 (2012) 5733−5779.

[5] J. P. Perdew, K. Burke, M. Ernzerhof, Phys. Rev. Lett. 77 (1996) 3865−3868.

[6] R. Laskowski, P. Blaha, F. Tran, Phys. Rev. B 87 (2013) 195130.

[7] A. Zheng, S.-B. Liu, F. Deng, J. Phys. Chem. C 113 (2009) 15018−15023.

[8] J. M. Griffin, J. R. Yates, A. J. Berry, S. Wimperis, S. E. Ashbrook, J. Am. Chem. Soc. 132 (2010) 15651–15660.

[9] A. Sadoc, M. Body, C. Legein, M. Biswal, F. Fayon, X. Rocquefelte, F. Boucher, Phys. Chem. Chem. Phys. 13 (2011) 18539–18550.

[10] T. Schaller. D. B. Dingwell, H. Keppler, W. Kneller, L. Merwin, A. Sebald, Geochim. Cosmochim. Acta, 56 (1992) 701–707.

[11] J. M. Miller, Prog. Nucl. Mag. Reson. 28 (1996) 255–281.

[12] P. J. Chupas, M. F. Ciraolo, J. C. Hanson, C. P. Grey, J. Am. Chem. Soc. 123 (2001) 1694−1702.

[13] T. J. Kiczenski, J. F. Stebbins, J. Non-Cryst. Solids 306 (2002) 160–168.

[14] G. Scholz, O. Korup, Solid State Sci. 8 (2006) 678–684.

[15] R. König, G. Scholz, K. Scheurell, D. Heidemann, I. Buchem, W.E.S. Unger, E. Kemnitz, J. Fluorine Chem. 131 (2010) 91–97.

[16] B. Bureau, G. Silly, J.-Y. Buzaré, J. Emery, Chem. Phys. 249 (1999) 89–104.

[17] S. P. Gabuda, S. G. Kozlova, R. L. Davidovich, Chem. Phys. Lett. 263 (1996) 253–258.

[18] P. E. Blochl, Phys. Rev. B 50 (1994) 17953–17979.

[19] M. Profeta, F. Mauri, C. J. Pickard, J. Am. Chem. Soc. 125 (2003) 541–548

[20] G. Silly, C. Legein, J.-Y. Buzaré, F. Calvayrac, Solid State Nucl. Magn. Reson. 25 (2004) 241–251.

[21] L. C. M. Van Gorkom, J. M. Hook, M. B. Logan, J. V. Hanna, R. E. Wasylishen, Magn. Reson. Chem. 33 (1995) 791–795.

[22] A. Bielecki, D. P. Burum, J. Magn. Reson., Ser. A 116 (1995) 215–220.

[23] D. Massiot, F. Fayon, M. Capron, I. King, S. Le Calvé, B. Alonso, J.-O. Durand, B. Bujoli, Z. Gan, G. Hoatson, Magn. Reson. Chem. 40 (2002) 70–76.

[24] S. J. Clark, M. D. Segall, C. J. Pickard, P. J. Hasnip, M. J. Probert, K. Refson, M. C. Payne, Z. Kristallogr. 220 (2005) 567–570.

[25] B. G. Pfrommer, M. Cote, S. G. Louie, M. L. Cohen, J. Comput. Phys. 131 (1997) 233–240.

[26] P. Pyykkö, Mol. Phys. 106 (2008) 1965–1974.

[27] P. Daniel, A. Bulou, M. Rousseau, J. Nouet, J.-L. Fourquet, M. Leblanc, R. Burriel, J. Phys.: Condens. Matter 2 (1990) 5663–5677.

[28] N. Herron, D. L. Thorn, R. L. Harlow, G. A. Jones, J. B. Parise, J. A. Fernandez-Baca, T. Vogt, Chem. Mater. 7 (1995) 75–83.

[29] A. Hess, E. Kemnitz, A. Lippitz, W. E. S. Unger, D.-H. Menz, J. Catal., 148, 1994, 270–280.

[30] A. Hess, E. Kemnitz, J. Catal. 149 (1994) 449–457.

[31] E. Kemnitz, D.-H. Menz, Progr. Solid State Chem. 26 (1998) 97–153.

[32] A. Le Bail, C. Jacoboni, M. Leblanc, R. de Pape, H. Duroy, J.-L. Fourquet, J. Solid State Chem. 77 (1988) 96–101.

[33] F. M. Brewer, G. Garton, D. M. L. Goodgame, J. Inorg. Nucl. Chem. 9 (1959) 56–64.

[34] M. Roos, G. Z. Meyer, Kristallogr. - New Cryst. Struct. 216 (2001) 18–18.

[35] B. Bureau, H. Guérault, G. Silly, J.-Y. Buzaré, J.-M. Grenèche, J. Phys.: Condens. Matter 11 (1999) L423–L431.

[36] B. Bureau, G. Silly, J.-Y. Buzaré, C. Legein, D. Massiot, Solid State Nucl. Magn. Reson. 14 (1999) 181–190.

[37] R. Hoppe, D. J. Kissel, J. Fluorine Chem. 24 (1984) 327–340.

[38] P. Berastegui, S. Hull, J. Solid State Chem. 150 (2000) 266–275.

[39] J. F. Hinton, Bull. Magn. Reson. 13 (1992) 90–108.

[40] R. K. Harris, E. D. Becker, S. M. Cabral De Menezes, R. Goodfellow, P. Granger, Pure Appl. Chem. 73 (2001) 1795–1818.

[41] D. R. Hamann, Phys. Rev. Lett. 76 (1996) 660–663.

[42] T. Demuth, Y. Jeanvoine, J. Hafner, J. G. Ángyán, J. Phys.: Condens. Matter 11 (1999) 3833–3874.

[43] M. Body, C. Legein, M. Body, C. Legein, J.-Y. Buzaré, G. Silly, P. Blaha, C. Martineau, F. Calvayrac, J. Phys. Chem. A 111 (2007) 11873–11884.

[44] P. Daniel, A. Bulou, M. Rousseau, J. Nouet, M. Leblanc, Phys. Rev. B 42 (1990) 10545–10552.

[45] A.-L. Rollet, M . Allix, E. Veron, M. Deschamps, V. Montouillout, M. R. Suchomel, E. Suard, M. Barré, M. Ocaña, A. Sadoc, F. Boucher, C. Bessada, D. Massiot, F. Fayon, Inorg. Chem. 51 (2012) 2272–2282.

[46] M. Biswal, M. Body, C. Legein, G. Corbel, A. Sadoc, F. Boucher, J. Phys. Chem. C 116 (2012) 11682–11693.

[47] C. Martineau, C. Legein, M. Body, O. Péron, B. Boulard, F. Fayon, J. Solid State Chem. 199 (2013) 326–333.

[48] C. Martineau, F. Fayon, M. R. Suchomel, M. Allix, D. Massiot, F. Taulelle, Inorg. Chem. 50 (2011) 2644–2653.

[49] M. Biswal, M. Body, C. Legein, A. Sadoc, F. Boucher, J. Solid. State Chem., http://dx.doi.org/10.1016/j.jssc.2013.09.001.

[50] A. Pedone, T. Charpentier, M. C. Menziani, J. Mater. Chem. 22 (2012) 12599–12608.

[51] M. H. Cohen, F. Reif, Solid State Phys. 5 (1957) 321–438.

[52] K. Robinson, G. V. Gibbs, P. H. Ribbe, Science, 172 (1971) 567–570.

[53] S. Ghose, T. Tsang, Am. Miner. 58 (1973) 748–755.

[54] K. J. D. MacKenzie, M. E. Smith, Multinuclear Solid-State NMR of Inorganic Materials. Pergamon: Amsterdam, 2002.

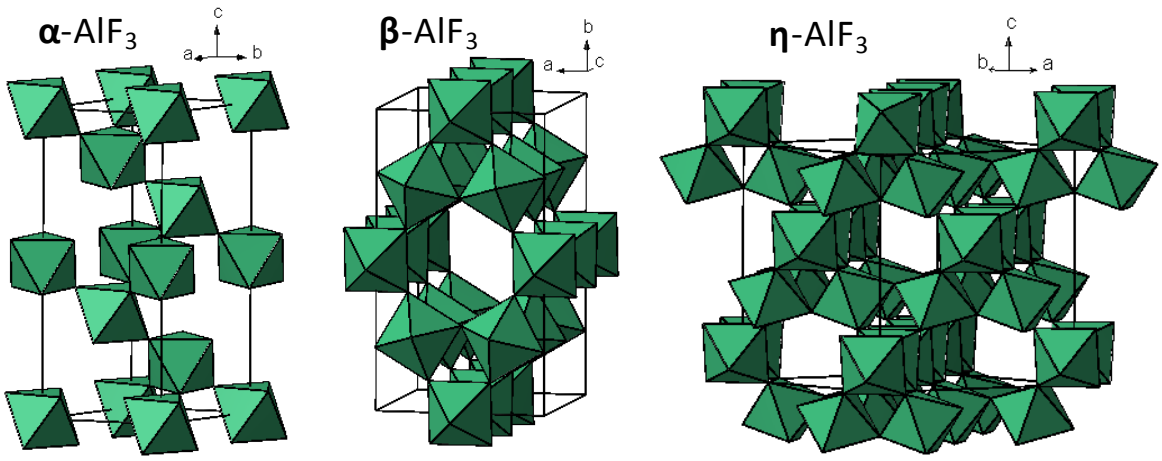

Fig. 1. Perspective views of the structures of α-, β- and η-AlF_3.

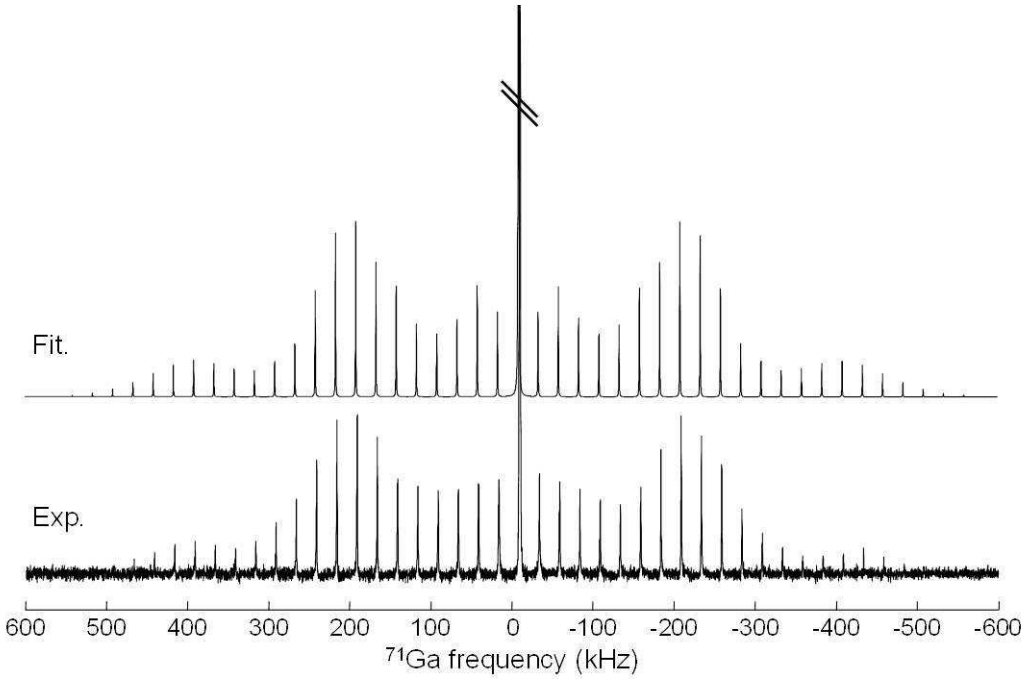

Fig. 2. Experimental and simulated ^{71}Ga MAS (25 kHz) NMR (B_0 = 7 T) spectra of GaF_3.

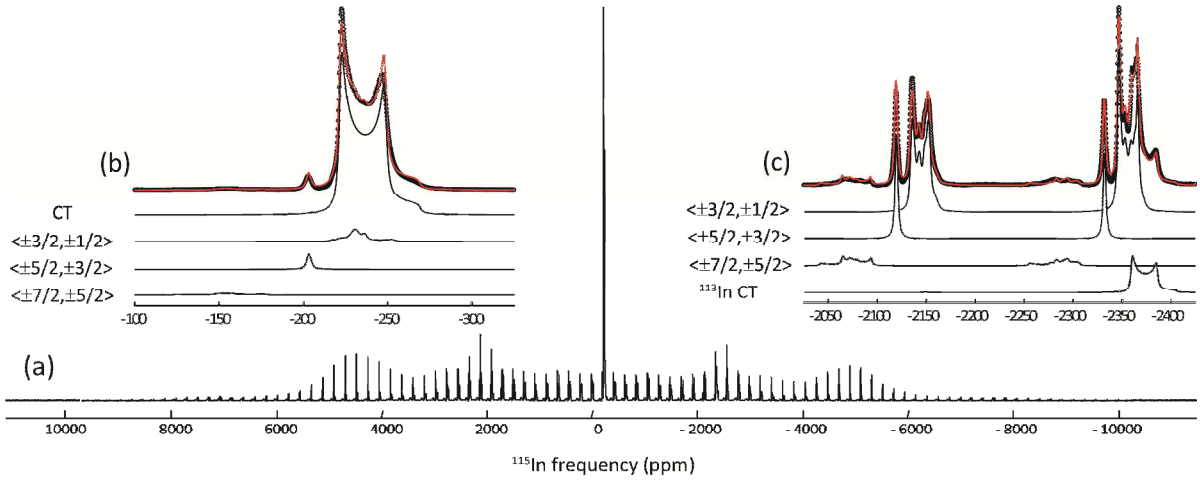

Fig. 3. (a) Experimental and simulated ^{115}In MAS NMR spectrum of InF_3 recorded at 17.6 T with a spinning frequency of 33 kHz. (b) Expansion of the center band region. (c) Expansion of a part of the ST spinning sideband manifold containing the ^{113}In CT signal.

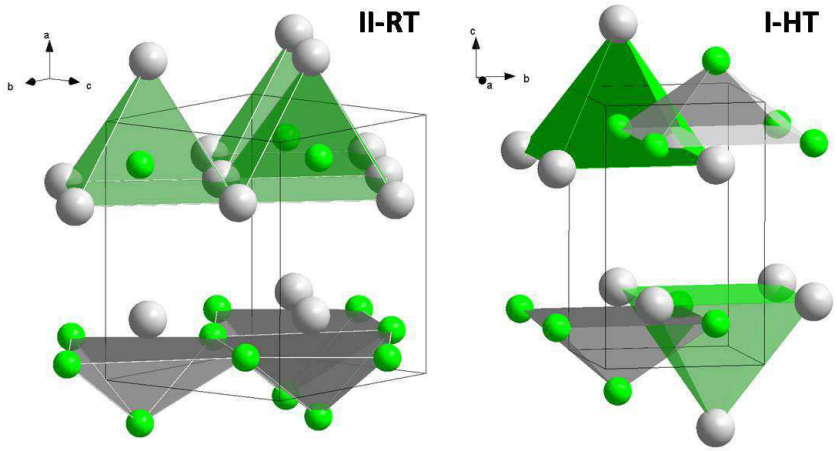

Fig. 4. Perspective views of TlF-II (left) and TlF-I (right). The F^- ions and the FTl_5^{4+} polyhedra are represented in green and the Tl^+ ions and the TlF_5^{4-} polyhedra are represented in grey.

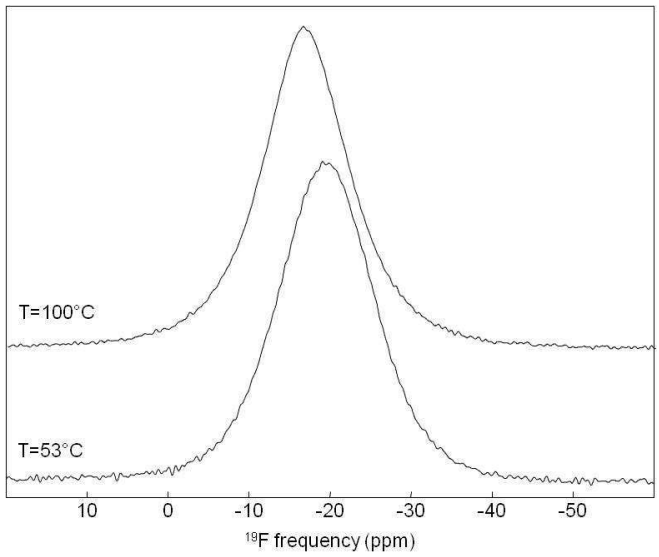

Fig. 5. ^{19}F VT MAS (25 kHz) spectra of TlF recorded at a temperature of 53°C (bottom) and 100°C (top).

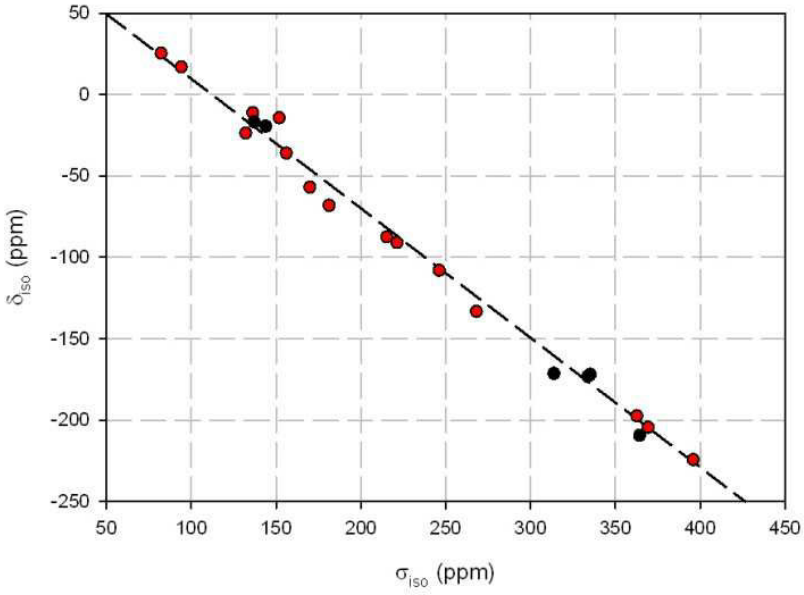

Fig. 6. Calculated ^{19}F σ_{iso} values versus experimentally measured ^{19}F δ_{iso} values. The black circles represent the compounds under study (values reported in Table 1). The red circles represent the compounds studied in ref. [9]. The dash line represents the linear regression calculated on all these values: $\delta_{iso}/CFCl_3 = - 0.795(15)\ \sigma_{iso} + 89(4)$.

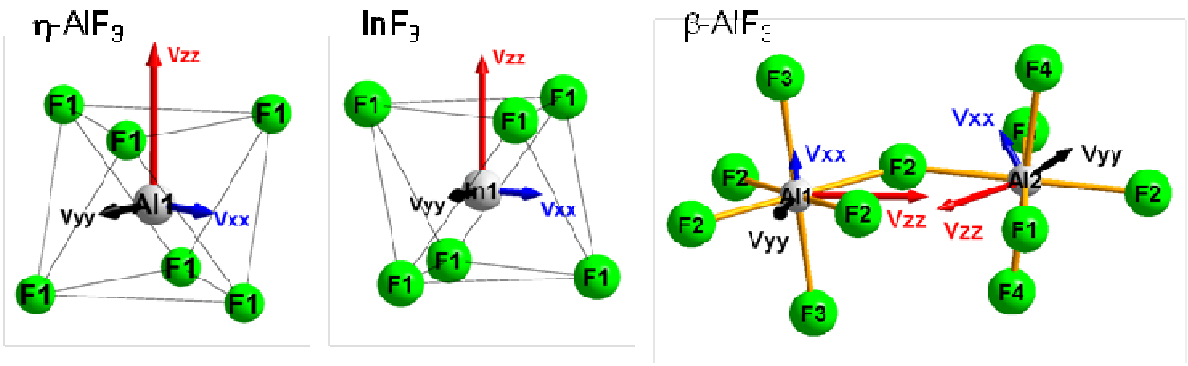

Fig. 7. Orientation of the principal components of the calculated ^{27}Al EFG tensor in η-AlF_3 (APO structure), ^{115}In EFG tensor in InF_3 (IS structure) and ^{27}Al EFG tensor in β-AlF_3 (APO structure). The vector lengths are proportional to the magnitude of the contributions.

Table 1

Experimental ^{19}F δ_{iso} values (uncertainties given in brackets when available), ^{19}F σ_{iso} values calculated using USPP within the GIPAW method for IS and APO structures, and calculated ^{19}F δ_{iso} values deduced from the linear regression $\delta_{iso}/CFCl_3 = -0.80(3)\ \sigma_{iso} + 89(9)$ [9].

	σ_{iso} calc/ppm[a]		δ_{iso} calc/ppm[a]		
Compound	IS	APO	IS	APO	δ_{iso} exp/ppm
α-AlF_3	**335.2**	334.6	**-179**	-179	-171.9(2)
β-AlF_3 (F1)	335.7	**335.2**	-180	**-179**	-172[b]
β-AlF_3 (F2)	335.7	**335.2**	-180	**-179**	-172[b]
β-AlF_3 (F3)	335.7	**335.2**	-180	**-179**	-172[b]
β-AlF_3 (F4)	335.7	**335.2**	-180	**-179**	-172[b]
η-AlF_3	334.3	**333.8**	-178	**-178**	-173.0[c]
GaF_3[d]	310.3	300.4	-159	-151	-171.3(2)
GaF_3[e]	**313.8**	300.9	**-162**	-152	-171.3(2)
InF_3	**364.3**	347.1	**-202**	-189	-209.3(2)
TlF-II (53°C)	145.2	**144.0**	-27	**-26**	-19.5(2)
TlF-I (100°C)	138.2	**137.1**	-22	**-21**	-16.7(2)

[a] The calculated values in bold are those reported in Fig. 6 [b] From ref. [12]. [c] From ref. [15]. [d] Crystalline structure from ref. [33]. [e] Crystalline structure from ref. [34].

Table 2

Experimental V_{ii}, C_Q and η_Q, calculated V_{ii}, C_Q and η_Q using NMR-CASTEP for IS and APO structures. Since only the absolute value of C_Q can be determined from NMR experiment on powdered samples, the sign of the experimental C_Q is set to the sign of the calculated C_Q. Uncertainties on experimental C_Q values are given in brackets (when available).

		$V_{zz}/10^{21}$ V m^2	$V_{yy}/10^{21}$ V m^2	$V_{xx}/10^{21}$ V m^2	C_Q/MHz	η_Q
α-AlF_3						
Exp.[a]		-0.0602	0.0301	0.0301	-0.213(0.027)	0
IS		-0.0630	0.0315	0.0315	-0.223	0
APO		-0.0211	0.0106	0.0106	-0.075	0
β-AlF_3						
Exp.[b]		-0.226	0.203	0.023	-0.800(0.100)	0.8(0.1)
IS	Al1	-0.341	0.276	0.065	-1.211	0.62
	Al2	-0.360	0.264	0.095	-1.275	0.47
APO	Al1	-0.332	0.210	0.121	-1.177	0.27
	Al2	-0.359	0.204	0.155	-1.270	0.14
η-AlF_3						
Exp.[c]		-0.433	0.216	0.216	-1.533	0
IS		-0.554	0.277	0.277	-1.964	0
APO		-0.468	0.234	0.234	-1.660	0
GaF_3						
Exp.		-0.383	0.191	0.191	-0.990(30)	0
IS[d]		-0.092	0.046	0.046	-0.239	0
APO[d]		0.175	-0.088	-0.088	0.454	0
IS[e]		-0.215	0.107	0.107	-0.556	0
APO[e]		0.153	-0.077	-0.077	0.397	0
InF_3						
Exp.		-1.114	0.557	0.557	-20.74(8)	0
IS		-1.083	0.542	0.542	-20.17	0
APO		-0.154	0.077	0.077	-2.86	0

[a] From ref. [20]. [b] From ref.[12]. [c] From ref. [15]. [d] IS from ref. [33]. [e] IS from ref. [34].

NMR parameters in column 13 metal fluoride compounds (AlF_3, GaF_3, InF_3 and TlF) from first principle calculations

Aymeric Sadoc, Mamata Biswal, Monique Body, Christophe Legein, Florent Boucher, Dominique Massiot, Franck Fayon

Supplementary data

Table of content

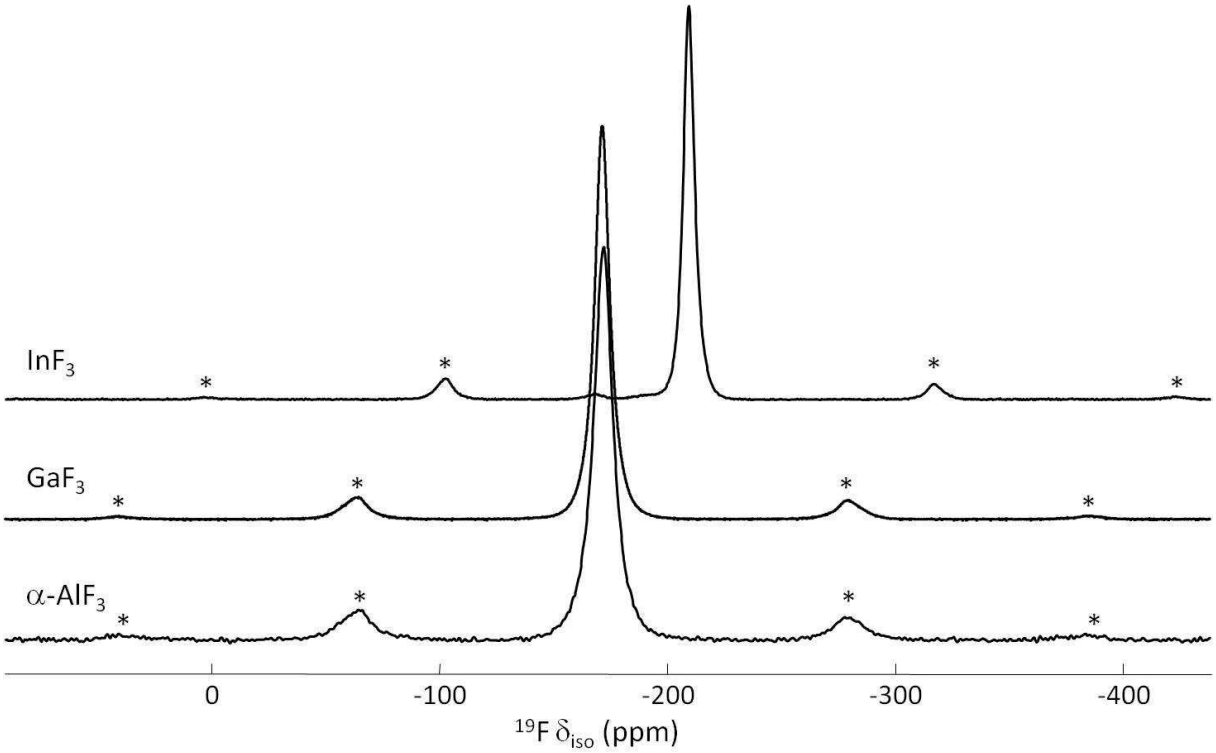

Figure S1. ^{19}F MAS (30 kHz) NMR spectra of α-AlF_3, GaF_3 and InF_3. The asterisks indicate spinning sidebands.

Table S1. Initial fractional atomic coordinates [1] (x, y, z), PBE-DFT geometry-optimized fractional atomic coordinates (x', y', z') and corresponding atomic displacements d (Å) for α-AlF_3.

Atom	Site	x	y	z	x'	y'	z'	d
Al	6b	0	0	0	0	0	0	0
F	18e	0.4275	0	1/4	0.4204	0	1/4	0.035

Table S2. Al-F bond length (Å), F-Al-F and Al-F-Al bond angles[a] (°) from X-ray powder structure refinement and PBE-DFT geometry-optimization (in italic) for α-AlF_3.

Bond lengths			Bond angles		
Al-F (x6)	1.797	*1.804*	F-Al-F (x6)	90.02	*90.25*
			F-Al-F (x6)	89.98	*89.75*
			Al-F-Al (x3)	157.05	*154.87*

[a] F-Al-F bond angles between two opposite bonds are equal to 180° since the site symmetry of Al is $\bar{3}$.

Table S3. Initial fractional atomic coordinates [2] (x, y, z), PBE-DFT geometry-optimized fractional atomic coordinates (x', y', z') and corresponding atomic displacements d (Å) for β-AlF_3.

Atom	Site	x	y	z	x'	y'	z'	d
Al1	4b	0	1/2	0	0	1/2	0	0
Al2	8d	1/4	1/4	0	1/4	1/4	0	0
F1	8f	0	0.2125	0.5257	0	0.2128	0.5322	0.047
F2	16h	0.3161	0.1054	0.9800	0.3151	0.1050	0.9741	0.043
F3	4c	0	0.5177	1/4	0	0.5226	1/4	0.059
F4	8g	0.2297	0.2352	1/4	0.2240	0.2303	1/4	0.074

Table S4. Al-F bond length (Å), F-Al-F and Al-F-Al bond angles[a] (°) from X-ray powder structure refinement and PBE-DFT geometry-optimization (in italic) for β-AlF_3.

Bond lengths			Bond angles		
Al1-F3 (x2)	1.7961	*1.8040*	F3-Al1-F2 (x4)	90.25	*90.22*
Al1-F2 (x4)	1.8015	*1.8068*	F3-Al1-F2 (x4)	89.75	*89.78*
Al2-F4 (x2)	1.7978	*1.8081*	F2-Al1-F2 (x2)	90.07	*90.35*
Al2-F1 (x2)	1.7996	*1.8040*	F2-Al1-F2 (x2)	89.93	*89.65*
Al2-F2 (x2)	1.8006	*1.8073*	F4-Al2-F1 (x2)	89.94	*89.86*
Bond angles			F4-Al2-F1 (x2)	90.06	*90.14*
Al2-F1-Al2	148.66	*147.68*	F4-Al2-F2 (x2)	90.19	*90.01*
Al1-F2-Al2	148.27	*146.95*	F4-Al2-F2 (x2)	89.81	*89.99*
Al1-F3-Al1	166.41	*162.71*	F1-Al2-F2 (x2)	90.24	*90.66*
Al2-F4-Al2	165.52	*161.07*	F1-Al2-F2 (x2)	89.76	*89.34*

[a] F-Al-F bond angles between two opposite bonds are equal to 180° since the site symmetries of Al1 and Al2 are 2/m and $\bar{1}$, respectively.

Table S5. Initial fractional atomic coordinates [3] (x, y, z), PBE-DFT geometry-optimized fractional atomic coordinates (x', y', z') and corresponding atomic displacements d (Å) for η-AlF_3.

Atom	Site	x	y	z	x'	y'	z'	d
Al	16c	0	0	0	0	0	0	0
F	48f	0.3121	1/8	1/8	0.3131	1/8	1/8	0.01

Table S6. Al-F bond length (Å), F-Al-F and Al-F-Al bond angles[a] (°) from X-ray powder structure refinement and PBE-DFT geometry-optimization (in italic) for η-AlF_3.

Bond lengths			Bond angles		
Al-F (x6)	1.803	*1.806*	F-Al-F (x6)	89.84	*90.24*
			F-Al-F (x6)	90.16	*89.76*
			Al-F-Al (x3)	141.29	*140.71*

[a] F-Al-F bond angles between two opposite bonds are equal to 180° since the site symmetry of Al is $\bar{3}$m.

Table S7. Initial fractional atomic coordinates [4] (x, y, z), PBE-DFT geometry-optimized fractional atomic coordinates (x', y', z') and corresponding atomic displacements d (Å) for GaF_3.

Atom	Site	x	y	z	x'	y'	z'	d
Ga	6b	0	0	0	0	0	0	0
F	18e	0.0527	-0.2807	0.5833	0.0395	-0.2939	0.5833	0.051

Table S8. Ga-F bond length (Å), F-Ga-F and Ga-F-Ga bond angles[a] (°) from single crystal structure refinement and PBE-DFT geometry-optimization (in italic) for GaF_3.

Bond lengths			Bond angles		
Ga-F (x6)	1.892	*1.913*	F-Ga-F (x6)	90.59	*91.20*
			F-Ga-F (x6)	89.41	*88.80*
			Ga-F-Ga (x3)	144.91	*141.15*

[a] F-Ga-F bond angles between two opposite bonds are equal to 180° since the site symmetry of Ga is $\bar{3}$.

Table S9. Initial fractional atomic coordinates [5] (x, y, z), PBE-DFT geometry-optimized fractional atomic coordinates (x', y', z') and corresponding atomic displacements d (Å) for GaF_3.

Atom	Site	x	y	z	x'	y'	z'	d
Ga	6b	0	0	0	0	0	0	0
F	18e	0.0591	-0.2742	0.0833	0.0410	-0.2923	0.0833	0.070

Table S10. Ga-F bond length (Å), F-Ga-F and Ga-F-Ga bond angles[a] (°) from single crystal structure refinement and PBE-DFT geometry-optimization (in italic) for GaF_3.

Bond lengths			Bond angles		
Ga-F (x6)	1.885	*1.914*	F-Ga-F (x6)	90.34	*91.15*
			F-Ga-F (x6)	89.66	*88.85*
			Ga-F-Ga (x3)	146.78	*141.57*

[a] F-Ga-F bond angles between two opposite bonds are equal to 180° since the site symmetry of Ga is $\bar{3}$.

Table S11. Initial fractional atomic coordinates [6] (x, y, z), PBE-DFT geometry-optimized fractional atomic coordinates (x', y', z') and corresponding atomic displacements d (Å) for InF_3.

Atom	Site	x	y	z	x'	y'	z'	d
In	6b	0	0	0	0	0	0	0
F	18e	0.6084	0	1/4	0.6331	0	1/4	0.133

Table S12. In-F bond length (Å), F-In-F and In-F-In bond angles[a] (°) from single crystal structure refinement and PBE-DFT geometry-optimization (in italic) for InF_3.

Bond lengths			Bond angles		
In-F (x6)	2.054	*2.096*	F-In-F (x6)	90.60	*89.44*
			F-In-F (x6)	89.40	*90.56*
			In-F-In (x3)	146.82	*139.82*

[a] F-In-F bond angles between two opposite bonds are equal to 180° since the site symmetry of In is $\bar{3}$.

Table S13. Initial fractional atomic coordinates [7] (x, y, z), PBE-DFT geometry-optimized fractional atomic coordinates (x', y', z') and corresponding atomic displacements d (Å) for TlF-II.

Atom	Site	x	y	z	x'	y'	z'	d
Tl	4d	0.2550	0.0096	1/4	0.2578	0.0110	1/4	0.019
F	4d	0.8593	0.0628	1/4	0.8530	0.0614	1/4	0.039

Table S14. Tl-F bond lengths (Å) from powder neutron structure refinement and PBE-DFT geometry-optimization (in italic) for TlF-II.

Bond lengths		Bond lengths	
2.430	*2.483*	3.115	*3.095*
2.549	*2.559*	3.695	*3.639*
2.713 (x2)	*2.707*		

Table S15. Initial fractional atomic coordinates [7] (x, y, z), PBE-DFT geometry-optimized fractional atomic coordinates (x', y', z') and corresponding atomic displacements d (Å) for TlF-I.

Atom	Site	x	y	z	x'	y'	z'	d
Tl	2c	1/4	1/4	0.2539	1/4	1/4	0.2556	0.016
F	2c	1/4	1/4	0.8574	1/4	1/4	0.8514	0.037

Table S16. Tl-F bond lengths (Å) from powder neutron structure refinement and PBE-DFT geometry-optimization (in italic) for TlF-I.

Bond lengths	
2.428 (x1)	*2.475 (x1)*
2.760 (x4)	*2.754 (x4)*
3.695 (x1)	*3.648 (x1)*

Table S17. Eigenvectors of the calculated ^{27}Al EFG tensor, expressed in the crystallographic axis, for IS and APO (in italic) α-AlF_3.

Axis	V_{XX}	V_{YY}	V_{ZZ}	*V_{XX}*	*V_{YY}*	*V_{ZZ}*
a	0.1976	0.1256	0	*-0.1905*	*0.1363*	*0*
b	-0.0999	0.2340	0	*-0.2133*	*-0.0968*	*0*
c	0	0	0.0804	*0*	*0*	*0.0804*

Table S18. Eigenvectors of the calculated ^{27}Al EFG tensors, expressed in the crystallographic axis, for IS and APO (in italic) β-AlF_3.

Site	Axis	V_{XX}	V_{YY}	V_{ZZ}	*V_{XX}*	*V_{YY}*	*V_{ZZ}*
Al1	a	0	-0.1443	0	*0*	*-0.1443*	*0*
	b	0.0017	0	-0.0833	*0.0061*	*0*	*-0.0831*
	c	0.1401	0	0.0028	*0.1398*	*0*	*0.0102*
Al2	a	0.0101	0.0689	-0.1259	*0.0360*	*-0.0515*	*-0.1299*
	b	0.0100	0.0720	0.0407	*0.0451*	*-0.0599*	*0.0363*
	c	0.1388	-0.0195	0.0003	*0.1125*	*0.0836*	*-0.0019*

Table S19. Eigenvectors of the calculated ^{27}Al EFG tensor, expressed in the crystallographic axis, for IS and APO (in italic) η-AlF_3.

Axis	V_{XX}	V_{YY}	V_{ZZ}	*V_{XX}*	*V_{YY}*	*V_{ZZ}*
a	0.0425	0.0734	-0.0600	*0.0425*	*0.0734*	*-0.0600*
b	-0.0848	0.0001	-0.0600	*-0.0848*	*0.0001*	*-0.0600*
c	0.0424	-0.0735	-0.0600	*0.0424*	*-0.0735*	*-0.0600*

Table S20. Eigenvectors of the calculated ^{71}Ga EFG tensor, expressed in the crystallographic axis, for IS and APO (in italic) GaF_3 (from ref. [4]).

Axis	V_{XX}	V_{YY}	V_{ZZ}	*V_{XX}*	*V_{YY}*	*V_{ZZ}*
a	-0.0953	0.2103	0	*0.0452*	*-0.2264*	*0*
b	0.1345	0.1876	0	*-0.1734*	*-0.1523*	*0*
c	0	0	0.0771	*0*	*0*	*0.0771*

Table S21. Eigenvectors of the calculated ^{71}Ga EFG tensor, expressed in the crystallographic axis, for IS and APO (in italic) GaF_3 (from ref. [5]).

Axis	V_{XX}	V_{YY}	V_{ZZ}	*V_{XX}*	*V_{YY}*	*V_{ZZ}*
a	0.2298	0.0167	0	*0.0281*	*0.2287*	*0*
b	0.1293	-0.1907	0	*0.2121*	*0.0900*	*0*
c	0	0	0.0770	*0*	*0*	*0.0770*

Table S22. Eigenvectors of the calculated ^{115}In EFG tensor, expressed in the crystallographic axis, for IS and APO (in italic) InF_3.

Axis	V_{XX}	V_{YY}	V_{ZZ}	*V_{XX}*	*V_{YY}*	*V_{ZZ}*
a	0.2127	0.0182	0	*0.0053*	*0.2134*	*0*
b	0.1221	-0.1751	0	*-0.1821*	*0.1113*	*0*
c	0	0	0.0695	*0*	*0*	*0.0695*

Table S23. Compound, site, calculated EFG tensor V_{ii} (10^{21} V/m^2) and angular distortions α and β (deg) from IS and APO structures.

Compound	Site	Structure	V_{ii} orthogonal to opposite faces	α	V_{ii} bisector of two adjacent Al-F bonds	β
α-AlF_3	Al1	IS	V_{zz} = -0.0630	0.02	$V_{xx} = V_{yy}$ = 0.0315	-0.02
		APO	V_{zz} = -0.0211	0.25	$V_{xx} = V_{yy}$ = 0.0106	-0.25
β-AlF_3	Al1	IS			V_{zz} = -0.341; V_{yy} = 0.276	0.07; -0.07
		APO			V_{zz} = -0.332; V_{yy} = 0.210	0.35; -0.35
	Al2	IS			V_{zz} = -0.360	0.24
		APO			V_{zz} = -0.359	0.66
η-AlF_3	Al1	IS	V_{zz} = -0.554	-0.16	$V_{xx} = V_{yy}$ = 0.277	0.16
		APO	V_{zz} = -0.468	0.24	$V_{xx} = V_{yy}$ = 0.234	-0.24
GaF_3[4]	Ga1	IS	V_{zz} = -0.092	0.59	$V_{xx} = V_{yy}$ = 0.046	-0.59
		APO	V_{zz} = 0.175	1.20	$V_{xx} = V_{yy}$ = -0.088	-1.20
GaF_3[5]	Ga1	IS	V_{zz} = -0.215	0.34	$V_{xx} = V_{yy}$ = 0.107	-0.34
		APO	V_{zz} = 0.153	1.15	$V_{xx} = V_{yy}$ = -0.077	-1.15
InF_3	In1	IS	V_{zz} = -1.083	-0.60	$V_{xx} = V_{yy}$ = 0.542	0.60
		APO	V_{zz} = -0.154	0.56	$V_{xx} = V_{yy}$ = -0.077	-0.56

References

[1] P. Daniel, A. Bulou, M. Rousseau, J. Nouet, J.-L. Fourquet, M. Leblanc, R. Burriel, J. Phys.: Condensed Matter 2 (1990) 5663–5677 (ICSD file number 68826).

[2] A. Le Bail, C. Jacoboni, M. Leblanc, R. de Pape, H. Duroy, J.-L. Fourquet, J. Solid State Chem. 77 (1988) 96–101 (ICSD file number 202681).

[3] N. Herron, D. L. Thorn, R. L. Harlow, G. A. Jones, J. B. Parise, J. A. Fernandez-Baca, T. Vogt, Chem. Mater. 7 (1995) 75–83.

[4] F. M. Brewer, G. Garton, D. M. L. Goodgame, J. Inorg. Nucl. Chem. 9 (1959) 56–64 (ICSD file number 22197).

[5] M. Roos, G. Z. Meyer, Kristallogr. - New Cryst. Struct. 216 (2001) 18–18 (ICSD file number 409507).

[6] R. Hoppe, D. J. Kissel, J. Fluorine Chem. 24 (1984) 327–340 (ICSD file number 38306).

[7] P. Berastegui, S. Hull, J. Solid State Chem. 150 (2000) 266–275 (ICSD file numbers 90992 and 90993).

2.4 Other binary fluorides (columns 11, 12 and 14 metal fluorides)

2.4.1 Structural features and solid state NMR study

As the alkali fluorides, silver (column 11) (I) fluoride, AgF, adopts the sodium chloride (NaCl) structural type (ICSD[3] file number 18008).[4] The ^{19}F δ_{iso} value of this compound has never been reported. Its ^{19}F MAS NMR spectrum is presented in Fig. 1. The ^{19}F δ_{iso} value is equal to -317.4 ppm.

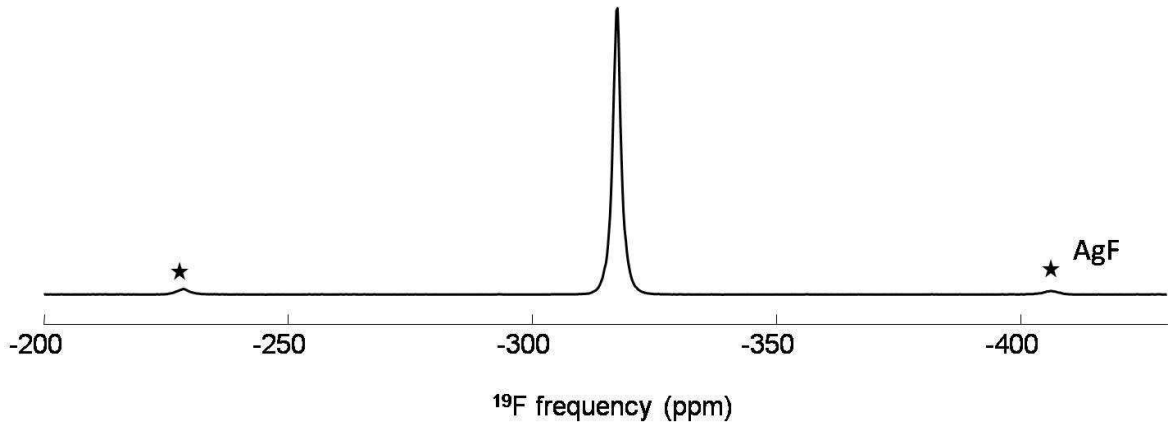

Fig. 1. ^{19}F MAS NMR spectrum of AgF obtained at a magnetic field of 7.0 T using spinning frequency of 25 kHz. The asterisks indicate spinning sidebands.

The three binary fluorides ZnF_2, CdF_2 and HgF_2 (column 12) have also been studied. Among these fluorides, ZnF_2[5] (ICSD[3] file number 280605) adopts, as MgF_2, the rutile (TiO_2) structural type whereas CdF_2[6] (ICSD[3] file number 28731) and HgF_2[7] (ICSD[3] file number 33614) adopt the fluorite (CaF_2) structural type. The ^{19}F δ_{iso} values of ZnF_2,[8,9] CdF_2[8-12] and HgF_2,[8,12] have been measured previously referenced relative to C_6F_6. Then the ^{19}F δ_{iso} values of CdF_2 and HgF_2 have been converted relative to $CFCl_3$.[13,14] The ^{19}F δ_{iso} values of this three compounds have been measured referenced relative to $CFCl_3$ (Fig. 2, -204.5 ppm, -194.7 ppm and -199.5 ppm for ZnF_2, CdF_2 and HgF_2, respectively) for the reasons given above (see 2.2 and 2.3).

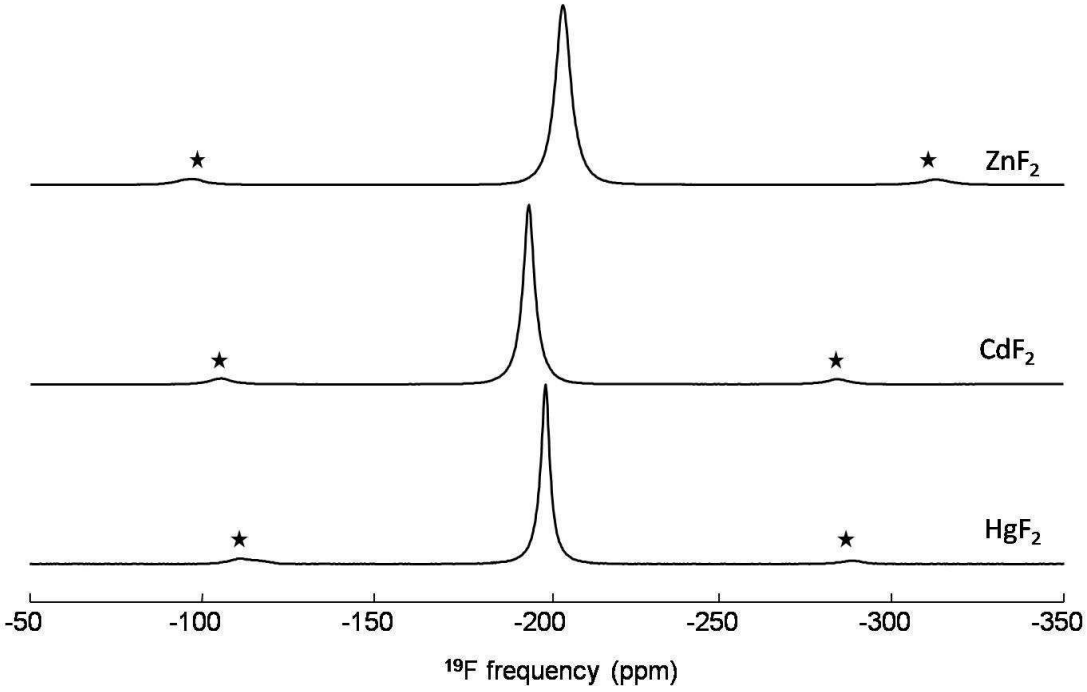

Fig. 2. ^{19}F MAS NMR spectra of ZnF_2, CdF_2 and HgF_2 obtained at a magnetic field of 7.0 T using spinning frequencies of 30 kHz for ZnF_2 and 25 kHz for CdF_2 and HgF_2. The asterisks indicate spinning sidebands.

The two binary lead (column 14) II fluoride compounds, α- and β-PbF_2, have been previously studied. The ^{19}F δ_{iso} values of α-PbF_2[9,15,16] and β-PbF_2[9,10,17] have been measured in the past referenced relative to C_6F_6 and more recently referenced relative to $CFCl_3$. The lead fluoride compounds have further interest since the ^{19}F-^{207}Pb *J*-coupling is large enough to be resolved on a ^{19}F MAS NMR spectra as shown previously for α-[15,16] and β-PbF_2.[17] Given the 22.6% ^{207}Pb natural abundance, each fluorine site has several possible environments $F(^{207}Pb)_x(Pb)_{n-x}$, that are magnetically inequivalent, where Pb represents the lead nuclei with no nuclear spin, and *n* is the number of these Pb atoms in the first fluorine coordination sphere with $0 \leq x \leq n$. Therefore, each ^{19}F resonance is the sum of individual multiplets (for example, for n = 2, a singlet, a doublet, and a triplet) whose relative intensities are given by their probabilities for occurrence.

β-PbF_2[18] (ICSD[3] file number 86738) adopts the fluorite (CaF_2) structural type and then contains one F site located at the centre of a regular tetrahedron of Pb atoms. The ^{19}F δ_{iso} value has been recently determined by C. Martineau during her thesis (-39.2 ppm).[17] The (absolute) ^{207}Pb-^{19}F *J*-coupling value in β-PbF_2 has been determined on single crystal (2.15 kHz[19]) and on polycrystalline powder from ^{19}F MAS NMR spectrum (2.60 kHz[17]).

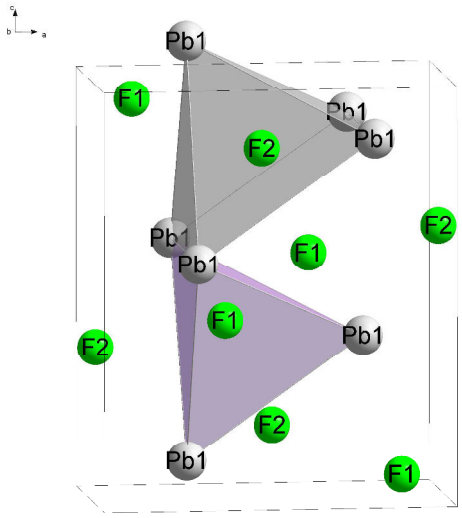

Fig. 3. Perspective view of α-PbF_2 showing the $F1Pb_4$ and $F2Pb_5$ polyhedra.

α-PbF_2[20] (ICSD[3] file number 14324) adopts the $PbCl_2$ structural type (Fig. 3) and has two fluorine sites with the same multiplicity. F1 is coordinated to four lead atoms and has F-Pb bond lengths that vary from 2.45 Å to 2.64 Å whereas the F2 site is coordinated to five lead atoms and has F-Pb bond lengths that vary from 2.41 to 3.03 Å (Fig. 3, Table 1).

Table 1. F-Pb and average F-Pb bond lengths in α-PbF_2.

F1	Pb	2x	2.447
	Pb	1x	2.534
	Pb	1x	2.641
	$\langle F1-Pb\rangle$		**2.517**
F2	Pb	1x	2.409
	Pb	2x	2.688
	Pb	2x	3.033
	$\langle F2-Pb\rangle$		**2.770**

The ^{19}F MAS NMR spectra (Fig. 4) show two resonances at -19.7 and -57.1 ppm, in agreement with the previously determined ^{19}F δ_{iso} values (-20.5 ppm and -57.7 ppm).[15,16] The ^{19}F NMR resonances were assigned to the crystallographic sites F1 and F2, respectively, on the basis of their different ^{207}Pb-^{19}F *J*-coupling patterns, the ^{207}Pb-^{19}F *J* coupling being likely to be larger for ^{19}F nuclei in site F1 (2.0 kHz) than for those in F2 (individual peaks not resolved at a spinning frequency of 22.5 (or 24.2?) kHz[15]), due to the shorter Pb-F1 internuclear distances.[15,16] This assignment - the first one which is not obvious in this chapter - is confirmed by the chemical shielding calculations (see 2.4.2). As shown previously[16] and on Fig. 4, the resolution increases with the spinning frequency. Nine peaks have been detected for the F2 site at 29 kHz but significant differences have been observed in the splittings between the first and second sets of satellite peaks of 0.75 and 0.50 kHz, respectively.[16] We observe less significant differences; indeed, for both NMR resonances, due to various F-Pb bond lengths, the splittings between the peaks are not constant (Fig. 5 and Table 2), varying from 0.87 kHz and 1.0 Hz for F1 and from 0.51 kHz to 0.62 kHz for F2 and leading to ^{207}Pb-^{19}F *J* coupling values equal to ~1.9 kHz and ~1.1 kHz for F1 and F2, respectively.

As expected and previously outlined,[15] the ^{207}Pb-^{19}F *J*-coupling is likely to be larger for ^{19}F nuclei in site F1 than for those in F2, due to the shorter F1-Pb distances. Five and six magnetically inequivalent environments are possible for F1 and F2, respectively. For F1, they give rise to a singlet, doublet, triplet, quartet, and quintet for x = 0-4, respectively and for F2, they give rise, in addition, to

a sextet for x = 5. Given the natural abundance (A) for ^{207}Pb, probabilities for the occurrence of each of these environments can be calculated using the formula $P = (1 - A)^{x-n} A^x C_x^n$ with $C_x^n = \frac{x!}{n!(x-n)!}$. Probabilities (%) for the occurrence of each of these environments of 35.9, 41.9, 18.4, 3.6, and 0.3, respectively, for F1 and of 27.8, 40.5, 23.7, 6.9, 1.0, and 0.1, respectively, for F2 are obtained. Thus, a nonet and an undectet, with relative intensities given in Table 1, are predicted for F1 and F2, respectively. The two outermost satellites of these multiplets have such small intensities (expected values equal to 0.02% and 0.002% for F1 and F2, respectively) that they are unlikely to be detected experimentally.

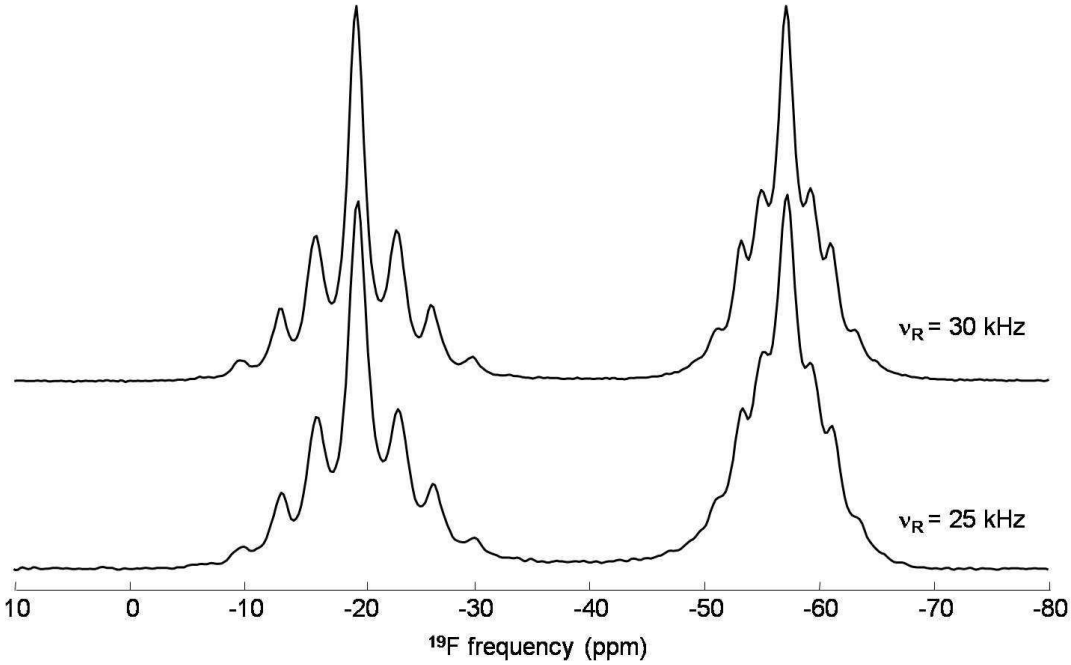

Fig. 4. ^{19}F MAS NMR spectra of α-PbF_2 recorded at a magnetic field of 7.0 T using spinning frequencies of 25 kHz and 30 kHz.

The intensities of the inner seven peaks of the nonet for F1 and of the inner nine peaks of the undectet for F2 measured by deconvoluting each NMR resonance of the spectrum recorded at a spinning frequency of 30 kHz (Fig. 5 and Table 2) are in agreement with those previously determined[15,16] but moderately close to those calculated. As previously explained,[15,16] differences between the measured and calculated intensities may arise from small differences in *J* couplings for the different Pb-F bonds; this will result in asymmetrical peak shapes for the outer transitions and lead to errors in intensities obtained from the deconvolution of the resonances.

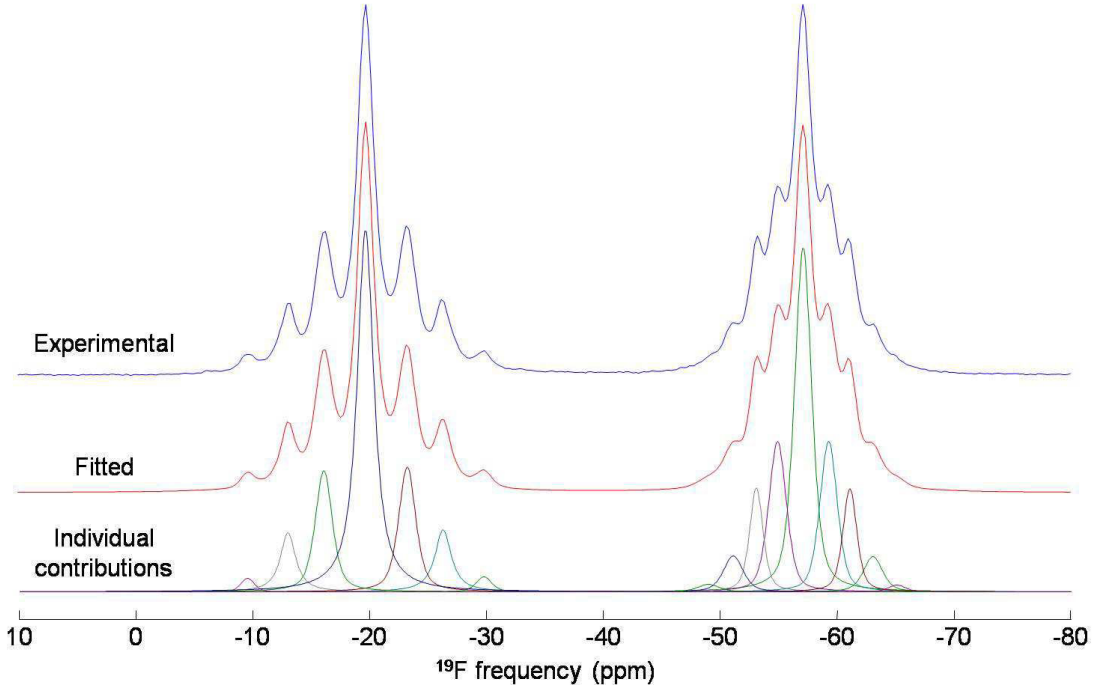

Fig. 5. Experimental ^{19}F MAS (30 kHz) NMR spectrum (blue) of α-PbF_2 obtained at a magnetic field of 7 T. The best fit of this spectrum is represented in red and the individual contributions to the fitted spectrum are shown below. The relative intensities of the multiplets are 47.5% and 52.5%.

Table 2. Parameters used for the reconstruction of the ^{19}F MAS NMR spectrum of α-PbF_2: positions (δ_{iso} (ppm)) and relative intensities (%) of the central lines, positions (ppm) and relative intensities (%) of the satellites, splitting (Hz) between each central line and their satellite peaks and expected relative intensities.

F1	position		-9.6	-13.0	-16.1	-19.7	-23.2	-26.3	-29.8	
	I		1.2	7.7	15.0	50.1	15.6	8.6	1.7	
	I expected	0.02	0.45	4.65	22.3	45.2	22.3	4.65	0.45	0.02
	splitting		2850	1873	1008		1007	1874	2860	
F2	δ_{iso}/ position	-49.0	-51.1	-53.1	-54.9	-57.1	-59.3	-61.1	-63.1	-65.1
	I	1.1	4.6	9.0	16.5	38.1	16.3	9.2	4.3	0.8
	I expected	0.1	0.9	6.2	22.9	40.0	22.9	6.2	0.9	0.1
	splitting	2289	1688	1130	618		616	1129	1687	2267

2.4.2 DFT calculations

The ^{19}F chemical shielding tensors of these fluorides have been calculated using the GIPAW method[21,22] implemented in the CASTEP code.[23,24] The calculations have been performed for experimental structures (named ES in the following) and, when allowed by symmetry, *i.e.* for ZnF_2 and α-PbF_2, for atomic position optimized (APO) structures. The σ_{iso} values are reported in Table 3. The fractional atomic coordinates and bond lengths for ES and APO structures of ZnF_2 and α-PbF_2 are gathered in Tables 4, 5, 6 and 7.

Table 3. Experimental ^{19}F δ_{iso} values, ^{19}F σ_{iso} values calculated using the GIPAW method for the ES and, when allowed by symmetry, APO structures and ^{19}F δ_{iso} values deduced from the linear correlation $\delta_{iso}/CFCl_3 = -0.80(3)\ \sigma_{iso} + 89(9)$ (see 2.2).[25] The σ_{iso} values in bold are those represented in Fig. 6.

Compound (site)	σ_{iso} calc/ppm		δ_{iso} calc/ppm		δ_{iso} exp/ppm
	ES	APO	ES	APO	
AgF	609.9	—	-398.9	—	-317.4
ZnF_2	**352.6**	352.6	-193.1	-193.1	-204.5
CdF_2	**351.3**	—	-192.0	—	-194.7
HgF_2	**355.2**	—	-195.1	—	-199.5
β-PbF_2	**169.1**	—	-46.3	—	-39.2
α-PbF_2 (F1)	140.2	**139.1**	-23.1	-22.3	-19.7
α-PbF_2 (F2)	181.0	**179.3**	-55.8	-54.4	-57.1

Table 4. Initial fractional atomic coordinates (x, y, z),[5] PBE-DFT geometry-optimized fractional atomic coordinates (x', y', z') and corresponding atomic displacements d (Å) for ZnF_2.

	Site	x	y	z	x'	y'	z'	d
Zn1	2a	0	0	0	0	0	0	0
F1	4f	0.30350	0.30350	0	0.30269	0.30269	0	0.005

Table 5. Initial fractional atomic coordinates (x, y, z),[20] PBE-DFT geometry-optimized fractional atomic coordinates (x', y', z') and corresponding atomic displacements d (Å) for α-PbF_2.

	Site	x	y	z	x'	y'	z'	d
Pb1	4c	0.2527	1/4	0.1042	0.2554	1/4	0.1052	0.019
F1	4c	0.8623	1/4	0.0631	0.8591	1/4	0.0665	0.033
F2	4c	0.4662	1/4	0.8457	0.4743	1/4	0.8443	0.053

Table 6. Zn-F and average Zn-F bond lengths (Å) and F-Zn-F bond angles (°) different from 90° from experimental[5] (ES) and PBE-DFT geometry-optimized (APO) structures of ZnF_2.

			Bond lengths		Bond angles	
			ES	APO	ES	APO
Zn1	F1	2x	2.019	2.014	79.7	79.9
	F1	4x	2.041	2.044	100.3	100.1
		$\langle Zn-F \rangle$	**2.033**	**2.034**		

Table 7. F-Pb and average F-Pb bond lengths (Å) from experimental[20] (ES) and PBE-DFT geometry-optimized (APO) structures of α-PbF_2.

			ES	APO
F1	Pb1	2x	2.447	2.464
	Pb1	1x	2.534	2.569
	Pb1	1x	2.642	2.599
		$\langle F1-Pb \rangle$	**2.517**	**2.524**
F2	Pb1	1x	2.409	2.444
	Pb1	2x	2.688	2.642
	Pb1	2x	3.034	3.055
		$\langle F2-Pb \rangle$	**2.770**	**2.768**

The ES and APO structures of ZnF_2 are very similar (Table 4) showing the accuracy of the former one. The average Zn-F bond lengths (Table 6) are very similar and consequently the calculated ^{19}F σ_{iso} values (Table 3) are equal (to the nearest tenth of ppm). As the shortest Zn-F bond length decreases whereas the longest Zn-F bond length increases, the radial distortion increase. On the other hand, the F-Zn-F bond angles, *i.e.* the angular distortion, are similar. Since we were not able to show from ^{67}Zn EFG calculation the efficiency and the usefulness of the optimization for this compound (see below), we retain the initial structure.

The effect of the optimization is greater for α-PbF_2 (Table 5). The shortest F-Pb bond lengths increase but the average F-Pb bond lengths remain similar (Table 7). As the longest F1-Pb bond length decreases, the $F1Pb_4$ tetrahedron is less distorted, after optimization, from a radial point of view. From an angular point of view, the distortion of this tetrahedron is similar before and after optimization (Pb-F-Pb angles between 98.4° and 115.0° for ES and between 98.3° and 116.0° for APO structure). Both σ_{iso} values (Table 3) slightly decrease after optimization but in any case, the calculated σ_{iso} values (σ_{iso} (F1) < (σ_{iso} (F2)) confirm the earlier assignment based on ^{207}Pb-^{19}F *J* coupling values.[15,16] We retain the APO structure even if it is not possible to show that the agreement after optimization of the structure geometry is better or worst.

On can remark that for ZnF_2, CdF_2 and HgF_2 the ^{19}F σ_{iso} values are not in reverse order with respect to their, close, experimental ^{19}F δ_{iso} values. Nevertheless, except for AgF, the agreement is nice between the experimental and the "calculated" ^{19}F δ_{iso} values (Table 3) obtained by using the linear correlation, $\delta_{iso}/CFCl_3$ = - 0.80(3) σ_{iso} + 89(9).[25] Even not efficient for AgF, for which a smaller slope absolute value would be necessary, this correlation is again ascertained.

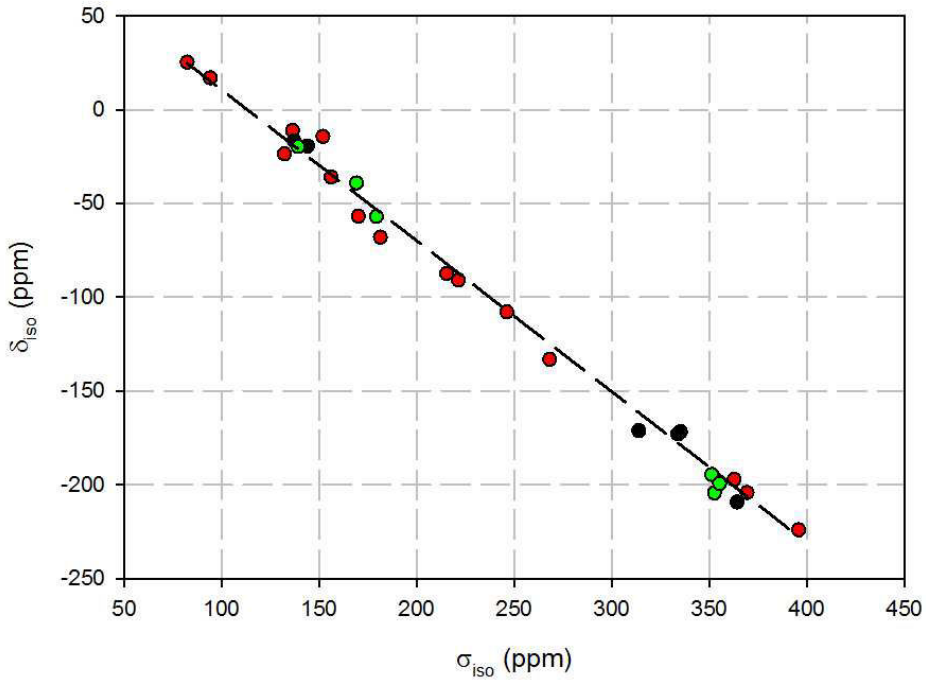

Fig. 6. Calculated ^{19}F σ_{iso} values versus experimentally measured ^{19}F δ_{iso} values. The red circles represent the alkali, alkaline and rare earth of column 3 fluorides (see 2.2),[25] the black circles represent the column 13 metal fluorides, (see 2.3) and the green circles represent the compounds under study in this part of the chapter (values reported in Table 3). The dash line represents the linear regression calculated on all these values: $\delta_{iso}/CFCl_3$ = - 0.805(13) σ_{iso} + 91.0(3.5), R^2 = 0.992.

In Fig. 6, the calculated ^{19}F σ_{iso} values are represented versus the experimental ^{19}F δ_{iso} values for the compounds under study in this part of this chapter, for alkali, alkaline earth and rare earth fluorides[25] (see 2.2) and for column 13 metal fluoride compounds (see 2.3). The slopes and the intercepts of the linear regressions, calculated on all these values ($\delta_{iso}/CFCl_3$ = - 0.805(13) σ_{iso} + 91.0(3.5)), and previously reported[25] ($\delta_{iso}/CFCl_3$ = - 0.80(3) σ_{iso} + 89(9)), are very similar. It confirms again that these correlations between experimental ^{19}F δ_{iso} values and calculated ^{19}F σ_{iso} values could allow predicting ^{19}F NMR spectra of fluoride crystalline compounds containing these metallic atoms, with a relatively good accuracy.

Table 8. Experimental and calculated ^{67}Zn quadrupolar parameters, quadrupolar coupling constant C_Q (MHz), V_{ZZ} (10^{21} V.m^{-2}) and asymmetry parameter η_Q, in ZnF_2.

	C_Q	V_{ZZ}	η_Q
Exp.[27]	7.87	2.17	0.18
Calc. LAPW[27]	8.30	2.29	0.13
Calc. PAW ES	5.77	1.59	0.67
Calc. PAW APO	6.05	1.67	0.92
Calc. LAPW ES	7.41	2.04	0.16

Table 9. Eigenvectors of the calculated ^{67}Zn EFG tensor, expressed in the crystallographic axis, for the experimental structure[5] of ZnF_2.

Axis	V_{XX}	V_{YY}	V_{ZZ}
a	0.707	0	0.707
b	0.707	0	-0.707
c	0	1	0

The experimental and calculated, using the linearized augmented plane wave (LAPW) method[26] implemented in the WIEN97 code, ^{67}Zn quadrupolar parameters of ZnF_2 were previously reported by Bastow.[27] A nice agreement was obtained (Table 8). On the other hand, the agreement is poor with the values calculated, using the PAW method[28,29] implemented in the CASTEP code,[23,24] for initial and atomic position optimized structures (Table 8). We then used, as Bastow,[27] the LAPW method, implemented in the WIEN2k code,[26,30] confirming the nice agreement (Table 8) and allowing to orientate the EFG tensor elements (Table 9, Fig. 7). The forces acting on all atoms being smaller than 1 mRy in the experimental structure, geometry optimization is not useful. ZnF_2 and MgF_2 being isostructural, the ^{25}Mg (see 2.2) and ^{67}Zn EFG orientation are similar. As shown in Fig. 7 which depicts the orientation of the ^{67}Zn EFG tensor, the V_{ii} components are along the intersections of the three mirror planes of the Zn site (mmm symmetry) and, for the Zn atom located at (0,0,0), V_{ZZ} and V_{XX} lie in the (*a,b*) plane while V_{YY} is along the *c* crystallographic axis. In the ZnF_2 structure, the ZnF_6 octahedron is characterized by low radial and high angular distortions (Table 6). In such a situation, the largest component of the EFG tensor (V_{ZZ}) is not expected to be oriented along M-F bonds.[31] Indeed, V_{ZZ} and V_{YY} are both oriented between two Zn-F bonds in the plane presenting the angular distortion while V_{XX} is oriented along the shortest Zn-F bond perpendicular to this plane. It should also be noted that the sign of the calculated V_{ii} components is in agreement with the angular distortion analysis model proposed by Body et al.,[31] i.e. a positive/above 90° (negative/below 90°) angular distortion leads to a charge depletion (concentration) in the V_{ii} direction and then to a positive (negative) V_{ii} value (Fig. 7).

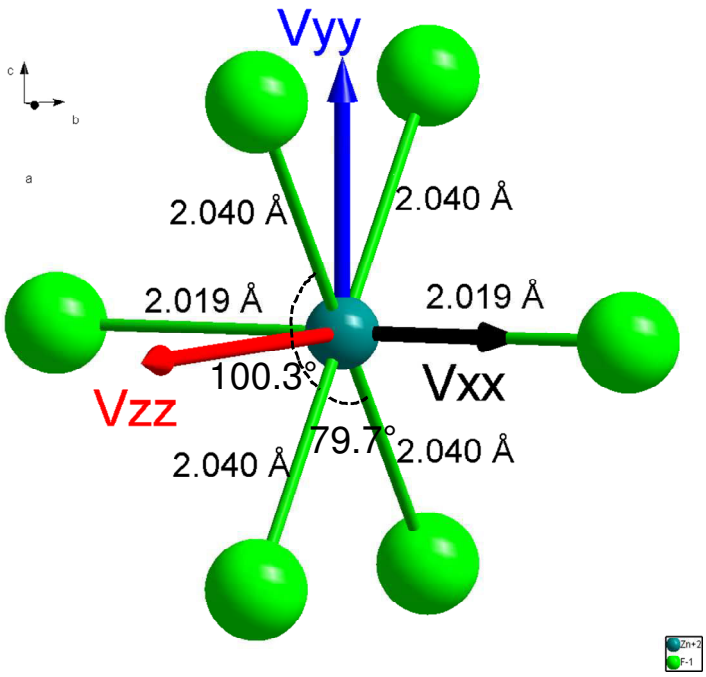

Fig. 7. Orientation of the ^{67}Zn EFG tensor components, calculated with WIEN2k on the experimental structure,[5] represented on the ZnF_6 octahedron. Zn–F bond lengths and F-Zn-F bond angles are indicated. The norms of the eigenvectors are proportional to the eigenvalues of the EFG tensor components: V_{ZZ} = 2.04 x 10^{21} V.m^{-2}, V_{YY} = -1.19 x 10^{21} V.m^{-2}, V_{XX} = -0.86 x 10^{21} V.m^{-2}.

2.4.3 Experimental section

2.4.3.1 Solid state NMR

The sample of AgF was purchased from Alfa Aesar (lot number J20Q110). The samples of CdF_2 and α-PbF_2 were purchased from Cerac (lot numbers 36410-D-(1-4) and 135797-B-1B, respectively). ZnF_2 is a lab-made (and/or purified) sample and the origin of the sample of HgF_2 could not be found. All these samples are kept in a dry glove box under nitrogen atmosphere. Prior to use, the purity of these samples was checked by X-Ray Powder Diffraction.

Solid-state NMR experiments were performed on an Avance 300 Bruker spectrometer operating at 7.0 T (^{19}F Larmor frequency of 282.2 MHz), using a 2.5 mm CPMAS probehead. ^{19}F one dimensional (1D) MAS NMR spectra were recorded using a Hahn echo sequence with an inter-pulse delay equals to one rotor period, with a recycle delay equal to 10 sec and using 90° pulse lengths of

2.2 µs, 1.5 µs, 1.5 µs, 1.5 µs and 2.7 µs for AgF, ZnF_2, CdF_2, HgF_2 and α-PbF_2, respectively. The ^{19}F 1D MAS NMR spectrum of α-PbF_2 was also acquired with ^{207}Pb decoupling (nutation frequency of 50 kHz). The ^{19}F chemical shifts are referenced to $CFCl_3$ at 0 ppm. The ^{19}F 1D MAS NMR spectra were fitted using DMfit[32] software.

2.4.3.2 DFT calculations

DFT calculations of the ^{19}F chemical shielding tensors, using the GIPAW method,[21,22] and ^{67}Zn EFG in ZnF_2, using the projector augmented-wave (PAW) approach[28,29] were performed with the NMR-CASTEP code[23,24] implemented in the Materials Studio 5.0 environment, for the experimental structure (named ES above) and atomic position optimized (APO) structures, when allowed by symmetry. The PBE (Perdew, Burke and Ernzerhof) functional[33] was used in the generalized gradient approximation (GGA) for the exchange-correlation energy, and the core-valence interactions were described by ultrasoft pseudopotentials (USPP) generated using the on the fly generator (OTF_USPP) included in CASTEP. The wave functions were expanded on a plane-wave basis set with a kinetic energy cutoff of 700 eV. The Brillouin zone was sampled using a Monkhorst-Pack grid spacing approximately equal to 0.04 $Å^{-1}$ (corresponding to a k-point mesh of $5 \times 5 \times 5$ for all structures except for ZnF_2 ($6 \times 6 \times 8$) and α-PbF_2 ($4 \times 7 \times 4$)). APO structures are obtained by minimizing the residual forces on the atom up to $|F|_{max}$ below 10 meV.$Å^{-1}$, keeping symmetry constraints and fixing the cell parameters to the experimentally determined values.

^{67}Zn EFG in ZnF_2 were also calculated using the LAPW method[26] implemented in the WIEN2k code.[26,30] The atomic sphere radii (R_{MT}) were set to 1.90 and 1.70 a.u. for Zn and F, respectively. The core electron states were separated from the valence states by -7.0 Ry. Core states are from 1s to 3s for Zn and 1s for F. The plane wave cut-off is defined by $R_{MT}K_{MAX} = 8$. We use a Monkhorst-Pack grid approximatively equal to 0.05 $Å^{-1}$ (corresponding to a *k*-point mesh of 4 × 4 × 6). Total energies are converged up to changes smaller than 1.4×10^{-3} eV.

The quadrupolar moment used for the calculation of quadrupolar coupling constant, C_Q, for ^{67}Zn is $0.150(15) \times 10^{-28} m^2$.[34]

2.5 Conclusion

A correlation between ^{19}F experimental isotropic chemical shifts and ^{19}F calculated isotropic chemical shieldings, allowing to predict ^{19}F NMR spectra of crystalline compounds with a relatively good accuracy, has been established on twelve binary fluorides containing twelve different metal atoms and further confirmed on eleven binary fluorides containing eight different metal atoms. This correlation was successfully applied to $RbLaF_4$,[35] $NaAsF_6$[36] (see 4.2) and α-$LaZr_2F_{11}$.[37] At this stage, the single atom which does not comply this correlation is Ag.

Moreover, the studies gathered in this chapter enable to show that when using the PBE exchange–correlation functional for the treatment of the cationic localized empty orbitals of Ca^{2+}, Sc^{3+} (3d) and La^{3+} (4f), a correction is needed to accurately calculate ^{19}F chemical shieldings.

In addition, we experimentally determine the quadrupolar parameters of ^{25}Mg in MgF_2, ^{71}Ga in GaF_3 and ^{115}In in InF_3, and calculate the electric field gradients of ^{25}Mg in MgF_2, ^{27}Al in α-, β- and η-AlF_3, ^{67}Zn in ZnF_2, ^{71}Ga in GaF_3, ^{115}In in InF_3 and ^{139}La in LaF_3 using PAW and/or LAPW methods. The orientation of the EFG components in the crystallographic frame, provided by DFT calculations, have been analyzed in terms of electron densities for ^{25}Mg in MgF_2 and ^{139}La in LaF_3. The study of α-AlF_3, GaF_3 and InF_3 highlights the care that must be taken when dealing with optimized structures.

2.6 References

(1) A. Zheng, S.-B. Liu, F. Deng, *J. Phys. Chem. C* **2009**, *113*, 15018–15023.
(2) J. M. Griffin, J. R. Yates, A. J. Berry, S. Wimperis, S. E. Ashbrook, *J. Am. Chem. Soc.* **2010**, 132, 15651–15660.
(3) Inorganic Crystal Structure Database (ICSD), version 1.9.1; FIZ Karlsruhe and NIST: Germany and Maryland, 2011.
(4) H. Ott, *Z. Kristallogr. Kristallgeom. Kristallphys. Kristallchem.* **1926**, *63*, 222–230.
(5) N. J. O'Toole, V. A. Streltsov, *Acta Crystallogr., Sec. B* **2001**, *57*, 128–135.
(6) F. Hund, K. Z. Lieck, *Z. Anorg. Allg. Chem.* **1953**, *271*, 17–28.
(7) F. Ebert, H. Z. Woitinek, *Z. Anorg. Allg. Chem.* **1933**, *210*, 269–272.
(8) R. W. Vaughan, D. D. Elleman, W.-K. Rhim, L. M. Stacey, *J. Chem. Phys.* **1972**, *57*, 5383–5391.
(9) B. Bureau, G. Silly, J.-Y. Buzaré, J. Emery, *Chem. Phys.* **1999**, *249*, 89–104.
(10) D. P. Burum, D. D. Elleman, W.-K. Rhim, *J. Chem. Phys.* **1978**, *68*, 1164–1169.
(11) N. Boden, P. K. Kahol, A. Mee, M. Mortimer, G. N. Peterson, *J. Magn. Reson.* **1983**, *54*, 419–426.
(12) A. T. Kreinbrink, C. D. Sazavsky, J. W. Pyrz, D. G. A. Nelson, R. S. Honkonen, *J. Magn. Reson.* **1990**, *88*, 267–276.
(13) R. K. Harris, P. Jackson, *Chem. Rev.* **1991**, *91*, 1427–1440.
(14) J. M. Miller, *Prog. Nucl. Magn. Reson. Spectrosc.* **1996**, *28*, 255–281.
(15) F. Wang, C. P. Grey, *J. Am. Chem. Soc.* **1995**, *117*, 6637–6638.
(16) F. Wang, C. P. Grey, *J. Am. Chem. Soc.* **1998**, *120*, 970–980.
(17) C. Martineau, Thèse de l'Université du Maine, **2008**.
(18) S. Hull, P. Berastegui, S. G. Eriksson, N. J. G. Gardner, *J. Phys.: Condens. Matter* **1998**, *10*, 8429–8446.
(19) R. E. J. Sears, Q. Z. Guo, H. J. Mackey, *J. Chem. Phys.* **1984**, *80*, 5448–5452.
(20) P. Boldrini, B. O. Loopstra, *Acta Crystallogr.* **1967**, *22*, 744–745.
(21) C. J. Pickard, F. Mauri, *Phys. Rev. B* **2001**, 63, 245101.
(22) J. R. Yates, C. J. Pickard, F. Mauri, *Phys. Rev. B* **2007**, *76*, 024401.
(23) M. D. Segall, P. L. D. Lindan, M. J. Probert, C. J. Pickard, P. J. Hasnip, S. J. Clark, M. C. Payne, *J. Phys.: Condens. Matter* **2002**, *14*, 2717–2744.
(24) S. J. Clark, M. D. Segall, C. J. Pickard, P. J. Hasnip, M. J. Probert, K. Refson, M. C. Payne, *Z. Kristallogr*. **2005**, *220*, 567–570.
(25) A. Sadoc, M. Body, C. Legein, M. Biswal, F. Fayon, X. Rocquefelte, F. Boucher, *Phys. Chem. Chem. Phys.* **2011**, *13*, 18539–18550.
(26) P. Blaha, K. Schwarz, P. Herzig, *Phys. Rev. Lett.* **1985**, *54*,1192–1195.
(27) T. J. Bastow, *Chem. Phys. Lett.* **2003**, *380*, 516–520.
(28) H. M. Petrilli, P. E. Blöchl, P. Blaha, K. Schwarz, *Phys. Rev. B* **1998**, *57*, 14690–14697.
(29) P. E. Blöchl, *Phys. Rev. B* **1994**, *50*, 17953–17979.
(30) P. Blaha, K. Schwarz, G. K. H. Madsen, D. Kvasnicka and J. Luitz, WIEN2k, An Augmented Plane WaVe Plus Local Orbitals Program for Calculating Crystal Properties (Vienna University of Technology, Vienna, 2001).
(31) M. Body, C. Legein, J.-Y. Buzaré, G. Silly, P. Blaha, C. Martineau, F. Calvayrac, *J. Phys. Chem. A*, **2007**, *111*, 11873–11884.
(32) D. Massiot, F. Fayon, M. Capron, I. King, S. Le Calvé, B. Alonso, J.-O. Durand, B. Bujoli, Z. Gan, G. Hoatson, *Magn. Reson. Chem.* **2002**, *40*, 70–76.
(33) J. P. Perdew, K. Burke, M. Ernzerhof, *Phys. Rev. Lett.* **1996**, *77*, 3865–3868.

(34) P. Pyykkö, *Mol. Phys.* **2008**, *106*, 1965–1974.
(35) A.-L. Rollet, M. Allix, E. Veron, M. Deschamps, V. Montouillout, M. R. Suchomel, E. Suard, M. Barré, M. Ocaña, A. Sadoc, F. Boucher, C. Bessada, D. Massiot, F. Fayon, *Inorg. Chem.* **2012**, *51*, 2272–2282.
(36) M. Biswal, M. Body, C. Legein, G. Corbel, A. Sadoc, F. Boucher, *J. Phys. Chem. C* **2012**, *116*, 11682–11693.
(37) C. Martineau, C. Legein, M. Body, O. Péron, B. Boulard, F. Fayon, *J. Solid State Chem.* **2013**, *199*, 326–333.

Chapter 3: Assignment of ^{19}F NMR lines of binary fluorides to crystallographic sites from GIPAW calculations.

3.1 Introduction

Up to this point, only binary fluorides with obvious assignment of the ^{19}F NMR lines to the fluorine crystallographic sites were considered. Confident linear regressions have been established between calculated ^{19}F σ_{iso} and experimental ^{19}F δ_{iso} values. In this chapter binary fluorides with several fluorine crystallographic sites are studied with one main objective: the assignment of their ^{19}F NMR lines to their crystallographic sites. Such compounds provide opportunities to test the efficiency and reliability of the linear regressions determined in the previous chapter. To assign the ^{19}F resonances to the fluorine crystallographic sites, the NMR lines are ranked in decreasing order of experimental δ_{iso} values whereas F atoms are ranked in increasing order of calculated σ_{iso} values. Of course, the multiplicity of the F site must be consistent with the relative intensity of the NMR line it is assigned to. In compounds having F sites with different multiplicities, this point gives us a first indication of the σ_{iso} calculation reliability. When multiplicities and relative intensities are in the same sequence, linear regression can be established between the calculated ^{19}F σ_{iso} and experimental ^{19}F δ_{iso} values and compared to the previously established ones.

Column 5 metal (Nb,Ta) fluorides study is reported in the section 3.2. No correlation experiments, which require long acquisition time, can be performed on these compounds due to their high hygroscopic nature. In the section 3.3, MF_4 (M = Zr, Hf, Ce, Th) fluorides with narrower chemical shift ranges are studied. Correlation experiments, based on through space ^{19}F-^{19}F dipolar coupling interaction, have been carried out on two of these compounds, with the expectation that experimental assignments of the ^{19}F NMR lines to the fluorine crystallographic sites can be achieved.

3.2 Column 5 metal (Nb, Ta) fluorides

Journal of Solid State Chemistry 207 (2013) 208–217

Contents lists available at ScienceDirect

Journal of Solid State Chemistry

journal homepage: www.elsevier.com/locate/jssc

NbF_5 and TaF_5: Assignment of ^{19}F NMR resonances and chemical bond analysis from GIPAW calculations

Mamata Biswal [a], Monique Body [a], Christophe Legein [a,*], Aymeric Sadoc [b], Florent Boucher [b]

[a] LUNAM Université, Université du Maine, CNRS UMR 6283, Institut des Molécules et des Matériaux du Mans, Avenue Olivier Messiaen, 72085 Le Mans Cedex 9, France

[b] Institut des Matériaux Jean Rouxel (IMN), Université de Nantes, CNRS, 2 rue de la Houssinière, BP 32229, 44322 Nantes Cedex 3, France

ARTICLE INFO

Article history:
Received 14 June 2013
Received in revised form
28 August 2013
Accepted 1 September 2013
Available online 8 September 2013

Keywords:
Inorganic fluorides
^{19}F solid state NMR
DFT calculations

ABSTRACT

The ^{19}F isotropic chemical shifts (δ_{iso}) of two isomorphic compounds, NbF_5 and TaF_5, which involve six nonequivalent fluorine sites, have been experimentally determined from the reconstruction of 1D ^{19}F MAS NMR spectra. In parallel, the corresponding ^{19}F chemical shielding tensors have been calculated using the GIPAW method for both experimental and DFT-optimized structures. Furthermore, the [M_4F_{20}] units of NbF_5 and TaF_5 being held together by van der Waals interactions, the relevance of Grimme corrections to the DFT optimization processes has been evaluated. However, the semi-empirical dispersion correction term introduced by such a method does not show any significant improvement. Nonetheless, a complete and convincing assignment of the ^{19}F NMR lines of NbF_5 and TaF_5 is obtained, ensured by the linearity between experimental ^{19}F δ_{iso} values and calculated ^{19}F isotropic chemical shielding σ_{iso} values. The effects of the geometry optimizations have been carefully analyzed, confirming among other matters, the inaccuracy of the experimental structure of NbF_5. The relationships between the fluorine chemical shifts, the nature of the fluorine atoms (bridging or terminal), the position of the terminal ones (opposite or perpendicular to the bridging ones), the fluorine charges, the ionicity and the length of the M–F bonds have been established. Additionally, for three of the ^{19}F NMR lines of NbF_5, distorted multiplets, arising from ^1J-coupling and residual dipolar coupling between the ^{19}F and ^{93}Nb nuclei, were simulated yielding to values of ^{93}Nb–^{19}F ^1J-coupling for the corresponding fluorine sites.

1. Introduction

Unambiguous assignment of complex ^{19}F solid-state NMR spectra of crystalline fluoride compounds having multiple crystallographic sites or fluoride glasses often remains a challenging task. In several studies [1–12], assignments of ^{19}F NMR resonances to environments were based on similarities to crystalline model compounds (similar ^{19}F isotropic chemical shifts (δ_{iso}) values intending to indicate similar structural environments). Nowadays, high resolution two-dimensional heteronuclear and homonuclear correlation experiments can be used for helping in the assignment of fluorine sites. The efficiency of these experiments to probe interatomic spatial proximities and through bond connectivities has been described in various studies [13–28]. An alternative approach consists in the calculation of ^{19}F isotropic chemical shieldings (σ_{iso}). These calculations have been first achieved in various crystalline fluoride materials [29–35] using a semi-empirical model, called superposition model [36]. Ab initio approaches devoted to molecular systems have been used for studying extended systems. In these cases, clusters of atoms were build such that the central atom experiences an environment similar to that in true extended solid, i.e., to mimic the crystalline periodic structures [14,30,37–44]. Recent advances in the theoretical calculations of NMR parameters for extended solids lead to the development of the Gauge Including Projector Augmented Wave (GIPAW) method [45,46] which integrates explicitly the periodic boundary conditions. This major breakthrough enables consequently the calculations of NMR tensors in solids [47,48] and was applied on inorganic fluorides for the calculation of ^{19}F σ_{iso} values [19–23,27,49–53].

When interested in the prediction of δ_{iso} values, the calculated ^{19}F σ_{iso} values have to be converted into the isotropic chemical shift scale. Assuming that the ^{19}F σ_{ref} can be obtained, the calculated ^{19}F σ_{iso} values can be converted into "calculated" ^{19}F δ_{iso} values applying the relation $\delta_{iso} \approx \sigma_{ref} - \sigma_{iso}$ [14,19,42,49,54]. Calculated ^{19}F σ_{iso} values can also be converted into "calculated" ^{19}F δ_{iso} values [29–41,43] using an experimental absolute scale for fluorine [55,56]. To avoid these referencing problems and possible

* Corresponding author. Tel.: +33 2 43 83 33 49; fax: +33 2 43 83 35 06.
E-mail addresses: Mamata.Biswal-Susanta_Kumar_Nayak.Etu@univ-lemans.fr (M. Biswal), monique.body@univ-lemans.fr (M. Body), christophe.legein@univ-lemans.fr (C. Legein), Aymeric.Sadoc@cnrs-imn.fr (A. Sadoc), Florent.Boucher@cnrs-imn.fr (F. Boucher).

0022-4596/$ - see front matter © 2013 Elsevier Inc. All rights reserved.
http://dx.doi.org/10.1016/j.jssc.2013.09.001

errors coming from the calculation of the ^{19}F σ_{ref} value, "calculated" ^{19}F δ_{iso} values can be deduced from the linear regression established between calculated ^{19}F σ_{iso} values and experimental ^{19}F δ_{iso} values for the compounds under study [20,21,23,50,51,53], implying that an assignment was already done. This third approach seems to become the standard practice [47,48]. Alternatively a linear regression previously established on various compounds [50] can be used [22,27,52]. For many nuclei, deviations from the theoretically expected slope of minus one have been reported for GIPAW calculations [48] using GGA (generalized gradient approximation) for the exchange and correlation potential. ^{19}F is not an exception with a large dispersion of reported slopes: −0.68 [20], −0.80 [50], 0.86 [49] and 0.83 [21], the last two positive values being obtained when "calculated" and experimental δ_{iso} are compared. Pedone et al. [53] were able to reach a nearly ideal slope value of −0.963 but only on few compounds.

The two binary pentafluorides NbF_5 and TaF_5 are isomorphs and consist of tetrameric structural units $[M_4F_{20}]$ (M=Nb,Ta), build up of MF_6 octahedra linked to each other by corners in a *cis*-configuration. Both the compounds involve six fluorine sites, 2 sites with multiplicity 4 and 4 sites with multiplicity 8 [57,58]. These two compounds, known to be very hygroscopic, have not been yet studied by solid state NMR. In the present work, we report for the first time the one dimensional (1D) ^{19}F magic angle spinning (MAS) NMR spectra of NbF_5 and TaF_5, allowing us to determine their experimental ^{19}F δ_{iso} values. Due to the hygroscopic character and reactivity (chemical attack of the caps of the rotors by NbF_5) of NbF_5 and TaF_5, we choose to avoid ^{19}F–^{19}F correlation experiments since they require long acquisition time. Anyway, in these cases, only fragmentary information could be obtained since some of the fluorine atoms have similar environments and since at least two ^{19}F NMR resonances overlap. Consequently, the only way to complete the initial partial assignment, based on NMR line relative intensities and ^{19}F δ_{iso} and chemical shift anisotropy (δ_{csa}) values, was to perform calculations of the ^{19}F chemical shielding tensors. These DFT (density functional theory) computations have been performed using the GIPAW [45,46] method implemented in the NMR-CASTEP code [59,60]. Since the agreement between the calculated and experimental NMR parameters is generally significantly improved after a DFT structural optimization [16,21,23,31,47–49,51,52,61], GIPAW calculations have been achieved on both experimental and optimized structures. In NbF_5 and TaF_5, however, $[M_4F_{20}]$ units are held together by van der Waals (vdW) interactions and those dispersion forces are not described by most of the exchange-correlation DFT functional used for the GIPAW calculations. A recently proposed method to work around this problem consists in adding a semi-empirical dispersion energy term to the conventional Kohn–Sham DFT energy [62]. For this purpose, structural optimizations were also done with the semi-empirical DFT-D2 approach of Grimme as implemented in the VASP package [63,64]. The semi-empirical parameters needed for describing the three elements under study (F, Nb and Ta) were taken from the work of Grimme [62].

In the present work, we show that GIPAW calculations enable a complete and convincing assignment of the lines of the ^{19}F NMR spectra of NbF_5 and TaF_5. Moreover, the effects of the geometry optimisations are carefully examined and the structural features deeply discussed. Relations are also clearly established between the fluorine chemical shifts and the nature of the fluorine atoms (bridging or terminal), the position of the terminal ones (opposite or perpendicular to the bridging ones), the fluorine Mulliken charges or the ionicity and length of the M–F bonds. Additionally, for three of the ^{19}F NMR lines of NbF_5, distorted multiplets, arising from ^1J-coupling and residual dipolar coupling between the ^{19}F and ^{93}Nb nuclei, were simulated yielding to values of ^{93}Nb–^{19}F ^1J-coupling for the corresponding fluorine sites.

2. Materials and methods

The samples of TaF_5 and NbF_5 were purchased from Alfa Aesar (lot numbers D20L30 and l11T005, respectively) and were kept in a dry glove box under nitrogen atmosphere. As both compounds are very hygroscopic, the rotors were filled inside the glove box to avoid any hydration of the samples.

Solid-state NMR experiments were performed on an Avance 300 Bruker spectrometer operating at 7.0 T (^{19}F Larmor frequency of 282.2 MHz), using a 2.5 mm CPMAS probehead. ^{19}F one dimensional (1D) MAS NMR spectra were recorded using a Hahn echo sequence with an inter-pulse delay equals to one rotor period. The 1D ^{19}F MAS NMR spectra of TaF_5 and NbF_5 were acquired using 90° pulse lengths of 2.6 μs and 2.5 μs (corresponding to nutation frequency of 96 kHz and 100 kHz), respectively. The recycle delay was set to 10 s. Discrimination between isotropic peaks and spinning sidebands was achieved by recording spectra at various spinning frequencies up to 34 kHz. The ^{19}F 1D MAS NMR spectrum of NbF_5 was also acquired with ^{93}Nb decoupling. The influence of the ^{93}Nb power level on the efficiency of the heteronuclear decoupling has been checked in the nutation frequency range 10–357 kHz. High power decoupling (357 kHz) is the most efficient.

The ^{19}F chemical shifts are referenced to $CFCl_3$ at 0 ppm. The ^{19}F 1D MAS NMR spectra of TaF_5 and NbF_5 acquired with ^{93}Nb decoupling were fitted with DMfit [65] software, including spinning sidebands, using four parameters, the isotropic chemical shift (δ_{iso}), the chemical shift anisotropy (δ_{csa}), the asymmetry parameter (η_{csa}), and the Gaussian–Lorentzian shape factor. Reconstructions of the *J*-multiplets observed on the 1D ^{19}F MAS NMR spectra of NbF_5 acquired without ^{93}Nb decoupling have been achieved using WSolids1 [66] software which allows to determine independently the direct dipole–dipole coupling constant and the quadrupolar coupling constant. On the other hand, WSolids1 does not allow to take into account the chemical shift anisotropy.

3. Calculation

The chemical shift tensor is described by three parameters, the isotropic chemical shift (δ_{iso}), the chemical shift anisotropy (δ_{csa}) and the asymmetry parameter (η_{csa}), determined experimentally, and defined as δ_{iso} (ppm) $=(1/3)(\delta_{xx}+\delta_{yy}+\delta_{zz})$, δ_{csa} (ppm) $=\delta_{zz}-\delta_{iso}$, $\eta_{csa}=(\delta_{yy}-\delta_{xx})/\delta_{csa}$, with the principal components defined in the sequence $|\delta_{zz}-\delta_{iso}|\geq|\delta_{xx}-\delta_{iso}|\geq|\delta_{yy}-\delta_{iso}|$.

The chemical shielding tensor is also described by three parameters, the isotropic chemical shielding (σ_{iso}), the chemical shielding anisotropy (σ_{csa}) and the asymmetry parameter (η_{csa}) defined as σ_{iso} (ppm) $=(1/3)(\sigma_{xx}+\sigma_{yy}+\sigma_{zz})$, σ_{csa} (ppm) $=\sigma_{zz}-\sigma_{iso}$ and $\eta_{csa}=(\sigma_{yy}-\sigma_{xx})/\sigma_{csa}$, with the principal components defined in the sequence $|\sigma_{zz}-\sigma_{iso}|\geq|\sigma_{xx}-\sigma_{iso}|\geq|\sigma_{yy}-\sigma_{iso}|$.

For nucleus having spin greater than 1/2, i.e. quadrupolar nuclei, the quadrupolar frequency ν_Q, the quadrupolar coupling constant C_Q and the asymmetry parameter η_Q are related to the electric field gradient (EFG) tensor components through the following equations: $\nu_Q=3\,C_Q/[2I(I-1)]$ with $C_Q=eQV_{zz}/h$, and $\eta_Q=(V_{xx}-V_{yy})/V_{zz}$. The V_{ii} are the eigenvalues of the EFG tensor with the convention $|V_{zz}|\geq|V_{yy}|\geq|V_{xx}|$, e is the electronic charge, I the nuclear spin quantum number and h is Planck's constant.

Ground state electronic structures of NbF_5 and TaF_5 were obtained within the DFT formalism using the PBE-GGA [67] approximation. The atomic position optimizations (APO) and full geometry optimizations (FO, atomic positions and cell parameters) were performed with the ab initio total energy and molecular dynamics VASP program [63]. The projector augmented-wave (PAW) [68,69] pseudopotentials used are the followings: Ta_sv_GW ($5s^2$ $5p^6$ $6s^2$ $5d^3$), Nb_sv_GW ($4s^2$ $4p^6$ $5s^1$ $4d^4$),

F_GW ($2s^2$ $2p^5$). The self-consistency on electronic density was obtained with a 600 eV plane wave energy cut-off and a $(4\times4\times6)$ shifted Monkhorst–Pack k-point mesh (30 k-points in the irreducible part of the Brillouin zone (IBZ)). Atomic positions were optimized by minimizing the residual Hellmann–Feynman forces on the atoms down to 0.02 eV/Å. Since van der Waals interactions are not taken into account on standard DFT-GGA calculations, semi-empirical vdW corrections of Grimme [62] called DFT-D2 were used. The followings (C_6, R_0) atomic parameters were used for the Grimme correction: Ta (81.24, 1.7721), Nb (24.67, 1.639), F(0.75, 1.287).

DFT calculations of the ^{19}F chemical shielding tensors in NbF_5 and TaF_5, using the GIPAW method [45,46] and ^{93}Nb EFG in NbF_5, using the PAW approach [68,69] were performed with the NMR-CASTEP code [59,60] implemented in the Materials Studio 5.0 environment, for the experimental and geometry optimized structures. The core-valence interactions were described by ultra-soft pseudopotentials (USPP) [46]. The USPP were generated using the on the fly generator (OTF_USPP) included in CASTEP. The wave functions were expanded on a plane-wave basis set with a kinetic energy cutoff of 700 eV. The Brillouin zone was sampled using a Monkhorst–Pack grid spacing approximately equal to 0.04 $Å^{-1}$ (corresponding to a k-point mesh of $4\times4\times6$). These calculations were done for the ES, APO, APO-vdW, FO and FO-vdW structures of each compound.

The quadrupolar coupling constants of ^{93}Nb in NbF_5 were calculated using the nuclear quadrupolar moment reported by Pyykkö: $Q(^{93}Nb) = -0.320(20)\times10^{-28}$ m^2 [70].

4. Results and discussion

TaF_5 and NbF_5 are isomorphs and crystallize in a monoclinic cell (space group C2/*m*, $a=9.62$ Å, $b=14.43$ Å, $c=5.12$ Å and $\beta=96.1^\circ$ for NbF_5 [57] (ICSD [71] file no. 26647) and $a=9.5462$ Å, $b=14.3678$ Å, $c=5.0174$ Å and $\beta=97.086^\circ$ for TaF_5 [58] (ICSD [71] file no. 171155)). They consist of tetrameric structural units, $[M_4F_{20}]$, build up of MF_6 octahedra linked to each other by corners in a *cis*-configuration (Fig. 1). The structures of both compounds contain six *F* crystallographic sites, two sites of multiplicity 4 and four sites of multiplicity 8. Fluorine atoms were inappropriately renumbered in the ICSD file of TaF_5; for consistency with NbF_5 [57], we adopt in the following the same numbering as Brewer et al. [58] (see Supporting information). F4 is then the bridging fluorine atom (F_b) for both compounds while others are terminal fluorine atoms (F_t). The M–F–M angles are close to 180°, giving nearly linear bridges and a square arrangement of the MF_6 octahedra (Fig. 1 and Supporting information).

4.1. ^{19}F solid state NMR: Initial partial assignments

More or less resolved multiplets are observed on the ^{19}F 1D MAS NMR spectrum of NbF_5 (Fig. 2). They arise from ^1J-coupling and residual dipolar coupling between the ^{19}F and ^{93}Nb nuclei as shown by their disappearances on the ^{19}F 1D MAS NMR spectrum recorded with ^{93}Nb decoupling. We will discuss these couplings in Section 4.4.

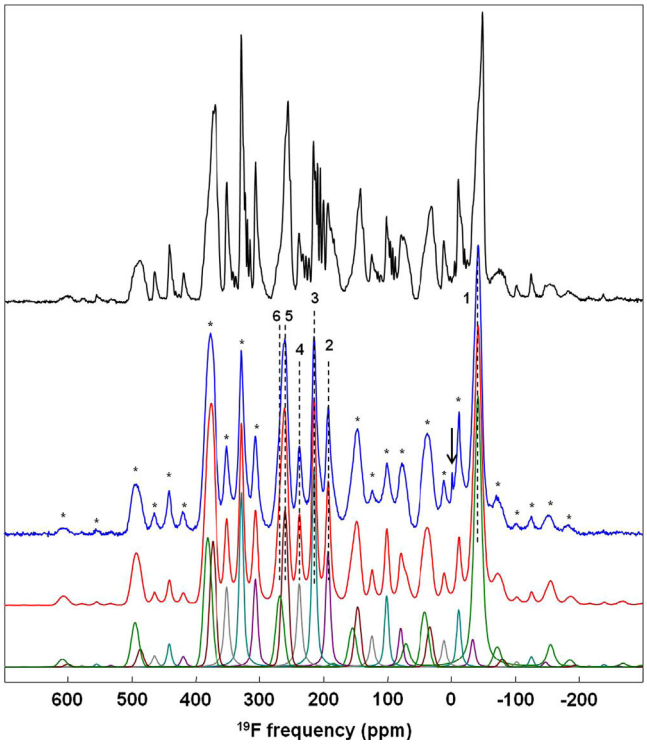

Fig. 2. ^{19}F experimental MAS NMR spectra of NbF_5 obtained at a magnetic field of 7 T and a spinning frequency of 32 kHz with (blue) and without (black) ^{93}Nb decoupling. The best fit of the spectrum recorded with ^{93}Nb decoupling is represented in red and the individual contributions to the fitted spectrum are shown below. The stars indicate spinning sidebands, the dashed lines indicate the positions of the isotropic resonances which are labeled and the arrow indicates an unidentified impurity. (For interpretation of the references to color in this figure legend, the reader is referred to the web version of this article.)

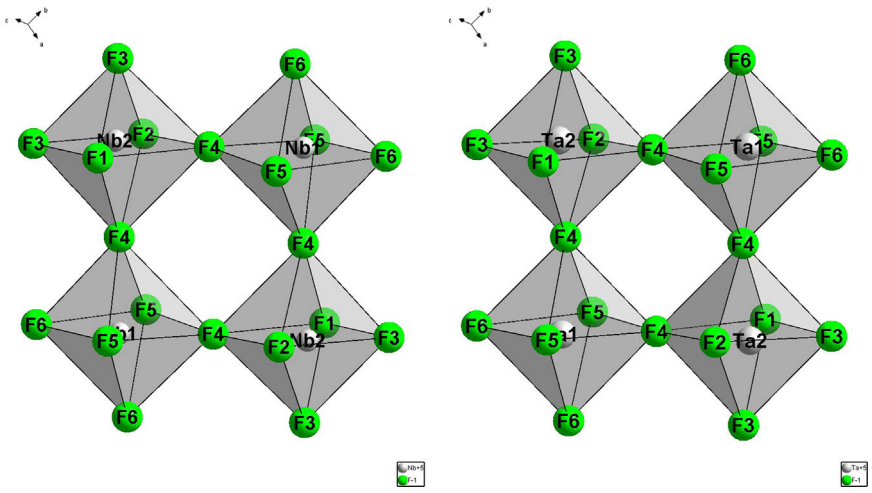

Fig. 1. Perspective views of the tetrameric units of NbF_5 (left) and TaF_5 (right).

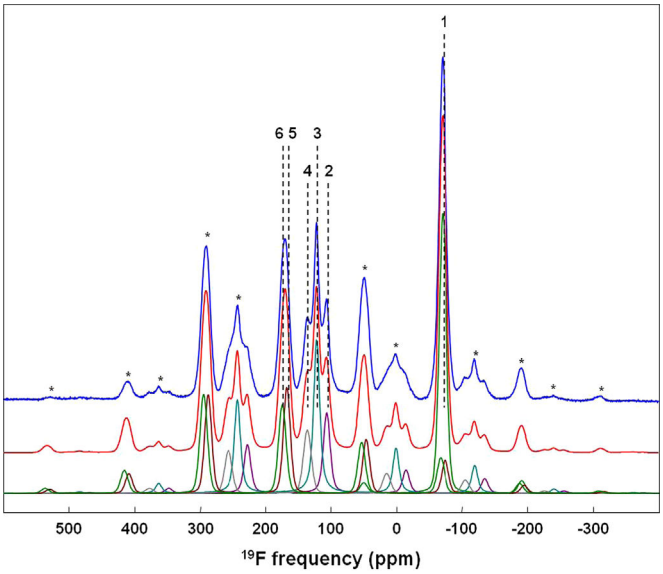

Fig. 3. ^{19}F experimental MAS NMR spectrum (blue) of TaF_5 obtained at a magnetic field of 7 T and a spinning frequency of 34 kHz. The best fit of this spectrum is represented in red and the individual contributions to the fitted spectrum are shown below. The stars indicate spinning sidebands and the dashed lines indicate the positions of the isotropic resonances which are labeled. (For interpretation of the references to color in this figure legend, the reader is referred to the web version of this article.)

For each compound, discrimination between the six expected isotropic lines and spinning sidebands was achieved by recording ^{19}F NMR spectra at various spinning frequencies. Both spectra were fitted (Figs. 2 and 3, Tables 1 and 2) and the relative intensities of the NMR resonances (including spinning sidebands) are in agreement with the presence of two sites of multiplicity 4 and four sites of multiplicity 8 (expected relative intensities of 10% and 20%, respectively). However, the fitting of the spectrum of the NbF_5 compound, the more hygroscopic among the two, is not entirely satisfactory and we cannot exclude the presence of amorphous oxy-hydroxy-fluoride impurities in this sample, in addition to the unidentified impurity indicated on Fig. 2. The uncertainties on the δ_{csa} and η_{csa} values and consequently on the relative intensities of the NMR lines are then larger for NbF_5 compared to TaF_5.

For both spectra, which are similar, according to their relative intensities, lines 1, 3, 5 and 6 can be assigned to the four sites of multiplicity 8 (F3–F6) and lines 2 and 4 to the two sites of multiplicity 4 (F1 and F2). Furthermore, on each spectrum, the NMR line 1, corresponding to a fluorine site of multiplicity 8, has an isotropic chemical shift significantly lower than the five others. It can be straightforwardly assigned to the fluorine site F4 because for each compound F4 is the only F_b among the six F sites and has the expected 8 multiplicity. This assignment is supported by previous liquid ^{19}F NMR studies on $M_2F_{11}^-$ and MF_6^- (M=Nb, Ta) species [72–76], showing that a F_b site has significantly lower chemical shift than a F_t one. The ^{19}F δ_{iso} values of F_b are in the ranges from −42 ppm to −58 ppm for $Nb_2F_{11}^-$ and from −74 ppm to −81 ppm for $Ta_2F_{11}^-$. On the other hand, the ^{19}F δ_{iso} values of F_t in $Nb_2F_{11}^-$ are in the ranges 182–193 ppm and 144–160 ppm for the axial (opposite to the F_b) sites and equatorial (perpendicular to the F_b) ones, respectively. The corresponding ranges in $Ta_2F_{11}^-$ are 115–124 ppm for the axial sites and 70–72 ppm for the equatorial ones. For MF_6^- species that only contain F_t, reported ^{19}F δ_{iso} values are in the ranges 103–104 ppm and 38–40 ppm for NbF_6^- and TaF_6^-, respectively. This assignment is also supported by the ^{19}F δ_{iso} values in NbO_2F and TaO_2F (ReO_3 type structure and only one anionic site partially occupied by O and F) which only contain F_b: −52 ppm [77,78] and −72 ppm [78], respectively. Moreover, the δ_{csa} values of the NMR lines are significantly larger for the F_t (Tables 1 and 2) in agreement with more anisotropic environments for these fluorine atoms (Fig. 1). This assignment (Tables 1 and 2), which is confirmed by the GIPAW calculations (see below), is only inconsistent with the surprising assignments of Köhler et al. [77] for $NbOF_3$ and $TaOF_3$. Those structure have a SnF_4 structural type with sheets of corner sharing MX_6 (X=O, F) octahedra stacked via vdW interactions. They gave the following assignment: the ^{19}F NMR lines with the lowest δ_{iso} (−10.4 ppm and −51.5 ppm) and δ_{csa} values to the F_t and the ^{19}F NMR lines with the highest δ_{iso} (196.3 ppm and 124.2 ppm) and δ_{csa} values to the F_b.

Table 1
Isotropic chemical shift (δ_{iso}, ppm), chemical shift anisotropy (δ_{csa}, ppm), asymmetry parameter of the CSA tensor (η_{csa}) and relative intensity (%) of the ^{19}F NMR resonances in NbF_5. The initial partial line assignments deduced from NMR line relative intensities, ^{19}F δ_{iso} and δ_{csa} values and the final line assignments deduced from σ_{iso} calculations are given.

Line	δ_{iso} (±0.5)	Intensity (±2)	δ_{csa} (±30)	η_{csa} (±0.2)	Initial assignment	Final assignment
1	−42.1	20.0	−110	0.9	F4	F4
2	192.9	11.5	−285	0.1	F1, F2	F2
3	214.8	20.0	−300	0	F3, F5, F6	F5
4	237.8	10.8	−310	0	F1, F2	F1
5	260.0	18.2	−290	0.3	F3, F5, F6	F6
6	268.1	19.5	−410	0.3	F3, F5, F6	F3

Table 2
Isotropic chemical shift (δ_{iso}, ppm), chemical shift anisotropy (δ_{csa}, ppm), asymmetry parameter of the CSA tensor (η_{csa}) and relative intensity (%) of the ^{19}F NMR resonances in TaF_5. The initial partial line assignments deduced from NMR line relative intensities, ^{19}F δ_{iso} and δ_{csa} values and the final line assignments deduced from σ_{iso} calculations are given.

Line	δ_{iso} (±0.5)	Intensity (±1)	δ_{csa} (±20)	η_{csa} (±0.1)	Initial assignment	Final assignment
1	−70.5	19.1	90	0.4	F4	F4
2	106.3	11.2	−277	0	F1, F2	F2
3	121.6	21.0	−277	0.1	F3, F5, F6	F5
4	135.8	9.6	−289	0.1	F1, F2	F1
5	166.9	19.3	−325	0.5	F3, F5, F6	F6
6	173.8	19.8	−350	0.5	F3, F5, F6	F3

4.2. Structural features, effects of geometry optimisation

Geometry optimizations of NbF_5 and TaF_5 were performed with the VASP package [63]. Two kinds of optimizations have been done: either full optimizations (FO) by relaxing both atomic positions and unit cell parameters or atomic position optimizations (APO) only while keeping the experimental unit cell parameters. In these compounds, vdW interactions are responsible for the cohesion between $[M_4F_{20}]$ units but those interactions are not taken into account by DFT which is very problematic when DFT structural optimizations are necessary. Thus, the performance of the semi-empirical DFT-D2 correction of Grimme [62] was here evaluated. When it is used in the optimization procedure, this is explicitly mentioned: namely APO-vdW or FO-vdW. Experimental [57,58], APO and APO-vdW fractional atomic coordinates are given as Supporting information.

For the two compounds under study, the full geometry optimizations lead to large deviations of the unit cell volumes with respect to the experimental ones: a large expansion for FO ($\approx$ 10%) and a large contraction for FO-vdW ($\approx$ −10%). For NbF_5 (TaF_5), the experimental unit cell volume increases from 706.72 Å^3

Table 3
Nb–F and average (in italic) Nb–F_t and Nb–F bond lengths (Å) from ES, APO-vdW and APO structures of NbF_5.

			ES	APO-vdW	APO
Nb1	F5	2*x*	1.778	1.873	1.871
	F6	2*x*	1.803	1.847	1.846
	F4	2*x*	2.064	2.090	2.091
		⟨*Nb1–F*$_t$⟩	*1.790*	*1.860*	*1.859*
		⟨*Nb1–F*⟩	*1.882*	*1.937*	*1.936*
Nb2	F1	1*x*	1.752	1.866	1.863
	F3	2*x*	1.778	1.845	1.844
	F2	1*x*	1.784	1.882	1.881
	F4	2*x*	2.073	2.096	2.097
		⟨*Nb2–F*$_t$⟩	*1.773*	*1.859*	*1.858*
		⟨*Nb2–F*⟩	*1.873*	*1.938*	*1.938*

Table 4
Ta–F and average (in italic) Ta–F_t and Ta–F bond lengths (Å) from ES, APO-vdW and APO structures for TaF_5.

			ES	APO-vdW	APO
Ta1	F6	2*x*	1.840	1.852	1.850
	F5	2*x*	1.857	1.882	1.880
	F4	2*x*	2.074	2.081	2.085
		⟨*Ta1–F*$_t$⟩	*1.848*	*1.867*	*1.865*
		⟨*Ta1–F*⟩	*1.923*	*1.939*	*1.938*
Ta2	F3	2*x*	1.797	1.850	1.847
	F1	1*x*	1.852	1.878	1.873
	F2	1*x*	1.879	1.900	1.888
	F4	2*x*	2.058	2.084	2.090
		⟨*Ta2–F*$_t$⟩	*1.831*	*1.867*	*1.864*
		⟨*Ta2–F*⟩	*1.907*	*1.939*	*1.939*

(682.92 Å^3) to 777.92 Å^3 (753.00 Å^3) with FO and decreases to 659.34 Å^3 (613.86 Å^3) with FO-vdW. Nevertheless, the structural features of the [M_4F_{20}] units are very similar whatever the used optimization procedure (APO, APO-vdW, FO, or FO-vdW). Effectively, the M–F bond lengths are very stable from one optimized structure to another (1.935 Å ≤ ⟨Nb1–F⟩ ≤ 1.939 Å, 1.936 Å ≤ ⟨Nb2–F⟩ ≤ 1.941 Å, 1.934 Å ≤ ⟨Ta1–F⟩ ≤ 1.942 Å, and 1.935 Å ≤ ⟨Ta2–F⟩ ≤ 1.943 Å) with all the time the same ranking (M2–F3 < M1–F6 < M2–F1 < M1–F5 < M2–F2 < M1–F4 < M2–F4). The APO and APO-vdW distances are reported in Table 3 for NbF_5 and Table 4 for TaF_5. As mentioned above, semi-empirical DFT-D2 corrections have the most noticeable effect on the fully optimized structures, avoiding large increase of unit cell volumes (i.e. large increase of distances between [M_4F_{20}] units) for FO structures, but leading to unrealistic small unit cell volume for FO-vdW structures. As the DFT-D2 approach overcorrects the problem of volume expansion related to the bad description of the vdW interactions with DFT, neither FO nor FO-vdW structures will be considered in the following. The shortcomings of this approach are meaningless for APO-vdW structures (for which the unit cell volumes are fixed) since inside the [M_4F_{20}] units the M–F distances are enforced by the strongest M–F covalent interactions.

Focussing now on the relaxation effects with respect to the experimental structures (Tables 3 and 4), named ES in the following, significant evolutions of the distances are observed on the [M_4F_{20}] units, especially for the NbF_5 compound. The TaF_5 compound is effectively more weakly affected by the relaxation with only a small increasing of all the Ta–F bond lengths (less than 3%). The ordering of the Ta–F bond lengths is also maintained except a slight inversion between Ta1–F4 and Ta2–F4. On the contrary, for the NbF_5 compound, the increase of the M–F bond lengths is more pronounced (up to 6.5%) with large displacements of the fluorine atoms (between 0.10 Å and 0.15 Å, see Tables S2 and S3 in Supplementary material) and the ordering of the Nb–F bond lengths is not maintained (only Nb1–F4 and Nb2–F4 bond lengths are in the same order before and after atomic position optimization). However, for both the compounds, the relaxation step leads to a smaller dispersion of the M–F bond lengths in the MF_6 octahedra and very comparable ⟨M–F⟩ bond lengths between TaF_5 and NbF_5 (Tables 3 and 4). Those evolutions can reasonably well be attributed to the intrinsic overestimation of interatomic distances by the PBE-GGA [67] in the case of TaF_5 but the lack of accuracy of the experimental structural data has to be invoked in the case of NbF_5. Indeed, the structures of both the compounds were determined by Edwards [57] on single crystals but the structure of TaF_5 has been re-evaluated, in 2006, by Brewer et al. [58] who show that the initial crystallographic determination was inaccurate. In particular, the ⟨Ta–F_t⟩ bond length is equal to 1.840 Å (Table 4) and the Ta1–F4–Ta2 angle is equal to 172.9° [58] (see Supplementary material) compared to 1.779 Å and 176.7° in the initial work [57]. The re-evaluation of the structure of TaF_5 then led to larger Ta–F_t bond lengths, ranging now from 1.80 Å to 1.88 Å (Table 4), in fine agreement with Ta–F_t bond lengths in $(ClF_2)(TaF_6)$ (1.82 Å and 1.88 Å) [79], $Ag(TaF_6)_2$ (from 1.82 Å to 1.87 Å) [80] and $Cd(BF_4)(TaF_6)$ (1.85 Å) [81]. The re-evaluation of the structure of NbF_5 remains to be done but the Nb–F_t bond lengths, ranging from 1.75 Å to 1.80 Å, are clearly too short compared to Nb–F_t bond lengths in $(ClF_2)(NbF_6)$ (1.85 Å and 1.86 Å) [79], $(XeF_5)(NbF_6)$ (1.84 Å and 1.85 Å) [82], $NbSbF_{10}$ (from 1.79 Å to 1.83 Å) [83] and $SeNb_2F_{14}$ (from 1.78 Å to 1.86 Å) [84].

The effects of optimization on F–M–F and M–F_b–M angles (see Supplementary material) are small for TaF_5. The angular distortions $\alpha = (1/12)\sum_{i=1}^{n}|\alpha_i - 90°|$ and $\beta = (1/3)\sum_{i=1}^{n}|\beta_i - 180°|$, with α_i the twelve angles between two adjacent M–F bonds and β_i the three angles between two opposite M–F bonds, are only slightly reduced (ES: α=5.1° and 5.8°, β=10.2° and 10.7°; APO-vdw: α=4.9° and 5.1°, β=10.1° and 10.6°; APO: α=4.8° and 5.3°; β=9.9° and 10.9°). For NbF_5, the evolutions of those angles are found to be more pronounced due to the inaccuracy of the experimental structure (ES: α=5.1° and 3.6°, β=9.1° and 7.6°; APO-vdw: α=5.0° and 5.3°, β=9.9° and 10.7°; APO: α=5.1° and 5.4°; β=9.8° and 10.8°). The value of the Nb1-F4-Nb2 angle decreases from 176.7° for ES to 173.5° or 173.8° for the APO-vdW or APO structures, respectively, and is now close to the equivalent angle in TaF_5. This is another evidence of the inaccuracy of the experimental structure of NbF_5.

Two distinct sets of M–F_t bond are observed in NbF_5 and TaF_5 (Fig. 1). The M–F_t bonds within the plane containing the M atoms and their bridging F atoms, M2–F3 and M1–F6, could be termed as equatorial while the M–F_t bonds perpendicular to this plane, M2–F1, M2–F2 and *M*1–F5, could be termed as axial [58,85]. However, these terms are potentially misleading in the context of this paper since axial (equatorial) F are opposite (perpendicular) to the M–F_b bond in $M_2F_{11}^-$ units and perpendicular (opposite) to both M–F_b bond in [M_4F_{20}] units. The terms opposite (M–$F_{t,opp}$) and perpendicular (M–$F_{t,per}$) are then used to distinguish the M–F_t bonds in the following. The M–$F_{t,opp}$ (M2–F3 and M1–F6) bonds are shorter than the M–$F_{t,per}$ (M2–F1, M2–F2 and M1–F5) bonds, except for the ES of NbF_5, in relation with its inaccuracy. Shorter M–$F_{t,opp}$ bonds also occur in RuF_5 [85] which adopts a different structural type but contains similar tetrameric [M_4F_{20}] units. The observed shortening of the trans set of terminal M–F bond lengths is due to the contraction toward the M atom of the electron clouds proximate to the M atom and in the same plane as the M atom and its bridging F ligands. This trans electrostatic effect is explained by the fact that the bridging F ligands are more electron rich than their non-bridging counterparts [85]. This is a kind of polarization mechanism where a more ionic and longer M–F_b bond of the MF_6 octahedron induces a more covalent and shorter M–$F_{t,opp}$ in the opposite direction (see Section 4.3).

Table 5
Experimental (exp.) ^{19}F δ_{iso} (ppm), δ_{csa} (ppm) and η_{csa} and calculated (calc.) ^{19}F σ_{iso} (ppm), δ_{iso} (ppm), σ_{csa} (ppm) and η_{csa} from the ES, APO and APO-vdw structures of NbF_5. The calculated ^{19}F δ_{iso} values were deduced from the relationships $\delta_{iso} = -1.107\ \sigma_{iso} + 158.6$, $\delta_{iso} = -1.028\ \sigma_{iso} + 100.4$ and $\delta_{iso} = -1.027\ \sigma_{iso} + 100.3$ for the ES, APO and APO-vdw structures, respectively.

F site		σ_{iso}	δ_{iso}	$\delta_{csa}/\sigma_{csa}$	η_{csa}
F1	exp.		237.8	−310	0.0
	calc. ES	−49.7	213.6	321.3	0.11
	calc. APO	−131.5	235.6	382.4	0.01
	calc. APO-vdW	−129.7	233.5	383.7	0.03
F2	exp.		192.9	−285	0.1
	calc. ES	−35.4	197.8	332.7	0.10
	calc. APO	−89.7	192.6	349.9	0.00
	calc. APO-vdW	−90.2	192.9	350.6	0.03
F3	exp.		268.1	−410	0.3
	calc. ES	−94.2	262.9[a]	338.6[a]	0.62[a]
	calc. APO	−163.9	268.9	409.8	0.35
	calc. APO-vdW	−165.1	269.9	410.3	0.36
F4	exp.		−42.1	−110	0.9
	calc. ES	180.2	−40.9	−119.2	0.79
	calc. APO	138.4	−41.9	−130.3	0.96
	calc. APO-vdW	138.2	−41.6	129.3	0.97
F5	exp.		214.8	−300	0.0
	calc. ES	−64.0	229.4	338.6	0.10
	calc. APO	−111.3	214.8	369.8	0.04
	calc. APO-vdW	−111.2	214.5	370.9	0.03
F6	exp.		260.0	−290	0.3
	calc. ES	−99.6	268.9[a]	348.1[a]	0.58[a]
	calc. APO	−156.8	261.6	400.4	0.37
	calc. APO-vdW	−158.1	262.7	401.5	0.38

[a] For the ES structure, the assignment of F3 and F6 fluorine atoms to the NMR lines L6 and L5 must be reversed.

Table 6
Experimental (exp.) ^{19}F δ_{iso} (ppm), δ_{csa} (ppm) and η_{csa} and calculated (calc.) ^{19}F σ_{iso} (ppm), δ_{iso} (ppm), σ_{csa} (ppm) and η_{csa} from the ES, APO and APO-vdw structures of TaF_5. The calculated ^{19}F δ_{iso} values were deduced from the relationships $\delta_{iso} = -0.803\ \sigma_{iso} + 101.6$, $\delta_{iso} = -0.777\ \sigma_{iso} + 86.2$ and $\delta_{iso} = -0.778\ \sigma_{iso} + 86.0$ for the ES, APO and APO-vdw structures, respectively.

F site		σ_{iso}	δ_{iso}	$\delta_{csa}/\sigma_{csa}$	η_{csa}
F1	exp.		135.8	−289	0.1
	calc. ES	−43.4	136.5	273.6	0.01
	calc. APO	−62.9	135.1	298.2	0.05
	calc. APO-vdW	−58.8	131.7	297.7	0.03
F2	exp.		106.3	−277	0
	calc. ES	10.1	93.5	235.6	0.03
	calc. APO	−22.5	103.7	266.5	0.08
	calc. APO-vdW	−23.1	104.0	267.2	0.04
F3	exp.		173.8	−350	0.5
	calc. ES	−86.2	170.8[a]	323.3[a]	0.26[a]
	calc. APO	−115.0	175.5	347.5	0.35
	calc. APO-vdW	−115.9	176.2	347.7	0.36
F4	exp.		−70.5	90	0.4
	calc. ES	210.5	−67.4	−74.5	0.25
	calc. APO	199.8	−69.0	−84.7	0.39
	calc. APO-vdW	198.9	−68.7	−82.7	0.44
F5	exp.		121.6	−277	0.1
	calc. ES	−31.4	126.8	276.0	0.07
	calc. APO	−41.7	118.6	286.4	0.08
	calc. APO-vdW	−43.6	119.9	287.6	0.07
F6	exp.		166.9	−325	0.5
	calc. ES	−89.5	173.5[a]	321.5[a]	0.44[a]
	calc. APO	−107.8	169.9	337.4	0.40
	calc. APO-vdW	−109.3	171.0	339.3	0.39

[a] For the ES structure, the assignment of F3 and F6 fluorine atoms to the NMR lines L6 and L5 must be reversed.

4.3. *GIPAW calculations of the ^{19}F chemical shielding tensors: Complete and unique assignment and chemical bond analysis*

In order to complete the initial partial assignments (see Section 4.1), the ^{19}F chemical shielding tensors have been calculated using the GIPAW method [45,46] implemented in the NMR-CASTEP code [59,60]. As expected, the experimental and APO/APO-vdW structures provide dissimilar ^{19}F σ_{iso} values (Tables 5 and 6), especially for NbF_5 (up to 80 ppm), while ^{19}F σ_{iso} values calculated from APO and APO-vdW structures are nearly identical (differences up to 4 ppm but most often lower than 1 ppm). This is in agreement with the structural differences and similarities described previously (see Section 4.2). As already noted, the full optimized structures are not considered in this part but the reader should be aware that, due to the similarities of the $[M_4F_{20}]$ units, the ^{19}F chemical shielding tensors calculated from the FO and FO-vdW structures are similar to those calculated from the APO and APO-vdW structures.

To assign the ^{19}F resonances to the fluorine crystallographic sites, the NMR lines are ranked in increasing order of experimental δ_{iso} values and F atoms are ranked in decreasing order of calculated σ_{iso} values. Except for the ES of NbF_5, the fine agreement obtained between the relative intensities of the NMR lines (2, 1, 2, 1, 2, 2) and the multiplicities (8, 4, 8, 4, 8, 8) of the F atoms (Tables 1, 2, 5 and 6) allow us to propose complete assignments. The inaccuracy of the experimental structure of NbF_5 leads to a disagreement between the multiplicities (8, 4, 4, 8, 8, 8) of the F atoms (F4, F2, F1, F5, F3, F6) and the relative intensities of the NMR lines. The achieved assignments are not exactly identical for the experimental and atomic position optimized structures since, for both compounds, F3 and F6 atoms, which have the same multiplicity, are reversed in the sequence of calculated σ_{iso} values from ES ($\sigma_{iso}(F3) > \sigma_{iso}(F6)$) and APO or APO-vdW ($\sigma_{iso}(F6) > \sigma_{iso}(F3)$) structures.

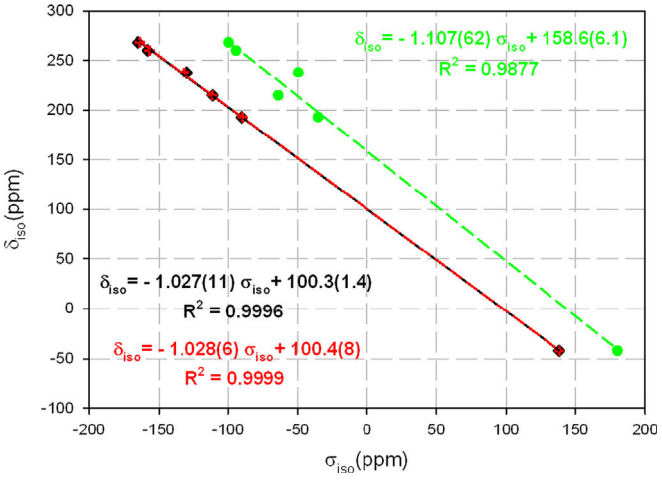

Fig. 4. Calculated ^{19}F σ_{iso} values versus experimental ^{19}F δ_{iso} values for NbF_5. The green circles, the black diamonds and the red plus represent the calculated values from ES, APO-vdW and APO structures, respectively. The dash green line, the solid black line and the dash red line represent the linear regressions when considering the calculated values from ES, APO-vdW and APO structures, respectively. Their equations are given in green, black and red, respectively. (For interpretation of the references to color in this figure legend, the reader is referred to the web version of this article.)

Except for the GIPAW calculations achieved with the experimental structure of NbF_5, very good linear correlations are observed between the calculated ^{19}F σ_{iso} values and the experimental ^{19}F δ_{iso} values (Figs. 4 and 5). The coefficients of determination, R^2, are better for APO and APO-vdW structures than for the experimental ones, even for TaF_5. As the linearity between

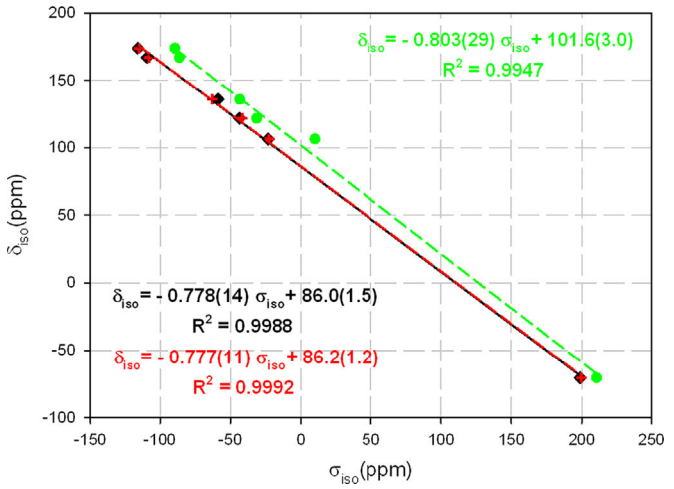

Fig. 5. Calculated ^{19}F σ_{iso} values versus experimental ^{19}F δ_{iso} values for TaF_5. The green circles, the black diamonds and the red plus represent the calculated values from ES, APO-vdW and APO structures, respectively. The dash green line, the solid black line and the dash red line represent the linear regressions when considering the calculated values from ES, APO-vdW and APO structures, respectively. Their equations are given in green, black and red, respectively. (For interpretation of the references to color in this figure legend, the reader is referred to the web version of this article.)

experimental ^{19}F δ_{iso} values and calculated ^{19}F σ_{iso} values ensures spectral assignments, we retain the assignments achieved from the atomic position optimized structures. The "calculated" ^{19}F δ_{iso} values (Tables 5 and 6) are obtained by using, for each structure, the linear regression established between GIPAW calculated ^{19}F σ_{iso} values and experimental ^{19}F δ_{iso} values. The agreement between experimental and "calculated" ^{19}F δ_{iso} values is, obviously, very good. The slopes obtained from APO and APO-vdW structures of NbF_5 (Fig. 4) are close to -1, i.e., the theoretical expected value, whereas those obtained from APO and APO-vdW structures of TaF_5 (Fig. 5) are equal to -0.777 and -0.778. The linear regression obtained for TaF_5 is however very close to the one established on numerous binary fluoride compounds ($\delta_{iso}=-0.80(3)\ \sigma_{iso}+89(9)$) [50], correlation which has been successfully applied for prediction of ^{19}F δ_{iso} values of various compounds such as $RbLaF_4$ [22], α-$LaZr_2F_{11}$ [27] and $NaAsF_6$ [52]. Thus, for TaF_5, this more general linear regression can also be used to predict the "calculated" δ_{iso} values with a good accuracy. Nevertheless, this study unfortunately shows that this linear regression cannot be systematically used and confirms the difficulty to predict "calculated" δ_{iso} values from PBE-DFT calculations since excellent but dissimilar correlations are established for each compound.

In the previous section, the M–F_t bonds have been discriminated as opposite (M–$F_{t,opp}$, F3 and F6) and perpendicular (M–$F_{t,per}$, F1, F2 and F5) to M–F_b bonds. The ^{19}F δ_{iso} values of the $F_{t,opp}$ are larger than the ^{19}F δ_{iso} values of the $F_{t,per}$. This is in agreement with larger ^{19}F δ_{iso} values for the axial F_t (opposite to F_b) in the $Nb_2F_{11}^-$ and $Ta_2F_{11}^-$ anions (see Section 4.1) [72–76]. Then in $[M_4F_{20}]$ units and $M_2F_{11}^-$ anions, the F_t atoms opposite to the M–F_b bonds have weaker shieldings. This is supported by the absolute values of the fluorine Mulliken charges which are in the sequence $F_b > F_{t,per} \geq F_{t,opp}$ and the M–F bond overlap populations which are in the sequence M–F_b < M–$F_{t,per} \leq$ M–$F_{t,opp}$, in NbF_5 and TaF_5, for experimental and atomic position optimized structures (see Supplementary material). Except for the experimental structure of NbF_5, the M–F_t bonds opposite to the M–F_b bonds are shorter than the M–F_t bonds perpendicular to the M–F_b bonds in the $[M_4F_{20}]$ units (Tables 3 and 4). This is also the case in the $M_2F_{11}^-$ anions (Nb–F_b=2.092–2.103 Å, Nb–$F_{t,opp}$=1.862–1.875 Å, Nb–$F_{t,per}$=1.895–1.898 Å [86]; Ta–F_b=2.066 Å, Ta–$F_{t,opp}$=1.855 Å, Ta–$F_{t,per}$=1.877 Å [87]). Moreover, for NbF_5 and TaF_5, good linear correlations are observed between the experimental ^{19}F δ_{iso} values (or the calculated ^{19}F σ_{iso} values) of F_t atoms and the optimized F_t–M bond lengths (see Supplementary material). But the ^{19}F δ_{iso} values (or the ^{19}F σ_{iso} values) of F_t atoms and F_t–M bond lengths both result from their positions compared to the more ionic and longer F_b–M bonds, the F_t atoms in opposite position being less negatively charged and then less shielded. The calculation done on the experimental structure of NbF_5 shows unambiguously that the F_t–M bond lengths is a consequence since, for this structure, the shortest bond lengths do not correspond to the Nb–$F_{t,opp}$ bonds whereas the lowest ^{19}F σ_{iso} values are observed to the $F_{t,opp}$ atoms (F3 and F6, Tables 3 and 5).

Table 7
Calculated C_Q (MHz) and η_Q values from the ES, APO and APO-vdw structures of NbF_5.

		ES	APO	APO-vdW
Nb1	C_Q	174.1	103.0	102.6
	η_Q	0.29	0.17	0.18
Nb2	C_Q	193.4	101.6	102.0
	η_Q	0.12	0.19	0.24

For APO and APO-vdW structures of TaF_5, the experimental δ_{csa} values and the calculated σ_{csa} values (Table 6) are, as expected, in inverse order. These values not only allow, as outlined in Section 4.1, to differentiate the F_b and the F_t atoms but also, to differentiate the $F_{t,opp}$ atoms and the $F_{t,per}$ atoms. Moreover, a nice agreement is obtained between the experimental δ_{csa} absolute values and the calculated σ_{csa} values (Table 6). Such agreement obtained without applying any scaling factor, whereas the slope of the linear regression determined from the calculated ^{19}F σ_{iso} values and the experimental ^{19}F δ_{iso} values deviates from -1, is somewhat surprising. The agreement between experimental and calculated η_{csa} values is satisfactory, considering the lower accuracy of the experimental values and the difficulty to accurately reproduce this parameter due to its intrinsic definition. Owing to inaccurate experimental values (see Section 4.1), the agreement between the experimental δ_{csa} absolute values and the calculated σ_{csa} values is not so good for NbF_5 (Table 5). Nonetheless, the calculated σ_{csa} values seem to be overestimated and a scaling factor around -0.8 would be necessary to reproduce the experimental δ_{csa} values whereas the slope of the linear regression determined from the calculated ^{19}F σ_{iso} values and the experimental ^{19}F δ_{iso} values is found close to -1. One can note that for F4, due to similar $|\sigma_{zz}-\sigma_{iso}|$ and $|\sigma_{xx}-\sigma_{iso}|$ values, the sign of σ_{csa} is not the same for APO and APO-vdW structures and is then uncertain (Table 5).

4.4. ^{93}Nb quadrupolar parameters and ^{93}Nb–^{19}F ^1J-coupling in NbF_5

The calculated ^{93}Nb quadrupolar parameters in NbF_5 for ES, APO and APO-vdW structures, are gathered in Table 7. The agreement is satisfying between calculated values from APO or APO-vdW structures and previously determined values from nuclear quadrupole resonance by Fuggle et al. [88] (C_Q= 115.8 MHz, η_Q=0.13 and C_Q=114.3 MHz, η_Q=0.17) and by Segel [89] (C_Q=115.5 MHz, η_Q=0.13 and C_Q=114.1 MHz, η_Q=0.17). This confirms the inaccuracy of the experimental structure and the efficiency of the atomic position optimizations. The closeness of the C_Q and η_Q values determined and calculated for both the sites prevents any assignment.

The distorted multiplet patterns observed for lines 2 (F2), 3 (F5) and 4 (F1) in the ^{19}F NMR spectrum of NbF_5 recorded without decoupling indicates the occurrence of ^1J-coupling between ^{93}Nb and ^{19}F (Figs. 2 and 6). Since F2, F5 and F1 atoms are bonded to one neighbouring niobium atom and since ^{93}Nb is a spin 9/2 nucleus, 10 peaks should be observed. The peaks are not so numerous

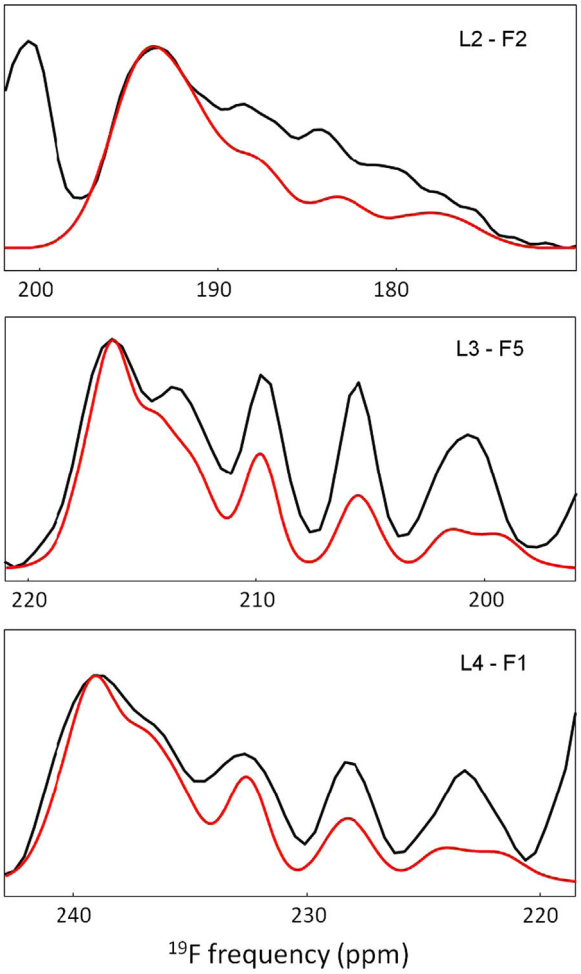

Fig. 6. Experimental (black) and simulated (red) ^{19}F NMR lines 2, 3 and 4 of NbF_5 (magnetic field of 7 T, spinning frequency of 32 kHz, recorded without ^{93}Nb decoupling) showing ^{19}F–^{93}Nb *J*-coupling for the three fluorine sites F2, F5 and F1, respectively. (For interpretation of the references to color in this figure legend, the reader is referred to the web version of this article.)

Table 8
Simulation results of the ^{19}F NMR line 2, 3 and 4 of NbF_5: ^{19}F–^{93}Nb ^1J-coupling (Hz), dipolar/quadrupolar cross term D' (Hz), ^{19}F δ_{iso} (ppm), ^{93}Nb C_Q (MHz) and η_Q, and polar angle β^D (°) of the dipolar tensor in the principal axes system of the EFG tensor.

Line (F site)	^1J (±5)	D' (±100)	δ_{iso} (±0.5)	C_Q (±5)	η_Q (±0.2)	β^D (±5)
2 (F2)	350	4400	189.8	115	0.2	15
3 (F5)	355	4100	212.0	105	0.2	5
4 (F1)	350	4300	234.8	115	0.2	15

and not evenly spaced, due to effective dipolar coupling which induces shifts and broadening. In the present case where $C_Q/(4S(2S-1)) \ll \nu_{0S}$ (ν_{0S} being the Larmor frequency of the quadrupolar nucleus *S*), the frequency shifts of the multiplet components can be calculated using the first order perturbation treatment [90] implemented in Wsolids1 software [66]. The effective dipolar coupling constant, D', depends on the dipolar coupling constant D and on the *J*-coupling anisotropy, ΔJ, according to $D' = D - \Delta J/3$ and assuming axially symmetric *J*-tensor with its unique axis directed along the bond vector, i.e., collinear with the dipolar tensor. The parameters used for the reconstructions of the multiplets (Fig. 6) are gathered in Table 8. The *J*-coupling anisotropy and the azimuthal angle of the dipolar vector with respect to the EFG tensor, α^D, have no observable effects on the ^{19}F spectra. The η_Q values are difficult to determine precisely, having slight effect on the ^{19}F spectra. These values have then been fixed equal to 0.2, close to the determined and calculated ones (Table 7). The ^{93}Nb C_Q values, 105 MHz for Nb1 bonded to F5 and 115 MHz for Nb2 bonded to F1 and F2 (Fig. 1), are in good agreement with the calculated and previously determined values (Table 7). The effective dipolar coupling constants D' are, since $D \gg \Delta J/3$, of the same magnitude as the dipolar coupling constants D calculated from the following formula $D = (\mu_0 \gamma_I \gamma_s \hbar/8\pi^2) r_{IS}^{-3}$, with γ_I and γ_S the gyromagnetic ratios of the *I* and *S* nuclei, respectively, and r_{IS} the distances between these nuclei; using the Nb–F bond lengths from APO structures, the *D* values range from 4100 to 4300 Hz. The experimental ^{93}Nb–^{19}F ^1J-coupling values (Table 8) are similar to reported values, for terminal fluorine atoms, from solution NMR experiments on $NbF_5.2(CH_3)_2SO$ (335 Hz, five-coordinated Nb) [91] and NbF_6^- (from 305 Hz to 345 Hz, six-coordinated Nb) [73–75,92,93] as well as from solid state NMR experiments on $Cdpy_4NbOF_5$ (362 Hz, six-coordinated Nb) [94] and $[pyH]_2Cdpy_4(NbOF_5)_2]$ (350 Hz, six-coordinated Nb) [94]. The experimental ^{93}Nb–^{19}F ^1J-coupling values are also similar to reported values for non-bridging fluorine atoms bonded to six-coordinated niobium atoms in $CsNbF_6$ (344 Hz) [95]. As expected, they are larger than the reported value in K_2NbF_7 (204 Hz) [96] where Nb is in a heptacoordinate (capped trigonal prism) arrangement.

For the lines 5 and 6 of the ^{19}F NMR spectrum of NbF_5 recorded without decoupling (Fig. 2), assigned to $F_{t,opp}$ atoms, the multiplets are not sufficiently resolved, due to their overlapping, to enable confident reconstruction. For the line 1, assigned to F_b (F4), the occurrence of ^1J-coupling between ^{93}Nb and ^{19}F, results in an asymmetric line shape but no resolved multiplet. The ^1J-coupling between the F_b and Nb atoms must be smaller, resulting from the longer Nb–F_b bond in comparison to the Nb–F_t bonds.

5. Conclusions

The ^{19}F δ_{iso} values in NbF_5 and TaF_5 are determined from the reconstruction of 1D ^{19}F MAS NMR spectra. An initial partial assignment is achieved, based on NMR line relative intensities and δ_{iso} values previously determined in several compounds containing also bridging and terminal fluorine atoms bonded to Nb and Ta atoms.

The atomic position optimizations and full geometry optimizations were performed using the VASP package [63] with and without vdW corrections (i.e. with and without using the semi-empirical DFT-D2 approach [62]). Even if the structural features of the $[M_4F_{20}]$ units are similar for all the optimized structures, the structures obtained after full geometry optimizations result in unrealistic unit cell volumes and are not further discussed. The shortcomings of this approach are meaningless for APO-vdW structures since inside the $[M_4F_{20}]$ units the M–F distances are enforced by the strongest M–F covalent interactions.

The ^{19}F chemical shielding tensors have been calculated using the GIPAW method [45,46] implemented in the NMR-CASTEP code [59,60]. The experimental and atomic position optimized structures provide dissimilar ^{19}F σ_{iso} values, especially for NbF_5, while ^{19}F σ_{iso} values calculated from APO and APO-vdW structures are nearly identical. The fine agreement obtained, from APO and APO-vdW structures, between the relative intensities of the NMR lines ranked in increasing order of experimental δ_{iso} values and the multiplicities of the F atoms ranked in decreasing order of calculated σ_{iso} values allows us to propose complete assignments of the ^{19}F resonances to the fluorine crystallographic sites. Very good linear correlations are observed between the experimental ^{19}F δ_{iso} values and the calculated ^{19}F σ_{iso} values, ensuring that the spectral assignments are done convincingly. The slopes obtained

from APO and APO-vdW structures are close to of -1 for NbF_5, i.e., the theoretical expected value, and -0.78 for TaF_5, a slope similar to those of the linear regression established on numerous binary fluoride compounds [50] and successfully applied [22,27,52] since then. This study unfortunately confirms the difficulty to predict calculated δ_{iso} values from PBE-DFT calculations since excellent but dissimilar correlations are established for each compound.

The absolute values of the fluorine Mulliken charges are in the sequence $F_b > F_{t,per} \geq F_{t,opp}$ and the M–F bond populations are in the sequence $M–F_b < M–F_{t,per} \leq M–F_{t,opp}$. Consequently, the $M–F_t$ bonds opposite to the $M–F_b$ bonds are shorter than the $M–F_t$ bonds perpendicular to the $M–F_b$ bonds and the F_t atoms opposite to the $M–F_b$ bonds have larger ^{19}F δ_{iso} values, i.e., weaker shieldings. The ^{19}F δ_{iso} values (or the ^{19}F σ_{iso} values) of F_t atoms and F_t–M bond lengths then result from their positions compared to the more ionic and longer F_b–M bonds.

The calculated ^{93}Nb quadrupolar parameters for APO and APO-vdW structures of NbF_5 are in agreement with previously determined values [88,89] but the closeness of the C_Q and η_Q values determined and calculated for both the sites prevents any assignment. For three lines of the ^{19}F NMR spectrum of NbF_5 recorded without decoupling, the effective dipolar coupling constant, the $^{93}Nb–^{19}F$ ^1J-coupling and the ^{93}Nb C_Q values have been determined. The $^{93}Nb–^{19}F$ ^1J-coupling values are similar to previously reported values for non-bridging fluorine atoms bonded to six-coordinated niobium atoms and the ^{93}Nb C_Q values are in good agreement with the calculated and previously determined values.

To conclude, this study shows the strong potential of GIPAW calculations for assignment of ^{19}F NMR spectra of crystalline fluoride compounds having multiple crystallographic sites but also for their structural and electronic characterizations.

Acknowledgments

The authors thank the Région Pays de la Loire for the financial support of the RMN3MPL project, especially M. Biswal (doctoral grant) and A. Sadoc (post-doctoral fellowship). The computational presented in this work have been carried out at the Centre Régional de Calcul Intensif des Pays de la Loire (CCIPL), financed by the French Research Ministry, the Région Pays de la Loire, and Nantes University. We thank CCIPL for CASTEP licenses financial support.

Appendix A. Supplementary Material

Supplementary data: experimental, APO-vdW and APO fractional atomic coordinates for NbF_5 and TaF_5, F-M-F and M-F-M angles, ^{19}F δ_{iso}, F Mulliken charge, M-F bond population and M-F bond length from ES, APO and APO-vdW structures of NbF_5 and TaF_5, optimized F_t-M bond lengths versus experimental ^{19}F δ_{iso} values for NbF_5 and TaF_5.

Supplementary data associated with this article can be found in the online version at http://dx.doi.org/10.1016/j.jssc.2013.09.001.

References

[1] J.M. Miller, Prog. Nucl. Magn. Reson. Spectrosc 28 (1996) 255–281.
[2] B. Bureau, G. Silly, J.-Y. Buzaré, J. Emery, C. Legein, C. Jacoboni, J. Phys. Condens. Matter 9 (1997) 6719–6736.
[3] L.-S. Du, F. Wang, C.P. Grey, J. Solid State Chem. 140 (1998) 285–294.
[4] B. Bureau, G. Silly, J.-Y. Buzaré, C. Jacoboni, J. Non-Cryst. Solids 258 (1999) 110–118.
[5] Q. Zeng, J.F. Stebbins, Am. Mineral. 85 (2000) 863–867.
[6] J.F. Stebbins, Q. Zeng, J. Non-Cryst. Solids 262 (2000) 1–5.
[7] J.C.C. Chan, H. Eckert, J. Non-Cryst. Solids 284 (2001) 16–21.
[8] R.E. Youngman, M.J. Dejneka, J. Am. Ceram. Soc. 85 (2002) 1077–1082.
[9] S. Chaudhuri, F. Wang, C.P. Grey, J. Am. Chem. Soc. 124 (2002) 11746–11757.
[10] T.J. Kiczenski, J.F. Stebbins, J. Non-Cryst. Solids 306 (2002) 160–168.
[11] T.J. Kiczenski, L.-S. Du, J.F. Stebbins, J. Non-Cryst. Solids 337 (2004) 142–149.
[12] R.E. Youngman, S. Sen, Solid State Nucl. Magn. Reson. 27 (2005) 77–89.
[13] C.D. Martin, S. Chaudhuri, C.P. Grey, J.B. Parise, Am. Mineral. 90 (2005) 1522–1533.
[14] T.M. Alam, J.S. Clawson, F. Bonhomme, S.G. Thomas, M.A. Rodriguez, S. Zheng, J. Autschbach, Chem. Mater. 20 (2008) 2205–2217.
[15] C. Martineau, F. Fayon, C. Legein, J.-Y. Buzaré, G. Silly, D. Massiot, Chem. Commun. (2007) 2720–2722.
[16] C. Martineau, F. Fayon, C. Legein, J.-Y. Buzaré, M. Body, D. Massiot, F. Goutenoire, Dalton Trans. (2008) 6150–6158.
[17] C. Martineau, F. Fayon, C. Legein, J.-Y. Buzaré, F. Goutenoire, E. Suard, Inorg. Chem. 47 (2008) 10895–10905.
[18] C. Martineau, C. Legein, J.-Y. Buzaré, F. Fayon, Phys. Chem. Chem. Phys. 11 (2009) 950–957.
[19] Q. Wang, B. Hu, F. Fayon, J. Trébosc, C. Legein, O. Lafon, F. Deng, J.-P. Amoureux, Phys. Chem. Chem. Phys. 11 (2009) 10391–10395.
[20] J.M. Griffin, J.R. Yates, A.J. Berry, S. Wimperis, S.E. Ashbrook, J. Am. Chem. Soc. 132 (2010) 15651–15660.
[21] C. Martineau, F. Fayon, M.R. Suchomel, M. Allix, D. Massiot, F. Taulelle, Inorg. Chem. 50 (2011) 2644–2653.
[22] A.-L. Rollet, M. Allix, E. Veron, M. Deschamps, V. Montouillout, M.R. Suchomel, E. Suard, M. Barre, M. Ocaña, A. Sadoc, F. Boucher, C. Bessada, D. Massiot, F. Fayon, Inorg. Chem. 51 (2012) 2272–2282.
[23] A. Cadiau, C. Martineau, M. Leblanc, V. Maisonneuve, A. Hémon-Ribaud, F. Taulelle, K. Adil, J. Mater. Chem. 21 (2011) 3949–3951.
[24] C. Martineau, C. Mellot-Draznieks, F. Taulelle, Phys. Chem. Chem. Phys. 13 (2011) 18078–18087.
[25] C. Martineau, B. Bouchevreau, Z. Tian, S.-J. Lohmeier, P. Behrens, F. Taulelle, Chem. Mater. 23 (2011) 4799–4809.
[26] C. Martineau, B. Bouchevreau, R. Siegel, J. Senker, A. Ristić, F. Taulelle, J. Phys. Chem. C 116 (2012) 21489–21498.
[27] C. Martineau, C. Legein, M. Body, O. Péron, B. Boulard, F. Fayon, J. Solid State Chem. 199 (2013) 326–333.
[28] C. Martineau, T. Loiseau, L. Beitone, G. Férey, B. Bouchevreau, F. Taulelle, Dalton Trans. 42 (2013) 422–431.
[29] M. Body, G. Silly, C. Legein, J.-Y. Buzaré, Inorg. Chem. 43 (2004) 2474–2485.
[30] G. Silly, M. Body, J.-Y. Buzaré, C. Legein, B. Bureau, C.R. Chim. 7 (2004) 403–416.
[31] M. Body, G. Silly, C. Legein, J.-Y. Buzaré, F. Calvayrac, P. Blaha, J. Solid State Chem. 178 (2005) 3655–3661.
[32] C. Martineau, M. Body, C. Legein, G. Silly, J.-Y. Buzaré, F. Fayon, Inorg. Chem. 45 (2006) 10215–10223.
[33] C. Legein, F. Fayon, C. Martineau, M. Body, J.-Y. Buzaré, D. Massiot, E. Durand, A. Tressaud, A. Demourgues, O. Péron, B. Boulard, Inorg. Chem. 45 (2006) 10639–10641.
[34] F. Le Berre, M.-P. Crosnier-Lopez, C. Galven, J.-L. Fourquet, C. Legein, M. Body, J.-Y. Buzaré, Dalton Trans. (2007) 2457–2466.
[35] L. Sronek, J. Lhoste, M. Gaudon, C. Legein, J.-Y. Buzaré, M. Body, G. Crinière, A. Tressaud, S. Pechev, A. Demourgues, J. Phys. Chem. C 112 (2008) 860–866.
[36] B. Bureau, G. Silly, J.-Y. Buzaré, J. Emery, Chem. Phys. 249 (1999) 89–104.
[37] M. Mortimer, E.A. Moore, N.F. Peirson, J. Chem. Soc., Faraday Trans. 92 (1996) 1117–1120.
[38] S.-H. Cai, Z. Chen, X. Hu, H.-L. Wan, Chem. Phys. Lett. 302 (1999) 73–76.
[39] S.-H. Cai, Z. Chen, H.-L. Wan, J. Phys. Chem. A 106 (2002) 1060–1066.
[40] S.-H. Cai, Z. Chen, Z.-W. Chen, H.-L. Wan, Chem. Phys. Lett. 362 (2002) 13–18.
[41] S.-H. Cai, X.-Y. Yu, Z. Chen, H.-L. Wan, Magn. Reson. Chem. 41 (2003) 902–907.
[42] Y. Liu, J. Tossell, J. Phys. Chem. B 107 (2003) 11280–11289.
[43] M. Body, G. Silly, C. Legein, J.-Y. Buzaré, J. Phys. Chem. B 109 (2005) 10270–10278.
[44] M. Gerken, P. Hazendonk, A Iuga, J. Nieboer, M. Tramšek, E. Goreshnik, B. Žemva, S. Zheng, J. Autschbach, Inorg. Chem. 46 (2007) 6069–6077.
[45] C.J. Pickard, F. Mauri, Phys. Rev. B: Condens. Matter 63 (2001) 245101.
[46] J.R. Yates, C.J. Pickard, F. Mauri, Phys. Rev. B: Condens. Matter 76 (2007) 024401.
[47] T. Charpentier, Solid State Nucl. Magn. Reson. 40 (2011) 1–20.
[48] C. Bonhomme, C. Gervais, F. Babonneau, C. Coelho, F. Pourpoint, T. Azaïs, S.E. Ashbrook, J.M. Griffin, J.R. Yates, F. Mauri, C.J. Pickard, Chem. Rev. 112 (2012) 5733–5779.
[49] A. Zheng, S.-B. Liu, F. Deng, J. Phys. Chem. C 113 (2009) 15018–15023.
[50] A. Sadoc, M. Body, C. Legein, M. Biswal, F. Fayon, X. Rocquefelte, F. Boucher, Phys. Chem. Chem. Phys. 13 (2011) 18539–18550.
[51] C. Martineau, A. Cadiau, B. Bouchevreau, J. Senker, F. Taulelle, K. Adil, Dalton Trans. 41 (2012) 6232–6241.
[52] M. Biswal, M. Body, C. Legein, G. Corbel, A. Sadoc, F. Boucher, J. Phys. Chem. C 116 (2012) 11682–11693.
[53] A. Pedone, T. Charpentier, M.C. Menziani, J. Mater. Chem. 22 (2012) 12599–12608.
[54] J.R. Yates, S.E. Dobbins, C.J. Pickard, F. Mauri, P.Y. Ghi, R.K. Harris, Phys. Chem. Chem. Phys. 7 (2005) 1402–1407.
[55] D.K. Hindermann, C.D. Cornwell, J. Chem. Phys. 48 (1968) 4148–4154.
[56] C.J. Jameson, A.K. Jameson, J. Honarbakhsh, J. Chem. Phys. 81 (1984) 5266–5267.
[57] A.J. Edwards, J. Chem. Soc. (1964) 3714–3718.
[58] S.A. Brewer, A.K. Brisdon, J. Fawcett, P.J. Holliman, J.H. Holloway, E.G. Hope, D.R. Russell, Z. Anorg. Allg. Chem. 632 (2006) 325–329.

[59] M.D. Segall, P.L.D. Lindan, M.J. Probert, C.J. Pickard, P.J. Hasnip, S.J. Clark, M.C. Payne, J. Phys. Condens. Matter 14 (2002) 2717–2744.
[60] S.J. Clark, M.D. Segall, C.J. Pickard, P.J. Hasnip, M.J. Probert, K. Refson, M.C. Payne, Z. Kristallogr. 220 (2005) 567–570.
[61] M. Body, G. Silly, C. Legein, J.-Y. Buzaré, F. Calvayrac, P. Blaha, Chem. Phys. Lett. 424 (2006) 321–326.
[62] S. Grimme, J. Comput. Chem. 27 (2006) 1787–1799.
[63] G. Kresse, J. Furthmüller, Phys. Rev. B: Condens. Matter 54 (1996) 11169–11186.
[64] T. Bučko, J. Hafner, S. Lebègue, J.G. Ángyán, J. Phys. Chem. A 114 (2010) 11814–11824.
[65] D. Massiot, F. Fayon, M. Capron, I. King, S. Le Calvé, B. Alonso, J.-O. Durand, B. Bujoli, Z. Gan, G. Hoatson, Magn. Reson. Chem. 40 (2002) 70–76.
[66] K., Eichele, WSolids1, Version 1.20.17; Universität Tübingen, 2012.
[67] J.P. Perdew, K. Burke, M. Ernzerhof, Phys. Rev. Lett. 77 (1996) 3865–3868.
[68] P.E. Blöchl, Phys. Rev. B: Condens. Matter 50 (1994) 17953–17979.
[69] H.M. Petrilli, P.E. Blöchl, P. Blaha, K. Schwarz, Phys. Rev. B: Condens. Matter 57 (1998) 14690–14697.
[70] P. Pyykkö, Mol. Phys. 106 (2008) 1965–1974.
[71] Inorganic Crystal Structure Database (ICSD), Version 1.4.2, FIZ Karlsruhe and NIST, Germany and Maryland, 2007.
[72] S. Brownstein, Inorg. Chem. 12 (1973) 584–589.
[73] M. Jura, W. Levason, G. Reid, M. Webster, Dalton Trans. (2009) 7610–7612.
[74] R. Bini, C. Chiappe, F. Marchetti, G. Pampaloni, S. Zacchini, Inorg. Chem. 49 (2010) 339–351.
[75] F. Marchetti, G. Pampaloni, S. Zacchini, J. Fluorine Chem. 131 (2010) 21–28.
[76] F. Marchetti, C. Pinzino, S. Zacchini, G. Pampaloni, Angew. Chem. Int. Ed. 49 (2010) 5268–5272.
[77] J. Köhler, A. Simon, L. van Wüllen, S. Cordier, T. Roisnel, M. Poulain, M. Somer, Z. Anorg. Allg. Chem. 628 (2002) 2683–2690.
[78] C. Legein, M. Body, S. Pylypko, Private Communication.
[79] A.M. Ellern, M. Yu. Antipin, A.V. Sharabarin, Yu.T. Struchkov, Zh. Neorg. Khim. 36 (1991) 2266–2270.
[80] B.G. Müller, Angew. Chem. 99 (1987) 685–686.
[81] K. Radan, M. Lozinsek, E. Goreshnik, B. Zemva, J. Fluorine Chem. 132 (2011) 767–771.
[82] B. Žemva, L. Golič, J. Slivnik, Acta Chim. Slov. 30 (1983) 365–376.
[83] A.J. Edwards, J. Chem. Soc., Dalton Trans. (1972) 2325–2328.
[84] A.J. Edwards, G.R. Jones, J. Chem. Soc. A (1970) 1491–1497.
[85] W.J. Casteel Jr., A.P. Wilkinson, H. Borrmann, R.E. Serfass, N. Bartlett, Inorg. Chem. 31 (1992) 3124–3131.
[86] F. Marchetti, G. Pampaloni, C. Pinzino, J. Organomet. Chem. 696 (2011) 1294–1300.
[87] M. Sobczyk, A. Sawicka, P. Skurski, Eur. J. Inorg. Chem. (2003) 3790–3797.
[88] J.C. Fuggle, D.A. Tong, D.W.A. Sharp, J.M. Winfield, J. Chem. Soc., Dalton Trans. (1974) 205–210.
[89] S.L. Segel, J. Chem. Phys. 69 (1978) 2434–2338.
[90] R.K. Harris, A.C. Oliviery, Prog. Nucl. Magn. Reson. Spectrosc 24 (1992) 435–456.
[91] K.C. Moss, J. Chem. Soc. A (1970) 1224–1226.
[92] J.V. Hatton, Y. Saito, W.G. Schneider, Can. J. Chem. 43 (1965) 47–56.
[93] F. Marchetti, G. Pampaloni, Inorg. Chim. Acta 376 (2011) 123–128.
[94] L.-S. Du, R.W. Schurko, N. Kim, C.P. Grey, J. Phys. Chem. A 106 (2002) 7876–7886.
[95] D. Massiot, F. Fayon, M. Deschamps, S. Cadars, P. Florian, V. Montouillout, N. Pellerin, J. Hiet, A. Rakhmatullin, C. Bessada, C.R. Chim. 13 (2010) 117–129.
[96] L.-S. Du, R.W. Schurko, K.H. Lim, C.P. Grey, J. Phys. Chem. A 105 (2001) 760–768.

NbF_5 and TaF_5: assignment of ^{19}F NMR resonances and chemical bond analysis from GIPAW calculations

Mamata Biswal, Monique Body, Christophe Legein, Aymeric Sadoc, Florent Boucher

Supplementary data

Table of Contents

Table S1. Experimental fractional atomic coordinates (*x*, *y*, *z*) for NbF_5 [1].

	site	*x*	*y*	*z*
Nb1	4g	0	0.201	0
Nb2	4i	0.260	0	0.743
F1	4i	0.148	0	0.450
F2	4i	0.345	0	0.070
F3	8j	0.360	0.092	0.627
F4	8j	0.125	0.098	0.871
F5	8j	0.108	0.184	0.300
F6	8j	0.118	0.282	0.871

Table S2. APO-vdW fractional atomic coordinates (*x′*, *y′*, *z′*) and corresponding atomic displacements *d′*(Å) for NbF_5.

	site	*x′*	*y′*	*z′*	*d′*
Nb1	4g	0	0.20411	0	0.045
Nb2	4i	0.26088	0	0.73935	0.021
F1	4i	0.13308	0	0.43851	0.149
F2	4i	0.34160	0	0.09070	0.114
F3	8j	0.36907	0.09674	0.63983	0.124
F4	8j	0.12279	0.09641	0.87689	0.045
F5	8j	0.10684	0.18605	0.32370	0.127
F6	8j	0.12086	0.28851	0.87404	0.099

Table S3. APO fractional atomic coordinates (*x″*, *y″*, *z″*) and corresponding atomic displacements *d″*(Å) for NbF_5.

	site	*x″*	*y″*	*z″*	*d″*
Nb1	4g	0	0.20356	0	0.037
Nb2	4i	0.26151	0	0.73707	0.035
F1	4i	0.13242	0	0.43882	0.155
F2	4i	0.34134	0	0.08874	0.106
F3	8j	0.36958	0.09628	0.63506	0.115
F4	8j	0.12336	0.09638	0.87490	0.036
F5	8j	0.10829	0.18476	0.32137	0.110
F6	8j	0.11897	0.28831	0.87040	0.092

Table S4. Experimental fractional atomic coordinates (*x*, *y*, *z*) for TaF_5 [2].

	site	*x*	*y*	*z*
Ta1	4h	0	0.20237	1/2
Ta2	4i	0.25891	0	0.24359
F1	4i	0.1299	0	-0.064
F2	4i	0.3372	0	0.606
F3	8j	0.3636	0.0955	0.148
F4	8j	0.1210	0.0945	0.3761
F5	8j	0.1098	0.1844	0.828
F6	8j	0.1209	0.2864	0.372

Table S5. APO-vdW fractional atomic coordinates (*x'*, *y'*, *z'*) and corresponding atomic displacements *d'*(Å) for TaF_5.

	site	*x'*	*y'*	*z'*	*d'*
Ta1	4h	0	0.20441	0.5	0.029
Ta2	4i	0.26021	0	0.24135	0.018
F1	4i	0.13061	0	-0.07229	0.043
F2	4i	0.34434	0	0.60262	0.072
F3	8j	0.3697	0.09736	0.14285	0.072
F4	8j	0.12137	0.90442	0.37869	0.020
F5	8j	0.10985	0.18677	0.83424	0.046
F6	8j	0.12179	0.28954	0.37382	0.047

Table S6. APO fractional atomic coordinates (*x''*, *y''*, *z''*) and corresponding atomic displacements *d''*(Å) for TaF_5.

	site	*x''*	*y''*	*z''*	*d''*
Ta1	4h	0	0.20467	0.5	0.033
Ta2	4i	0.26177	0	0.24202	0.029
F1	4i	0.13114	0	-0.06881	0.028
F2	4i	0.34398	0	0.60403	0.067
F3	8j	0.37109	0.09707	0.14231	0.083
F4	8j	0.12225	0.09604	0.37832	0.027
F5	8j	0.11134	0.18728	0.83223	0.048
F6	8j	0.1202	0.2897	0.36954	0.049

Table S7. F-Nb-F and Nb-F-Nb angles (°) from ES [1], APO-vdW and APO structures for NbF_5.

	ES	APO-vdW	APO
F4-Nb1-F4	87.9	83.9	84.6
F6-Nb1-F6	99.2	97.5	97.0
F6-Nb1-F4	86.5	89.3	89.2
F5-Nb1-F6	94.2	95.4	95.9
F5-Nb1-F6	96.1	95.1	95.1
F5-Nb1-F4	82.5	83.6	83.2
F5-Nb1-F4	86.0	84.5	84.5
F5-Nb1-F5	164.1	164.0	163.3
F6-Nb1-F4	174.3	173.2	173.7
F4-Nb2-F4	86.0	83.2	83.1
F3-Nb2-F3	96.6	98.3	97.8
F3-Nb2-F4	88.6	89.2	89.5
F1-Nb2-F3	91.1	96.5	96.6
F2-Nb2-F3	95.9	94.4	94.9
F1-Nb2-F4	85.5	83.8	83.4
F2-Nb2-F4	86.8	83.7	83.5
F1-Nb2-F2	169.4	163.3	162.4
F3-Nb2-F4	173.9	172.3	172.6
Nb1-F4-Nb2	176.7	173.5	173.8

Table S8. F-Ta-F and Ta-F-Ta angles (˚) from ES [2], APO-vdW and APO structures of TaF_5.

	ES	APO-vdW	APO
F6-Ta1-F6	98.0	97.3	97.4
F6-Ta1-F5	95.2	95.1	95.4
F6-Ta1-F5	95.3	95.1	94.7
F5-Ta1-F4	84.5	84.7	85.2
F6-Ta1-F4	89.4	90.0	89.8
F5-Ta1-F4	83.5	83.7	83.4
F4-Ta1-F4	83.3	82.6	83.1
F5-Ta1-F5	164.0	164.5	164.7
F6-Ta1-F4	172.6	172.6	172.7
F3-Ta2-F3	99.5	98.3	98.0
F3-Ta2-F1	96.4	96.4	96.6
F3-Ta2-F2	95.2	94.0	94.5
F3-Ta2-F4	88.9	89.6	89.7
F1-Ta2-F4	83.3	84.1	83.5
F2-Ta2-F4	83.2	84.0	83.8
F4-Ta2-F4	82.6	82.4	82.6
F1-Ta2-F2	162.0	164.1	163.0
F3-Ta2-F4	171.5	172.0	172.2
Ta2-F4-Ta1	172.9	172.5	172.8

Table S9. ^{19}F σ_{iso} (ppm), F Mulliken charge (e), Nb-F bond population (e) and Nb-F bond length (Å) from ES of NbF_5.

F	σ_{iso}	charge	Nb-F bond population	Nb-F bond length
F3	-94.2	-0.39	0.32	1.778
F6	-99.6	-0.41	0.33	1.803
F1	-49.7	-0.41	0.27	1.752
F5	-64.0	-0.41	0.29	1.778
F2	-35.4	-0.43	0.29	1.783
F4	180.2	-0.51	0.19	2.064
			0.19	2.073

Table S10. ^{19}F σ_{iso} (ppm), F Mulliken charge (e), Nb-F bond population (e) and Nb-F bond length (Å) from APO structure of NbF_5.

	σ_{iso}	charge	Nb-F bond population	Nb-F bond length
F3	-163.9	-0.39	0.36	1.844
F6	-156.8	-0.4	0.36	1.846
F1	-131.5	-0.42	0.34	1.863
F5	-111.3	-0.42	0.34	1.871
F2	-89.7	-0.43	0.36	1.881
F4	138.4	-0.5	0.2	2.091
			0.2	2.097

Table S11. ^{19}F σ_{iso} (ppm), F Mulliken charge (e), Nb-F bond population (e) and Nb-F bond length (Å) from APO-vdW structure of NbF_5.

	σ_{iso}	charge	Nb-F bond population	Nb-F bond length
F3	-165.1	-0.39	0.36	1.845
F6	-158.1	-0.4	0.36	1.847
F1	-129.7	-0.42	0.34	1.866
F5	-111.2	-0.42	0.35	1.873
F2	-90.2	-0.43	0.36	1.882
F4	138.2	-0.49	0.2	2.090
			0.2	2.096

Table S12. ^{19}F σ_{iso} (ppm), F Mulliken charge (e), Ta-F bond population (e) and Ta-F bond length (Å) from ES of TaF_5.

	σ_{iso}	charge	Ta-F bond population	Ta-F bond length
F3	-86.2	-0.33	0.59	1.797
F6	-89.5	-0.36	0.57	1.840
F1	-43.4	-0.39	0.53	1.852
F5	-31.4	-0.39	0.53	1.857
F2	10.1	-0.41	0.53	1.879
F4	210.5	-0.46	0.27	2.058
			0.28	2.074

Table S13. ^{19}F σ_{iso} (ppm), F Mulliken charge (e), Ta-F bond population (e) and Ta-F bond length (Å) from APO structure of TaF_5.

	σ_{iso}	charge	Ta-F bond population	Ta-F bond length
F3	-115.0	-0.35	0.57	1.847
F6	-107.8	-0.36	0.56	1.850
F1	-62.9	-0.39	0.52	1.873
F5	-41.7	-0.39	0.52	1.880
F2	-22.5	-0.4	0.53	1.888
F4	199.8	-0.47	0.28	2.085
			0.27	2.090

Table S14. ^{19}F σ_{iso} (ppm), F Mulliken charge (e), Ta-F bond population (e) and Ta-F bond length (Å) from APO-vdW structure of TaF_5.

	σ_{iso}	charge	Ta-F bond population	Ta-F bond length
F3	-115.9	-0.35	0.57	1.850
F6	-109.3	-0.36	0.56	1.852
F1	-58.8	-0.39	0.52	1.878
F5	-43.6	-0.39	0.52	1.882
F2	-23.1	-0.4	0.53	1.890
F4	198.9	-0.46	0.28	2.081
			0.27	2.084

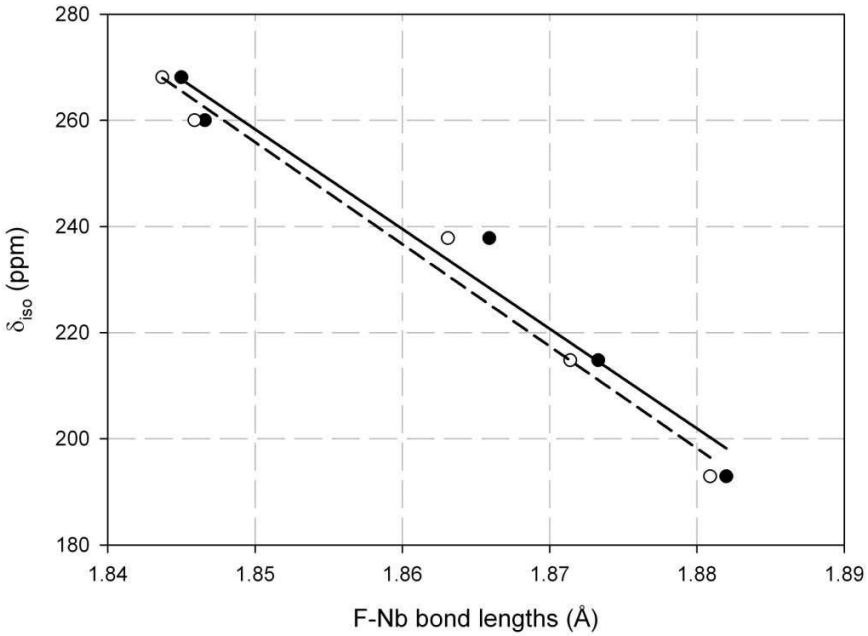

Figure 1. Optimized F_t-Nb bond lengths versus experimental ^{19}F δ_{iso} values for NbF_5. The black and white circles represent the F_t-Nb bond lengths from APO-vdW and APO structures, respectively. The solid and dash black lines represent the linear regressions when considering the F_t-Nb bond lengths from APO-vdW (*a* = -1879(208) ppm.Å^{-1}, *b*= 3735(387) ppm, R^2 = 0.965) and APO (*a* = -1923(158) ppm.Å^{-1}, *b* = 3814(294) ppm, R^2 = 0.980) structures, respectively.

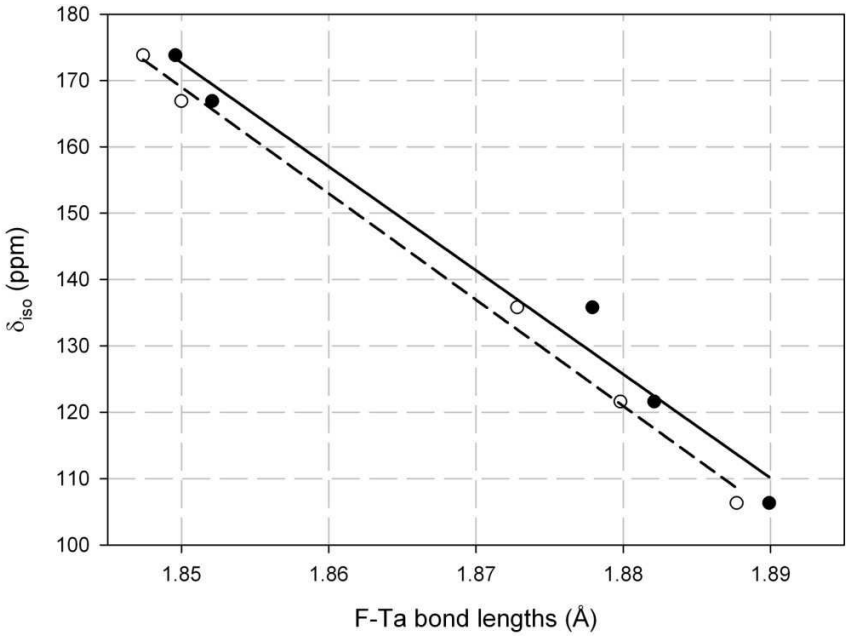

Figure 2. Optimized F_t-Ta bond lengths versus experimental ^{19}F δ_{iso} values for TaF_5. The black and white circles represent the F_t-Ta bond lengths from APO-vdW and APO structures, respectively. The solid and dash black lines represent the linear regressions when considering the F_t-Ta bond lengths from APO-vdW (a = -1565(130) ppm.Å^{-1}, b = 3068(244) ppm, R^2 = 0.980) and APO (a = -1603(74) ppm.Å^{-1}, b = 3134(138) ppm, R^2 = 0.994) structures, respectively.

References

[1] A. J. Edwards, J. Chem. Soc. (1964) 3714–3718.
[2] S. A. Brewer, A. K. Brisdon, J. Fawcett, P. J. Holliman, J. H. Holloway, E. G. Hope, D. R. Russell, Z. Anorg. Allg. Chem. 632 (2006) 325–329.

3.3 MF_4 fluorides

In the previous part (3.2), confident assignments from GIPAW[1,2] calculations were achieved for column 5 metal (Nb, Ta) fluorides. However, the isotropic chemical shift ranges observed on the ^{19}F spectra for the five non bridging fluorine atoms are equal to 75 ppm (NbF_5) and 68 (TaF_5). The question that arises now is to determine whether this method is still accurate when the chemical shift ranges are narrower.

3.3.1 Structural features and solid state NMR study

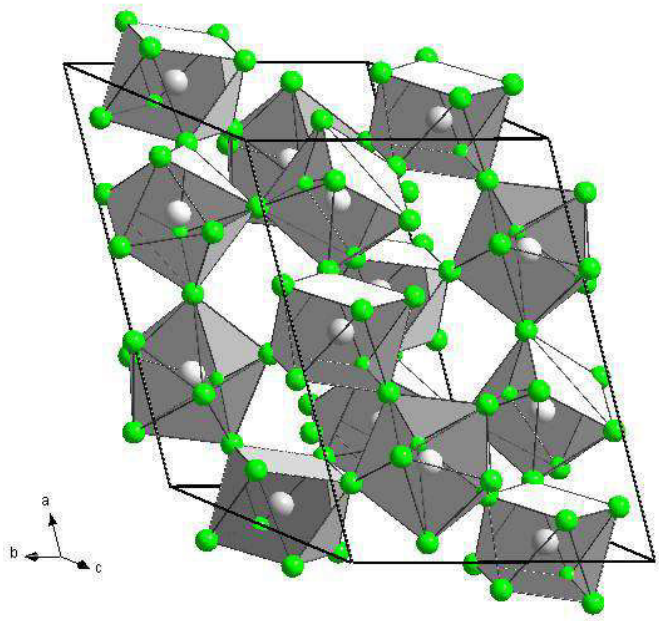

Fig. 1. Perspective view of ThF_4[6] structure showing ThF_8^{4-} square Archimedean antiprisms.

In this part is then presented the study of four MF_4 fluorides, two from column 4, i.e. β-ZrF_4[3] (ICSD[4] file number 165289[5]) and HfF_4[6] (ICSD[4] file number 66008), one lanthanide fluoride, CeF_4[7] (ICSD[4] file number 89621), and one actinide fluoride, ThF_4[6] (ICSD[4] file number 66009). These four compounds adopt the same structure (space group 15, C2/c, Fig. 1) but the structure of β-ZrF_4 was not described in the same setting (I2/c[3,5]) than the three others (C2/c,[6,7] standard setting). In addition, in the ICSD[4] file number 165289, the value of the β angle (94°28')[3,5] is not correctly reported (94.28°). The data are then erroneous in this ICSD[4] file. Moreover, β-ZrF_4 does not present the same atomic number ordering as HfF_4, CeF_4 and ThF_4. Then we have changed the setting (a=11.82 Å, b=9.93 Å, c=7.73 Å, β=126.2°, atomic positions are given below) and renumbered both the F and Zr atoms of the β-ZrF_4 structure to keep the same setting and atomic number ordering and thus facilitate comparison

Table 1. Renumbering and multiplicity of atoms in β-ZrF_4 structure.

ICSD n°165289	Zr1	Zr2	F1	F2	F3	F4	F5	F6	F7
this study	Zr2	Zr1	F4	F1	F6	F5	F7	F2	F3
multiplicity	4e	8f	4d	4e	8f	8f	8f	8f	8f

between the four compounds (Table 1). These compounds contain seven inequivalent crystallographic fluorine sites, two (F1 and F4) with multiplicity of 4 and the remaining five with multiplicity of 8. Their structures consist of a three dimensional network of corner-sharing MF_8^{4-} square Archimedean antiprism (Fig. 1). Each fluorine atom is coordinated by two metal atoms.

For β-ZrF_4 and CeF_4, the experimental ^{19}F δ_{iso} values and an assignment of the ^{19}F NMR resonances to the fluorine sites, using the semi-empirical superposition model,[8] have been reported previously.[5] The ^{91}Zr δ_{iso} and quadrupolar parameters of β-ZrF_4 have been also determined previously.[9] Bessada et al.[10] have reported the ^{19}F MAS NMR spectrum of ThF_4, recorded at 9.4 T, and discussed about its isotropic resonance range (from 53 ppm to 101 ppm) but no precise ^{19}F δ_{iso} values were given. We then record the ^{19}F NMR spectra of ThF_4 (at 7 T) and HfF_4 (at 19.9 T) and, for the first time, determine precisely the ^{19}F δ_{iso} values for both these compounds. Discrimination between isotropic lines and spinning sidebands was achieved by recording ^{19}F spectra at several spinning frequencies. Since ThF_4 and HfF_4 structures present seven inequivalent crystallographic sites (1 4d, 1 4e and 5 8f sites), seven lines among which two lines with relative intensity equal to 8.3 % and five lines with relative intensity equal to 16.7 % are expected in the ^{19}F NMR spectra.

The experimental ^{19}F NMR spectrum of HfF_4 is shown in Fig. 2. Its reconstruction was achieved using the seven expected lines and relative intensities; the corresponding parameters are gathered in Table 2. An initial partial assignment is done, based on the relative intensities. Lines 2 and 6, with respective relative intensities of 8.6 and 10.4 %, are assigned to the multiplicity 4 F sites.

Table 2. Isotropic chemical shifts (δ_{iso}, ppm), chemical shift anisotropy (δ_{csa}, ppm), asymmetry parameter of the CSA tensor (η_{csa}) and relative intensities (%) of the ^{19}F NMR resonances in HfF_4. The initial partial assignments are deduced from NMR line relative intensities.

Line	δ_{iso} (±0.5)	Intensity (±2)	δ_{csa} (±30)	η_{csa} (±0.2)	Initial assignment
1	-7.0	17.5	-170	0.4	F2, F3, F5, F6, F7
2	-9.2	8.6	-175	0.65	F1, F4
3	-10.9	15.5	-150	0.8	F2, F3, F5, F6, F7
4	-18.0	15.5	-160	0.5	F2, F3, F5, F6, F7
5	-21.9	14.9	-155	0.7	F2, F3, F5, F6, F7
6	-26.0	10.4	-150	0.6	F1, F4
7	-28.1	17.1	-150	0.6	F2, F3, F5, F6, F7

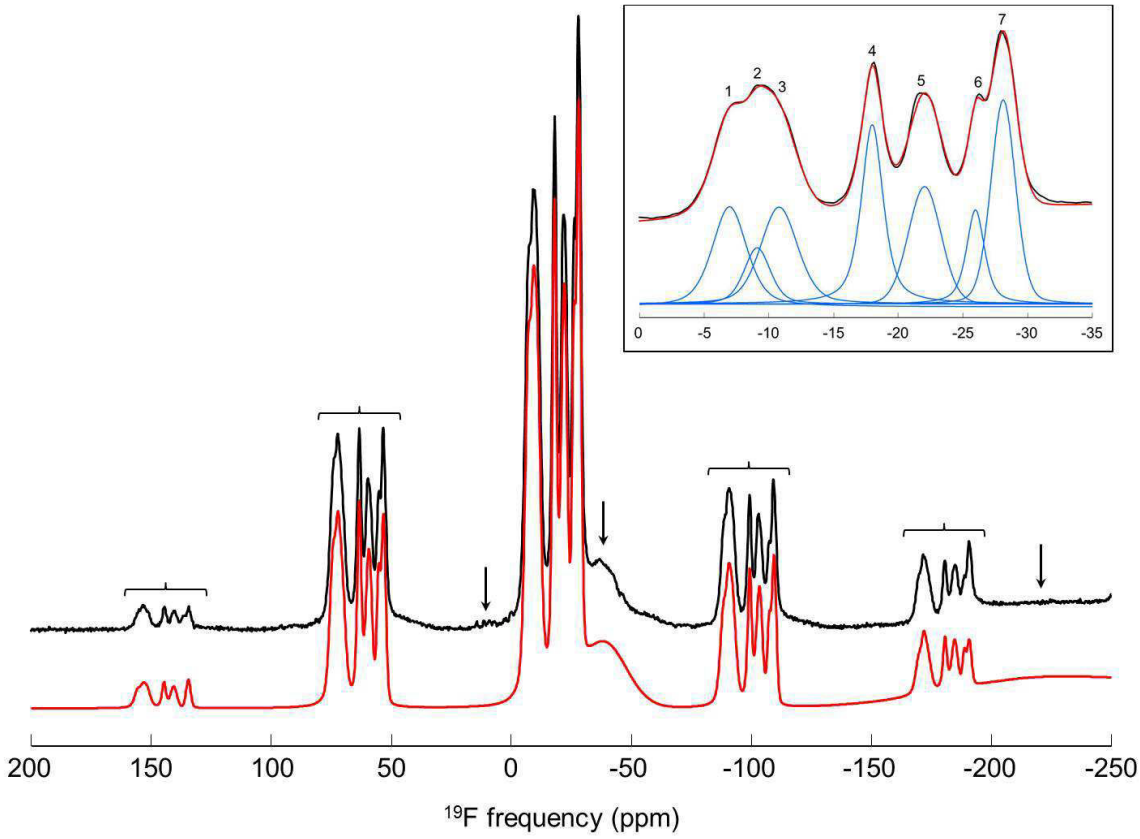

Fig. 2. Experimental (black) and reconstructed (red) ^{19}F MAS (65 kHz) NMR spectra of HfF_4 recorded at a magnetic field of 19.9 T. Braces indicate spinning sidebands whereas arrows indicate unidentified impurities. The inset shows the numbered isotropic lines and their individual reconstructions.

The experimental ^{19}F NMR spectrum of ThF_4 is presented in Fig. 3 and was fitted with only six NMR lines. The parameters used for this reconstruction are gathered in Table 3. As for HfF_4, an initial partial assignment was carried out based on these relative intensities. Lines 1 and 5, with respective relative intensities of 7.2 and 8.8 %, are assigned to the multiplicity 4 F sites. The relative intensity of line 3 is equal to 33.6 %, which corresponds to twice the expected relative intensity for one 8f F site. Therefore, this line is assigned to two of the five 8f F sites.

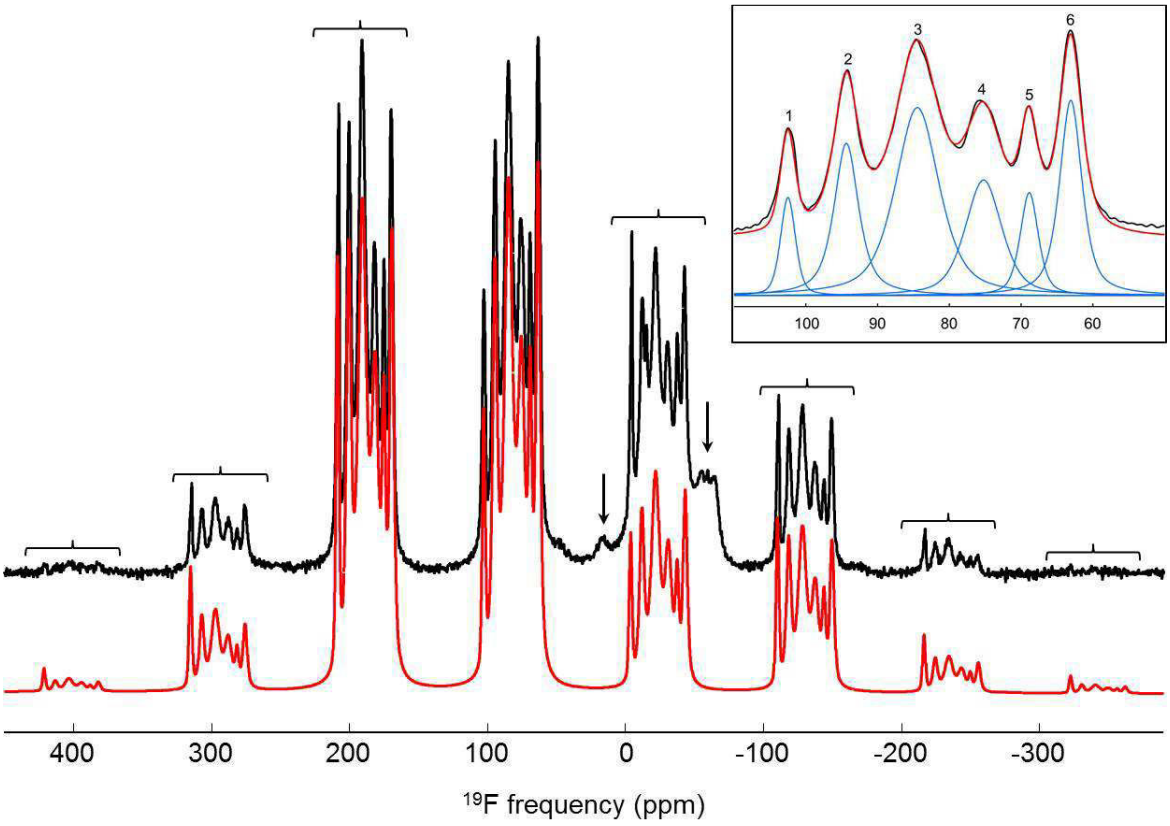

Fig. 3. Experimental (black) and reconstructed (red) ^{19}F MAS (30 kHz) NMR spectra of ThF_4 recorded at a magnetic field of 7 T. Braces indicate spinning sidebands whereas arrows indicate unidentified impurities. The inset shows the numbered isotropic lines and their individual reconstructions.

Table 3. Isotropic chemical shift (δ_{iso}, ppm), chemical shift anisotropy (δ_{csa}, ppm), asymmetry parameter of the CSA tensor (η_{csa}) and relative intensity (%) of the ^{19}F NMR resonances in ThF_4. The initial partial assignments are deduced from NMR line relative intensities.

Line	δ_{iso} (±0.5)	Intensity (±2)	δ_{csa} (±30)	η_{csa} (±0.2)	Initial assignment
1	102.5	8.8	-360	0.35	F1, F4
2	94.3	16.9	-300	0.2	F2, F3, F5, F6, F7
3	84.5	33.6	-290	0.3	F2, F3, F5, F6, F7
4	75.2	16.7	-290	0.3	F2, F3, F5, F6, F7
5	68.9	7.2	-285	0.1	F1, F4
6	63.1	16.9	-280	0.2	F2, F3, F5, F6, F7

The δ_{iso} ranges being small for the four compounds (20 to 40 ppm depending on the MF_4 compound), to obtain a reliable assignment is a real challenge. Thus, correlation experiments, based on through space ^{19}F-^{19}F dipolar coupling interaction, were planned, at high magnetic field at CEMHTI (Fédération TGIR RMN Très Hauts Champs - FR3050 CNRS), in order to probe the F-F proximities in β-ZrF_4, HfF_4 and CeF_4. Unfortunately, it was not possible to perform correlation experiments for CeF_4, the relaxation time T_2 being too short. Since thorium is radioactive (α radiation), experiments on ThF_4 are planned by F. Fayon at the Institute for Transuranium Elements (ITU, Karlsruhe).

In the obtained 2D spectra, spatial proximities between inequivalent F sites are revealed by off-diagonal cross-correlation peaks, while proximities between equivalent F sites give rise to diagonal autocorrelation peaks. It has been shown that the correlation peak amplitudes globally decrease with increasing ^{19}F-^{19}F distances[11,12] and that, in the best cases (no overlapping), most of ^{19}F-^{19}F proximities shorter than 4.5 Å are revealed by correlation peaks in the DQ-SQ spectrum.[12] Then, from the F-F bond lengths, we can estimate the intensities of both the autocorrelation and cross-correlation peaks.

Table 4. Expected intensities of autocorrelation and cross-correlation peaks on β-ZrF_4 ^{19}F DQ-SQ experiment.

F sites	Autocorrelation peak	Cross-correlation peaks
F1	weak: d(F1-F1) = 4.327 Å	with all F sites weak with F5: d(F1-F5) = 4.010 Å
F2	strong	with all F sites
F3	weak: d(F3-F3) = 3.892 Å	with all F sites
F4	none: d(F4-F4) = 4.785 Å	with all F sites
F5	strong	with all F sites weak with F1: d(F1-F5) = 4.010 Å
F6	weak: d(F6-F6) = 4.016 Å	with all F sites
F7	weak: d(F7-F7) = 3.899 Å	with all F sites

β-ZrF_4 and HfF_4 ^{19}F DQ-SQ spectra are presented in Fig. 4 and 5, respectively. The expected intensities for autocorrelation and cross-correlation peaks are deduced from the F-F distances, using the experimental structures (Tables 4 and 5, respectively). The seven isotropic NMR lines, ranging within ~20 ppm, overlap and as many ^{19}F nuclei correlate, the ^{19}F DQ-SQ spectra present a lack of resolution. Two strong autocorrelation peaks are expected for F2 and F5 but only the ^{19}F DQ-SQ spectrum of HfF_4 presents clearly a strong autocorrelation peak for line 5. This NMR line is then assigned to F2 or F5. Unfortunately, the lack of resolution prevents from additional confident assignment. For ThF_4, the seven isotropic lines range within ~40 ppm, twice the δ_{iso} range observed on the β-ZrF_4 and HfF_4 ^{19}F spectra. We may then expect to get a better resolution for the ^{19}F DQ-SQ spectra.

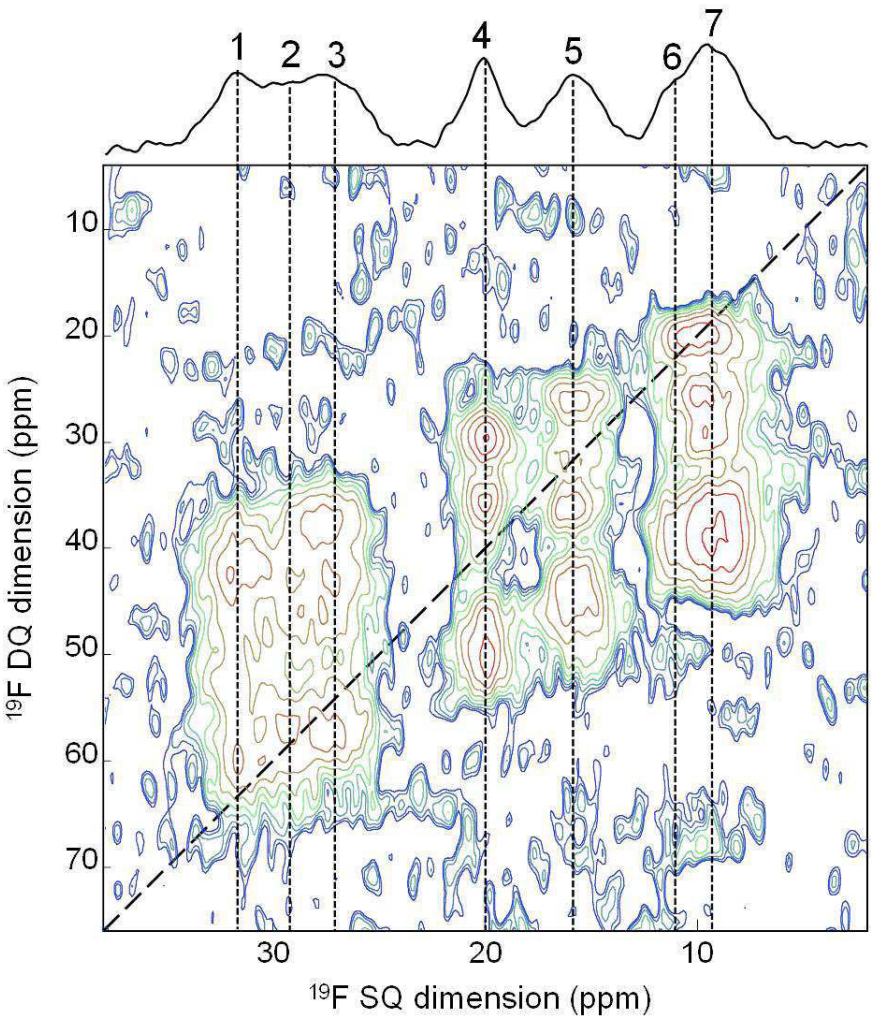

Fig. 4. 2D ^{19}F DQ-SQ MAS (32 kHz) NMR correlation spectrum of β-ZrF_4. The long dashed line indicates the diagonal of the spectrum on which autocorrelation peaks appear. The projection of the 2D spectrum onto the ^{19}F SQ dimension is shown on top of the figure. Short dashed lines indicate the positions of the isotropic NMR lines which are numbered.

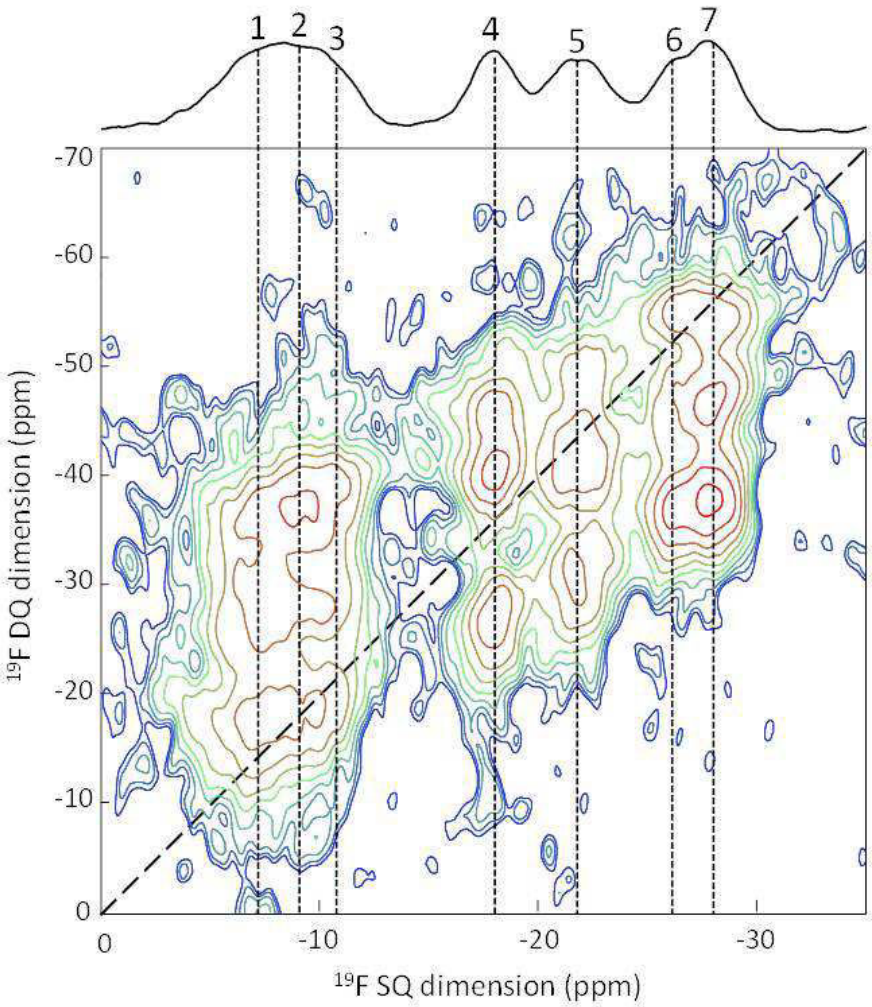

Fig. 5. 2D ^{19}F DQ-SQ MAS (65 kHz) NMR correlation spectrum of HfF_4. The long dashed line indicates the diagonal of the spectrum on which autocorrelation peaks appear. The projection of the 2D spectrum onto the ^{19}F SQ dimension is shown on top of the figure. Short dashed lines indicate the positions of the isotropic NMR lines which are numbered.

Table 5. Expected intensities of autocorrelation and cross-correlation peaks on HfF_4 ^{19}F DQ-SQ experiment.

F sites	Autocorrelation peak	Cross-correlation peaks
F1	weak: d(F1-F1) = 4.240 Å	with all F sites weak with F5: d(F1-F5) = 3.914 Å
F2	strong	with all F sites
F3	weak: d(F3-F3) = 3.956 Å	with all F sites
F4	none: d(F4-F4) = 4.748 Å	with all F sites
F5	strong	with all F sites weak with F1: d(F1-F5) = 3.914 Å
F6	weak: d(F6-F6) = 3.968 Å	with all F sites
F7	weak: d(F7-F7) = 3.858 Å	with all F sites

3.3.2 DFT calculations

In order to achieve an unambiguous assignment of the MF_4 compounds, ^{19}F chemical shielding (σ) calculations were performed using the GIPAW[1,2] method, implemented in the CASTEP code.[13,14] For the four compounds, calculations are performed on both the experimental structure (ES) and atomic position optimized (APO) structure. Additionally, the ^{91}Zr quadrupolar parameters were calculated using the projector augmented wave (PAW) method[15,16] implemented in CASTEP,[13,14] and using the linearized augmented plane wave (LAPW) method[17] implemented in WIEN2k,[17,18] from the ES and the structures geometry optimized with CASTEP and WIEN2k, respectively.

Atomic fractional coordinates of ES and APO structures, and the corresponding atomic displacements *d* are given in Tables 6, 7, 8, 9 and 10 for β-ZrF_4 (with CASTEP), β-ZrF_4 (with WIEN2k), HfF_4, CeF_4 and ThF_4, respectively. As usually observed,[19-22] the positions of the heavy atoms do not vary much after geometry optimization, while the lighter F atoms show larger atomic displacements. For β-ZrF_4, CeF_4 and ThF_4, the maximum *d* values for F atoms are equal to 0.101, 0.100 and 0.096 Å, respectively. Geometry optimization has a greater effect for HfF_4, as three F atoms present higher *d* values (0.200, 0.113, and 0.108 Å).

The M-F bond lengths and average M-F bond lengths ($\langle M-F \rangle$) for ES and APO structures are compared in Tables 11, 12, 13 and 14 for β-ZrF_4, HfF_4, CeF_4 and ThF_4, respectively. The $\langle M-F \rangle$ increase slightly for HfF_4 and CeF_4 (+0.01 Å) and very slightly for ThF_4 (+0.003Å). Among the four compounds, β-ZrF_4 is the single one for which the $\langle M1-F \rangle$ and $\langle M2-F \rangle$ calculated from the ES differ significantly and the geometry optimizations result, as expected, in closer $\langle M-F \rangle$ bond lengths.

Table 6. ES[3] (x, y, z) and CASTEP APO (x', y', z') fractional atomic coordinates and corresponding atomic displacements *d* (Å) for β-ZrF_4.

	site	x	y	z	x'	y'	z'	*d*
Zr1	8f	0.7056	0.0711	0.8334	0.7051	0.0717	0.8325	0.010
Zr2	4e	0	0.7852	1/4	0	0.7869	1/4	0.017
F1	4e	0	0.402	1/4	0	0.3919	1/4	0.101
F2	8f	0.621	0.875	0.783	0.6188	0.8788	0.7837	0.046
F3	8f	0.622	0.654	0.650	0.6225	0.6536	0.6486	0.013
F4	4d	1/4	3/4	0	1/4	3/4	0	0
F5	8f	0.885	0.941	0.046	0.8837	0.9479	0.0460	0.070
F6	8f	0.889	0.711	0.929	0.8902	0.70919	0.9236	0.048
F7	8f	0.788	0.474	0.892	0.7882	0.4702	0.8934	0.040

Table 7. ES[3] (x, y, z) and WIEN2k APO (x', y', z') fractional atomic coordinates and corresponding atomic displacements *d* (Å) for β-ZrF_4.

	site	x	y	z	x'	y'	z'	*d*
Zr1	8f	0.7056	0.0711	0.8334	0.7048	0.0713	0.8316	0.014
Zr2	4e	0	0.7852	1/4	0	0.7864	1/4	0.012
F1	4e	0	0.402	1/4	0	0.3934	1/4	0.085
F2	8f	0.621	0.875	0.783	0.6184	0.8789	0.7816	0.051
F3	8f	0.622	0.654	0.650	0.6228	0.6526	0.6495	0.017
F4	4d	1/4	3/4	0	1/4	3/4	0	0
F5	8f	0.885	0.941	0.046	0.8822	0.9456	0.0442	0.058
F6	8f	0.889	0.711	0.929	0.8907	0.7073	0.9255	0.050
F7	8f	0.788	0.474	0.892	0.7880	0.4706	0.8945	0.039

Table 8. ES[7] (x, y, z) and APO (x', y', z') fractional atomic coordinates and corresponding atomic displacements *d* (Å) for HfF_4.

	site	x	y	z	x'	y'	z'	*d*
Hf1	8f	0.2058	0.4287	0.3342	0.2042	0.4276	0.3308	0.029
Hf2	4e	0	0.7857	1/4	0	0.7888	1/4	0.030
F1	4e	1/2	0.9066	1/4	1/2	0.8863	1/4	0.200
F2	8f	0.1178	0.6188	0.2818	0.1182	0.6209	0.2809	0.022
F3	8f	0.1269	0.8443	0.1580	0.1219	0.8452	0.1453	0.113
F4	4d	1/4	3/4	0	1/4	3/4	0	0
F5	8f	0.8823	0.9475	0.0461	0.8859	0.9532	0.0472	0.071
F6	8f	0.8857	0.7047	0.9287	0.8876	0.7147	0.9236	0.108
F7	8f	0.2112	0.5279	0.1044	0.2118	0.5319	0.1053	0.040

Table 9. ES[6] (x, y, z) and APO (x', y', z') fractional atomic coordinates and corresponding atomic displacements *d* (Å) for CeF_4.

	site	x	y	z	x'	y'	z'	*d*
Ce1	8f	0.20458	0.42819	0.33140	0.20428	0.42718	0.32967	0.017
Ce2	4e	0	0.78665	1/4	0	0.78937	1/4	0.029
F1	4e	0	0.39630	1/4	0	0.39275	1/4	0.038
F2	8f	0.88149	0.62068	0.21774	0.88095	0.62157	0.21616	0.017
F3	8f	0.37545	0.34651	0.34651	0.37985	0.34611	0.35668	0.100
F4	4d	1/4	3/4	0	1/4	3/4	0	0
F5	8f	0.88022	0.94650	0.04392	0.88375	0.95064	0.04779	0.070
F6	8f	0.10934	0.29393	0.0713	0.11281	0.28930	0.07584	0.076
F7	8f	0.21075	0.52943	0.10382	0.21345	0.53107	0.10733	0.048

Table 10. ES[6] (x, y, z) and APO (x', y', z') fractional atomic coordinates and corresponding atomic displacements *d* (Å) for ThF_4.

	site	x	y	z	x'	y'	z'	*d*
Th1	8f	0.2041	0.4282	0.3309	0.2053	0.4280	0.3326	0.018
Th2	4e	0	0.7869	1/4	0	0.7863	1/4	0.006
F1	4e	0	0.3996	1/4	0	0.3961	1/4	0.039
F2	8f	0.1172	0.6196	0.2800	0.1182	0.6199	0.2819	0.021
F3	8f	0.1274	0.8460	0.1579	0.1230	0.8472	0.1497	0.092
F4	4d	1/4	3/4	0	1/4	3/4	0	0
F5	8f	0.8799	0.9482	0.0442	0.8803	0.9462	0.0447	0.023
F6	8f	0.8910	0.7052	0.9334	0.8905	0.7060	0.9297	0.033
F7	8f	0.2104	0.5279	0.1018	0.2125	0.5299	0.1058	0.049

Table 11. Zr-F and average (in italic) Zr-F lengths (Å) from ES[3] and APO structures of β-ZrF_4.

			ES	APO CASTEP	APO WIEN2k
Zr1	F1	1x	2.132	2.143	2.140
	F2	1x	2.118	2.096	2.092
	F3	1x	2.131	2.118	2.117
	F4	1x	2.072	2.070	2.075
	F5	1x	2.180	2.140	2.142
	F6	1x	2.148	2.102	2.097
	F7	1x	2.032	2.057	2.059
		1x	2.127	2.115	2.109
		$\langle Zr1-F\rangle$	*2.117*	*2.105*	*2.104*
Zr2	F2	2x	2.052	2.078	2.076
	F3	2x	2.088	2.099	2.100
	F5	2x	2.048	2.091	2.086
	F6	2x	2.139	2.186	2.179
		$\langle Zr2-F\rangle$	*2.082*	*2.113*	*2.110*

Table 12. Hf-F and average (in italic) Hf-F lengths (Å) from ES[7] and APO structure of HfF_4.

			ES	APO
Hf1	F1	1x	2.110	2.130
	F2	1x	2.063	2.085
	F3	1x	2.099	2.101
	F4	1x	2.051	2.052
	F5	1x	2.108	2.122
	F6	1x	2.091	2.107
	F7	1x	2.043	2.052
		1x	2.071	2.084
		$\langle Hf1-F\rangle$	*2.080*	*2.092*
Hf2	F2	2x	2.070	2.082
	F3	2x	2.068	2.083
	F5	2x	2.084	2.092
	F6	2x	2.139	2.146
		$\langle Hf2-F\rangle$	*2.090*	*2.101*

Table 13. Ce-F and average (in italic) Ce-F lengths (Å) from ES[6] and APO structure of CeF_4.

			ES	APO
Ce1	F1	1x	2.271	2.277
	F2	1x	2.237	2.254
	F3	1x	2.254	2.257
	F4	1x	2.213	2.210
	F5	1x	2.269	2.284
	F6	1x	2.240	2.234
	F7	1x	2.200	2.200
		1x	2.241	2.261
		$\langle Ce1-F\rangle$	*2.241*	*2.247*
Ce2	F2	2x	2.222	2.238
	F3	2x	2.228	2.234
	F5	2x	2.238	2.229
	F6	2x	2.304	2.323
		$\langle Ce2-F\rangle$	*2.248*	*2.256*

Table 14. Th-F and average (in italic) Th-F lengths (Å) from ES[6] and APO structure of ThF_4.

			ES	APO
Th1	F1	1x	2.344	2.359
	F2	1x	2.328	2.335
	F3	1x	2.330	2.334
	F4	1x	2.312	2.305
	F5	1x	2.350	2.357
	F6	1x	2.349	2.342
	F7	1x	2.292	2.293
		1x	2.317	2.326
		$\langle Th1-F \rangle$	*2.328*	*2.331*
Th2	F2	2x	2.324	2.319
	F3	2x	2.316	2.323
	F5	2x	2.345	2.330
	F6	2x	2.367	2.385
		$\langle Th2-F \rangle$	*2.338*	*2.339*

To assign the ^{19}F resonances to the fluorine crystallographic sites, the NMR lines are ranked in decreasing order of experimental δ_{iso} values whereas F atoms are ranked in increasing order of calculated σ_{iso} values.

For β-ZrF_4, the ^{19}F σ_{iso} values calculated with the ES and APO structure are compared to the experimental data[5] in Table 15. For the ES, the F site multiplicities (8:4:8:8:8:4:8) and the experimental relative intensities (2:1:2:2:2:1:2) are in the same sequence. However, the coefficient of determination of the linear correlation issued from this assignment is not satisfactory (Fig. 6) and the calculated σ_{iso} range (34 ppm) is large compared to the experimental δ_{iso} range (21 ppm). On the contrary, the F site multiplicities (4:8:8:8:8:4) issued from APO are no more in the same sequence with the experimental relative intensities but the σ_{iso} range is reduced to 17 ppm and closer to the δ_{iso} range. With respect to the site multiplicities and relative intensities, L1 to L7 can be tentatively assigned to F7, F4, F2, F3, F5, F1 and F6, respectively, leading to a better R^2 coefficient (Fig. 6, Table 16). The ^{19}F δ_{iso} values are then calculated by using the linear regression determined from calculated ^{19}F σ_{iso} and experimental ^{19}F δ_{iso} values (Table 16).

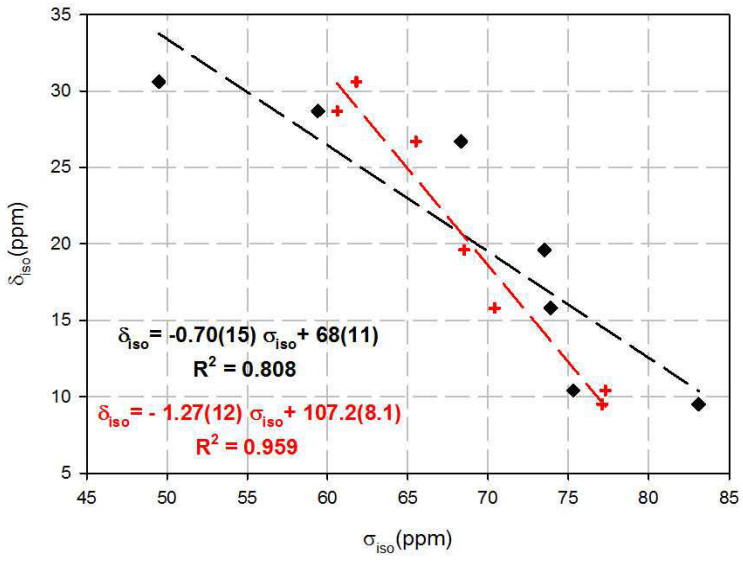

Fig. 6. Calculated ^{19}F σ_{iso} values from ES (black diamond) and APO structure (red +) versus experimental ^{19}F δ_{iso} values for β-ZrF_4. The dashed black and red lines represent the linear regressions whose equations are given on the graph.

Table 15. Experimental isotropic chemical shift (δ_{iso}, ppm) and relative intensity (I, %) of the ^{19}F NMR resonances in β-ZrF_4, fluorine site, ^{19}F σ_{iso} (ppm) from ES and APO structure of β-ZrF_4.

Exp. [5]			ES			APO		
Line	δ_{iso} (±0.5)	I (±2)	F	σ_{iso}	multiplicity	F	σ_{iso}	multiplicity
1	30.6	16.2	F7	49.5	8	F4	60.6	4
2	28.7	8.1	F4	59.4	4	F7	61.8	8
3	26.7	17.3	F2	68.3	8	F2	65.5	8
4	19.6	16	F5	73.5	8	F3	68.5	8
5	15.8	17	F3	73.9	8	F5	70.4	8
6	10.4	8.3	F1	75.3	4	F6	77.1	8
7	9.5	17.1	F6	83.1	8	F1	77.3	4

Table 16. Experimental[5] (exp.) ^{19}F δ_{iso} (ppm), δ_{csa} (ppm) and η_{csa} and calculated (calc.) ^{19}F σ_{iso} (ppm), δ_{iso} (ppm), σ_{csa} (ppm) and η_{csa} from the APO structure of ZrF_4. The calculated ^{19}F δ_{iso} values were deduced from the relationship δ_{iso} = -1.27 σ_{iso} + 107.2.

F site		σ_{iso}	δ_{iso}	$\delta_{csa}/\sigma_{csa}$	η_{csa}
F1	exp.		10.4	-160	0.3
	calc.	77.3	9.0	208.4	0.24
F2	exp.		26.7	-170	0.55
	calc.	65.5	24.0	199.9	0.67
F3	exp.		19.6	-170	0.4
	calc.	68.5	20.2	210.8	0.51
F4	exp.		28.7	-180	0.55
	calc.	60.6	30.2	252.0	0.50
F5	exp.		15.8	-165	0.4
	calc.	70.4	17.8	211.5	0.50
F6	exp.		9.5	-175	0.3
	calc.	77.1	9.3	203.2	0.40
F7	exp.		30.6	-170	0.45
	calc.	61.8	28.7	201.3	0.62

Due to the small δ_{iso} range, and the large uncertainties of the slopes of the linear regression, these assignments cannot be considered as confident. Moreover, the slopes of the linear regressions are very different from each other. This may be partly explained by the small δ_{iso} range. Anyway, for both ES and APO structure, the σ_{iso} values of F1 and F4 (multiplicity 4) on the one hand and the σ_{iso} values of F7 and F6 (multiplicity 8) on the other hand are in the bottom end and in the top end of the range. The assignments of L1 to F7, L2 to F4, L6 to F1 and L7 to F6 can then certainly be considered as confident.

As for NbF_5 (see 3.2), the calculated chemical shielding anisotropy σ_{csa} values seem to be overestimated and a scaling factor around -0.8 would be necessary to reproduce the experimental chemical shift anisotropy δ_{csa} values (Table 16). The agreement between experimental and calculated η_{csa} values is satisfactory, considering the low accuracy of the experimental values and the difficulty to accurately reproduce this parameter.

Table 17. ^{91}Zr experimental δ_{iso} (ppm), C_Q (MHz) and η_Q values, calculated σ_{iso} (ppm), C_Q (MHz) and η_Q values with CASTEP (PAW) and calculated C_Q (MHz) and η_Q values with WIEN2k (LAPW), from the ES and the APO structure of β-ZrF_4.

		Exp. [9]	PAW		LAPW	
			ES	APO	ES	APO
Zr1	C_Q	34.7(2)	-36.4	-32.1	-38.8	-34.4
	η_Q	0.33(1)	0.42	0.20	0.42	0.30
	$\delta_{iso}/\sigma_{iso}$	-360(25)	2137	2138		
Zr2	C_Q	30.0(5)	-27.7	-34.3	-29.2	-34.8
	η_Q	1.00(5)	0.66	0.40	0.68	0.46
	$\delta_{iso}/\sigma_{iso}$	-280(80)	2133	2129		

The two zirconium sites having multiplicities of 4 and 8, the assignment is straightforward, based on the NMR line relative intensities.[9] Calculated C_Q and η_Q values are compared to the experimental data[9] in Table 17. For both sites, the best agreement is obtained with quadrupolar parameters calculated with WIEN2k, from the APO structure for the Zr1 site and from the ES for the Zr2 site. The ^{91}Zr experimental δ_{iso} and calculated σ_{iso} values are in the good sequence (δ_{iso} (Zr1) < δ_{iso} (Zr2) and σ_{iso} (Zr1) > σ_{iso} (Zr2)) for ES and APO structure. Nevertheless, the uncertainties on the δ_{iso} values are large and the differences between δ_{iso} values (80 ppm) and σ_{iso} values (4 and 9 ppm for ES and APO structure, respectively) are very dissimilar.

For HfF_4, the ^{19}F σ_{iso} values calculated from the ES and the APO structure are compared with the experimental ^{19}F δ_{iso} and relative intensities in Table 18. For both the ES and APO structure, the F site multiplicities ((8:8:8:4:8:4:8) and (4:8:8:8:8:8:4), respectively) are not in agreement with the experimental relative intensities (2:1:2:2:2:1:2). As done for the APO structure of β-ZrF_4, with respect to the site multiplicities and relative intensities, L1 to L7 can be tentatively assigned to F7, F4, F3, F2, F5, F1 and F6, respectively, but the coefficient of determination, R^2, of the linear correlation between the ^{19}F experimental δ_{iso} and calculated σ_{iso} values (not shown), is not satisfactory (R^2= 0.857). Nevertheless, for both ES and APO structure, the σ_{iso} values of F1 and F4 (multiplicity 4) are calculated in the same order and the σ_{iso} values of F7 and F6 (multiplicity 8) are in the bottom end and in the top end of the range. L1, L2, L6 and L7 can then tentatively be assigned to F7, F4, F1 and F6, respectively.

Table 18. Experimental isotropic chemical shift (δ_{iso}, ppm) and relative intensity (%) of the ^{19}F NMR resonances in HfF_4, fluorine site, ^{19}F σ_{iso} (ppm) from ES and APO structure of HfF_4.

Exp.			ES			APO		
Line	δ_{iso} (±0.5)	I (±2)	F	σ_{iso}	multiplicity	F	σ_{iso}	multiplicity
1	-7.0	17.5	F2	106.6	8	F4	105.0	4
2	-9.2	8.6	F7	107.9	8	F7	107.4	8
3	-10.9	15.5	F3	120.6	8	F3	110.5	8
4	-18.0	15.5	F4	121.4	4	F2	113.9	8
5	-21. 9	14.9	F5	125.9	8	F5	114.3	8
6	-26.0	10.4	F1	128.2	4	F6	122.3	8
7	-28.1	17.1	F6	128.3	8	F1	126.3	4

Table 19. Experimental[5] isotropic chemical shift (δ_{iso}, ppm) and relative intensity (%) of the ^{19}F NMR resonances in CeF_4, fluorine site, ^{19}F σ_{iso} (ppm) from ES and APO structure of CeF_4.

Exp.			ES			APO		
Line	δ_{iso} (±0.5)	I (±2)	F	σ_{iso}	multiplicity	F	σ_{iso}	multiplicity
1	235.0	16.7	F2	-553.7	8	F2	-553.4	8
2	228.6	11.2	F1	-517.8	4	F4	-539.8	4
3	221.8	16.9	F4	-514.5	4	F1	-520.7	4
4	220.3	15.5	F7	-510.4	8	F5	-512.5	8
5	210.4	15.2	F3	-488.2	8	F7	-510.9	8
6	199.5	16.3	F5	-486.7	8	F3	-510.2	8
7	196.2	8.2	F6	-463.1	8	F6	-475.5	8

Table 20. Experimental isotropic chemical shift (δ_{iso}, ppm) and relative intensity (%) of the ^{19}F NMR resonances in ThF_4, fluorine site, ^{19}F σ_{iso} (ppm) from ES and APO structure of ThF_4.

Exp.			ES			APO		
Line	δ_{iso} (±0.5)	I (±2)	F	σ_{iso}	multiplicity	F	σ_{iso}	multiplicity
1	102.5	8.8	F7	-15.8	8	F4	-21.6	4
2	94.3	16.9	F4	-15.3	4	F7	-15.5	8
3	84.5	33.6	F2	-6.7	8	F2	-7.3	8
4			F3	-5.8	8	F3	-3.6	8
5	75.2	16.7	F1	5.9	4	F5	3.7	8
6	68.9	7.2	F5	8.3	8	F1	9.5	4
7	63.1	16.9	F6	17.4	8	F6	17.3	8

In Table 19, the ^{19}F σ_{iso} values calculated from the ES and APO structure of CeF_4 are compared with the experimental data.[5] As for HfF_4, whatever the structure, the F site multiplicities (8:4:4:8:8:8:8) are not in agreement with the experimental relative intensities (2:1:2:2:2:2:1). Moreover, it is not possible to assign F1 and F4, as their σ_{iso} values are not in the bottom end and in the top end of the range and are not ranked in the same order for ES and APO structure. Furthermore, the ^{19}F σ_{iso} ranges (90 and 78 ppm, for ES and APO structure, respectively) are two times larger than the ^{19}F δ_{iso} ranges (39 ppm). These results are really unsatisfactory.

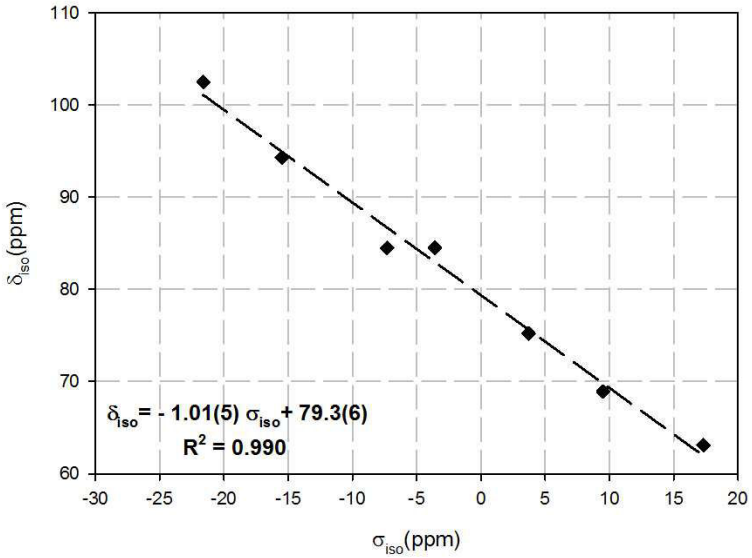

Fig. 7. Calculated ^{19}F σ_{iso} values versus experimental ^{19}F δ_{iso} values for ThF_4. The dashed black line represents the linear regression whose equation is given on the graph.

For ThF_4, the ^{19}F σ_{iso} values calculated from the ES and APO structure are compared with the experimental ^{19}F δ_{iso} and relative intensities in Table 20. The relative intensities of the NMR lines (1:2:2:2:2:1:2) and the multiplicities of the F atoms (4:8:8:8:8:4:8) are in agreement only for the APO structure. A nice linear correlation is observed between the experimental δ_{iso} and the APO ^{19}F σ_{iso} values (Fig. 7). The ^{19}F δ_{iso} values are then calculated by using the linear regression determined from calculated ^{19}F σ_{iso} and experimental ^{19}F δ_{iso} values (Table 21). As the linearity between experimental ^{19}F δ_{iso} values and calculated ^{19}F σ_{iso} values ensures that the spectral assignments are done without any ambiguity, the assignments achieved from the APO structure are retained for ThF_4. Experiments at higher field may allow discrimination of the isotropic lines of F2 and F3, which will improve the R^2 coefficient of the linear regression. As for NbF_5 (see 3.2), the slope of the linear regression between calculated ^{19}F σ_{iso} values and experimental ^{19}F δ_{iso} values obtained from ThF_4 APO structure (δ_{iso} = -1.01(5) σ_{iso} + 79.3(6)) is close to -1, i.e., the theoretical expected value, and far from the slopes of the linear regressions established previously (see chapter 2). The ^{19}F NMR resonances of the impurities at the same chemical shift as the first right set of spinning sidebands (Fig. 3) are a hindrance to a

precise determination of the chemical shift anisotropy. Nevertheless, as for NbF_5 (see 3.2) and β-ZrF_4, the calculated chemical shielding anisotropy σ_{csa} values seem to be overestimated and a scaling factor around -0.8 would be necessary to reproduce the experimental chemical shift anisotropy δ_{csa} values (Table 21) whereas the slope of the linear regression determined from the calculated σ_{iso} values and the experimental δ_{iso} values is found close to -1. The agreement between experimental and calculated η_{csa} values is satisfactory, considering the low accuracy of the experimental values and the difficulty to accurately reproduce this parameter.

Table 21. Experimental (exp.) ^{19}F δ_{iso} (ppm), δ_{csa} (ppm) and η_{csa} and calculated (calc.) ^{19}F σ_{iso} (ppm), δ_{iso} (ppm), σ_{csa} (ppm) and η_{csa} from the APO structure of ThF_4. The calculated ^{19}F δ_{iso} values were deduced from the relationship δ_{iso} = -1.01 σ_{iso} + 79.3.

F site		σ_{iso}	δ_{iso}	$\delta_{csa}/\sigma_{csa}$	η_{csa}
F1	exp.		68.9	-285	0.1
	calc.	9.5	69.7	357.4	0.01
F2	exp.		84.5	-290	0.3
	calc.	-7.3	86.7	351.4	0.28
F3	exp.		84.5	-290	0.3
	calc.	-3.6	82.9	371.7	0.19
F4	exp.		102.5	-360	0.35
	calc.	-21.6	101.0	401.1	0.28
F5	exp.		75.2	-290	0.2
	calc.	3.7	75.6	359.7	0.24
F6	exp.		63.1	-280	0.2
	calc.	17.3	61.9	350.3	0.16
F7	exp.		94.3	-300	0.2
	calc.	-15.5	95.0	366.5	0.19

3.3.3 Experimental section

β-ZrF_4 was obtained from Ultra Fluor, Air products and chemicals (lot number 10921-PG78A). HfF_4 and ThF_4 were obtained from BDH-Limited supplier (lot numbers 581532F and 68104, respectively). All these samples are kept in a dry glove box under nitrogen atmosphere. CeF_4 samples were prepared by fluorination of highly divided CeO_2 with F_2 gas at T = 400-500 °C.[5]

3.3.3.1 ^{19}F solid state NMR

β-ZrF_4 2D homonuclear DQ-SQ MAS ^{19}F NMR correlation spectra were recorded on an Avance 750 Bruker spectrometer operating at 17.6 T (^{19}F Larmor frequency of 705.85 MHz), using a CPMAS 2.5 mm probehead. These spectra were collected at 32 kHz, using the sandwiched PI pulses (SPIP)[23] pulse sequence, which allows efficient broad-band homonuclear DQ recoupling in inorganic fluorides.[12,24] ^{19}F nutation frequencies of 225 kHz for the π pulse and of 280 kHz for the spin lock were used and the DQ excitation and reconversion times were set to 16 rotor periods (corresponding to ~500 μs). A total of 40 rotor-synchronized t_1 increments with 32 transients (recycle delay of 60 s) each were accumulated. Phase-sensitive detection in the indirect dimension was obtained using the States method.[25] The 2D DQ-SQ MAS spectra were converted in a SQ-SQ correlation representation by a shearing transformation.[26,27]

HfF_4 1D and 2D ^{19}F MAS NMR spectra were recorded on an Avance 850 spectrometer operating at 19.9T (^{19}F Larmor frequency of 800.04 MHz), using an ultrafast CPMAS 1.3 mm probehead. 1D spectra were acquired using a Hahn echo sequence with an inter-pulse delay equal to one rotor period. A 1.5 μs 90° pulse was used, corresponding to a ^{19}F nutation frequency of 170 kHz. The recycle delay was set to 10 s to ensure no saturation. The same SPIP[23] pulse sequence was used to collect the DQ-SQ MAS ^{19}F NMR correlation spectrum at 65 kHz. ^{19}F nutation frequency of 160 kHz for the π pulse was used, but no spin lock power was needed. The DQ excitation and reconversion times were set to 8 rotor periods (corresponding to ~123 μs). A total of 34 rotor-synchronized t_1 increments with 2176 transients (recycle delay of 3s) each were accumulated.

For ThF_4, ^{19}F Hahn echo MAS NMR spectra were recorded on an Avance 300 Bruker spectrometer operating at ^{19}F Larmor frequency of 282.2 MHz and using a 2.5mm CPMAS probehead. A 2.0 μs 90° pulse was used, corresponding to a ^{19}F nutation frequency of 125 kHz. The recycle delay was set to 10 s to ensure no saturation.

The ^{19}F chemical shifts are referenced to $CFCl_3$ at 0 ppm. All solid state NMR spectra were fitted using DMfit[28] software.

3.3.3.2 DFT Calculations

DFT calculations of the ^{19}F chemical shielding tensors, using the GIPAW method,[1,2] and ^{91}Zr EFG in ZrF_4, using the projector augmented-wave (PAW) approach[15,16] were performed with the NMR-CASTEP code[13,14] implemented in the Materials Studio 5.0 environment, for the experimental structure (named ES above) and atomic position optimized (APO) structures. The PBE (Perdew, Burke and Ernzerhof) functional[29] was used in the generalized gradient approximation (GGA) for the exchange-correlation energy, and the core-valence interactions were described by ultrasoft pseudopotentials (USPP) generated using the on the fly generator (OTF_USPP) included in CASTEP. The wave functions were expanded on a plane-wave basis set with a kinetic energy cutoff of 700 eV. The Brillouin zone was sampled using a Monkhorst-Pack grid spacing approximately equal to 0.04 $Å^{-1}$ (corresponding to a *k*-point mesh of 4 x 4 x 4). APO structures were obtained by minimizing (Fletcher-Goldfarb-Shanno (BFGS) method)[30] the residual forces on the atom up to $|F|_{max}$ below 10 meV.$Å^{-1}$, keeping symmetry constraints and fixing the cell parameters to the experimentally determined values.

^{91}Zr EFG in ZrF_4 were also calculated using the LAPW method[17] implemented in the WIEN2k code.[17,18] The atomic sphere radii (R_{MT}) were set to 2.00 and 1.70 a.u. for Zr and F, respectively. The core electron states were separated from the valence states by -6.0 Ry. Core states are from 1s to 3d for Zr and 1s for F. The plane wave cut-off is defined by $R_{MT}K_{MAX}$ = 8. We use the same Monkhorst-Pack grid spacing as with CASTEP. Total energies are converged up to changes smaller than 1.4×10^{-3} eV. APO structure was obtained by minimizing the residual forces acting on the atoms up to $|F|_{max}$ below 0.05 eV.$Å^{-1}$

The ^{91}Zr quadrupolar moment used for the calculation of quadrupolar coupling constant, C_Q, is $-0.176(3) \times 10^{-28} m^2$.[31]

3.3.4 Conclusion

The challenging study of these MF_4 compounds containing seven fluorine crystallographic sites and characterized by small or very small ^{19}F chemical shift ranges shows limits of both the correlation experiments, based on through space ^{19}F-^{19}F dipolar coupling interaction, and GIPAW[1,2] methods for the assignment of the ^{19}F NMR resonances to the fluorine crystallographic sites. Due to the small chemical shift ranges (7 ^{19}F isotropic NMR lines within a 21 ppm range for β-ZrF_4 and HfF_4), correlation spectra are not sufficiently resolved. Unfortunately, whereas the chemical shift range is larger for CeF_4 (39 ppm) the relaxation time T_2 is too short to perform correlation experiments. The chemical shift range is also larger for ThF_4 (39 ppm) and we are hopeful that correlation experiments could ensure the assignments done from GIPAW calculations. Indeed, from GIPAW calculations, only one complete and confident assignment is obtained, from the APO structure of ThF_4. For β-ZrF_4, a complete assignment is proposed but only a partial assignment of four of the seven NMR resonances can be considered as confident. For HfF_4 and CeF_4, no agreement between the experimental relative intensities of the NMR lines and the F site multiplicity sequences was obtained.

3.4 Conclusion

These studies of inorganic fluorides containing several fluorine crystallographic sites, NbF_5 and TaF_5 (3.2) on the one hand and β-ZrF_4, HfF_4, CeF_4 and ThF_4 (3.3) on the other hand, show that complete and unambiguous assignment of the ^{19}F NMR lines from GIPAW[1,2] calculations are achievable if the ratio δ_{iso} range/number of resonances is not too small.

Limits of experimental assignment from DQ-SQ correlation spectra are also observed with β-ZrF_4 and HfF_4. No confident assignment could be established as some isotropic lines overlap inducing lack of resolution in the correlation peaks.

For NbF_5, TaF_5 and ThF_4, a fine agreement is obtained, from APO structures, between the relative intensities of the NMR lines ranked in increasing order of experimental δ_{iso} values and the multiplicities of the F atoms ranked in decreasing order of calculated σ_{iso} values. Complete assignments of the ^{19}F resonances to the fluorine crystallographic sites are carried out and excellent linear correlations are observed between the experimental ^{19}F δ_{iso} and calculated ^{19}F σ_{iso} values. However, for NbF_5 and ThF_4, the slopes of the linear regressions are nearly equal to -1, when it is equal to -0.79 forTaF_5. This highlights the fact that, even if the exceptions are few (Ag (see 2.4), Nb and Th), the linear regression established in the chapter 2 is not universal.

3.5 References

(1) C. J. Pickard, F. Mauri, *Phys. Rev. B* **2001**, *63*, 245101.
(2) J. R. Yates, C. J. Pickard, F. Mauri, *Phys. Rev. B* **2007**, *76*, 024401.
(3) R. D. Burbank, F. N. Bensey Jr., *USAEC Rep.***1956**, *K-1280*, 1–19.
(4) Inorganic Crystal Structure Database (ICSD), version 1.9.1; FIZ Karlsruhe and NIST: Germany and Maryland, 2011.
(5) C. Legein, F. Fayon, C. Martineau, M. Body, J.-Y. Buzaré, D. Massiot, E. Durand, A. Tressaud, A. Demourgues, O. Péron, B. Boulard, Inorg. Chem. **2006**, 45, 10639–10641.
(6) G. Benner, B. G. Müller, *Z. Anorg. Allg. Chem.* **1990**, *588*, 33–42.
(7) R. Schmidt, B. G. Müller, *Z. Anorg. Allg. Chem.* **1999**, *625*, 605–608.
(8) B. Bureau, G. Silly, J-.Y. Buzaré, J. Emery, *Chem. Phys.* **1999**, *249*, 89–104
(9) O. Pauvert, F. Fayon, A. Rakhmatullin, S. Krämer, M. Horvatić, D. Avignant, C. Berthier, M. Deschamps, D. Massiot, C. Bessada, *Inorg. Chem.* **2009**, *48*, 8709–8717.
(10) C. Bessada, A. Rakhmatullin, A.-L.Rollet, D. Zanghi, *J. Nucl. Mater.* **2007**, *360*, 43–48.
(11) C. Martineau, C. Legein, J.-Y. Buzaré, F. Fayon, *Phys. Chem. Chem. Phys.* **2009**, *11*, 950–957.
(12) Q. Wang, B. Hu, F. Fayon, J. Trébosc, C. Legein, O. Lafon, F. Deng, J.-P. Amoureux, *Phys. Chem. Chem. Phys.* **2009**, *11*, 10391–10395.
(13) M. D. Segall, P. L. D. Lindan, M. J. Probert, C. J. Pickard, P. J. Hasnip, S. J. Clark, M. C. Payne, *J. Phys.: Condens. Matter* **2002**, *14*, 2717–2744.
(14) S. J. Clark, M.D. Segall, C. J. Pickard, P. J. Hasnip, M. J. Probert, K. Refson, M. C. Payne, Z. Kristallogr. 2005, 220, 567–570.
(15) H. M. Petrilli, P. E. Blöchl, P. Blaha, K. Schwarz, *Phys. Rev. B* **1998**, *57*, 14690–14697.
(16) P. E. Blöchl, *Phys. Rev. B* **1994**, *50*, 17953–17979.
(17) P. Blaha, K. Schwarz, P. Herzig, *Phys. Rev. Lett.* **1985**, *54*,1192–1195.
(18) P. Blaha, K. Schwarz, G. K. H. Madsen, D. Kvasnicka and J. Luitz, WIEN2k, An Augmented Plane WaVe Plus Local Orbitals Program for Calculating Crystal Properties (Vienna University of Technology, Vienna, 2001).
(19) M. Body, G. Silly, C. Legein, J.-Y. Buzaré, F. Calvayrac, P. Blaha, *J. Solid State Chem.* **2005**, *178*, 3655-3661.
(20) M. Body, G. Silly, C. Legein, J.-Y. Buzaré, F. Calvayrac, P. Blaha, *Chem. Phys. Lett.* **2006**, *424*,321-326.
(21) C. Martineau, M. Body, C. Legein, G. Silly, J.-Y. Buzaré, F. Fayon, *Inorg. Chem.* **2006**,*45*, 10215-10223.
(22) M. Body, C. Legein, J.-Y.Buzaré, G. Silly, P. Blaha, C. Martineau, F. Calvayrac, *J. Phys. Chem. A* **2007**, *111*, 11873-11884.
(23) B. Hu, Q. Wang, O. Lafon, J. Trébosc, F. Deng, J. P. Amoureux, *J. Magn. Reson.* **2009**, *198*, 41-48.
(24) Q. Wang, B. Hu, O. Lafon, J. Trébosc, F. Deng, J. P. Amoureux, *J. Magn. Reson.* **2010**, *203*, 113-138.
(25) D. States, R. Haberkorn, D. J. Ruben, *Magn. Reson.* **1982**, *48*, 286-292.
(26) R. R. Ernst, G. Bodenhausen, A. Wokaun, Principles of Nuclear Magnetic Resonance in One and Two Dimensions; Clarendon Press: Oxford, U.K., **1987**.
(27) F. Fayon, I. J. King, R. K.Harris, R. K. B. Gover, J. S. O. Evans, D. Massiot, *Chem. Mater.* **2003**, *15*, 2234-2239.
(28) D. Massiot, F. Fayon, M. Capron, I. King, S. Le Calvé, B. Alonso, J. O. Durand, B. Bujoli, Z. H. Gan, G. Hoatson, *Magn. Reson. Chem.* **2002**, *40*, 70-76.

(29) J. P. Perdew, K. Burke, M. Ernzerhof, *Phys. Rev. Lett.* **1996**, *77*, 3865–3868.
(30) B. G. Pfrommer, M. Cote, S. G. Louie, M. L. Cohen, *J. Comput. Phys.* **1997**, *131*, 233-240.
(31) P. Pyykkö, *Mol. Phys.* **2008**, *106*, 1965–1974.

Chapter 4: Structural investigation of ternary fluorides exhibiting large ^{19}F-X ^{1}J couplings by variable temperature X-ray powder diffraction and multinuclear solid-state NMR, and DFT calculations

4.1 Introduction

One of the purposes of the RMN3PL project was to calculate ^{19}F-X ^{1}J-couplings using the first-principles method presented by Joyce *et al.*[1] Indeed, in inorganic fluorides, some large heteronuclear ^{19}F-X ^{1}J-couplings are resolved on 1D solid-state NMR spectra. This is the case for the ^{31}P-^{19}F ^{1}J-coupling in Ag_2PO_3F,[2] K_2PO_3F, β-Na_2PO_3F, $BaPO_3F$, $K_2P_2O_5F_2$,[3] Hg_2PO_3F,[4] $NaPF_6$ and KPF_6,[5] the ^{69,71}Ga-^{19}F ^{1}J-coupling in $(NH_4)_3GaF_6$,[6] the ^{75}As-^{19}F ^{1}J-coupling in $KAsF_6$,[7] $[Mg(XeF_2)_4][AsF_6]_2$, $[Ca(XeF_2)_{2,5}][AsF_6]_2$, $[Ba(XeF_2)_3][AsF_6]_2$ and $[Ba(XeF_2)_5][AsF_6]_2$,[8] the ^{93}Nb-^{19}F ^{1}J-coupling in K_2NbF_7,[9] $Cdpy_4NbOF_5$, $[pyH]_2[Cdpy_4(NbOF_5)_2]$ (py = C_5H_5N)[10] and $CsNbF_6$,[11] the ^{115}In-^{19}F ^{1}J-coupling in β-$(NH_4)_3InF_6$,[12,13] the ^{119}Sn-^{19}F ^{1}J-coupling in $K_2SnF_6.H_2O$,[14] the ^{121,123}Sb-^{19}F ^{1}J-coupling in $KSbF_6$,[7] the ^{129}Xe-^{19}F ^{1}J-coupling in XeF_2,[15] $[Mg(XeF_2)_4][AsF_6]_2$, $[Ca(XeF_2)_{2,5}][AsF_6]_2$, $[Ba(XeF_2)_3][AsF_6]_2$ and $[Ba(XeF_2)_5][AsF_6]_2$,[8] the ^{207}Pb-^{19}F ^{1}J-coupling in α-[16,17] (see 2.4) and β-PbF_2[12,18] and the ^{209}Bi-^{19}F ^{1}J-coupling in α-$KBiF_6$.[19] Moreover, ^{207}Pb-^{19}F ^{1}J-couplings have been measured in $Pb_5Ga_3F_{19}$[20] and β-Pb_2ZnF_6[21] thanks to the multiple-quantum filtered *J*-resolved experiment[22] and ^{19}F-^{139}La ^{1}J-couplings have been determined in $RbLaF_4$ thanks to heteronuclear DQ-filtered *J*-resolved experiment.[23] The reported results for solids[2-23] or for molecules or ions (liquid state NMR)[24-54] show that the reduced ^{19}F-X ^{1}J-coupling constants, $K(^{19}F-X) = \frac{4\pi^2 J(^{19}F-X)}{(h\gamma_{^{19}F}\gamma_X)}$, allowing to remove the nuclear dependence of the coupling by factoring out the gyromagnetic ratios of the spin coupled nuclei,[55] increase with X atomic number in rows and columns of the periodic table.[24] Then this coupling increases with the size of the electronic cloud of X and with the covalent character of the F-X bond.

Except for ^{207}Pb-^{19}F and ^{19}F-^{139}La, the ^{19}F-X ^{1}J-couplings are observed only for compounds containing isolated $X(O)F_n$ ions. We then decided to study such compounds, KPF_6 (see 4.3) and $NaAsF_6$[56] (see 4.2), considering that precise structural determination remained to achieve. Unfortunately, ^{75}As-^{19}F ^{1}J-coupling calculations are not feasible at the moment; since the publication of the first results,[1] calculations of *J*-couplings remain only possible between light elements (Z < 20).[1,57-62] A. Sadoc achieved ^{31}P-^{19}F ^{1}J-coupling calculations, in collaboration with J. R. Yates, Department of Materials, University of Oxford, but not on the low temperature (LT) phases of KPF_6 (see 4.3) since we have encountered difficulties in determining their precise structures.

4.2 $NaAsF_6$

THE JOURNAL OF PHYSICAL CHEMISTRY C

Article

pubs.acs.org/JPCC

Structural Investigation of α- and β-Sodium Hexafluoroarsenate, $NaAsF_6$, by Variable Temperature X-ray Powder Diffraction and Multinuclear Solid-State NMR, and DFT Calculations

Mamata Biswal,[†] Monique Body,[†] Christophe Legein,*[,†] Gwenaël Corbel,[†] Aymeric Sadoc,[‡] and Florent Boucher[‡]

[†]LUNAM Université, Université du Maine, CNRS UMR 6283, Institut des Molécules et des Matériaux du Mans, Avenue Olivier Messiaen, 72085 Le Mans Cedex 9, France

[‡]Institut des Matériaux Jean Rouxel (IMN), Université de Nantes, CNRS, 2 rue de la Houssinière, BP 32229, 44322 Nantes Cedex 3, France

Supporting Information

ABSTRACT: We report the phase transition between the α- and β-phases of $NaAsF_6$ monitored by DTA, variable temperature ^{19}F solid-state NMR and temperature controlled X-ray powder diffraction (XRPD) as well as their crystalline structures determined from XRPD data. The structural type of β-$NaAsF_6$ has been determined thanks to ^{19}F and ^{75}As solid-state NMR experiments. ^{19}F, ^{23}Na, and ^{75}As NMR parameters, including $^{19}F-^{75}As$ ^1J coupling, have been measured for both phases. The ^{19}F, ^{23}Na, and ^{75}As solid-state NMR investigations are in full agreement with both crystalline structures from a qualitative point of view. Chemical shielding tensors have been calculated from the gauge including projector augmented wave approach. The electric field gradient tensors of ^{23}Na and ^{75}As have been calculated in α-$NaAsF_6$ from the all-electrons method and the projector augmented-wave approach. Two difficulties were encountered: the libration of the rigid and regular AsF_6^- anions in the β-phase, highlighted by the atomic anisotropic displacement parameters for F, which leads to erroneous shortened As−F bond length, and the overestimation of the As−F bond length with the PBE functional used in the density functional theory calculations. We show that both difficulties can be overcome by full optimization and rescaling of the cell parameters of the crystalline structures. Additionally, a linear correlation is observed between experimental ^{23}Na δ_{iso} values and calculated ^{23}Na σ_{iso} values from previously reported data and from our own measurements and calculations.

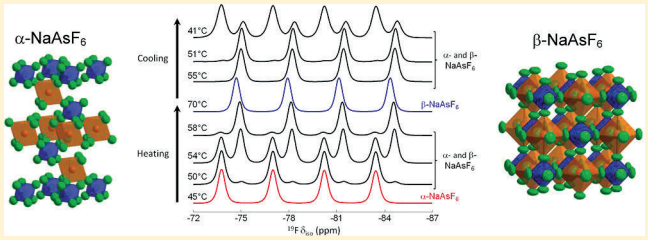

1. INTRODUCTION

Over the years, solid-state nuclear magnetic resonance (NMR) spectroscopy has become an important tool for structural investigation of materials, giving a local insight into nucleus surrounding that is complementary to the structural information provided by diffraction techniques. As compared with other NMR interactions, the J coupling, which is characteristic of the chemical bond, has received far less attention because it is usually so small in magnitude that it is masked by the linewidths. Nevertheless, the scalar (isotropic) part of J coupling, which is not averaged by magic angle spinning (MAS), can be evidenced in many systems and exploited to characterize the extended coordination sphere. In inorganic fluorides, some large heteronuclear $^{19}F-X$ ^1J couplings are resolved on 1D solid-state NMR spectra. This is the case for the $^{19}F-^{75}As$ ^1J coupling in $KAsF_6$,[1] $[Mg(XeF_2)_4][AsF_6]_2$, $[Ca(XeF_2)_{2.5}][AsF_6]_2$, $[Ba(XeF_2)_3][AsF_6]_2$, and $[Ba(XeF_2)_5][AsF_6]_2$,[2] which contain isolated AsF_6^{5-} ions.

In the past decade, the Gauge Including Projector Augmented Wave (GIPAW) approach[3,4] has been used to compute chemical shielding and electric field gradient (EFG) tensors using periodic boundary conditions. More recent work has enabled the calculation of J-coupling between light elements ($Z < 20$).[5−11] Developments are in progress to extend this approach to heavy elements.[8] In this context, as compounds with well characterized crystalline structures and known J values will be required, our attention was focused on the fluoride compound $NaAsF_6$.

Recently, Zhang et al.[12] have shown that the complex between $NaAsF_6$ salt and polyethylene oxide (PEO) exhibits at 25 °C an alkali ionic conductivity higher than the one of the $LiAsF_6$ analogue.[13] However, little is known about this sodium hexafluoroarsenate. $NaAsF_6$ displays a structural phase transition, reported at 37 °C, from a low temperature rhombohedral α form (PDF[14] file 00-051-1767), adopting the $LiSbF_6$ structural type (space group $R\bar{3}$),[15,16] to a high temperature cubic β form (PDF file 00-051-1768, space group $Fm\bar{3}m$). The cell parameters were determined for α-[15]

Received: April 27, 2012
Revised: May 3, 2012
Published: May 4, 2012

and β-$NaAsF_6$ (PDF[14] file 00-051-1768), but no atomic coordinates were reported for both polymorphs. In the present article, the thorough structural analysis carried out on this compound by solid-state NMR, X-ray powder diffraction (XRPD), and density functional theory (DFT) calculations is reported.

At first, the phase transition was investigated by differential thermal analysis (DTA), variable temperature (VT) ^{19}F solid-state NMR, and temperature controlled XRPD. The refinements of the crystal structures of α and β forms were performed from X-ray diffraction data. For the β-phase, solid-state NMR, which reveals the number of nonequivalent crystallographic sites for each nucleus and provides information about the local symmetry of these sites, supplies decisive information in the selection of a structural model. Moreover, ^{19}F, ^{23}Na, and ^{75}As NMR parameters have been determined and calculated for both phases. Chemical shielding tensors have been calculated from the GIPAW approach[3,4] using the CASTEP code.[17] The nonrelativistic version of the GIPAW Hamiltonian was sufficient, being only concerned by shielding tensors of light elements (^{19}F and ^{23}Na). EFG tensors of ^{23}Na and ^{75}As have been calculated in α-$NaAsF_6$ from the all-electrons (AE) method and the projector augmented-wave (PAW) approach[18,19] using the WIEN2k[20,21] and CASTEP[17] codes, respectively. Considering the low accuracy of atomic positions of light elements from XRPD data and the high sensitivity of DFT calculations to the structural data set, structure optimizations, by minimization of the forces acting on the nuclei, are usually necessary. The coupling of XRPD with a precise determination of quadrupolar NMR parameters and ab initio calculations of these NMR parameters has proven to be a reliable way to improve atomic coordinate accuracy.[22−32] Concerning $NaAsF_6$, two difficulties are encountered: the libration of the AsF_6^- anions in the β-phase leading to short As−F bond length and the overestimation of the As−F bond length in relation with the functional used in the DFT calculations. These difficulties can be overcome by full optimization and rescaling of the cell parameters of the crystalline structures.

2. EXPERIMENTAL SECTION

2.1. Sample. The $NaAsF_6$ sample was purchased from Sigma-Aldrich (lot number 223719). Prior to use, the phase purity of the as-received powder was checked by XRPD at RT. In addition to the diffraction lines of a major α-$NaAsF_6$ phase (PDF[14] file 00-051-1767), an unknown impurity was evidenced. Since fluorides are well-known to be hygroscopic, an attempt to dehydrate the sample was carried out. Pure α-$NaAsF_6$ powder was finally obtained by heating at 190 °C for 9 h under vacuum the as-received sample, thus confirming that it was partially hydrated. All characterizations reported hereafter were therefore performed on freshly dehydrated powder.

2.2. Thermal Analysis. DTA was performed on a 102 mg dehydrated powder sample of $NaAsF_6$ with a TGA/DTA Q600 SDT TA Instruments apparatus (Pt crucibles, α-Al_2O_3 as a reference) under nitrogen flow (100 mL/min) in the room temperature (RT) 68 °C range (heating/cooling rate of 1 °C/min).

2.3. Solid-State NMR Experiments. NMR experiments were performed on a Bruker Avance 300 (7 T) spectrometer operating at Larmor frequencies of 282.4, 79.39, and 51.39 MHz for ^{19}F, ^{23}Na, and ^{75}As, respectively. A ^{19}F optimized 2.5 mm CP-MAS probe head was used to perform all the experiments, except the ^{23}Na and ^{75}As experiments with ^{19}F decoupling on β-$NaAsF_6$, which were achieved with a 4 mm CP-MAS probe. ^{19}F, ^{23}Na, and ^{75}As chemical shifts are referenced to $CFCl_3$, 1 M NaCl aqueous solution, and 0.05 M $NaAsF_6$ acetonitrile solution, respectively.

The VT (from 40 to 70 °C, at increasing and decreasing temperature) ^{19}F MAS Hahn echo spectra were acquired using a 2.75 μs 90° pulse and an interpulse delay synchronized with the rotor period. The recycle delays were set to 5 s, and 32 transients were accumulated. No change in NMR spectrum was noted ~30 min after changing the temperature, thus indicating that the temperature of the sample is stable.

The ^{23}Na MAS spectrum of the α-phase was acquired at a spinning frequency of 20 kHz. The recycle delay was set to 1 s. The linear regime was ensured by using short pulse duration (1 μs) at a radio frequency (RF) field strength of 62 kHz. For the β-phase, a ^{23}Na MAS Hahn echo spectrum was acquired with ^{19}F continuous wave decoupling (nutation frequency of 58 kHz), at a spinning frequency of 5 kHz, using a pulse duration equal to 12 μs (RF field strength equal to 21 kHz). For both the spectra, the recycle delay was set to 5 s.

The ^{75}As MAS Hahn echo spectra were recorded, without and with ^{19}F continuous wave decoupling (nutation frequency of 40 kHz and 58 kHz for the α- and β-phase, respectively), at spinning frequency of 20 kHz for the α-phase and at spinning frequencies of 5 kHz and 25 kHz for the β-phase. The ^{75}As experiments were performed using, for the α-phase, a 6 μs pulse (RF field strength equal to 40 kHz), and for the β-phase, a 10 μs pulse (RF field strength equal to 25 kHz) and a 14 μs pulse (RF field strength equal to 18 kHz) at spinning frequencies of 25 kHz and 5 kHz, respectively. For all the ^{75}As spectra, the recycle delay was set to 5 s.

The temperature of the sample was calibrated for the 2.5 mm and 4 mm probes, at the same spinning frequencies as in the ^{19}F, ^{23}Na, and ^{75}As experiments, using the ^{207}Pb isotropic chemical shift of $Pb(NO_3)_2$.[33,34] The temperature gradient over the dimension of the rotor was estimated by these experiments, about 1 °C for the 4 mm probe at 5 kHz and 10 °C for the 2.5 mm probe at 25 kHz. All solid-state NMR spectra were fitted by using the DMFit software.[35]

2.4. X-ray Powder Diffraction. Temperature-controlled X-ray diffractograms were collected under flowing nitrogen at 1 °C intervals between 30 and 82 °C (heating rate of 1 °C/min) using a PANalytical θ/θ Bragg−Brentano X'pert MPD PRO diffractometer ($CuK\alpha_{1+2}$ radiations) equipped with the X'Celerator multielements detector and a HTK 1200 Anton Paar furnace attachment using an Al_2O_3 sample holder cup. To determine the transition temperatures of $NaAsF_6$ upon heating and cooling, patterns were recorded in the [15−35°] scattering angle range with a 0.0167° step for 15 min at each temperature (with a prior temperature stabilization for 15 min). The crystal structures of α- and β-$NaAsF_6$ have been refined with the Fullprof program[36] by the Rietveld method[37] from high resolution diffractograms collected during 7 h in the [15−130°] scattering angle range with a 0.0167° step at room temperature and 74 °C, respectively.

Note that a temperature calibration of the HTK 1200 Anton Paar furnace was carried out using the structural phase transitions of VO_2 (metal to insulator transition), $Bi_4V_2O_{11}$ ($\alpha \rightarrow \beta$ and $\beta \rightarrow \gamma$), and of $Ba_2In_2O_5$ (brownmillerite to perovskite transition).[38]

2.5. Theoretical Calculations. The isotropic chemical shielding is defined as $\sigma_{iso} = (\sigma_{xx} + \sigma_{yy} + \sigma_{zz})/3$, σ_{ii} being the

principal components of the shielding tensor defined in the sequence $|\sigma_{zz} - \sigma_{iso}| \geq |\sigma_{xx} - \sigma_{iso}| \geq |\sigma_{yy} - \sigma_{iso}|$. The isotropic chemical shift is defined as $\delta_{iso} \approx -[\sigma_{iso} - \sigma_{ref}]$.

Several structural data sets were used for the calculations with the CASTEP[17] code: the experimental structures determined from XRPD data (named IS in the following for initial structures), the structures obtained after PBE (Perdew, Burke, and Ernzerhof)[39]−DFT atomic position optimization (APO structures), and the structures obtained after full geometry optimization (FO structure, variation of both the lattice parameters and atomic coordinates). Nevertheless, it is well-known that the GGA (generalized gradient approximation) with the PBE functional overestimates interatomic bond lengths and consequently cell parameters and unit-cell volumes.[40−53] In the present case, the overestimation was well above the classically admitted values and to take this effect into account, the optimized lattice parameters were rescaled to the experimental volume but keeping atomic positions unchanged, leading to a fourth structural data set (FO rescaled structures). To obtain converged σ values, a plane wave basis set energy cutoff of 700 eV was necessary using an ultrasoft pseudopotential and a Monkhorst−Pack grid density approximately equal to 0.04 Å^{-1} (corresponding to a k-point mesh of 6 × 6 × 6 for the primitive cells of the α- and β-phases) was enough. For the electronic loops, the PBE functional[39] was used for the exchange-correlation potential. Geometries were converged for total energy changes smaller than 1×10^{-6} eV, minimizing the residual forces on the atom up to 10 meV·Å^{-1}, with a displacement convergence parameter of 5×10^{-4} Å and a stress convergence parameter of 2×10^{-2} GPa.

The EFG at a nucleus arises from the distribution of charges about it in space. For the nucleus having spin greater than 1/2, i.e., quadrupolar nuclei, the quadrupolar frequency ν_Q, the quadrupolar coupling constant C_Q, and the asymmetry parameter η_Q are related to the EFG tensor components through the following equations: $\nu_Q = 3C_Q/2I(2I - 1)$ with $C_Q = eQV_{zz}/h$, and, $\eta_Q = (V_{xx} - V_{yy})/V_{zz}$. The V_{ii} are the eigenvalues of the EFG tensor with the convention $|V_{zz}| \geq |V_{yy}| \geq |V_{xx}|$, e is the electronic charge, I the nuclear spin quantum number, and h Planck's constant. The corresponding quadrupolar frequencies were calculated using the nuclear quadrupolar moments reported by Pykko:[54] $Q(^{23}Na) = 0.104 \times 10^{-28}$ m^2 and $Q(^{75}As) = 0.314 \times 10^{-28}$ m^2.

EFG tensors were calculated for ^{23}Na and ^{75}As in both phases using the PAW approach implemented in CASTEP[17] and also the linearized augmented plane wave (LAPW) method implemented in the WIEN2k[20,21] package. For consistency with the results obtained using the PAW method, the same PBE functional was used in WIEN2k. The atomic sphere radii (R_{MT}) were set to 1.80 au and 1.82 au for Na and As and 1.30 au and 1.20 au for F in the α- and β-phases, respectively. The plane wave cutoff was defined by $R_{MT}K_{MAX} = 8$. We use the same Monkhorst−Pack scheme as for CASTEP. Two sets of structures were used, the initial one and the WIEN2k APO structure, obtained by minimizing the residual forces on the atom up to 2 mRy/au (50 meV·Å^{-1}).

3. RESULTS AND DISCUSSION

3.1. Phase Transition Monitored by DTA, Temperature-Controlled XRPD, and VT ^{19}F NMR. *3.1.1. DTA and Temperature-Controlled XRPD.* The DTA curve (Figure 1) of $NaAsF_6$ exhibits one endothermic peak on heating up and one exothermic event on cooling down with a hysteresis of 16 °C. It

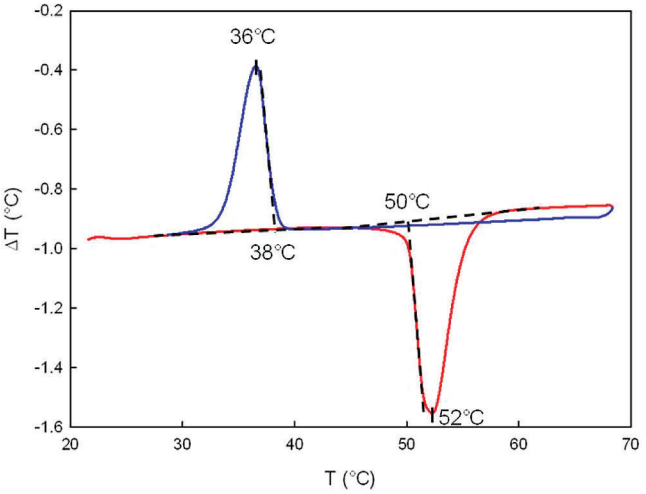

Figure 1. DTA curve of $NaAsF_6$ recorded, under nitrogen flow (100 mL/min), from 22 to 68 °C (in red) and from 68 to 29 °C (in blue), with heating/cooling rate of 1 °C/min. The starting temperatures T_{onset} and the temperatures at the signal maxima that correspond to a conversion rate of 50% are indicated.

indicates that a reversible transformation takes place in $NaAsF_6$ that we have ascribed from temperature-controlled XRPD (Figure 2) to the first order $\alpha \rightarrow \beta$ structural transition since the diffraction diagrams at temperature higher than 61 °C on heating up and higher than 42 °C on cooling down are in agreement with the PDF[14] file 00-051-1768 displayed for the β-$NaAsF_6$ phase. The starting temperature T_{onset} and the temperature at the signal maximum that corresponds to a conversion rate of 50% are reported for the $\alpha \rightarrow \beta$ and $\beta \rightarrow \alpha$ transformations in Figure 1 and Table 1. On the temperature controlled XRPD patterns (Figure 2), one can observe that, with increasing temperature, the phase transition $\alpha \rightarrow \beta$ starts at 49 °C and ends at 61 °C (it is difficult to distinguish the α-phase for higher temperatures), and with decreasing temperature, the $\beta \rightarrow \alpha$ phase transition starts at 42 °C (it is difficult to distinguish the α-phase for higher temperatures) and ends at 35 °C. More precisely, the fraction of α-$NaAsF_6$ at any temperature upon heating and cooling was calculated from the ratio between the integrated intensity[55] of the (101) Bragg reflection ($2\theta \approx 20.2°$) at this temperature and at room temperature. Then, the starting temperature T_{onset} and the temperature that corresponds to a conversion rate of 50% have been also deduced from the XRPD data (Figure 2c) and are reported, for the $\alpha \rightarrow \beta$ and $\beta \rightarrow \alpha$ transformations, in Table 1.

3.1.2. VT ^{19}F NMR. The phase transition was also studied by VT ^{19}F NMR (Figure 3). α-$NaAsF_6$ being isostructural with $LiSbF_6$,[56] it contains one F and one As crystallographic sites and each F atom is neighbored by $n = 1$ As atom. Thereby, the ^{19}F NMR spectrum of α-$NaAsF_6$ recorded at 45 °C exhibits four lines of equal intensities, i.e., a 1:1:1:1 quartet, arising from the J-coupling between ^{19}F and ^{75}As ($2nI + 1$ lines with $n = 1$ and $I = 3/2$). The VT ^{19}F NMR spectra confirm the occurrence of a hysterisis and show that both α- and β-phases exist simultaneously on a temperature range approximately equal to 20 °C. With increasing temperature, the phase transition starts at ~50 °C and ends at ~70 °C, whereas with decreasing temperature, the phase transition starts at ~51 °C, and the β-phase still exists at 41 °C. The ^{19}F NMR spectrum of β-$NaAsF_6$ recorded at 70 °C exhibits also four lines of equal intensities.

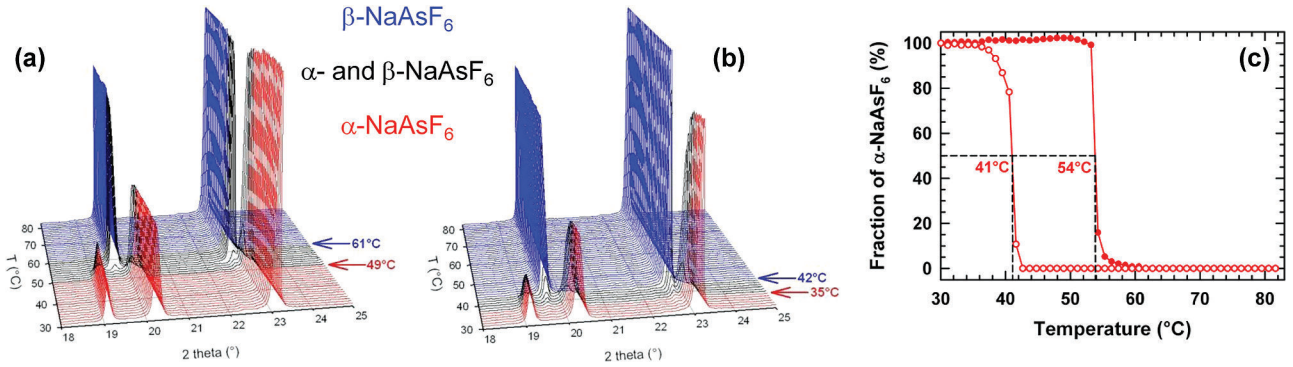

Figure 2. Temperature-controlled XRPD patterns ([18−25°] 2θ range) of $NaAsF_6$ recorded with increasing (a) and decreasing temperature (b). The diagrams corresponding to α-, β-, and mixture of α- and β-$NaAsF_6$ are represented in red, blue, and black, respectively. Temperatures at which the transition starts and ends upon heating or on cooling are indicated. Temperature dependence of the fraction of α-$NaAsF_6$ (c) upon heating (solid circle) and cooling (open circle). The temperatures that correspond to a conversion rate of 50% are indicated.

Table 1. Transition Temperatures (°C) (Starting Temperature (T_{onset}) and Temperature at the Signal Maximum Corresponding to a Conversion Rate of 50% (T_{max})) Determined by DTA, Temperature-Controlled XRPD, and VT ^{19}F NMR on Heating Up ($\alpha \rightarrow \beta$) and on Cooling Down ($\beta \rightarrow \alpha$)

	$\alpha \rightarrow \beta$		$\beta \rightarrow \alpha$	
	T_{onset}	T_{max}	T_{onset}	T_{max}
DTA	50	52	38	36
XRPD	49	54	42	41
^{19}F NMR	∼50	∼54	∼51	∼41

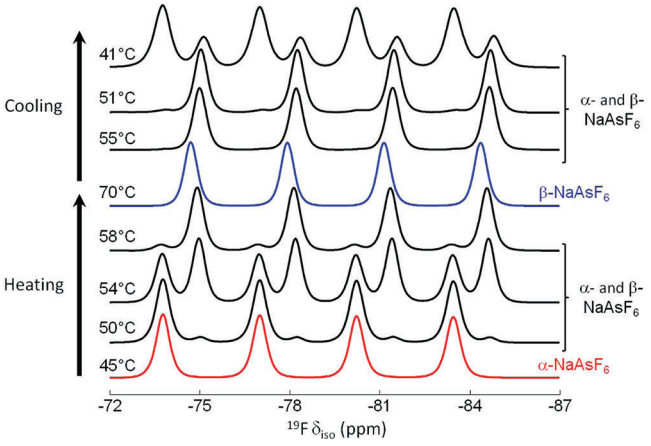

Figure 3. VT MAS (25 kHz) ^{19}F NMR spectra of $NaAsF_6$ on heating, from 45 to 70 °C, and on cooling, from 70 to 41 °C. The spectra corresponding to α-, β-, and a mixture of α- and β-$NaAsF_6$ are represented in red, blue, and black, respectively.

Then β-$NaAsF_6$ also contains one F and one As crystallographic site and each F atom is neighbored by n = 1 As atom.

A fine agreement is observed between the transition temperatures determined from DTA, temperature-controlled XRPD and VT ^{19}F NMR experiments (Table 1). Apart from the T_{onset} on cooling down determined by VT ^{19}F NMR, the slight differences in temperature are of the same order of magnitude than the uncertainties on temperature. Inhomogeneous temperature of the sample due to temperature gradient (see experimental section) could be invoked to explain this discrepancy. The single transition temperature reported in the PDF[14] files 00-051-1767 and 00-051-1768, i.e., 37 °C, is actually the temperature of the $\beta \rightarrow \alpha$ transition.

The fits (not shown) of the ^{19}F MAS NMR spectra of α- and β-$NaAsF_6$ (Figure 3) lead to similar δ_{iso} and $^{19}F-^{75}As$ ^1J-coupling values (Table 2) for both phases, indicating similar As−F and Na−F bond lengths in α- and β-$NaAsF_6$. The $^{19}F-^{75}As$ ^1J-coupling values in α- and β-$NaAsF_6$ are also similar to the previously reported ones in $KAsF_6$ (905 Hz),[1] $[Mg(XeF_2)_4][AsF_6]_2$ (920 Hz),[2] $[Ca(XeF_2)_{2.5}][AsF_6]_2$ (930 Hz),[2] $[Ba(XeF_2)_3][AsF_6]_2$ (946 Hz),[2] and $[Ba(XeF_2)_5][AsF_6]_2$ (950 Hz).[2]

J-couplings would normally be difficult to observe in the ^{19}F MAS NMR spectra due to line broadening caused by the large fluorine homonuclear dipolar couplings. The ^{19}F MAS NMR spectra of α- and β-$NaAsF_6$ indicate fluorine motion since they exhibit sharp lines (∼150 Hz), well-resolved quadruplets with constant spacing between the peaks, and small spinning sidebands ($\delta_{aniso} \approx 50$ ppm). Actually, $^{19}F-X$ ^1J couplings are resolved on 1D solid-state NMR spectra in several compounds, containing isolated XF_n anions, where intranionic fluorine motions have been evidenced: $^{19}F-^{75}As$ in $KAsF_6$,[1] $^{31}P-^{19}F$ in $NaPF_6$ and KPF_6,[57] $^{69,71}Ga-^{19}F$ in $(NH_4)_3GaF_6$,[58] $^{93}Nb-^{19}F$ in K_2NbF_7,[59] $^{115}In-^{19}F$ in $(NH_4)_3InF_6$,[60] $^{121,123}Sb-^{19}F$ in

Table 2. Experimental ^1J $^{19}F-^{75}As$ (Hz), ^{19}F Experimental Isotropic Chemical Shifts ($\delta_{iso,exp}$, ppm), Calculated Isotropic Chemical Shieldings ($\sigma_{iso,cal}$, ppm), and Shifts ($\delta_{iso,cal}$, ppm) from Initial Structure (IS) and after Atomic Position Optimization (APO Structures), Full Geometry Optimization (FO structures), and Full Geometry Optimization with Rescaling of the Cell Parameters (FO Rescaled Structures) in α-$NaAsF_6$ and β-$NaAsF_6$

			$\sigma_{iso,cal}$				$\delta_{iso,cal}$			
	^1J	$\delta_{iso,exp}$	IS	APO	FO	FO rescaled	IS	APO	FO	FO rescaled
α-$NaAsF_6$	910 (±5)	−78.5 (±0.2)	221.8	155.5	156.0	209.3	−88	−35	−36	−78
β-$NaAsF_6$	910 (±5)	−79.5 (±0.2)	277.8	174.1	160.6	233.2	−133	−50	−39	−98

dx.doi.org/10.1021/jp3040727 | J. Phys. Chem. C 2012, 116, 11682−11693

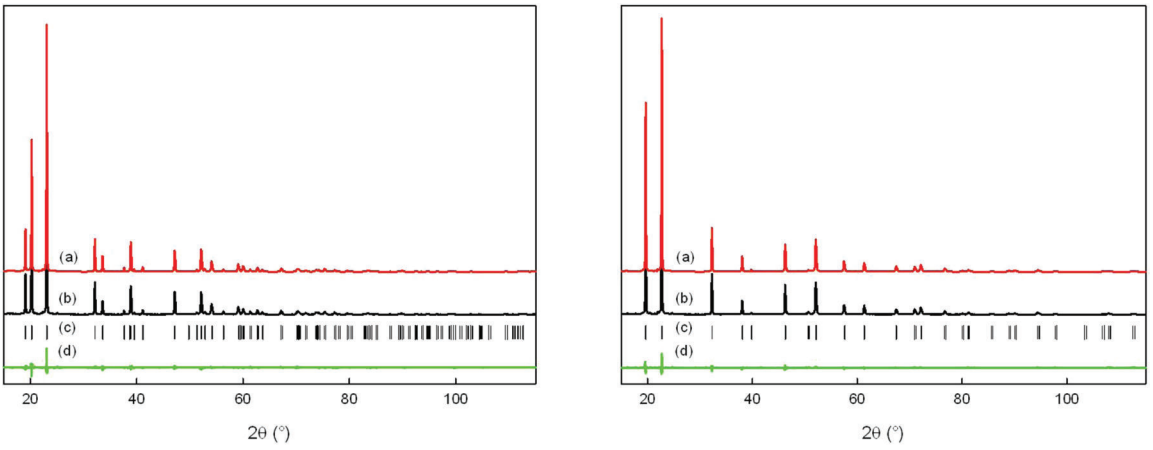

Figure 4. Calculated (a), observed (b), and difference (d) diffraction patterns of α-$NaAsF_6$ at RT (left) and β-$NaAsF_6$ at 74 °C (right). Vertical markers give Bragg peak positions (c).

Table 3. Site Symmetry, Atomic Coordinates (x, y, z), IDPs (U_{iso}, Å^2) or ADPs (U_{xx}, Å^2), and Calculated Bond Valence Deduced from Rietveld Refinements for α- and β-$NaAsF_6$ (Space Groups $R\bar{3}$ (no. 148) and $Fm\bar{3}m$ (no. 225), Respectively)

	sym.	x	y	z	U_{iso}	U_{11}	U_{22}	U_{33}	bond valence
α-$NaAsF_6$									
F	1	0.0402(8)	0.2763(9)	0.0713(4)	0.053(3)				0.99(3)
As	$\bar{3}$	0	0	0	0.035(1)				4.8(1)
Na	$\bar{3}$	0	0	1/2	0.042(3)				1.11(3)
β-$NaAsF_6$									
F	$4mm$	0.2068(6)	0	0		0.060(3)	0.156(4)	0.156(4)	1.17(3)
As	$m\bar{3}m$	0	0	0	0.040(1)				5.91(6)
Na	$m\bar{3}m$	1/2	1/2	1/2	0.051(2)				1.10(1)

Table 4. As−F and Na−F Bond Lengths (Å) for α- and β-$NaAsF_6$ and F−Na−F, F−As−F, and Na−F−As Angles (deg) for α-$NaAsF_6$ from Initial Structure (IS) and after Atomic Position Optimization (APO Structures) using Wien2k and CASTEP and Full Geometry Optimization (FO Structures) and Full Geometry Optimization with Rescaling of the Cell Parameters (FO Rescaled Structures) using CASTEP

		Wien2k		CASTEP		
	bond lengths and angles	IS	APO	APO	FO	FO rescaled
α-$NaAsF_6$	As−F	1.702(5)	1.764	1.763	1.766	1.715
	Na−F	2.303(4)	2.315	2.324	2.360	2.292
β-$NaAsF_6$	As−F	1.626(5)	1.752	1.750	1.764	1.690
	Na−F	2.305(5)	2.178	2.181	2.338	2.240
α-$NaAsF_6$	F−Na−F	90.10(16), 89.90(16)	91.10, 88.90	91.31, 88.69	90.11, 89.89	90.11, 89.89
	F−As−F	90.77(23), 89.23(23)	90.10, 89.90	90.08, 89.92	90.02, 89.98	90.02, 89.98
	Na−F−As	148.9(3)	142.0	141.4	148.5	148.5

$KSbF_6$,[1,57] and $^{209}Bi-^{19}F$ in $KBiF_6$.[61] The width of the ^{19}F NMR line does not evolve between the α- and β-phases or with temperature for each phase. In this small range of temperature, the motion of fluorine atoms cannot be probed by powder VT ^{19}F MAS NMR since the line width is much smaller than the inverse of the correlation time τ_c for the motion. In α- and β-$NaAsF_6$, the fluorine motions partially average $^{19}F-^{19}F$ homonuclear (and lower $^{19}F-^{23}Na$ and $^{19}F-^{75}As$ heteronuclear) dipolar interactions and ^{19}F chemical shift anisotropy.

3.2. Crystal Structure Refinements. *3.2.1. α-$NaAsF_6$ at Room Temperature.* XRPD diagram of the α-$NaAsF_6$ phase recorded at RT was satisfactorily fitted by the Le Bail method in an hexagonal cell with the space group $R\bar{3}$ (no. 148) reported for $LiSbF_6$.[56] The cell parameters are in good agreement with those previously reported.[15] Therefore, the atomic positions of $LiSbF_6$ were used as starting structural model for the Rietveld refinement, replacing Li and Sb atoms by Na and As atoms, respectively. Unit cell parameters, atomic coordinates of fluorine atom and atomic isotropic displacement parameters (IDPs) of all atoms were refined together, thus leading to satisfactory reliability factors: R_{wp} = 9.3%, R_{Bragg} = 2.8%, and R_{exp} = 3.3%. The refined parameters of the hexagonal cell are a = 5.3375(5) Å and c = 13.9645(12) Å. Figure 4 shows the observed, calculated, and difference diffraction patterns of α-$NaAsF_6$ at RT. Atomic positions and IDPs, bond valence values,[62] and structural features are gathered in Tables 3 and 4.

3.2.2. β-$NaAsF_6$ at 74 °C. A full-profile pattern matching of the XRPD diagram of the β-phase recorded at 74 °C leads to a perfect agreement with the data displayed in the PDF[14] file 00-051-1768 confirming the $Fm\bar{3}m$ space group. The crystal structure types of $A^IM^VF_6$ compounds have been classified into six main groups:[16] the $LiSbF_6$ type (rhomboedral, space group

dx.doi.org/10.1021/jp3040727 | J. Phys. Chem. C 2012, 116, 11682−11693

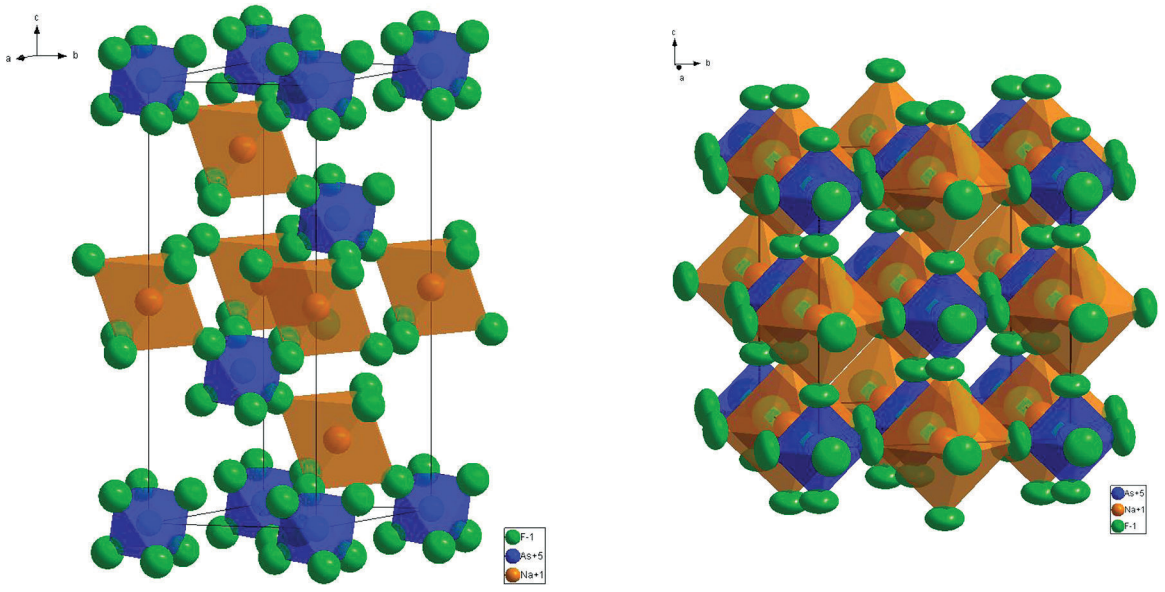

Figure 5. Structural view of α-$NaAsF_6$ (left) and β-$NaAsF_6$ (right). Thermal ellipsoids at 50% probability of Na^+ (orange), As^{5+} (blue), and F^- (green) atoms are drawn. Thermal ellipsoids are drawn for atoms at 50% probability level. The AsF_6^- anions and NaF_6^{5-} octahedra are represented in blue and orange, respectively.

$R\bar{3}$), the $NaSbF_6$ type (cubic, space group $Fm\bar{3}m$), structures of cubic APF_6 and $AAsF_6$ with orientational disorder of the $M^VF_6^-$ anions ($AgPF_6$ and $CsPF_6$ types, space group $Fm\bar{3}m$), the tetragonal $KSbF_6$ (T) types and similar structures, the $AgSbF_6$ type and similar structures (cubic, space group $Ia\bar{3}$), and, finally, the $KOsF_6$ type (rhombohedral, space group $R\bar{3}$). Three of these structural types adopt the cubic $Fm\bar{3}m$ space group: $NaSbF_6$, $AgPF_6$, and $CsPF_6$. In the $AgPF_6$ structure, the fluorine atoms reside on two distinct crystallographic sites (special positions 24e and 48h), both sites having an occupancy factor of 1/3.[63] This leads to two sets of regular PF_6^- octahedra oriented in a different way and differing in P−F bond length. Assuming that β-$NaAsF_6$ isotypic with $AgPF_6$ would then imply two ^{19}F resonances, two ^{75}As resonances, and two different $^{19}F-^{75}As$ ^1J coupling constants. In the $CsPF_6$ structure,[63] the fluorine atoms partially occupy a single crystallographic site (special position 96k of the space group $Fm\bar{3}m$ with an occupancy ratio of 1/4). This description of the orientational disorder of the $M^VF_6^-$ anions induces a large number of differently oriented and distorted $M^VF_6^-$ octahedra. Consequently, the $NaSbF_6$ structural type, which contains a single fully occupied F crystallographic site and regular SbF_6^- octahedra, remains the only one that is consistent with the solid-state NMR study of β-$NaAsF_6$ showing a single isotropic ^{19}F NMR line and, as shown below, ^{75}As quadrupolar parameters equal to zero indicating regular AsF_6^- octahedra.

Therefore, the crystal structure of β-$NaAsF_6$ has been refined from XRPD pattern by the Rietveld method using the cubic structure of $NaSbF_6$[64] as a starting structural model. The atomic IDPs of all the atoms were refined. This led to satisfactory reliability factors but quite large atomic IDP for F (U_{iso} = 0.110 Å^2), compared to Na and As atoms or to F atom in α-$NaAsF_6$ (Table 3). The analysis of Fourier difference maps around the fluorine sites give evidence for anisotropic electronic density deformation (ellipsoidal shape). It confirms that the structures of $AgPF_6$ (two F crystallographic sites) and $CsPF_6$ (F atoms on a special position (96k) with an occupancy ratio of 1/4) were effectively irrelevant. Subsequently, a second refinement including atomic anisotropic displacement parameters (ADPs) for fluorine atom leads to better reliability factors: R_{wp} = 7.8%, R_{Bragg} = 1.9%, and R_{exp} = 3.2% (Figure 4). The refined cell parameter is a = 7.8608(2) Å. Atomic positions, atomic IDPs (required by site symmetry) for Na and As atoms and ADPs for F atoms, and bond valence values[62] are gathered in Table 3, and the structural features are gathered in Table 4.

3.3. Crystal Structure Descriptions, AsF_6^- Anion Libration, and Phase Transition. *3.3.1. Crystal Structure of α-$NaAsF_6$.* The structure of α-$NaAsF_6$ (Figure 5) consists of pseudo NaCl-type (6,6)-coordination arrangement of hexafluoroarsenate and sodium ions. The Na^+ ion is then 6-fold coordinated by fluorine ions from six hexafluoroarsenate groups. This structure could also be described as a distorted derivative of the ReO_3 structure since it consists of layers of AsF_6^- and NaF_6^{5-} octahedra alternating along the hexagonal c-axis of the structure. Because of the $\bar{3}$ local symmetry the AsF_6^- and NaF_6^{5-} octahedra present only angular distortions that are small in magnitude for both polyhedrons (Table 4). The As−F bond length (Table 4) is shorter than the sum of the ionic radii ($^{[6]}As^V + {}^{[2]}F^-$ = 1.745 Å)[65] but similar to As−F bond lengths previously reported in crystalline structures containing such $As^VF_6^-$ groups, for instance, in $LiAsF_6$ (1.743 Å),[66] $KAsF_6$ (1.720 or 1.712 Å),[67,68] $RbAsF_6$ (1.713 Å),[69] $CsAsF_6$ (1.714 Å),[69] $AgAsF_6$ (1.660 and 1.689 Å),[70] $InAsF_6$ (1.709 Å),[71] and $TlAsF_6$ (1.721 Å).[71] The Na−F distance (Table 4) is in good agreement with the sum of the ionic radii ($^{[6]}Na^+ + {}^{[2]}F^-$ = 2.305 Å).[65] The value of the Na−F−As angle (Table 4), which characterizes the relative orientation of the AsF_6^- and NaF_6^{5-} octahedra, indicates that the Na−F−As chain is not straight, but bent (Figure 5). Actually, the AsF_6^- and NaF_6^{5-} octahedra of two successive layers are tilted at ω = 21.6° from one to the other around the 3-fold axis of the structure.

3.3.2. Crystal Structure of β-$NaAsF_6$, AsF_6^- Anion Libration, and Phase Transition. β-$NaAsF_6$ (Figure 5) adopts the $NaSbF_6$ type structure, which has the highest symmetry of the AMF_6 structures. This type is not widespread and was only found for the sodium hexafluorometallates of transition metals

with limited ionic radii of 0.72−0.78 Å, with the exception of $NaPF_6$[63] in spite of the small size of the phosphorus atom.[16] β-$NaAsF_6$ is then the second exception with an ionic radii of 0.60 Å for $^{[6]}As^{V}$. β-$NaAsF_6$ contains a NaCl type arrangement of the Na^+ cations and AsF_6^- anions and could also be described as an A deficient double perovskite ($A_2BB'O_6$) structure with regular AsF_6^- and NaF_6^{5-} octahedra. Contrary to what is observed in the RT α-phase, the 1:1 cation ordering in the β-phase occurs along the three crystallographic axes of the structure. No more tilting of the octahedra is observed, the Na−F−As chain being straight and the Na−F−As angle being equal to 180°. While the Na−F distance in the α- and β-phases (Table 4) are similar, the As−F bond length in the latter is shorter than those observed in the former and in previously reported crystalline structures (see section 3.3.1). The As−F bond length in β-$NaAsF_6$ is then undoubtedly erroneous as shown by the similar δ_{iso} and $^{19}F-^{75}As$ ^1J-coupling values (Table 2), indicating similar As−F and Na−F bond lengths in α- and β-$NaAsF_6$. Moreover, bond valence calculations (Table 3) confirm that the average As−F bond length is not correctly determined, being much too short. Looking at the fluorine site (Table 3), large atomic ADPs may represent either atomic motion or possible static displacive disorder. The first assumption is retained since the ^{19}F MAS NMR spectrum (Figure 3) of β-$NaAsF_6$ shows a well-resolved quadruplet of sharp NMR lines and then indicates fluorine motion (see section 3.1.2). The second assumption is excluded since this spectrum does not show any signs of static disorder for the fluorine atoms, i.e., δ_{iso} distribution. In addition, from ^{75}As solid-state NMR, the AsF_6^- octahedra are found to be regular ones (see below). Consequently, the unusual atomic ADPs for F originate from an orientational disorder of these rigid and regular octahedra and support the assumption of AsF_6^- anions libration. Actually, it cannot be excluded from the NMR results that F motions are not correlated, i.e., individual As−F bonds could be librating independently, but this is less chemically plausible. One can notice that fluorine atoms are located on the 4-fold symmetry axes of the AsF_6^- octahedron (4mm point group) with a higher local symmetry on the arsenic site ($m\bar{3}m$ point group). Consequently, the atomic displacement parameter is isotropic in nature for the arsenic atom, while the oblate spheroid of thermal vibration for fluorine atom is oriented in a plane orthogonal to the 4-fold symmetry axes (Figure 5). When fluorine atoms are moving away, orthogonally from the 4-fold axes, an elongation of the As−F bond necessarily takes place (Figure 6). Thus, the average As−F bond length reduction is only apparent, the real one being effectively longer and the Na−F−As angle being smaller than 180°.

In α-$NaAsF_6$, the libration of the AsF_6^- octahedra does not affect the tilting of the AsF_6^- and NaF_6^{5-} octahedra, the system maintaining a distortion from cubic symmetry to rhombohedral $R\bar{3}$ symmetry. The libration of the AsF_6^- octahedra increases with temperature and a fluctuation induced first-order phase transition takes place; the phase now appears cubic on average, although a snapshot of the structure would reveal bent As−F−Na bonds.

3.4. ^{23}Na and ^{75}As Solid-State NMR Study. *3.4.1. ^{23}Na Solid-State NMR Study.* A ^{23}Na MAS NMR spectrum has been recorded for α-$NaAsF_6$ (Figure 7). For β-$NaAsF_6$, the ^{23}Na site having a cubic symmetry, the quadrupolar parameters are equal to zero. Consequently, the effect of the $^{23}Na-^{19}F$ heteronuclear dipolar interaction is no more negligible, especially at low MAS frequency. Then, a ^{23}Na MAS Hahn echo spectrum has been acquired with ^{19}F decoupling in order to reduce (by a factor 3) the line broadening (Figure 7). The fit of these experimental spectra allows the determination of the ^{23}Na NMR parameters. The δ_{iso} values are equal to −16.6 ppm and −18.0 ppm in α- and β-$NaAsF_6$, respectively. For α-$NaAsF_6$ (Table 5), the small value of ν_Q is in agreement with the slightly distorted NaF_6^{5-} octahedron, and the η_Q value equal to zero is in agreement with the ^{23}Na site symmetry ($\bar{3}$). The correlation time for the fluorine motion in α-$NaAsF_6$ is not sufficiently short for averaging the ^{23}Na quadrupolar interaction for which a nice agreement is obtained between experimental and calculated (see section 3.5.2) quadrupolar frequencies. The ^{23}Na NMR spectrum of the β-phase is fitted using quadrupolar parameters equal to zero in agreement with the high symmetry of the sodium site ($m\bar{3}m$). Nutation frequency measurements confirm that the quadrupolar frequency is negligible.

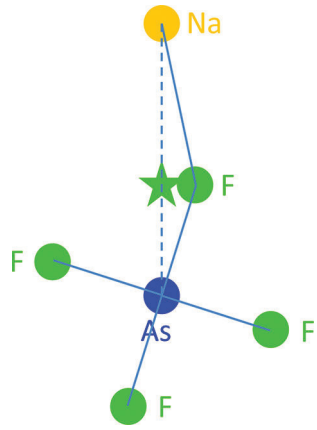

Figure 6. Representation of an AsF_4 plane of an AsF_6^- anion and a Na atom. The circles represent the atoms. The star indicates the average position of the F atom.

3.4.2. ^{75}As Solid-State NMR Study. ^{75}As MAS Hahn echo spectra have been recorded, with and without ^{19}F decoupling, for the α- and the β-phases (Figure 8). As the nuclear spin of ^{19}F is $I = 1/2$ and as each arsenic atom is bounded to $n = 6$ equivalent fluorine atoms, due to the J-coupling between ^{19}F and ^{75}As, the ^{75}As signal is split into seven ($2nI + 1$) lines, i.e., a septet, with intensity ratios 1:6:15:20:15:6:1, on the ^{75}As spectra recorded without ^{19}F decoupling. The fits of these spectra allowed us to determine the ^{75}As NMR parameters in α- and β-$NaAsF_6$ (Figure 8, Table 5). The $^{19}F-^{75}As$ ^1J-coupling values, 900 (±20) Hz and 900 (±10) Hz for α- and β-$NaAsF_6$, respectively, determined from the ^{75}As spectra recorded without ^{19}F decoupling are in agreement with the J-coupling values determined from ^{19}F NMR. The δ_{iso} values are equal to −11.2 ppm and −12.9 ppm in α- and β-$NaAsF_6$, respectively. For α-$NaAsF_6$, the asymmetry parameter is equal to zero in agreement with the ^{75}As site symmetry ($\bar{3}$). The ^{75}As quadrupolar interaction is also not averaged by the fluorine motion in α-$NaAsF_6$. The ^{75}As NMR spectra of the β-phase confirm that the AsF_6^- octahedron is regular (site symmetry $m\bar{3}m$) since quadrupolar parameters are equal to zero. As previously outlined, this result, combined with the single ^{19}F NMR line, allowed us to assume that β-$NaAsF_6$ adopts the $NaSbF_6$ type.

3.5. Ab Initio Calculations. *3.5.1. ^{19}F Isotropic Chemical Shielding.* The ^{19}F σ_{iso} values (Table 2) were calculated using the CASTEP code. The need for a significant scaling factor between σ_{iso} values and δ_{iso} values has been observed in GIPAW

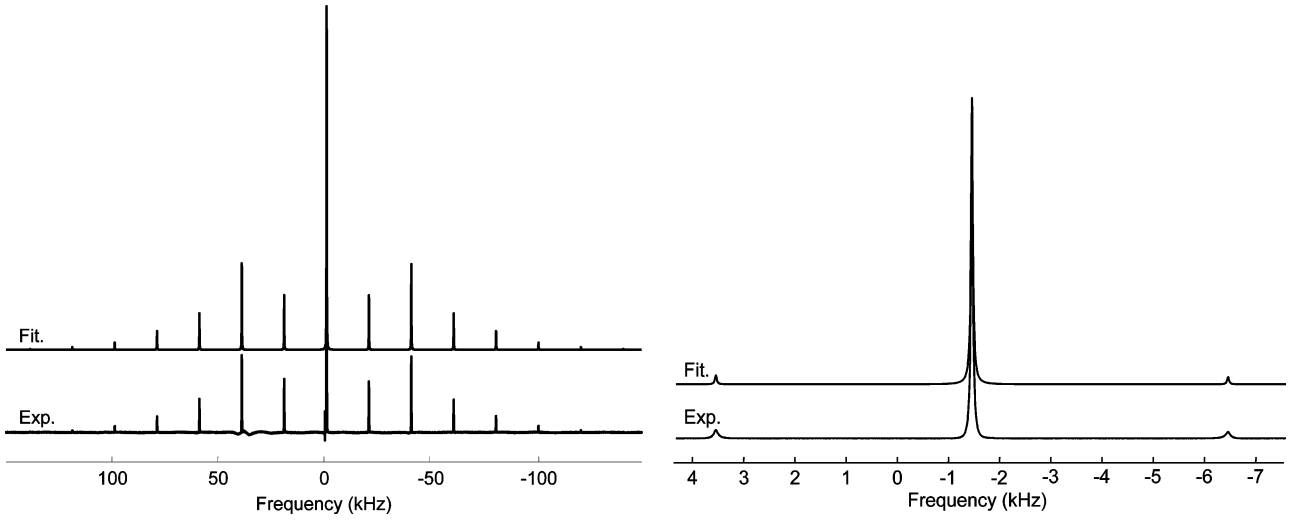

Figure 7. Experimental (Exp.) and fitted (Fit.) ^{23}Na MAS (20 kHz) NMR spectra of α-$NaAsF_6$ at 35 °C (left) and ^{23}Na MAS (5 kHz) Hahn echo spectra of β-$NaAsF_6$ at 70 °C (right).

Table 5. ^{23}Na and ^{75}As Experimental and Calculated ν_Q[a] (kHz) from Initial Structure (IS) and after Atomic Position Optimization (APO Structures) using CASTEP and Wien2k and after Full Geometry Optimization (FO structure) and Full Geometry Optimization with Rescaling of the Cell Parameters (FO Rescaled Structures) using CASTEP in α-$NaAsF_6$[b]

		Wien2k		CASTEP			
	exptl	IS	APO	IS	APO	FO	FO rescaled
^{23}Na	−106(5)	−105	−17	−122	−11	−97	−94
^{75}As	−410(10)	−2061	−372	−1483	−413	−401	−387

[a]Since only the absolute value of ν_Q can be determined from NMR experiments on powdered samples, the sign of the experimental ν_Q is set to the sign of the calculated ν_Q. [b]Experimental and calculated η_Q values are all equal to zero.

studies of ^{19}F.[10,72,73] The ^{19}F δ_{iso} values were estimated by using the reliable linear correlation δ_{iso} (ppm) = −0.80(3)σ_{iso} + 89(9).[73] In a first step, the σ_{iso} values were calculated from crystalline structures determined by XRPD (named initial structure (IS) in the following). The agreement between experimental and calculated ^{19}F δ_{iso} values is acceptable for the IS of α-$NaAsF_6$ but not for the IS of β-$NaAsF_6$. This is not surprising for the β-phase since the As−F bond length is too short, the chemical shift (shielding) being strongly correlated to the first neighbor bond lengths.

In a second step, the atomic positions were optimized (APO structures) but those two structures lead to bad agreements (Table 2). Table 4 gathers the As−F and Na−F bond lengths for both phases, before and after structure optimizations. Looking at the α-phase, the As−F bond length is overestimated by about 3.5% that is greater than the classical overestimation observed with the PBE functional.[40−53] This optimized As−F bond length (1.76 Å) is effectively significantly longer than the average As−F bond length (1.71 Å) found for the previously reported structures (see section 3.3.1). This leads to a chemical shift much too small in absolute value (−35 ppm) compared to the experimental one (−78.5 ppm). On the β-phase, the deviation compared to IS is larger (7.6%) due to the fact that the experimental As−F bond length (1.63 Å), which results from the structural disorder discussed previously, is erroneous. The Na−F bond length slightly increases in the APO structure of α-$NaAsF_6$ but decreases dramatically in the APO structure of β-$NaAsF_6$ since the sum of the Na−F and As−F bond lengths, which is equal to $a/2$, and the Na−F−As angle, which is equal to 180°, are fixed. In the APO structure of α-$NaAsF_6$, the Na−F−As angle decreases noticeably (Table 4) allowing both Na−F and As−F bond lengths to increase.

In a third step, full geometry optimizations were achieved (FO structures), but it also leads to unsatisfactory agreements concerning the ^{19}F δ_{iso} values for both phases (Table 2). The reasons are the same as those explained above, i.e., too long As−F bond lengths. Compared to initial structures, both the As−F and Na−F bond lengths are now increased. In α-$NaAsF_6$, the Na−F−As angle does not evolve significantly (148.5°) indicating that its decrease in the APO structure is caused by the overestimation of the As−F bond length. The cell parameters and unit-cell volumes are especially overestimated for both phases: 3.3%, 2.2%, and 9.1% for a, c, and volume, respectively, in FO α-$NaAsF_6$ and 4.4% and 13.7% for a and volume, respectively, in FO β-$NaAsF_6$ (see Supporting Information). Indeed, GGA-PBE usually overestimates the bond lengths by 1−2% and the equilibrium volumes by 3−6%.

Finally, as already done to take this effect into account,[42,43,46,47,50,51,53] the optimized lattice parameters were rescaled to the experimental volume but keeping atomic positions unchanged (FO rescaled structures). A perfect agreement between experimental and calculated ^{19}F δ_{iso} values is then obtained for α-$NaAsF_6$. Now, both As−F and Na−F bond lengths seem reasonable in the FO rescaled structure of α-$NaAsF_6$. However, the Na−F bond length seems quite short in the FO rescaled structure of β-$NaAsF_6$, but this structure presents the most realistic set of bond lengths and leads to the best agreement between experimental and calculated ^{19}F δ_{iso} values.

3.5.2. ^{23}Na and ^{75}As Quadrupolar Parameters. The quadrupolar parameters were calculated for ^{23}Na and ^{75}As, in both the phases, using the CASTEP and WIEN2k codes. Only the IS and APO structures were considered for the latter. As expected, they are found equal to zero in the β-phase. The calculated quadrupolar frequencies are reported for α-$NaAsF_6$ in the Table 5. A good agreement with the experimental

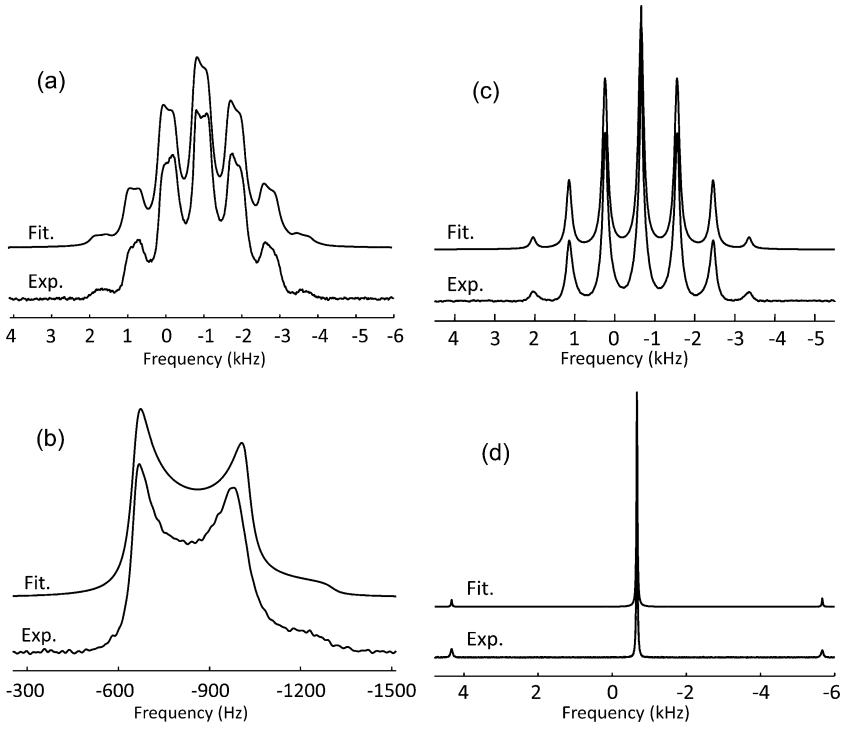

Figure 8. Experimental (Exp.) and fitted (Fit.) ^{75}As MAS Hahn echo NMR spectra of α-$NaAsF_6$ (a,b) at 35 °C and a spinning frequency of 20 kHz and of β-$NaAsF_6$ (c,d) at 70 °C and a spinning frequency of 25 kHz (c) and 5 kHz (d), recorded without (a,c) and with ^{19}F decoupling (b,d).

quadrupolar frequencies is obtained for ^{23}Na with the IS, FO, and FO rescaled structures and for ^{75}As considering the APO, FO, and FO rescaled ones. Because of the symmetry of the ^{23}Na and ^{75}As sites ($\bar{3}$), $V_{xx} = V_{yy}$, and the V_{zz} directions lie along the 3-fold axis, parallel to the *c*-axis (Figure 9). In such cases, the angular distortion is measured through one parameter defined as $\alpha = 1/6\sum_{i=1}^{6} \alpha_i - 90°$ where α_i are the six angles between two adjacent M−F bonds involving fluorine atoms belonging to octahedron faces orthogonal to the V_{ii} direction.[29] A negative (positive) angular distortion is expected to correspond to a charge concentration (depletion) in the V_{zz} direction and then to a negative (positive) V_{zz} value. For α-$NaAsF_6$, all the quadrupolar frequencies, i.e., V_{zz} values, are negative (Table 5), whereas the six angles between two adjacent M−F bonds involving fluorine atoms belonging to octahedron faces orthogonal to the V_{zz} direction are lower than 90° for both nuclei before optimization but higher than 90° after optimization (see Supporting Information). For ^{75}As, the disagreement is probably due to the very small value of the angular distortion after optimization (Table 4), which makes the expectation questionable. Moreover, considering absolute values, angular distortion (Table 4) and quadrupolar frequency (Table 5) both decrease after optimization, and the agreement is fine whatever the considered optimized structure. However, the EFG at the ^{23}Na nucleus is not quantitatively sensitive to the angular distortion (F−Na−F angle) of the NaF_6^{5-} octahedra since the largest (smallest) angular distortions correspond to the smallest (largest) ν_Q values (Tables 4 and 5). Indeed, the EFG at the ^{23}Na nucleus is sensitive to the Na−F−As angle, i.e., to the orientation of the AsF_6^- units (the Na and As atoms are both located on special positions, and consequently, the Na−As distances and As−Na−As angles remain the same as long as the cell parameters do not evolve). As shown by these calculations, the relative orientation of the AsF_6^- units and the Na^+ ion is properly described in the IS and FO structures. This proves again that the increase of the As−F bond lengths in the APO structures, leading to the Na−F−As angle decrease, is not realistic. In conclusion, the ^{19}F σ_{iso} and ^{23}Na and ^{75}As EFG calculations show that the best description of the structures of the α- and β-phases are obtained from the FO rescaled structures.

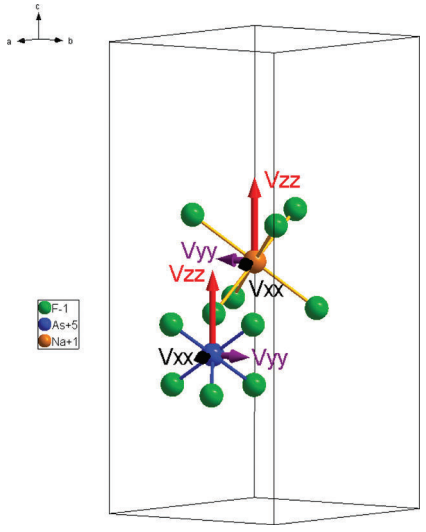

Figure 9. Orientation of the calculated ^{23}Na and ^{75}As EFG tensors in the FO rescaled structure of α-$NaAsF_6$. The vector lengths are proportional to the magnitude of the contributions.

3.5.3. ^{23}Na Isotropic Chemical Shielding. The ^{23}Na σ_{iso} values calculated for α- and β-$NaAsF_6$ (Table 6) show that the ^{23}Na σ_{iso} values globally increase with the Na−F bond length (Table 4). ^{23}Na σ_{iso} calculations have been reported in sodium

Table 6. ^{23}Na Experimental Isotropic Chemical Shifts ($\delta_{iso,exp}$, ppm) and Calculated Isotropic Chemical Shieldings ($\sigma_{iso,cal}$, ppm), from Full Geometry Optimization with Rescaling of the Cell Parameters (FO Rescaled Structures), in Na_2SiO_3 and α- and β-$Na_2Si_2O_5$, and from Initial Structure (IS), after Atomic Position Optimization (APO Structures), after Full Geometry Optimization (FO structure), and Full Geometry Optimization with Rescaling of the Cell Parameters (FO Rescaled Structures) using CASTEP in α-$NaAsF_6$ and β-$NaAsF_6$

		$\sigma_{iso,cal}$			
	$\delta_{iso,exp}$	IS	APO	FO	FO rescaled
α-$NaAsF_6$	−16.6(0.5)	572.95	573.91	579.65	571.64
β-$NaAsF_6$	−18.0(0.5)	576.39	562.77	582.54	569.58
Na_2SiO_3	22.1(0.5)[a]				525.71[c]
α-$Na_2Si_2O_5$	16.9(1.0)[b]				532.49[c]
β-$Na_2Si_2O_5$: Na1	15.6(1.5)[b]				534.87[c]
β-$Na_2Si_2O_5$: Na2	9.4(1.5)[b]				542.25[c]

[a]From ref 75. [b]From ref 74. [c]From ref 43.

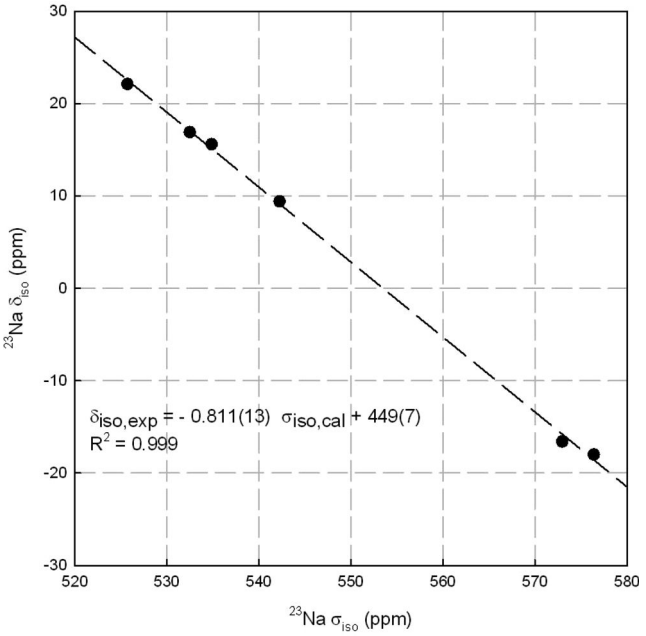

Figure 10. Calculated ^{23}Na σ_{iso} values for FO rescaled structures of Na_2SiO_3, α- and β-$Na_2Si_2O_5$,[43] and IS structures of α- and β-$NaAsF_6$ versus experimental ^{23}Na δ_{iso} values. The dashed line represents the calculated linear regression whose equation is given.

silicate[43] (Table 6) and in sodium phosphate.[53] In the first study,[43] the calculations were achieved on FO rescaled structures. A linear regression, with the constraint of unity slope, is reported between calculated ^{23}Na σ_{iso} values and experimental ^{23}Na δ_{iso} values[74,75] (δ_{iso} (ppm) = $-\sigma_{iso}$ + 549.83), whereas a linear regression without constraint would have led to an absolute value of the slope smaller than unity (δ_{iso} (ppm) = $-0.764\sigma_{iso}$ + 424). In the second study,[53] one of the sites of the NaH_2PO_4 compound was adopted as internal reference for the prediction of the ^{23}Na δ_{iso} values from the ^{23}Na σ_{iso} values, and unfortunately, the calculated ^{23}Na σ_{iso} values are not reported. A linear regression, between experimental ^{23}Na δ_{iso} values and calculated ^{23}Na σ_{iso} values reported in Table 6, is shown in Figure 10: δ_{iso} (ppm) = $-0.811(13)\sigma_{iso}$ + 449(7). For α- and β-$NaAsF_6$, we decided to use the calculated ^{23}Na σ_{iso} values obtained from the initial structures since both the Na−F bond lengths seem correct only for this set of structures, but for the α-phase, the data obtained from the FO rescaled structure could also have been used. The agreement obtained for the linear correlation is remarkable. More data points are certainly required to ascertain this linear correlation before using it, but this result is promising for the prediction of ^{23}Na δ_{iso} values.

4. CONCLUSIONS

The fluctuation-induced first-order phase transition occurring between the α- and β-phases of $NaAsF_6$ has been monitored by DTA, VT ^{19}F solid-state NMR, and temperature-controlled XRPD. The crystalline structures of α- and β-$NaAsF_6$ have been determined from XRPD data. The structural type of β-$NaAsF_6$ has been unambiguously determined thanks to ^{19}F and ^{75}As solid-state NMR experiments. The ^{19}F, ^{23}Na, and ^{75}As solid-state NMR investigations are in full agreement with both crystalline structures from a qualitative point of view (number and symmetry of the crystallographic sites). Nevertheless, the refinement of the structure of the β-phase leads to a shorter As−F bond length, whereas ^{19}F δ_{iso} and ^{19}F−^{75}As J-coupling values are similar in both phases indicating similar As−F bond lengths. This erroneous short As−F bond length is due to AsF_6^- anion libration in agreement with the ^{19}F and ^{75}As solid-state NMR study and the atomic ADPs for F indicating a disorder of the orientation of the regular AsF_6^- octahedra.

This incorrect As−F bond length in β-$NaAsF_6$ prevents precise calculation of the ^{19}F δ_{iso} value from the experimental structure. Moreover, an overestimation of the As−F bond lengths by the PBE functional, leading to unusual cell parameter expansions, prevents precise calculations of the ^{19}F δ_{iso} values in α- and β-$NaAsF_6$ after PBE-DFT atomic position and full optimizations. Rescaling the cell parameters allows overcoming this difficulty and leads to a better agreement between experimental and calculated ^{19}F δ_{iso} values in α- and β-$NaAsF_6$. The overestimation of the As−F bond lengths by the PBE functional leads, in APO structures of α-$NaAsF_6$, to erroneous Na−F−As angle values while the EFG at the ^{23}Na nucleus is sensitive to this angle, i.e., to the orientation of the AsF_6^- units. Then, the ^{23}Na quadrupolar frequency is not correctly reproduced with APO structures of α-$NaAsF_6$. The ^{75}As EFG is sensitive to the angular distortion of the AsF_6^- octahedra, which is too large in the initial structure. After optimization, angular distortion decreases, and the agreement between experimental and calculated ^{75}As quadrupolar frequency is fine whatever the considered optimized structure. The best compromises between ^{19}F σ_{iso} and ^{23}Na and ^{75}As EFG calculations are then obtained from the FO rescaled structures.

This work illustrates the great potential in combining XRPD, multinuclear NMR, and DFT calculations to determine structures and to refine the atomic positions of crystalline compounds, even for β-$NaAsF_6$ in which AsF_6^- anions libration occurs.

Additionally, from previously reported data[43] and from our own measurements and calculations, a linear correlation is observed between experimental ^{23}Na δ_{iso} values and calculated ^{23}Na σ_{iso} values.

■ ASSOCIATED CONTENT

Supporting Information

Cif file of the initial and optimized (after atomic position optimization using Wien2k and CASTEP and full geometry optimization without and with rescaling of the cell parameters using CASTEP) structures of α- and β-$NaAsF_6$. This material is available free of charge via the Internet at http://pubs.acs.org.

■ AUTHOR INFORMATION

Corresponding Author

*E-mail: christophe.legein@univ-lemans.fr.

Notes

The authors declare no competing financial interest.

■ ACKNOWLEDGMENTS

We thank the Région Pays de la Loire for the financial support of the RMN3MPL project, especially M. Biswal (doctoral grant) and A.S. (postdoctoral fellowship). The computations presented in this work have been carried out at the Centre Régional de Calcul Intensif des Pays de la Loire (CCIPL), financed by the French Research Ministry, the Région Pays de la Loire, and Nantes University. We thank CCIPL for the CASTEP licenses financial support.

■ REFERENCES

(1) Andrew, E. R.; Farnell, L. F.; Gledhill, T. D. *Phys. Rev. Lett.* **1967**, *19*, 6−7.
(2) Gerken, M.; Hazendonk, P.; Iuga, A.; Nieboer, J.; Tramšek, M.; Goreshnik, E.; Žemva, B.; Zheng, S.; Autschbach, J. *Inorg. Chem.* **2007**, *46*, 6069−6077.
(3) Pickard, C. J.; Mauri, F. *Phys. Rev. B* **2001**, *63*, 245101.
(4) Yates, J. R.; Pickard, C. J.; Mauri, F. *Phys. Rev. B* **2007**, *76*, 024401.
(5) Joyce, S. A.; Yates, J. R.; Pickard, C. J.; Mauri, F. *J. Chem. Phys.* **2007**, *127*, 204107.
(6) Joyce, S. A.; Yates, J. R.; Pickard, C. J.; Brown, S. P. *J. Am. Chem. Soc.* **2008**, *130*, 12663−12670.
(7) Hung, I.; Uldry, A.-C.; Becker-Baldus, J.; Webber, A. L.; Wong, A.; Smith, M. E.; Joyce, S. A.; Yates, J. R.; Pickard, C. J.; Dupree, R.; et al. *J. Am. Chem. Soc.* **2009**, *131*, 1820−1834.
(8) Yates, J. R. *Magn. Reson. Chem.* **2010**, *48*, S23−S31.
(9) Bonhomme, C.; Gervais, C.; Coelho, C.; Pourpoint, F.; Azaïs, T.; Bonhomme-Coury, L.; Babonneau, F.; Jacob, G.; Ferrari, M.; Canet, D.; et al. *Magn. Reson. Chem.* **2010**, *48*, S86−S102.
(10) Griffin, J. M.; Yates, J. R.; Berry, A. J.; Wimperis, S.; Ashbrook, S. E. *J. Am. Chem. Soc.* **2010**, *132*, 15651−15660.
(11) Barrow, N. S.; Yates, J. R.; Feller, S. A.; Holland, D.; Ashbrook, S. E.; Hodgkinson, P.; Brown, S. P. *Phys. Chem. Chem. Phys.* **2011**, *13*, 5778−5789.
(12) Zhang, C.; Gamble, S.; Ainsworth, D.; Slawin, A. M. Z.; Andreev, Y. G.; Bruce, P. G. *Nat. Mater.* **2009**, *8*, 580−584.
(13) Christie, A. M.; Lilley, S. J.; Staunton, E.; Andreev, Y. G.; Bruce, P. G. *Nature* **2005**, *433*, 50−53.
(14) *PDF-4+ Database*; The International Centre for Diffraction Data (ICDD): Newtown Square, PA, 2007.
(15) Kemmit, R. D. W.; Russel, D. R.; Sharp, D. W. A. *J. Chem. Soc.* **1963**, 4408−4413.
(16) Mazej, Z.; Hagiwara, R. *J. Fluorine Chem.* **2007**, *128*, 423−437.
(17) Clark, S. J.; Segall, M. D.; Pickard, C. J.; Hasnip, P. J.; Probert, M. J.; Refson, K.; Payne, M. C. *Z. Kristallogr.* **2005**, *220*, 567−570.
(18) Blöchl, P. E. *Phys. Rev. B* **1994**, *50*, 17953−17979.
(19) Petrilli, H. M.; Blöchl, P. E.; Blaha, P.; Schwarz, K. *Phys. Rev. B* **1998**, *57*, 14690−14697.
(20) Blaha, P.; Schwarz, K.; Madsen, G. K. H.; Kvasnicka, D.; Luitz, J. *WIEN2k*, An Augmented Plane Wave + Local Orbitals Program for Calculating Crystal Properties, 2001.
(21) Blaha, P.; Schwarz, K.; Herzig, P. *Phys. Rev. Lett.* **1985**, *54*, 1192−1195.
(22) Siegel, R.; Hirschinger, J.; Carlier, D.; Ménétrier, M.; Delmas, C. *Solid State Nucl. Magn. Reson.* **2003**, *23*, 243−262.
(23) Zhou, B.; Giavani, T.; Bildsøe, H.; Skibsted, J.; Jakobsen, H. J. *Chem. Phys. Lett.* **2005**, *402*, 133−137.
(24) Hansen, M. R.; Madsen, G. K. H.; Jakobsen, H. J.; Skibsted, J. *J. Phys. Chem. A* **2005**, *109*, 1989−1997.
(25) Body, M.; Silly, G.; Legein, C.; Buzaré, J.-Y.; Calvayrac, F.; Blaha, P. *J. Solid State Chem.* **2005**, *178*, 3655−3661.
(26) Hansen, M. R.; Madsen, G. K. H.; Jakobsen, H. J.; Skibsted, J. *J. Phys. Chem. B* **2006**, *110*, 5975−5983.
(27) Body, M.; Silly, G.; Legein, C.; Buzaré, J.-Y.; Calvayrac, F.; Blaha, P. *Chem. Phys. Lett.* **2006**, *424*, 321−326.
(28) Martineau, C.; Body, M.; Legein, C.; Silly, G.; Buzaré, J.-Y.; Fayon, F. *Inorg. Chem.* **2006**, *45*, 10215−10223.
(29) Body, M.; Legein, C.; Buzaré, J.-Y.; Silly, G.; Blaha, P.; Martineau, C.; Calvayrac, F. *J. Phys. Chem. A* **2007**, *111*, 11873−11884.
(30) Rocquefelte, X.; Clabau, F.; Paris, M.; Deniard, P.; Le Mercier, T.; Jobic, S.; Whangbo, M.-H. *Inorg. Chem.* **2007**, *46*, 5456−5458.
(31) Martineau, C.; Fayon, F.; Legein, C.; Buzaré, J.-Y.; Body, M.; Massiot, D.; Goutenoire, F. *Dalton Trans.* **2008**, 6150−6158.
(32) Martineau, C.; Fayon, F.; Suchomel, M. R.; Allix, M.; Massiot, D.; Taulelle, F. *Inorg. Chem.* **2011**, *50*, 2644−2653.
(33) Van Gorkom, L. C. M.; Hook, J. M.; Logan, M. B.; Hanna, J. V.; Wasylishen, R. E. *Magn. Reson. Chem.* **1995**, *33*, 791−795.
(34) Bielecki, A.; Burum, D. P. *J. Magn. Reson., Ser. A* **1995**, *116*, 215−220.
(35) Massiot, D.; Fayon, F.; Capron, M.; King, I.; Le Calvé, S.; Alonso, B.; Durand, J.-O.; Bujoli, B.; Gan, Z.; Hoatson, G. *Magn. Reson. Chem.* **2002**, *40*, 70−76.
(36) Rodriguez-Carjaval, J. R. *FULLPROF: A Program for Rietveld Refinement and Pattern Matching Analysis*; Abstracts of the Satellite Meeting on Powder Diffraction of the XV Congress of the IUCr, Toulouse, France, 1990; p 127.
(37) Rietveld, H. M. *J. Appl. Crystallogr.* **1969**, *2*, 65−71.
(38) Corbel, G.; Mestiri, S.; Lacorre, P. *Solid State Sci.* **2005**, *7*, 1216−1224.
(39) Perdew, J. P.; Burke, K.; Ernzerhof, M. *Phys. Rev. Lett.* **1996**, *77*, 3865−3868.
(40) Hamann, D. R. *Phys. Rev. Lett.* **1996**, *76*, 660−663.
(41) Demuth, T.; Jeanvoine, Y.; Hafner, J.; Ángyán, J. G. *J. Phys.: Condens. Matter* **1999**, *11*, 3833−3874.
(42) Profeta, M.; Benoit, M.; Mauri, F.; Pickard, C. J. *J. Am. Chem. Soc.* **2004**, *126*, 12628−12635.
(43) Charpentier, T.; Ispas, S.; Profeta, M.; Mauri, F.; Pickard, C. J. *J. Phys. Chem. B* **2004**, *108*, 4147−4161.
(44) Du, J.; Corrales, L. R. *J. Phys. Chem. B* **2006**, *110*, 22346−22352.
(45) Ashbrook, S. E.; Cutajar, M.; Pickard, C. J.; Walton, R. I.; Wimperis, S. *Phys. Chem. Chem. Phys.* **2008**, *10*, 5754−5764.
(46) Vasconcelos, F.; Cristol, S.; Paul, J.-F.; Tricot, G.; Amoureux, J.-P.; Montagne, L.; Mauri, F.; Delevoye, L. *Inorg. Chem.* **2008**, *47*, 7327−7337.
(47) Charpentier, T.; Kroll, P.; Mauri, F. *J. Phys. Chem. C* **2009**, *113*, 7917−7929.
(48) Cuny, J.; Furet, E.; Gautier, R.; Le Pollès, L.; Pickard, C. J.; d'Espinose de Lacaillerie, J.-B. *ChemPhysChem* **2009**, *10*, 3320−3329.
(49) Brouwer, D. H.; Moudrakovski, I. L.; Darton, R. J.; Morris, R. E. *Magn. Reson. Chem.* **2010**, *48*, S113−S121.
(50) Ispas, S.; Charpentier, T.; Mauri, F.; Neuville, D. R. *Solid State Sci.* **2010**, *12*, 183−192.
(51) Soleilhavoup, A.; Delaye, J.-M.; Angeli, F.; Caurant, D.; Charpentier, T. *Magn. Reson. Chem.* **2010**, *48*, S159−S170.
(52) Truflandier, L. A.; Boucher, F.; Payen, C.; Hajjar, R.; Millot, Y.; Bonhomme, C.; Steunou, N. *J. Am. Chem. Soc.* **2010**, *132*, 4653−4668.
(53) Vasconcelos, F.; Cristol, S.; Paul, J.-F.; Montagne, L.; Mauri, F.; Delevoye, L. *Magn. Reson. Chem.* **2010**, *48*, S142−S150.
(54) Pyykko, P. *Mol. Phys.* **2008**, *106*, 1965−1974.

(55) The integrated intensity of the (101) diffraction peak was determined using the fit profile option of the program or software: *X'Pert HighScore Plus*, version 2.0a; PANanalytical B.V.: Almelo, The Netherlands, 2004.
(56) Burns, J. H. *Acta Crystallogr.* **1962**, *15*, 1098−1101.
(57) Andrew, E. R.; Firth, M.; Jasinski, A.; Randall, P. J. *Phys. Lett.* **1970**, *31*, 446−447.
(58) Krahl, T.; Ahrens, M.; Scholz, G.; Heidemann, D.; Kemnitz, E. *Inorg. Chem.* **2008**, *47*, 663−670.
(59) Du, L. S.; Schurko, R. W.; Lim, K. H.; Grey, C. P. *J. Phys. Chem. A* **2001**, *105*, 760−768.
(60) Scholz, G.; Krahl, T.; Ahrens, M.; Martineau, C.; Buzaré, J.-Y.; Jäger, C.; Kemnitz, E. *J. Fluorine Chem.* **2011**, *132*, 244−249.
(61) Fukushima, E.; Mastin, S. H. *J. Magn. Reson.* **1969**, *1*, 648−651.
(62) Brown, I. D.; Altermatt, D. *Acta Crystallogr., Sect. B: Struct. Sci.* **1985**, *41*, 244−247.
(63) Kitashita, K.; Hagiwara, R.; Ito, Y.; Tamada, O. *J. Fluorine Chem.* **2000**, *101*, 173−179.
(64) Teufer, G. *Acta Crystallogr.* **1956**, *9*, 539−540.
(65) Shannon, R. D. *Acta Crystallogr., Sect. A: Found. Crystallogr.* **1976**, *32*, 751−767.
(66) Roehr, C.; Kniep, R. *Z. Naturforsch., B: Chem. Sci.* **1994**, *49*, 650−654.
(67) Gafner, G.; Kruger, G. J. *Acta Crystallogr., Sect. B: Struct.Sci.* **1974**, *30*, 250−251.
(68) Peterkova, J.; Dusek, M.; Petricek, V.; Loub, J. *Acta Crystallogr., Sect. B: Struct. Sci.* **1998**, *54*, 809−818.
(69) Loss, S.; Rohr, C. *Z. Naturforsch., B: Chem. Sci.* **1998**, *53*, 75−80.
(70) Hagiwara, R.; Kitashita, K.; Ito, Y.; Tamada, O. *Solid State Sci.* **2000**, *2*, 237−241.
(71) Goreshnik, E.; Mazej, Z. *Solid State Sci.* **2008**, *10*, 303−306.
(72) Zheng, A.; Liu, S.-B.; Deng, F. *J. Phys. Chem. C* **2009**, *113*, 15018−15023.
(73) Sadoc, A.; Body, M.; Legein, C.; Biswal, M.; Fayon, F.; Rocquefelte, X.; Boucher, F. *Phys. Chem. Chem. Phys.* **2011**, *13*, 18539−18550.
(74) Xue, X.; Stebbins, J. F. *Phys. Chem. Miner.* **1993**, *20*, 297−307.
(75) Clark, T.; Grandinetti, P.; Florian, P.; Stebbins, J. F. *J. Phys. Chem.* **2001**, *105*, 12257−12265.

4.3 KPF_6

4.3.1 Introduction

Hexafluorophosphates (V) of univalent metals $M^{(I)}P^{(V)}F_6$ (M = Li, Na, K, Cs, Ag, In, Tl), except $LiPF_6$[63] which has a rhomboedral lattice (space group n°148, $R\bar{3}$, $LiSbF_6$ type[64]), have cubic lattices (space group n°225, $Fm\bar{3}m$) at room temperature (RT). The array of cations and anions is rock salt type, variation of the structure arising from the orientations of PF_6^- anions. Only $NaPF_6$ structure[65] appears to be ordered. PF_6^- anions in other compounds demonstrate different kinds of orientational disordering, *i.e.* threefold in $AgPF_6$[65,66] (two F sites, both with occupancy equal to 1/3), fourfold orientational disordering in KPF_6,[65] $CsPF_6$,[65] and $TlPF_6$[67] (1 F site with occupancy equal to 1/4) and eightfold orientational disordering in $InPF_6$[67] (1 F site with occupancy equal to 1/8). These differences represent just a distinction in formal description of disordered anion.

Table 1. ^{31}P-^{19}F ^1J-coupling values (Hz)

$NaPF_6$	724 (± 12)[5]
KPF_6	743 (± 12)[5] or 747[68]
K_2PO_3F	-830 (±60)[3]
β-Na_2PO_3F	-790 (±60)[3]
$BaPO_3F$	-810 (±60)[3]
$K_2P_2O_5F_2$	P1: -784 (±50)
	P2: -800 (±50)[3]
Hg_2PO_3F	-1072[4]
Ag_2PO_3F	-1045(± 20)[2]

The ^{31}P-^{19}F ^1J-coupling values range, in hexafluorophosphates and fluorophosphates, from ~720 Hz to ~1070 Hz (Table 1). Two slightly different ^{31}P-^{19}F ^1J-coupling values have been reported for KPF_6.[5,68]

Numerous studies (single crystal and powder X-Ray diffraction, DSC, vibrational spectroscopy, NMR,...)[69, 70, 71, 72, 73, 74, 75] have been devoted to the polymorphism of KPF_6. An ordered rhombohedral phase occurs at high pressure[75] (phase IV, $KOsF_6$ structure type[64]). The results, in particular those obtained at lower temperatures are, however, to a high degree inconsistent. The structures proposed for the RT and the LT phases and the values of the corresponding transition temperatures vary significantly between the various groups of authors. The value of the temperature of the cubic-non cubic transition varies from about 0 °C to about -25 °C. Several authors have produced evidence for a second phase transition at lower temperatures, others mention coexisting phases or point out effects of the thermal history or presume that the conditions of sample preparation, the sample purity or whether it is very dry (*i.e.* pumped at 10^{-4} Pa for 24 hours) or still slightly damp following purification influence the structural behavior of KPF_6. According to Huber *et al.*[74] which investigated KPF_6 by X-ray powder diffraction, calorimetry and Brillouin spectroscopy, three crystallographic phases occur: the RT cubic (I) phase (space group n°225, $Fm\bar{3}m$) and two LT monoclinic phases:

phase II, space group n°15, setting A2/n, a = 9.582 Å, b = 5.390 Å, c = 18.131 Å, β = 101.037°, and phase III, space group n°15, setting C2/n, a = 9.423 Å, b = 4.9058 Å, c = 9.466 Å and β = 103.35° (both from powder diffraction with synchrotron radiation).[73] From DSC measurements on single crystal, the phase transition I-II occurs at -17 °C on cooling and at -13 °C on heating, whereas the phase transition II-III occurs between -45 °C and -65 °C on cooling and at -22 °C on heating. LT rhombohedral phases have been reported below -25 °C and in the temperature ranges [-18 °C, 7 °C] and [-33 °C, 2 °C] in the PDF[76] files 00-007-0317,[69] 00-052-1827 (space group n°148, $R\bar{3}$) and 00-052-1828 (space group n°148, $R\bar{3}$), respectively. Another monoclinic phase has also been reported, occurring below -33 °C (space group n°14, $P2_1/c$), in the PDF[76] file 00-052-1829. Although the cell parameters are reported for all the different phases exhibited by KPF_6, the atomic co-ordinates are reported only for the RT[65] and the high pressure phases.[75] Since atomic co-ordinates are required for the calculation of NMR parameters, we planned to determine precisely the crystalline structure, expected to be less symmetric and ordered, of the first LT phase of KPF_6.

4.3.2. Differential scanning calorimetry, temperature controlled X-Ray powder diffraction and variable temperature solid-state NMR study.

The study of KPF_6 by differential scanning calorimetry (DSC) shows the occurrence of two phase transitions (Fig. 1, left), one at -14 °C on cooling (phase I → phase II) and -12 °C on heating (phase II → phase I) and one at -48 °C on cooling (phase II → phase III) and at -19 °C on heating (phase III → phase II), in agreement with Huber *et al.*[74] Nevertheless, a careful examination of this curve reveals a small peak, on cooling only, at ~ -10 °C. Further DSC experiments (Fig. 1, right) were then achieved at a lower heating/cooling rate, in the range RT to -12 °C, in order to avoid the phase I→ phase II transition, showing that a reversible phase transition occurs at ~-10 °C. Whereas on heating the phase II seems to transform directly in phase I, on cooling, an intermediate phase can be detected between -10 °C and -14 °C.

Temperature controlled X-Ray powder diffraction (XRPD) diagrams recorded under partial vacuum (~100 mbar) confirm the occurrence, on cooling, of three phases and consequently the occurrence of two phase transitions in the RT to -20 °C range (Fig. 2). Moreover these diagrams allow confirming the occurrence of an intermediate phase, mainly evidenced by the splitting of the [222] (2θ = 40°) and [224] (2θ = 58°, Fig. 3) Bragg reflections of the cubic phase. Moreover, these diagrams indicate that, on heating, phase II does not transform directly in phase I. As on cooling, the intermediate phase occurs on a small range of temperature (Fig. 2 and Fig. 3). The temperatures of

transition being closer on heating, the transition phase II → intermediate phase certainly hides the transition intermediate phase → phase I on DSC curves and only one transition is detected in the RT to -20 °C range.

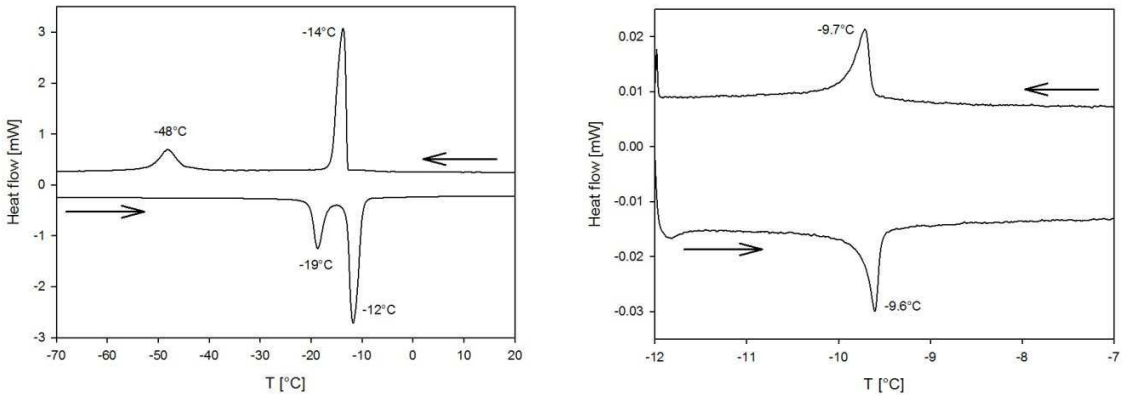

Fig. 1. DSC curves of KPF_6 recorded from 40 °C to -100 °C and from -100 °C to 400 °C (heating/cooling rate of 5 °C/min, left) and from RT to -12 °C and from -12 °C to RT (heating/cooling rate of 0.2 °C/min, right). The temperature at the signal maxima are indicated.

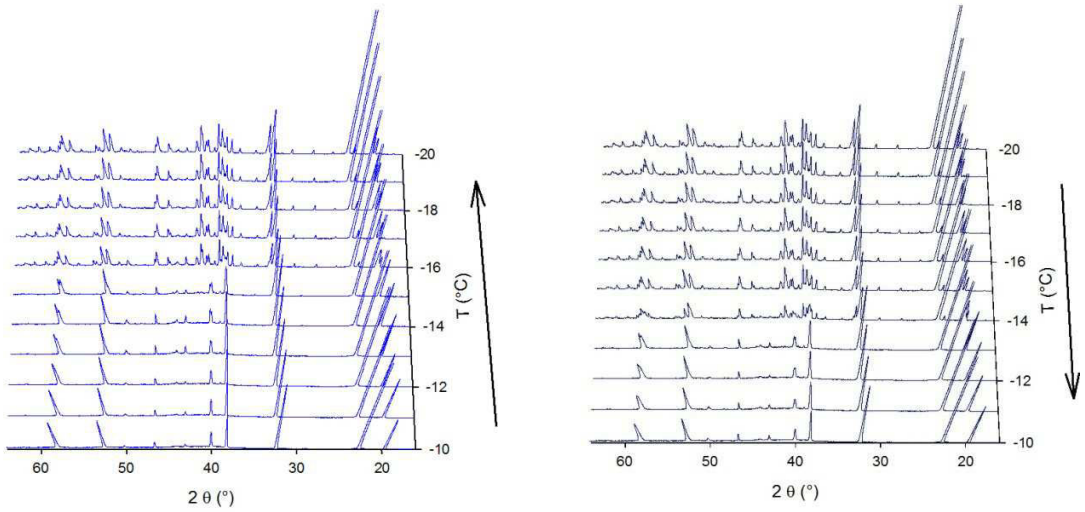

Fig. 2. Temperature controlled XRPD diagrams ([16−64°] 2θ range) of KPF_6 recorded on cooling from RT to -20 °C (left) and on heating from -20 °C to RT (right).

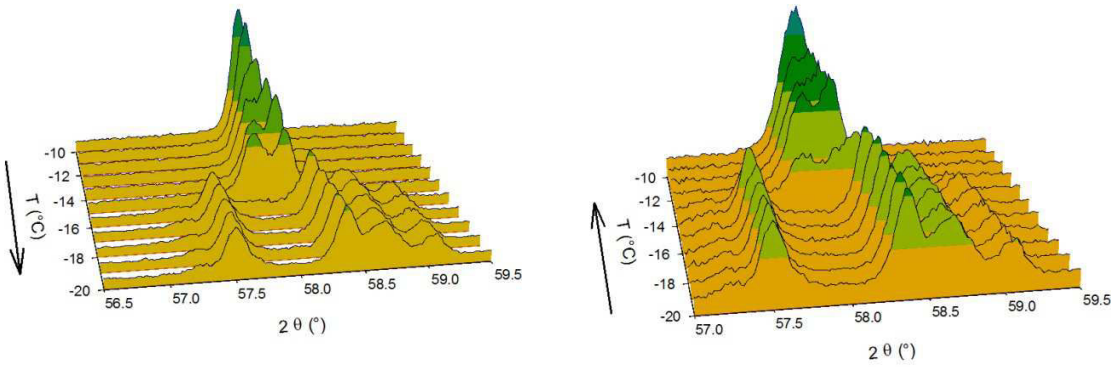

Fig. 3. Temperature controlled XRPD diagrams ([56.5–59.5°] 2θ range) of KPF_6 recorded on cooling from RT to -20 °C (left) and on heating from -20 °C to RT (right).

High resolution XRPD diagrams have been recorded at -13 °C and -20 °C. Using the Fullprof program,[77] full profile pattern matching of the diagram recorded at -20 °C allows confirming the space group (A2/n) of the phase II and determining its cell parameters (a = 9.5866 Å, b = 5.394 Å, c = 18.1411 Å and β = 101.05° at -20 °C, Fig. 4) which are in fine agreement with those determined by Fitch *et al.*[73] Full profile pattern matching of the diagram recorded at -13 °C allows determining the space group and the cell parameters of this phase which is rhombohedral (space group $R\bar{3}$, hexagonal cell: a = 5.481 Å and c = 13.489 Å, Fig. 5) and which seems to adopt the $LiSbF_6$ type.[64]

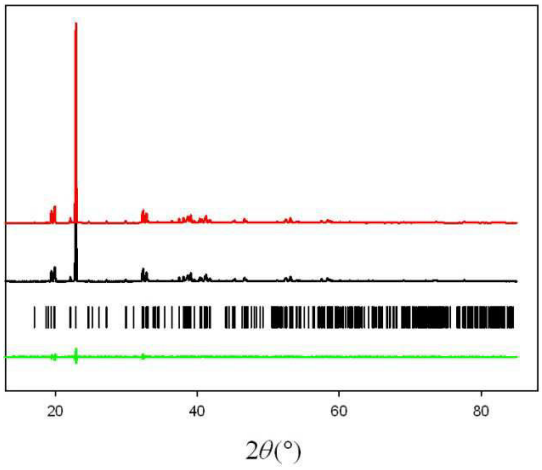

Fig. 4. Profile pattern matching diagram of the phase II of KPF_6. The diagram shows calculated (red), observed (black), and difference (green) diffraction patterns. Vertical markers give Bragg peak positions. R_{wp} = 11.9 %, R_{exp} = 4.9 % and R_{Bragg} = 9.8 %.

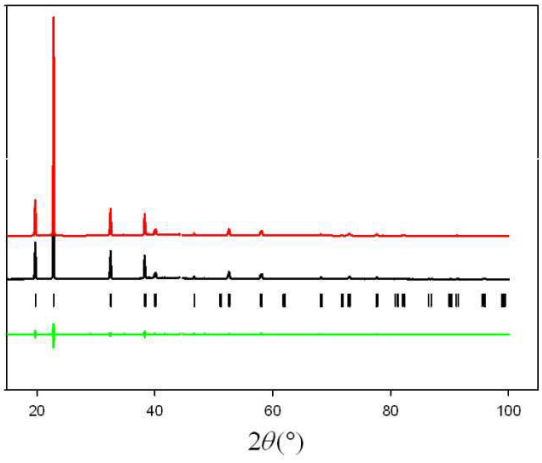

Fig. 5. Profile pattern matching diagram of the rhombohedral phase of KPF_6. The diagram shows calculated (red), observed (black), and difference (green) diffraction patterns. Vertical markers give Bragg peak positions. R_{wp} = 9.0 %, R_{exp} = 3.9 % and R_{Bragg} = 8.4 %.

Temperature controlled XRPD experiments were previously conducted under high vacuum, in Nantes by F. Boucher. In such conditions, the transition phase I - phase II starts, on cooling, at nearly the same temperature but spreads on a larger range of temperature. A XRPD diagram of a pure phase II similar to the one recorded on partial vacuum at -20 °C (Fig. 4) is obtained only at -120 °C. It confirms the influence of the experimental conditions on the phase transition temperature of KPF_6.

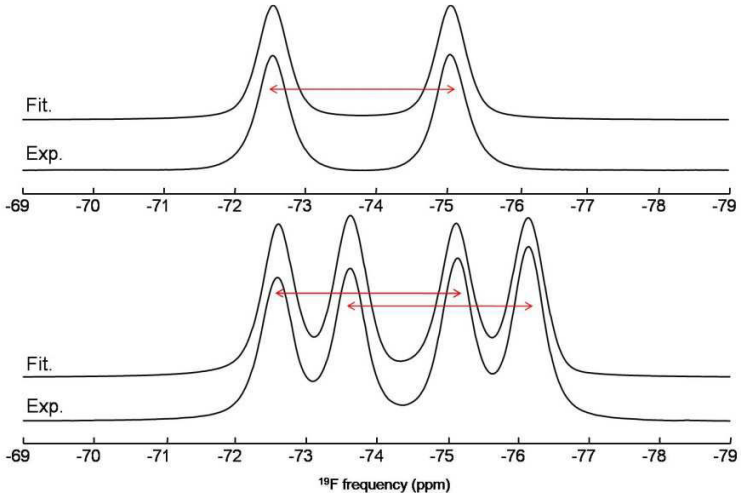

Fig. 6. Experimental (Exp.) and fitted (Fit.) ^{19}F MAS NMR spectra of KPF_6 recorded without ^{31}P decoupling at 60 °C (top, ν_R = 30 kHz) and at -25 °C (bottom, ν_R = 25 kHz). The double arrows represent the ^{31}P-^{19}F ^1J-couplings.

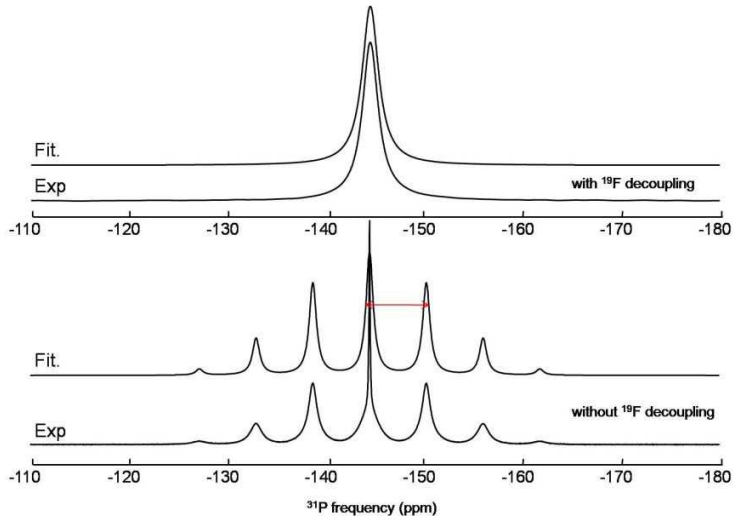

Fig. 7. Experimental (Exp.) and fitted (Fit.) ^{31}P MAS (ν_R = 30 kHz) NMR spectra of KPF_6 at 60 °C recorded without (bottom) and with ^{19}F decoupling (top). The double arrow represents the ^{31}P-^{19}F ^1J-coupling.

Attempts to determine atomic positions of these two LT phases of KPF_6 have so far been unsuccessful. We assume it is due to the libration of PF_6^- anions.

The ^{19}F and ^{31}P spectra (Fig. 6 and Fig. 7) recorded at RT confirm the presence of 1 F site and 1 P site in the phase I of KPF_6. As the RT structure of KPF_6 contains one F and one P site and as each fluorine atom is linked to one P (I = ½) atom, due to the ^1J-coupling between ^{19}F and ^{31}P, two lines with equal intensities, *i.e.* a doublet, is observed on the ^{19}F NMR spectrum (Fig. 6). As the nuclear spin of ^{19}F is I = 1/2 and as each phosphorous atom is linked to 6 equivalent fluorine atoms, due to the J-coupling between ^{19}F and ^{31}P, a septet is observed on the ^{31}P spectrum of the RT phase recorded without ^{19}F decoupling (Fig. 7).

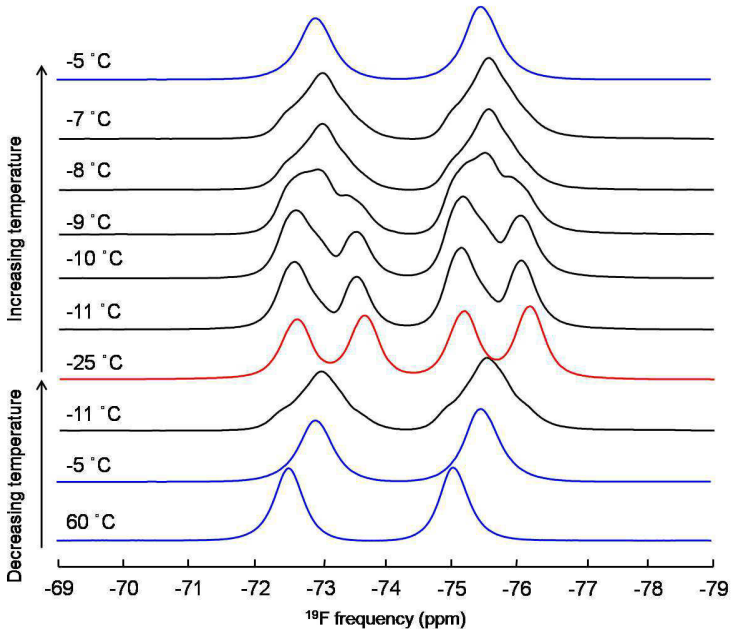

Fig. 8. VT ^{19}F MAS (ν_R = 25 kHz, except at 60 °C, 30 kHz) NMR spectra of KPF_6 recorded from RT to -25 °C and from -25 °C to -5 °C. The spectra corresponding to RT, phase II and a mixture of phases of KPF_6 are represented in blue, red, and black respectively.

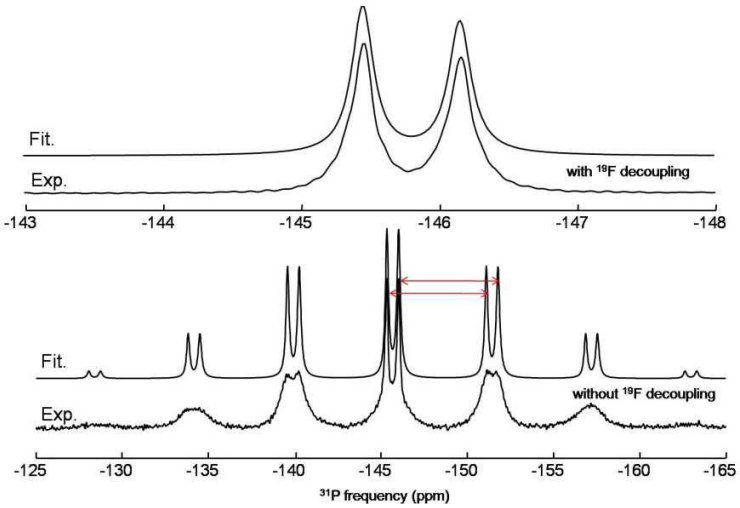

Fig. 9. Experimental and fitted ^{31}P MAS (ν_R = 25 kHz) NMR spectra of KPF_6 with (top) and without ^{19}F decoupling (bottom) at -21 °C. The double arrows represent the ^{31}P-^{19}F ^1J-couplings.

The phase transitions were also studied by ^{19}F and ^{31}P variable temperature (VT) NMR. The VT ^{19}F solid state NMR spectra (Fig. 8) of KPF_6 were recorded from RT to -25 °C with decreasing temperature and thereafter with increasing temperature. They confirm the occurrence of, at least, one phase transition in this temperature range. Moreover, the spectra recorded below -15 °C showing four lines (two doublets), the phase II of KPF_6 contains two F sites of same multiplicity. Due to the gradient of temperature of the sample inside the rotor (~10 °C, see 4.3.3.2) it seems impossible to observe the spectrum of the pure rhombohedral phase and the three phases may coexist between -7 °C and -15 °C. The ^{31}P NMR spectra of the phase II of KPF_6 (at -21 °C) recorded with and without decoupling (Fig. 9) show that this phase contains also 2 P sites of same multiplicity.

The ^{19}F and ^{31}P δ_{iso} values and the ^{19}F -^{31}P ^1J-coupling values determined from the reconstruction of their respective spectra are gathered in Table 2. The ^{19}F -^{31}P ^1J-coupling values are

Table 2. ^{19}F and ^{31}P δ_{iso} values (ppm) and ^{19}F-^{31}P ^{1}J-coupling values (Hz) determined from the reconstruction of ^{19}F and ^{31}P NMR spectra of phase I and II of KPF_6.

	Phase I (RT)		Phase II	
	δ_{iso} (±0.5)	^{1}J-coupling (±10)	δ_{iso} (±0.5)	^{1}J-coupling (±10)
^{19}F	-73.9	710	-73.9	710
			-74.9	710
^{31}P	-144.5	700	-145.3	700
			-146.0	700

slightly smaller than those previously reported[5,68] (Table 2) but in fine agreement with values obtained for PF_6^- anions from liquid state NMR (~710 Hz).[78-80]

4.3.3 Experimental section

KPF_6 was obtained from Janssen Chimica (lot number 003220). Prior to use, the purity of this sample was checked by XRPD.

4.3.3.1 DSC and temperature controlled XRPD

The data collections have been performed by Pierrick Durand at the X-ray diffraction facility of the Institute Jean Barriol of Université de Lorraine, http://www.crystallography.fr/crm2/fr/services/servicecommun/index.php.

The XRPD experiments were performed using a Panalytical X'Pert Pro diffractometer equipped with a Cu tube, a Ge(111) incident-beam monochromator (λ=1.5406 Å) and an X'Celerator detector. Temperature-controlled diffractograms were collected with an Oxford cryostat (Oxford cryosystems Phenix) from 20 °C to -20 °C (under reduced vacuum (~ 100 mbar), increments of 5 °C or 1 °C, temperature stabilization of 5 min). Data collection was carried out in the scattering angle range 2θ = 3-70° with a 0.0167° step for 65 min. High resolution XRPD diagrams were recorded at -20 °C, in the scattering angle range 2θ = 8-85° with a 0.0084° step for 4 h and at -13 °C, in the scattering angle range 2θ = 15-100° with a 0.0084° step for 18 h.

DSC were performed using a Mettler Toledo DSC1 equipped with a HSS8 sensor under nitrogen flow, with an aluminum crucible (40 µL) at various heating/cooling rates.

4.3.3.2 ^{19}F and ^{31}P VT solid state NMR

NMR experiments were performed on a Bruker Avance 300 (7 T) spectrometer operating at Larmor frequencies of 282.4 and 121.5 MHz for ^{19}F and ^{31}P, respectively. A ^{19}F optimized 2.5 mm CP-MAS probe head was used to perform all the experiments. ^{19}F and ^{31}P chemical shifts are referenced to $CFCl_3$ and 85% H_3PO_4 solution, respectively. The RT and VT ^{19}F MAS Hahn echo spectra were acquired using a 2.7 µs 90° pulse and an interpulse delay synchronized with the rotor period. The recycle delays were set to 10 s and 5 s, respectively. The RT and VT ^{31}P MAS Hahn echo spectra were

acquired using a 6 µs 90° pulse and an interpulse delay synchronized with the rotor period. The recycle delays were set to 5 s.

The temperature of the sample was calibrated for the 2.5 mm NMR probe at 25 kHz using the ^{207}Pb isotropic chemical shift of $Pb(NO_3)_2$.[81,82] The temperature gradient over the dimension of the rotor was estimated, by these experiments, at about 10 °C.

All solid state NMR spectra were fitted using DMfit[83] software.

4.3.4 Conclusion

DSC and temperature controlled XRPD experiments give evidence for three successive phase transitions from RT to -100 °C: Phase I → Rhombohedral → Phase II → Phase III. The number of F and P sites in phase II have been determined from VT ^{19}F and ^{31}P NMR experiments. Unfortunately, attempts to determine atomic positions of the rhombohedral and phase II have so far been unsuccessful.

4.4 Conclusion

Many inorganic fluorides with large heteronuclear ^{19}F-X ^{1}J-couplings contain isolated X(O)F_n ions prone to libration and adopt consequently either disordered high symmetry structures or ordered lower symmetry structures depending on the temperature. The studies of $NaAsF_6$ and KPF_6 provide us the opportunity to follow phase transitions by VT MAS NMR as well as by temperature-controlled XRPD and DSC or DTA.

For both the RT and HT phases of $NaAsF_6$, structures have been refined and the ^{19}F, ^{23}Na and ^{75}As NMR parameters determined. The HT phase presents a libration of the AsF_6^- anions, leading to large anisotropic displacement parameter for the fluorine atom and unusual short F-As distances. For this phase, the best agreement between experimental and calculated NMR results is reached using the FO-rescaled structure. The calculations done on $NaAsF_6$ highlight the overestimation of the bond length with the PBE[84] functional used in the density functional theory calculations and the attention that must be paid to optimization.

Hexafluorophosphates and fluorophosphates would be perfect candidates for ^{1}J-coupling calculations if orientational disordering were not occurring in these compounds. We have shown that KPF_6 presents three successive phase transitions from RT to -100 °C. The RT structure presents one K site, one P and one F site, with unfortunately, partial site occupancy for this last atom which prevents from ab initio calculation. From the ^{19}F and ^{31}P NMR spectra of phase II, two F sites and two P sites have been identified. ^{39}K NMR by revealing whether there is one or two sites of potassium, would be a plus for the structural refinement. Attempts to determine atomic positions of the rhombohedral and phase II will be resumed expecting that they are ordered.

4.5 References

(1) S. A. Joyce, J. R. Yates, C. J. Pickard, F. Mauri, *J. Chem. Phys.* **2007**, *127*, 204107.
(2) M. Weil, M. Puchberger, E. Fuglein, E. J. Baran, J. Vannahme, H. J. Jakobsen, J. Skibsted, *Inorg. Chem.* **2007**, *46*, 801–808.
(3) U. Haubenreisser, U. Sternberg, A.-R. Grimmer, *Mol. Phys.* **1987**, *60*, 151-163.
(4) M. Weil, M. Puchberger, E. J. Baran, *Inorg. Chem.* **2004**, *43*, 8330-8335.
(5) E. R. Andrew, M. Firth, A. Jasinski, P. J. Randall, *Phys. Lett.* **1970***, 31*, 446–447.
(6) T. Krahl, M. Ahrens, G. Scholz, D. Heidemann, E. Kemnitz, *Inorg. Chem. 2008*, *42*, 663–670.
(7) E. R. Andrew, L. F. Farnell, T. D. Gledhill, *Phys. Rev. Lett.* **1967**, *19*, 6–7.
(8) M. Gerken, P. Hazendonk, A. Iuga, J. Nieboer, M. Tramsek, E. Goreshnik, B. Zemva, S. Zheng, J. Autschbach, *Inorg. Chem.* **2007**, *46*, 6069–6077.
(9) L. S. Du, R. W. Schurko, K. H. Lim, C. P. Grey, *J. Phys. Chem. A* **2001**, *105*, 760–768.
(10) L-S. Du, R. W. Schurko, N. Kim, C. P. Grey, *J. Phys. Chem. A* **2002**, *106*, 7876-7886.
(11) D. Massiot, F. Fayon, M. Deschamps, S. Cadars, P. Florian, V. Montouillout, N. Pellerin, J. Hiet, A. Rakhmatullin, C. Bessada, *C. R. Chimie* **2010**, *13*, 117–129.
(12) C. Martineau, Thèse de l'Université du Maine, 2008.
(13) G. Scholz, T. Krahl, M. Ahrens, C. Martineau, J.-Y. Buzaré, C. Jäger, E. Kemnitz, *J. Fluorine Chem.* **2011**, *132*, 244–249
(14) S. P. Gabuda, V. Ya. Kavun, S. G. Kozlova, V. V. Tverskikh, *Russ. J. Coord. Chem.* **2003**, *29*, 1–5.
(15) M. Gerken, P. Hazendonk, J. Nieboer, G. J. Schrobilgen, *J. Fluorine Chem.* **2004**, *125*, 1163–1168.
(16) F. Wang, C. P. Grey, *J. Am. Chem. Soc.* **1998**, *120*, 970–980.
(17) F. Wang, C. P. Grey, *J. Am. Chem. Soc.* **1995**, *117*, 6637–6638.
(18) R. E. Sears, Q. Zh. Guo, H. J. Mackey, *J. Chem. Phys.* **1984**, *80*, 5448–5452.
(19) E. Fukushima, S. H. Mastin, *J. Magn. Reson.* **1969**, *1*, 648-651.
(20) C. Martineau, F. Fayon, C. Legein, J.-Y. Buzaré, F. Goutenoire, E. Suard, *Inorg. Chem.* **2008**, *47*, 10895–10905.
(21) C. Martineau, F. Fayon, C. Legein, J.-Y. Buzaré, M. Body, D. Massiot, F. Goutenoire, *Dalton Trans.* **2008**, 6150–6158.
(22) C. Martineau, F. Fayon, C. Legein, J.-Y. Buzaré, G. Silly, D. Massiot, *Chem. Commun.* **2007**, 2120–2122.
(23) A.-L. Rollet, M. Allix, E. Veron, M. Deschamps, V. Montouillout, M. R. Suchomel, E. Suard, M. Barré, M. Ocaña, A. Sadoc, F. Boucher, C. Bessada, D. Massiot, F. Fayon, *Inorg. Chem.* **2012**, *51*, 2272–2282.
(24) J. F. Lehmann, G. J. Schrobilgen, K. O. Christie, A. Kornath, R. J. Suontamo, *Inorg. Chem.* **2004**, *43*, 6905–6921.
(25) G. L. Smith, H. P. A. Mercier, G. J. Schrobilgen, *Inorg. Chem.* **2007**, *46*, 1369–1378.
(26) K. Koppe, V. Bilir, H.-J. Frohn, H. P. A. Mercier, G. J. Schrobilgen, *Inorg. Chem.* **2007**, *46*, 9425–9437.
(27) W. J. Casteel Jr., P. Kolb, N. LeBlond, H. P. A. Mercier, G. J. Schrobilgen, *Inorg. Chem.* **1996**, *35*, 929–942.
(28) W. J. Casteel Jr., D. M. MacLeod, H. P. A. Mercier, G. J. Schrobilgen, *Inorg. Chem.* **1996**, *35*, 7279–7288.
(29) W. J. Casteel Jr., D. A. Dixon, N. LeBlond, H. P. A. Mercier, G. J. Schrobilgen, *Inorg. Chem.* **1998**, *37*, 340–353.
(30) H. P. A. Mercier, J. C. P. Sanders, G. J. Schrobilgen, *Inorg. Chem.* **1995**, *34*, 5261–5273.

(31) H. P. A. Mercier, M. D. Moran, J. C. P. Sanders, G. J. Schrobilgen, R. J. Suontamo, *Inorg. Chem.* **2005**, *44*, 49–60.
(32) N. Keller, G. J. Schrobilgen, *Inorg. Chem.* **1981**, *20*, 2118–2129.
(33) H. P. A. Mercier, J. C. P. Sanders, G. J. Schrobilgen, *J. Am. Chem. Soc.* **1994**, *116*, 2921–2937.
(34) M. D. Moran, H. P. A. Mercier, G. J. Schrobilgen, *Inorg. Chem.* **2007**, *46*, 5034–5045.
(35) M. Gerken, P. Kolb, A. Wegner, H. P. A. Mercier, H. Borrmann, D. A. Dixon, G. J. Schrobilgen, *Inorg. Chem.* **2000**, *39*, 2813–2824.
(36) B. Fir, J. M. Whalen, H. P. A. Mercier, D. A. Dixon, G. J. Schrobilgen, *Inorg. Chem.* **2006**, *45*, 1978–1996.
(37) D. S. Brock, V. Bilir, H. P. A. Mercier, G. J. Schrobilgen, *J. Am. Chem. Soc.* **2007**, *129*, 3598-3611.
(38) F. Y. Fujiwara, J. S. Martin, *J. Am. Chem. Soc.* **1974**, *96*, 7625–7631.
(39) K. O. Christe, D. A. Dixon, J. C. P. Sanders, G. J. Schrobilgen, W. W. Wilson, *Inorg. Chem.* **1994**, *33*, 4911–4919.
(40) K. O. Christe, E. C. Curtis, D. A. Dixon, H. P. Mercier, J. C. P. Sanders, G. J. Schrobilgen, *J. Am. Chem. Soc.* **1991**, *113*, 3351–3361.
(41) K. O. Christe, D. A. Dixon, H. G. Mack, H. Oberhammer, A. Pagelot, J. C. P. Sanders, G. J. Schrobilgen, *J. Am. Chem. Soc.* **1993**, *115*, 11279–11284.
(42) K. O. Christe, D. A. Dixon, J. C. P. Sanders, G. J. Schrobilgen, W. W. Wilson, *J. Am. Chem. Soc.* **1993**, *115*, 9461–9467.
(43) K. O. Christe, D. A. Dixon, H. P. A. Mercier, J. C. P. Sanders, G. J. Schrobilgen, W. W. Wilson, *J. Am. Chem. Soc.* **1994**, *116*, 2850–2858.
(44) K. O. Christe, D. A. Dixon, G. J. Schrobilgen, W. W. Wilson, *J. Am. Chem. Soc.* **1997**, *119*, 3918–3928.
(45) K. O. Christe, J. C. P. Sanders, G. J. Schrobilgen, W. W. Wilson, *J. Chem. Soc., Chem. Commun.* **1991**, 837–840.
(46) R. J. Gillespie, B . Landa, G. J. Schrobilgen, *J. Chem. Soc., Chem. Commun.* **1972**, 607–609.
(47) R. J. Gillespie, G. J. Schrobilgen, *J. Chem. Soc., Chem. Commun.* **1974**, 90–92.
(48) J. H. Holloway, G. J. Schrobilgen, P. Taylor, *J. Chem. Soc., Chem. Commun.* **1975**, 40–41.
(49) J. F. Sawyer, G. J. Schrobilgen, S. J. Sutherland, *J. Chem. Soc., Chem. Commun.* **1982**, 210–211.
(50) G. A. Schumacher, G. J. Schrobilgen, *Inorg. Chem.* **1983**, *22*, 2178–2183.
(51) G. A. Schumacher, G. J. Schrobilgen, *Inorg. Chem.* **1984**, *23*, 2923–2929.
(52) R. G. Syvret, K. M. Mitchell, J. C. P. Sanders, G. J. Schrobilgen, *Inorg. Chem.* **1992**, *31*, 3381–3385.
(53) R. G. Syvret, G. J. Schrobilgen, *Inorg. Chem.* **1989**, *28*, 1564–1573.
(54) R. G. Syvret, G. J. Schrobilgen, *J. Chem. Soc., Chem. Commun.* **1985**, 1529–1530.
(55) J. Mason, Multinuclear NMR, Ed. J. Mason, Plenum Press: New York, 1987, 623–629.
(56) M. Biswal, M. Body, C. Legein, G. Corbel, A. Sadoc, F. Boucher, *J. Phys. Chem. C* **2012**, *116*, 11682–11693.
(57) S. A. Joyce, J. R. Yates, C. J. Pickard, S. P. Brown, *J. Am. Chem. Soc.* **2008**, *130*, 12663−12670.
(58) I. Hung, A.-C. Uldry, J. Becker-Baldus, A. L. Webber, A. Wong, M. E. Smith, S. A. Joyce, J. R. Yates, C. J. Pickard, R. Dupree, S. P. Brown, *J. Am. Chem. Soc.* **2009**, *131*, 1820−1834.
(59) J. M. Griffin, J. R. Yates, A. J. Berry, S. Wimperis, S. E. Ashbrook, *J. Am. Chem. Soc.* **2010**, *132*, 15651−15660.
(60) J. R. Yates, *Magn. Reson. Chem.* **2010**, *48*, S23−S31.

(61) C. Bonhomme, C. Gervais, C. Coelho, F. Pourpoint, T. Azaïs, L. Bonhomme-Coury, F. Babonneau, G. Jacob, M. Ferrari, D. Canet, J. R. Yates, C. J. Pickard, S. A. Joyce, F. Mauri, D. Massiot, *Magn. Reson. Chem.* **2010**, *48*, S86−S102.
(62) N. S. Barrow, J. R. Yates, S. A. Feller, D. Holland, S. E. Ashbrook, P. Hodgkinson, S. P. Brown, *Phys. Chem. Chem. Phys.* **2011**, *13*, 5778−5789.
(63) C. Roehr, R. Kniep, *Z. Naturforsch., B: Chem. Sci.* **1994**, *49*, 650–654.
(64) Z. Mazej, R. Hagiwara, *J. Fluorine Chem.* **2007**, *128*, 423–437.
(65) K. Kitashita, R. Hagiwara, Y. Ito, O.J. Tamada, *J. Fluorine Chem.* **2000**, *101*, 173–179.
(66) R. Hagiwara, K. Kitashita, Y. Ito, O. Tamada, *Solid State Sci.* **2000**, *2*, 237–241.
(67) E. Goreshnik, Z. Mazej, *Solid State Sci.* **2008**, *10*, 303–306.
(68) R. Challoner, T. Schaller, A. Sebald, *J. Magn. Reson. A* **1993**, *101*, 106–108.
(69) H. Bode, H. Clausen, *Z. Anorg. Allg. Chem.* **1951**, *265*, 229–243.
(70) G. R. Miller, H. S. Gutowsky, *J. Chem. Phys.* **1963**, *39*, 1983–1994.
(71) H. S. Gutowsky, S. Albert, *J. Chem. Phys.* **1973**, *58*, 5446–5452.
(72) A. M. Heyns, C. W. F. T. Pistorius, *Spectrochim. Acta, Part A* **1974**, *30*, 99–116.
(73) A. N. Fitch, J. K. Cockcroft, *Phase Transitions* **1992**, *39*, 161–170.
(74) P. Huber, H. Krummeck, J. Baller, J. K. Krüger, K. Knorr, S. Haussühl, *Ferroelectrics* **1997**, *203*, 211–219.
(75) H. Sowa, H. Ahsbahs, *Z. Kristallogr.* **1999**, *214*, 751–757.
(76) PDF-4+ Database; The International Centre for Diffraction Data (ICDD): Newtown Square, PA, 2007.
(77) J. R. Rodriguez-Carjaval, FULLPROF: A Program for Rietveld Refinement and Pattern Matching Analysis; Abstracts of the Satellite Meeting on Powder Diffraction of the XV Congress of the IUCr, Toulouse, France, **1990**; p 127.
(78) E. L. Muetterties, W. D. Phillips, *J. Am. Chem. Soc.* **1959**, *81*, 1084-1088.
(79) T. Endo, S. Widgeon, P. Yu, S. Sen, K. Nishikawa, *Phys. Rev. B* **2012**, *85*, 054307.
(80) L. Viau, M.-A. Néouze, C. Biolley, S. Volland, D. Brevet, P. Gaveau, P. Dieudonné, A. Galarneau, A. Vioux, *Chem. Mater.* **2012**, *24*, 3128−3134.
(81) L. C. M. Van Gorkom, J. M. Hook, M. B. Logan, J. V. Hanna, R. E. Wasylishen, *Magn. Reson. Chem.* **1995**, *33*, 791–795.
(82) A. Bielecki, D. P. Burum, *J. Magn. Reson., Ser. A* **1995**, *116*, 215–220.
(83) D. Massiot, F. Fayon, M. Capron, I. King, S. Le Calvé, B. Alonso, J. O. Durand, B. Bujoli, Z. H. Gan, G. Hoatson, *Magn. Reson. Chem.* **2002**, *40*, 70–76.
(84) J. P. Perdew, K. Burke, M. Ernzerhof, *Phys. Rev. Lett.* **1996**, *77*, 3865−3868.

Conclusions and perspectives

The work presented in this thesis describes the application of GIPAW method to inorganic fluoride materials.

It has been shown that, when using the PBE[1] exchange-correlation functional for the treatment of the cationic localized empty orbitals of Ca^{2+}, Sc^{3+}(3d) and La^{3+}(4f), a correction of the ultra-soft pseudopotential (USPP) is needed to accurately calculate ^{19}F shieldings. A correlation has then been established on alkali, alkaline earth and rare earth fluorides[2] and further improved on column 13 metal fluorides[3] and on columns 11, 12 and 14 metal fluorides. It allows predicting ^{19}F NMR spectra of crystalline compounds with a relatively good accuracy. Indeed, it has been successfully applied on to $RbLaF_4$,[4] $NaAsF_6$[5] and α-$LaZr_2F_{11}$,[6] and a similar correlation has been obtained for TaF_5. The last correlation established on twenty four binary fluorides containing twenty different metal atoms admits few exceptions (Nb, Ag and Th). In addition, we experimentally determine the quadrupolar parameters of ^{25}Mg in MgF_2, ^{71}Ga in GaF_3 and ^{115}In in InF_3, and calculate the EFG of ^{25}Mg in MgF_2, ^{27}Al in α-, β- and η-AlF_3, ^{67}Zn in ZnF_2, ^{69}Ga in GaF_3, ^{115}In in InF_3 and ^{139}La in LaF_3 using PAW and/or LAPW methods.

Calculations were achieved on experimental and APO structures (when allowed by symmetry) and the effects of optimization were carefully examined. APO structures are retained except when the agreement between experimental and calculated EFG is better with the experimental one. The study of α-AlF_3, GaF_3 and InF_3 confirms the care that must be taken when dealing with optimized structures. The orientations of the EFG components in the crystallographic frame, provided by DFT calculations, have been given for all quadrupolar nuclei and analyzed in terms of electron densities for ^{25}Mg in MgF_2 and ^{139}La in LaF_3.

We have then studied binary fluorides having multiple crystallographic sites with the aim to assign the ^{19}F NMR resonances to their fluorine crystallographic sites. The studied binary fluorides are column 5 fluorides (TaF_5 and NbF_5[7]) and MF_4 compounds (M = Zr, Hf (column 4), Ce and Th). Complete and unambiguous assignment of the ^{19}F NMR lines from GIPAW calculations are achieved for TaF_5 and NbF_5, ensured by the linearity between experimental ^{19}F δ_{iso} values and calculated ^{19}F σ_{iso} values. The study of the MF_4 compounds containing seven fluorine crystallographic sites and characterized by small or very small ^{19}F chemical shift ranges was particularly challenging. Moreover ^{19}F-^{19}F correlation experiments were performed only for β-ZrF_4 and HfF_4 having the smallest chemical shift ranges (~20 ppm). No confident assignment could be established as some isotropic lines overlap inducing lack of resolution in the correlation peaks. From GIPAW calculations, only one complete and confident assignment is obtained, from the APO structure of ThF_4. The ^{19}F chemical

shift range being two times larger compared to β-ZrF_4 and HfF_4, a better resolved ^{19}F DQ-SQ correlation spectrum is expected and could ascertain this assignment.

Finally, two ternary fluorides, $NaAsF_6$ and KPF_6, exhibiting large ^{19}F-X ^1J-coupling resolved on 1D MAS NMR spectra and phase transitions at temperatures close to room temperature have been investigated by DTA or DSC, temperature controlled X-ray powder diffraction (XRPD) and variable temperature solid-state NMR. The crystalline structures of α-and β-$NaAsF_6$ have been determined from XRPD data and thus ^{19}F, ^{23}Na and ^{75}As NMR parameters have been calculated.[5] Two difficulties were encountered: the libration of the rigid and regular AsF_6^- anions in the β-phase, highlighted by the atomic anisotropic displacement parameters for F, which leads to erroneous shortened As-F bond length, and the overestimation of the As-F bond length with the PBE functional used in the density functional theory calculations. We show that both difficulties can be overcome by full optimization and rescaling of the cell parameters of the crystalline structures.

KPF_6 adopts an orientationally disordered high symmetry structure at room temperature (phase I) and presents phase transitions when cooled. The structure of the monoclinic phase (phase II) is expected to be ordered, so ^{31}P-^{19}F ^1J-coupling calculations could be carried out. Two F sites and two P sites have been identified from NMR spectra of this phase. Unfortunately, attempts to determine the atomic positions remain unsuccessful. The structural determinations of this phase and the rhombohedral one, whose occurrence has been evidenced between phases I and II, are still in progress.

The work described above has demonstrated the potential of GIPAW calculations for the prediction of NMR parameters of inorganic fluorides. However, the agreement between calculated and experimental EFG is most often better when calculations are carried out using the WIEN2k code. For these parameters, we will still use both codes. The GIPAW method will be used for calculations of NMR parameters on the numerous compounds we study in collaboration with our colleagues from the department of Oxydes et Fluorures, from ICMCB (Pessac), from PECSA (Paris) or from ICCF (Clermont-Ferrand). Application of this method to inorganic oxifluorides is promising as solid state NMR experiments combined with GIPAW calculations are powerful tools to characterize the F/O ordering in such compounds. The use of super-cells is required if F and O are distributed on the same anionic site. For instance, calculations are in progress on nanostructured fluorinated anatase with cationic vacancies ($Ti_{1-x}\square_xF_{4x}O_{2-4x}$).

Finally, some limitations have been encountered. They are certainly partly due to the fact we study fluorides compounds with numerous different metal atoms. A particular attention was paid to

the fluorine USPP and GIPAW results using PBE-DFT were faced to GIAO ones using all-electrons basis sets for a benchmark of molecules. The perfect agreement proves the correctness of the fluorine USPP.[2] However, most of the metal atom studied in this manuscript have not been so extensively studied preventing the refinement of their pseudopotentials. Clearly in the future, USPP evaluation needs to be extended to nuclei that have not been as well studied, giving the ability to perform calculations on any system with confidence.[8]

References

(1) J. P. Perdew, K. Burke, M. Ernzerhof, *Phys. Rev. Lett.***1996**, *77*, 3865−3868.

(2) A. Sadoc, M. Body, C. Legein, M. Biswal, F. Fayon, X. Rocquefelte, F. Boucher, *Phys. Chem. Chem. Phys.* **2011***, 13,* 18539-18550.

(3) A. Sadoc, M. Biswal, M. Body, C. Legein, F. Boucher, D. Massiot, F. Fayon, submitted to *Solid State Nucl. Magn. Reson.*, September 11th 2013.

(4) A.-L. Rollet, M. Allix, E. Veron, M. Deschamps, V. Montouillout, M. R. Suchomel, E. Suard, M. Barré, M. Ocaña, A. Sadoc, F. Boucher, C. Bessada, D. Massiot, F. Fayon, *Inorg. Chem.* **2012**, *51*, 2272–2282.

(5) M. Biswal, M. Body, C. Legein, G. Corbel, A. Sadoc, F. Boucher, *J. Phys. Chem. C* **2012**, *116*, 11682–11693.

(6) C. Martineau, C. Legein, M. Body, O. Péron, B. Boulard, F. Fayon, *J. Solid State Chem.***2013**, *199*, 326–333.

(7) M. Biswal, M. Body, C. Legein, A. Sadoc, F. Boucher, *J. Solid State Chem.* **2013**, *207*, 208-217.

(8) C. Bonhomme, C. Gervais, F. Babonneau, C. Coelho, F. Pourpoint, T. Azaïs, S. E. Ashbrook, J. M. Griffin, J. R. Yates, F. Mauri, C. J. Pickard, *Chem. Rev.* **2012**, *112*, 5733−5779.

Annexes

Annex 1: parameters used to generate the on-the-fly ultrasoft pseudopotentials

In Table 1 are gathered the parameters used to generate the on-the-fly (OTF) ultrasoft pseudopotentials used in the manuscript, except the OTF USPP used in section 2.2, which are given in the ESI of the paper. Details on the string can be found on the Castep website (http://www.castep.org/) in the documentation section.

Table 1. Parameters used to generate the OTF USPP pseudopotentials.

Atom	OTF USPP string
Ag	1|2.2|2.3|1.6|9|11|12|50U=-0.185U=+0.4:42U=-0.3U=+0[]
Al	2|2|3.675|5.512|7.717|30UU:31UU:32LGG[]
As	2|1.6|1.6|0.9|6|7.3|9.9|40U=-0.54U=+0.5:41U=-0.195U=+0.25[]
Cd	1|2.2|2.2|1.6|8.7|9.6|10.7|50U+0U+0.1:42UU(qc=5,q0=4)[]
Ce	2|2.1|2|1.3|8|11|13|50U:60U:51UU:52L:43UU(qc=6)[]
Ga	3|2|2|1.5|9.9|11|12.4|40U=-0.335U=+0.25:41U=-0.1U=+0.25:32U=-0.715U=+0.25[]
Hf	1|2.4|2.4|1.2|6.6|8.5|11.3|60U=-0.195U=+1.75:52U=-0.105U=+0[]
Hg	1|2.2|2.2|1.7|11.8|13.6|15.3|60UU:61P:52UU[]
In	3|2.3|2.3|1.6|9|10.5|12|50UU:51UU:42UU[]
Na	2|1.3|1.3|1|11.8|13.6|15.3|20U=-2.07:30U=-0.105:21U=-1.06U=+0.25[]
Nb	3|2.2|2.2|1|7.7|8.8|10|40U=-2.145:50U=-0.145:41U=-1.27U=+0.25:42U=-0.1U=+0[]
Pb	3|2.4|2.35|1.6|9.2|12.9|16.5|60UU:61UU:52UU[]
Ta	1|2.4|2.4|1.2|7|8.8|10|60U=-0.2U=+1.75:52U=-0.14U=+0[]
Th	2|2.0|2.0|1.6|6|12|13|60U:70U:61:53:62P(qc=6)[]
Tl	3|2.4|2.4|1.9|8.5|9.6|11|60UU:61U+0U+0.5:52UU(qc=4.5)[]
Zn	3|2|2|1|10.8|11.5|12.5|40UU:41UU:32UU(qc=6)[]
Zr	3|2.1|2.1|1.05|8.5|10|11.4|40U=-2.005:50U=-0.17:41U=-1.195U=+0.1:42U=-0.135U=+0.25[]

Annex 2: publications and communications

A2.1 Publications

1) "NMR parameters in alkali, alkaline earth and rare earth fluorides from first principle calculations"
A. Sadoc, M. Body, C. Legein, M. Biswal, F. Fayon, X. Rocquefelte, F. Boucher
Phys. Chem. Chem. Phys. 2011*,* 13*,* 18539-18550.

2) "Structural investigation of α- and β-sodium hexafluoroarsenate, $NaAsF_6$, by variable temperature X-ray powder diffraction and Multinuclear Solid-State NMR and DFT calculations"
M. Biswal, M. Body, C. Legein, G. Corbel, A. Sadoc, F. Boucher
J. Phys. Chem. C 2012, 116, 11682-11693.

3) "NbF_5 and TaF_5: Assignment of ^{19}F NMR Resonances from GIPAW Calculations"
M. Biswal, M. Body, C. Legein, A. Sadoc, F. Boucher
J. Solid State Chem. 2013, 207, 208–217.

4) "NMR parameters in column 13 metal fluoride compounds (AlF_3, GaF_3, InF_3 and TlF) from first principle calculations"
A. Sadoc, M. Biswal, M. Body, C. Legein, F. Boucher, D. Massiot, F. Fayon
Submitted to *Solid Sate Nucl. Magn. Reson.* September 11th 2013.

A2.2 Oral communications

1) "Calculs de paramètres RMN du ^{19}F par la méthode GIPAW"
Réseau RMN structurale dans le Bassin Parisien, Journée Hiver 2009/2010, 18 Janvier 2010, Collège de France, Paris
A. Sadoc, F. Boucher, M. Biswal, M. Body, C. Legein

2) "NMR parameters in fluorides from first principles calculations"
ICAMM 2010, 1st edition of the International Conference on Advanced Materials Modelling, July 8-10, 2010, Nantes
A. Sadoc, F. Boucher, M. Biswal, M. Body, C. Legein

3) "Structural investigation of α- and β-$NaAsF_6$ by coupling variable temperature X-ray powder diffraction, multinuclear solid state NMR and ab-initio calculations"
Réseau RMN structurale dans le Bassin Parisien, Journée Hiver 2011, 20 Janvier 2011, CEA-Saclay, IRAMIS – SIS2M
M. Biswal, M. Body, G. Corbel, C. Legein, A. Sadoc, F. Boucher

4) "First-principles quantum-mechanical methods for full prediction of NMR parameters in fluorides"
75th Annual Meeting of the DPG and DPG Spring Meeting, 13th - 18th March 2011, Dresden, Germany
A. Sadoc, F. Boucher, M. Biswal, M. Body, C. Legein

5) "Structural investigation of α- and β-$NaAsF_6$ by coupling variable temperature X-ray powder diffraction, multinuclear solid-state NMR and ab-initio calculations"
Journées de l'Ecole Doctorale (JED) 3MPL 2011, June 30th & July 1st, Le Mans, France
M. Biswal

6) "Détermination ab initio de paramètres RMN du ^{19}F dans des fluorures cristallisés (Round n°2)"
Réseau RMN structurale dans le Bassin Parisien, Journée Eté 2011- IMN Jean Rouxel – Nantes, 23 Juin 2011
F. Boucher, A. Sadoc, M. Biswal, M. Body, C. Legein

7) "NMR parameters in basic fluorides from first-principles calculations"
Conférenceinvité**,** 8thJapanese-French Joint Seminar on Fluorine Chemistry, Kyoto, Japan, July19-21, 2012
M. Body, A. Sadoc, M. Biswal, C. Legein, F. Boucher, F. Fayon

8) "Structural investigation of alpha and beta sodium hexafluoroarsenate by variable temperature X-ray powder diffraction and multinuclear solid-state NMR and DFT calculations"
20th International Symposium on Fluorine Chemistry, Kyoto, Japan, July 22-27, 2012
M. Body, M. Biswal, C. Legein, G. Corbel, A. Sadoc, F. Boucher

9) "NbF_5 and TaF_5: assignment of ^{19}F NMR resonances from first principles calculations"
Réseau RMN structurale dans le Bassin Parisien, Journée Hiver 2013, 15 Janvier 2013, Orléans
M. Body, M. Biswal, C. Legein, A. Sadoc, F. Boucher

10) "Assignment of ^{19}F NMR resonances and prediction of ^{19}F isotropic chemical shifts of inorganic fluorides: α-$LaZr_2F_{11}$, NbF_5 and TaF_5"
Conférence invité**,** 17th European Symposium on Fluorine Chemistry, France, Paris, July 21-25, 2013
C. Legein**,** M. Biswal**,** M. Body, F. Fayon, F. Boucher, C. Martineau, A. Sadoc

A2.3 Poster communications

1) "Solid state NMR and modelisation of the parameters of inorganic fluoride materials"
Journées de l'Ecole Doctorale (JED) 3MPL 2010, 23 & 24juin 2010, Nantes, France
M. Biswal

2) "NMR parameters in alkali, alkaline earth and rare earth basic fluorides from first principles quantum mechanical calculations"
7th French - Japanese Seminar on Fluorine in Material Chemistry and Electrochemistry, May 25-27, 2011, Le Mans – Brissac, France
C. Legein, A. Sadoc, M. Body, M. Biswal, X. Rocquefelte, F. Fayon, F. Boucher

3) "NMR parameters in alkali, alkaline earth basic fluoridesfrom first principles quantum mechanical calculations"
7th Alpine Conference on Solid State NMR, 11th-15th September, 2011, Chamonix, France
A. Sadoc, M. Body, C. Legein, M. Biswal, X. Rocquefelte, F. Fayon, F. Boucher

4) "Structural investigation of α- and β-$NaAsF_6$ by coupling temperature controlled X-ray powder diffraction, multinuclear solid state NMR and *ab-initio* calculations"

7^{th} Alpine Conference on Solid State NMR, 11^{th}-15^{th} September, 2011, Chamonix, France

M. Biswal, M.Body, A. Sadoc, G. Corbel, F. Boucher, C. Legein

5) "High resolution solid-state NMR and modelisation of the parameters of inorganic fluoride materials"

Forum Jeunes Recherche, Université du Maine, 16 Novembre 2011

M. Biswal

l'université nantes angers le mans
PÔLE DE RECHERCHE ET D'ENSEIGNEMENT SUPÉRIEUR

Université du Maine
Le Mans - Laval

Thèse de Doctorat

Mamata BISWAL

Détermination et calcul premiers principes, par la méthode PAW/GIPAW de paramètres RMN de fluorures inorganiques

Determination and first principles calculations, using the PAW/GIPAW method, of NMR parameters in inorganic fluorides

Résumé

Cette thèse porte sur la détermination et la modélisation, par la méthode PAW/GIPAW (Gauge Including Projector Augmented Waves), de paramètres RMN de fluorures inorganiques.
Dans la première partie, une corrélation entre valeurs expérimentales de déplacements chimiques isotropes (δ_{iso}) de ^{19}F et de constantes d'écran isotropes (σ_{iso}) de ^{19}F calculées de fluorures binaires, dont les attributions sont triviales, est établie. Elle permet de prédire les spectres RMN de ^{19}F avec une bonne précision. Les paramètres quadripolaires de ces fluorures sont aussi déterminés et calculés.
Dans la seconde partie, la linéarité entre valeurs expérimentales de δ_{iso} de ^{19}F et valeurs calculées de σ_{iso} de ^{19}F permet une attribution non ambigüe des raies RMN de ^{19}F de NbF_5 et TaF_5. Par contre, pour trois des quatre composés MF_4 étudiés (β-ZrF_4, HfF_4, CeF_4, ThF_4), caractérisés par des gammes de valeurs de δ_{iso} de ^{19}F plus petites, les corrélations médiocres entre valeurs de δ_{iso} et de σ_{iso} de ^{19}F ne le permettent pas.
Enfin, $NaAsF_6$ et KPF_6 qui présentent des valeurs élevées de couplage ^1J ^{19}F-X et des transitions de phase à des températures proches de l'ambiante sont étudiés par DTA ou DSC et diffraction des rayons X sur poudre et RMN du solide multinucléaire à température variable. Les structures de α- et β-$NaAsF_6$ sont déterminées. KPF_6 adopte une structure de haute symétrie désordonnée à température ambiante mais les tentatives de détermination des positions atomiques des deux premières phases basse température sont restées vaines.
Ce travail souligne les potentialités et quelques limites de cette méthode ainsi que l'attention qui doit être prêtée aux effets des optimisations.

Mots clés
RMN du solide, Calculs DFT, Fluorures inorganiques

Abstract

This thesis focuses on the determination and the modeling, by the PAW/GIPAW (Gauge Including Projector Augmented Waves) method, of NMR parameters in inorganic fluorides.
In the first part, a correlation between experimental ^{19}F isotropic chemical shift (δ_{iso}) and calculated ^{19}F isotropic shieldings (σ_{iso}) of binary fluorides with obvious assignments is established that allows to predict ^{19}F NMR spectra with a good accuracy. The quadrupolar parameters of these fluorides are also determined and calculated.
In the second part, a complete and unambiguous assignment of the ^{19}F NMR lines of NbF_5 and TaF_5 is obtained, ensured by the linearity between experimental ^{19}F δ_{iso} values and calculated ^{19}F σ_{iso} values. On the other hand, for the studied MF_4 (β-ZrF_4, HfF_4, CeF_4, ThF_4) compounds, characterized by smaller ^{19}F δ_{iso} ranges, except for ThF_4, the poor correlations between experimental ^{19}F δ_{iso} and calculated ^{19}F σ_{iso} values prevent us to propose an assignment of the ^{19}F NMR lines.
In the last part, $NaAsF_6$ and KPF_6, exhibiting large ^{19}F-X ^1J-coupling and phase transitions at temperatures close to room temperature (RT) are investigated by DTA or DSC and variable temperature X-ray powder diffraction and multinuclear solid-state NMR. The structures of α- and β-$NaAsF_6$ are determined. KPF_6 adopts a disordered high symmetry structure at RT. Unfortunately, attempts to determine the atomic positions of the two first low temperature phases remain unsuccessful.
This work highlights the potentialities and some limitations of this method as well as the care that must be taken when dealing with optimized structures.

Key Words
Solid State NMR, DFT calculations, Inorganic Fluorides